HEINZ-MAIER LEIBNITZ ZENTRUM
UND FAKULTÄT FÜR PHYSIK

Instrumentation of the Positron Diffractometer at NEPOMUC and Measurements on Epitaxial Graphene Grown on 6H-SiC(0001)

DISSERTATION
VON

MATTHIAS RALPH DODENHÖFT

TECHNISCHE UNIVERSITÄT MÜNCHEN

TECHNISCHE UNIVERSITÄT MÜNCHEN

Fakultät für Physik

Instrumentation of the Positron Diffractometer at NEPOMUC and Measurements on Epitaxial Graphene Grown on 6H-SiC(0001)

Matthias Ralph Dodenhöft

Vollständiger Abdruck der von der Fakultät für Physik der Technischen Universität München zur Erlangung des akademischen Grades eines

Doktors der Naturwissenschaften (Dr. rer. nat.)

genehmigten Dissertation.

Vorsitzender:		Prof. Dr. Martin Zacharias
Prüfer der Dissertation:	1.	Prof. Dr. Christoph P. Hugenschmidt
	2.	Prof. Dr. Winfried Petry

Die Dissertation wurde am 16.05.2022 bei der Technischen Universität München eingereicht und durch die Fakultät für Physik am 31.08.2022 angenommen.

Abstract

The knowledge of the surface structure plays a crucial role for understanding a variety of physical phenomena and is a prerequisite to calculate the electronic band structure of the surface. The structure of topmost and subsurface atomic layers can be precisely determined using Total-Reflection High-Energy Positron Diffraction (TRHEPD), which features outstanding surface sensitivity due to the repulsive crystal potential for positrons.

On these grounds, we developed a new positron diffractometer at the NEutron induced POsitron source MUniCh (NEPOMUC) located at the research reactor FRM II in Garching. To adapt the remoderated NEPOMUC beam for diffraction experiments in grazing incidence, we designed and tested several customized components comprising the magnetic field termination, the optional transmission-type remoderator for brightness enhancement as well as the electrostatic lens system for acceleration and beam optics. The lens system allows beam energies of up to 20 keV and has been optimized by simulations to obtain a parallel positron beam of small diameter. For the 10 keV twofold remoderated beam, we experimentally achieved a beam diameter of less than 1.3 mm, which agrees well with the simulation. The new TRHEPD setup will particularly benefit from the continuous beam and the unprecedented positron intensity of NEPOMUC, thus reducing the measurement time and allowing the resolution of weaker diffraction spots as well.

By employing TRHEPD rocking curves analysis, we determined the interlayer spacings of Monolayer Graphene (MLG) and hydrogen intercalated Quasi-Free-Standing Monolayer Graphene (QFMLG) grown on 6H-SiC(0001). For QFMLG, the spacing between the graphene layer and the SiC substrate was determined to be $d_{\mathrm{QFMLG}} = (4.18 \pm 0.06)\,\text{Å}$, which is in excellent agreement with DFT calculations from Sforzini *et al.* [1]. For the buckled structure of MLG, we find average graphene and buffer layer spacings of $d_{\mathrm{MLG}} = (5.81 \pm 0.08)\,\text{Å}$ and $d_{\mathrm{buffer}} = (2.34 \pm 0.08)\,\text{Å}$ with respect to the top Si layer of the substrate. These values are in good agreement with DFT calculations, the magnitude of buckling, however, was found to be significantly smaller than theoretically predicted, but in the same range as reported for complementary (synchrotron-based) measurement techniques.

Kurzfassung

Die Kenntnis der Oberflächenstruktur spielt eine entscheidende Rolle für das Verständnis einer Vielzahl physikalischer Phänomene und ist eine Grundvoraussetzung für die Berechnung der elektronischen Bandstruktur der Oberfläche. Die Struktur der obersten und darunter liegenden Atomschichten lässt sich mit Hilfe der hochenergetischen Positronenbeugung (TRHEPD) präzise bestimmen, die sich aufgrund des abstoßenden Kristallpotentials für Positronen durch eine hervorragende Oberflächenempfindlichkeit auszeichnet.

Aus diesen Gründen haben wir ein neues Positronendiffraktometer entwickelt das sich an der Neutronen-induzierten Positronenquelle München (NEPOMUC) am Forschungsreaktor FRM II in Garching befindet. Um den remoderierten NEPOMUC-Strahl für Beugungsexperimente unter streifendem Einfall zu adaptieren, haben wir mehrere speziell angepasste Komponenten entwickelt und getestet, darunter den Magnetfeldabschluss, den optionalen Transmissions-Remoderator zur Erhöhung der Strahlbrillianz sowie das elektrostatische Linsensystem für die Beschleunigung und Strahloptik. Das Linsensystem erlaubt Strahlenergien von bis zu 20 keV und wurde durch Simulationen optimiert, um einen parallelen Positronenstrahl mit kleinem Durchmesser zu erhalten. Für den zweifach remoderierten Strahl mit 10 keV Energie haben wir experimentell einen Strahldurchmesser von weniger als 1,3 mm erreicht, was gut mit der Simulation übereinstimmt. Der neue TRHEPD-Aufbau wird insbesondere von dem kontinuierlichen Strahl und der beispiellosen Positronenintensität von NEPOMUC profitieren, wodurch die Messzeit verkürzt wird und auch die Auflösung schwächerer Beugungsreflexe möglich ist.

Durch die Analyse von TRHEPD Rockingkurven haben wir die Zwischenschichtabstände von Graphen Monolagen (MLG) und Wasserstoff interkalierten quasi-frei-stehenden Graphen Monolagen (QFMLG) bestimmt, die auf 6H-SiC(0001) gewachsen wurden. Für QFMLG wurde der Abstand zwischen der Graphenschicht und dem SiC Substrat zu $d_{\mathrm{QFMLG}} = (4.18 \pm 0.06)\,\text{Å}$ bestimmt, was hervorragend mit DFT Berechnungen von Sforzini *et al.* übereinstimmt [1]. Für die gewölbte Struktur von MLG finden wir durchschnittliche Graphen- und Pufferschichtabstände von $d_{\mathrm{MLG}} = (5.81 \pm 0.08)\,\text{Å}$ und $d_{\mathrm{buffer}} = (2.34 \pm 0.08)\,\text{Å}$ relativ zur obersten Si Lage des Substrats. Diese Werte stimmen gut mit DFT

Berechnungen überein, das Ausmaß der Graphen Wölbung ist jedoch deutlich geringer als theoretisch vorhergesagt, liegt aber in demselben Bereich wie bei komplementären (Synchrotron-basierten) Messverfahren.

Contents

1

Chapter 1.

Introduction

The surface is probably the most intriguing part of a solid because it represents the interface with the environment and often features distinct physical properties. In general, solid surfaces are characterized by their elementary composition, the chemical bonds and the surface structure [2]. On the other hand, the complexity of surfaces is usually significantly higher than for the bulk. Besides the abundant compositions and structures, there is a variety of surface-related processes that have to be considered, e.g. adsorption, segregation or reconstruction [3].

The research of surfaces is not only fascinating from a fundamental point of view, but also relevant for various industrial applications, ranging from ultra-thin coatings to heterogeneous catalysis or semiconductor device fabrication [4]. In fact, surface engineering plays a key role in the development of functional materials and future technologies, enabling a better and more sustainable life. Coated or nano-structured surfaces can, e.g., enhance the device functionality and simultaneously reduce the consumption of limited natural resources. Moreover, harvesting renewable sources of energy would not have been possible without the persistent progress in catalysis (e.g. for fuel cells) and thin film technology (e.g. for photovoltaic) [5].

For the modern information and communication technology, electronic structures are miniaturized down to the nanometer scale, which inherently requires to consider surface effects. Naturally, there are physical and technological limitations of silicon-based devices, motivating a progressive search for novel materials, which need to be characterized comprehensively. One promising candidate is graphene, a monoatomic crystalline layer of carbon atoms that was the first two-dimensional (2D) material experimentally investigated [6]. Since its discovery, graphene has demonstrated several intriguing properties, e.g. the relativistic nature of its charge carriers or the extremely high heat conductivity [7] and mechanical strength [8, 9], thus attracting enormous attention in both academia and industry. More recent research comprises the stacking of various 2D materials with different electronic properties to realize van der Waals heterostructures [10, 11]. Apart from the manifold possibilities of combination, the interlayer twist angle is a further parameter that can be tuned to study emergent phenomena, such as unconventional superconductivity [12], Wigner crystals [13] or (ultra-)flat electronic bands [14, 15]. In this regard, the interaction of the graphene layer (or other 2D materials) with the substrate surface has to be considered, which strongly influences the electronic structure but can also cause substantial buckling or unintended doping, thereby deteriorating the desired properties.

In general, the precise knowledge of the crystalline surface structure is particularly important to understand the interaction of individual atoms or overlayers with the substrate. Furthermore, realistic models of the surface structure are necessary to accurately calculate the electronic band structure of the surface [16, 17]. Since most surface structures are rather complex, a variety of different measurement techniques has been evolved, which are often used as complementary analysis tools.

In this context, Total-Reflection High-Energy Positron Diffraction (TRHEPD), i.e. positron diffraction in grazing incidence, has demonstrated to be an ideal technique to determine the crystalline surface structure of topmost and subsurface atomic layers [18]. Positrons inherently experience a repulsive crystal potential and thus exhibit total reflection for small glancing angles. For this reason, TRHEPD allows structure analysis with outstanding surface sensitivity. Furthermore, information about the immediate subsurface layers can be obtained by increasing the glancing angle above the critical angle. However, to exploit the full strength of TRHEPD, the positron beam must have a sufficiently high intensity and brightness, which can only be provided by large-scale research facilities. For this reason, so far, there has been just a single TRHEPD setup available worldwide.

The main objective of the present work was thus the instrumentation and commissioning of a new positron diffractometer, adapted to the specific conditions at the NEutron induced POsitron source MUniCh (NEPOMUC) located at the research reactor FRM II in Garching. The new TRHEPD setup particularly required that sample and detector can be biased to potentials of several kV, which is in contrast to the existing setup based on a Linear Accelerator (LINAC).
Within the framework of this thesis, we further performed TRHEPD measurements on two different graphene samples epitaxially grown on 6H-SiC(0001).

After hydrogen intercalation, this material system is particularly promising because it combines excellent graphene properties with the possibility of wafer-scale fabrication directly on a semi-insulating substrate [19].

This thesis is organized as follows:

In chapter 2 common techniques to generate, transport and manipulate a positron beam are introduced. We review the characteristics of different positron sources and the mechanism of positron moderation in solids, which can be utilized to obtain a monoenergetic beam. Moreover, we discuss the adiabatic transport by magnetic fields and the fundamentals of electrostatic beam optics. Since diffraction experiments require a coherent positron beam, positron remoderation, which has been employed to enhance the brightness and coherence length of the beam, is described in more detail.

The measurement technique TRHEPD and its application for surface structure determination are introduced in chapter 3. At first, we provide the theoretical background in surface crystallography and diffraction on a two-dimensional lattice. Conventional techniques for surface structure analysis are briefly reviewed, emphasizing their particular strengths and weaknesses. Subsequently, the benefits of TRHEPD are explained in detail and we derive the refractive index and the condition for total reflection. Furthermore, the established procedure of rocking curve analysis is outlined, i.e. the iterative comparison of calculated and experimental beam intensities, which allows the precise determination of structural parameters.

In chapter 4 we discuss the instrumentation of the positron diffractometer at the high intensity positron source NEPOMUC. We summarize the experimental requirements for TRHEPD and explain the positron beam adaption and detection. Customized elements such as the magnetic field termination, the optional transmission-type remoderator and the electrostatic beam optics are explained in detail. Moreover, simulations of the positron trajectories with and without additional remoderator are presented and compared with the experimental characterization of the direct positron beam. Altogether, we thus demonstrate that the properties of the two-fold remoderated NEPOMUC beam are well suited for diffraction experiments.

In chapter 5 the results from TRHEPD measurements on Monolayer Graphene (MLG) and hydrogen intercalated Quasi-Free-Standing Monolayer Graphene

(QFMLG) grown on 6H-SiC(0001) are presented. To the best of our knowledge, this is the first study of these material systems using TRHEPD. In a first step, the diffraction patterns were analyzed qualitatively by assignment of the observed diffraction spots. The subsequent rocking curve analysis of the specular spot allowed the quantitative determination of the graphene interlayer spacings to the SiC substrate with highest accuracy and in excellent agreement with DFT calculations performed by Sforzini *et al.* [1].

Finally, the results are summarized in chapter 6, including a brief outlook. Since TRHEPD is a rather exotic measurement technique, its full potential has not yet been widely recognized by the scientific community. After having set up a new instrument and further demonstrated the power of TRHEPD, we expect that this work will serve as a useful reference and stimulus for scientist in the field of surface structure analysis.

2

Chapter 2.

Positron physics and beam techniques

The positron is the antiparticle of the electron. In 1930, it has been postulated by P. Dirac as a solution of the Dirac equation for electron states with "negative kinetic energy" [20–22]. Only two years later, in 1932, C. Anderson detected the positron in a cloud chamber during the investigation of cosmic rays [23, 24]. As the electron, the positron has a lifetime of $\tau > 2{\cdot}10^{21}$ years in (ideal) vacuum and is thus a stable antiparticle [25, 26]. However, in matter it annihilates with electrons predominantly into two γ - quanta, each with an energy of $\sim 511\,\mathrm{keV}$. Depending on the material, the positron lifetime is reduced to a timescale in the order of several hundred pico- up to nanoseconds [27].

Since its discovery, the positron has been comprehensively investigated and established as a non-destructive microprobe for bulk [28, 29] and surface [30] analysis. In particular, Positron Annihilation Lifetime Spectroscopy (PALS) has been developed as a standard technique for defect spectroscopy to identify defect types and their respective concentrations [31–33]. A complementary technique for defect analysis is (Coincident) Doppler Broadening Spectroscopy (CDBS), which can additionally provide information about the chemical environment of defects [34, 35]. By measuring the angular correlation of the annihilation γ - quanta (ACAR), positrons can be utilized to study the electronic properties of the sample, i.e. the Fermi surface [36, 37]. To investigate the elementary composition of the surface, Positron annihilation induced Auger Electron Spectroscopy (PAES) can be applied [38]. In comparison to conventional Auger electron spectroscopy, PAES exhibits almost no secondary electron background and features an outstanding surface sensitivity due to the trapping of thermal positrons in surfaces states [39]. Recently, time-resolved PAES has been carried out to observe surface segregation in the systems Cu/Pd [40] and Ni/Pd [41, 42]. Furthermore, information about the crystalline surface structure can be obtained by positron diffraction, as discussed in detail in section 3.3.

In the following, fundamental methods to form, transport and focus a positron beam are introduced. Moreover, positron moderation (section 2.2) and remoderation (section 2.4) are reviewed, which can be employed to create a monoenergetic beam and to enhance the brightness of the beam, respectively.

2.1. Positron sources

Positrons are either produced by β^+ decay of radioactive nuclides or by pair production from high-energy γ-radiation. The positron source and its respective properties play a crucial role in each experiment.

2.1.1. β^+ decay of radioactive nuclides

For experiments in laboratories, radioisotopes are used as small and convenient positron sources. ^{22}Na is the most commonly applied source and has the main decay channel

$$^{22}_{11}Na \longrightarrow \, ^{22}_{10}Ne^* + e^+ + \nu_\mathrm{e}\,. \tag{2.1}$$

^{22}Na is artificially produced in cyclotrons or other accelerators and has a half-life of 2.6 years. Analogous to electrons in the β^- decay, the emitted positrons exhibit a continuous energy spectrum with an endpoint of 545 keV in the case of ^{22}Na [27]. As a result of the parity violation in the weak interaction, positrons from radioisotope sources intrinsically feature right-handed, longitudinal spin-polarization [43, 44]. The main disadvantage is the relatively low intensity, which is limited by self-absorption in the source. For ^{22}Na, beam intensities in the range of 10^4 - 10^5 e^+/s can be obtained [45–47]. For other radioisotope sources with shorter half-life, such as ^{58}Co or ^{64}Cu, beam intensities up to 10^7 e^+/s have been reported [48].

2.1.2. Pair production

Higher beam intensities can be achieved in large-scale facilities, where positrons are generated by pair production via

$$\gamma \longrightarrow e^+ + e^-\,. \tag{2.2}$$

During this fundamental interaction, energy is converted into mass, which is mathematically described by Einstein's famous equation

$$E = m \cdot c^2 \,. \tag{2.3}$$

To satisfy conservation of momentum, pair production can only take place in the vicinity of a third charged particle, that picks up the recoil momentum. This is usually a nucleus or, with much lower probability, an electron [49]. Therefore, the energy of the γ-quantum has to be at least

$$E_{\gamma,min} = 2m_\mathrm{e}c^2 \cdot \left(1 + \frac{m_\mathrm{e}}{m_\mathrm{p}}\right) , \tag{2.4}$$

to provide the rest mass of the electron-positron pair and the kinetic energy transferred to the third particle with mass $\mathrm{m_p}$ [50]. Since the energy transfer to a nucleus is negligible, the threshold energy is $E_\gamma \approx 2m_\mathrm{e}c^2 = 1.022\,\mathrm{MeV}$. If the third particle is an electron, the threshold energy is doubled.

The cross-section for pair production σ_pp depends on the photon energy E_γ and the atomic number Z of the nucleus,

$$\sigma_\mathrm{pp} \propto Z^2 \cdot f(Z, E_\gamma). \tag{2.5}$$

The function $f(Z, E_\gamma)$ changes only slightly with Z and increases logarithmically with E_γ for energies above, but close to the threshold energy [49, 51]. Therefore, high-Z materials are used for an efficient conversion, such as tungsten [52], platinum [53] or tantalum [54]. Different cross-sections for photon interaction are exemplarily shown for tungsten in figure 2.1; pair production is the dominant process for energies above 5 MeV.

There are different possibilities to generate the γ-radiation, that is necessary for pair production. In a Linear Accelerator (LINAC) electrons are accelerated up to energies of several tens of MeV. In the field of a high-Z target material they are rapidly decelerated to produce bremsstrahlung. LINAC-based positron sources are inherently pulsed. Examples of such facilities are the Elbe Positron Source (EPOS) at the Helmholtz-Zentrum Dresden-Rossendorf (HZDR) [56] or the Slow Positron Facility (SPF) at KEK in Japan [57, 58]. In section 3.3.5, the TRHEPD station at the SPF is discussed.

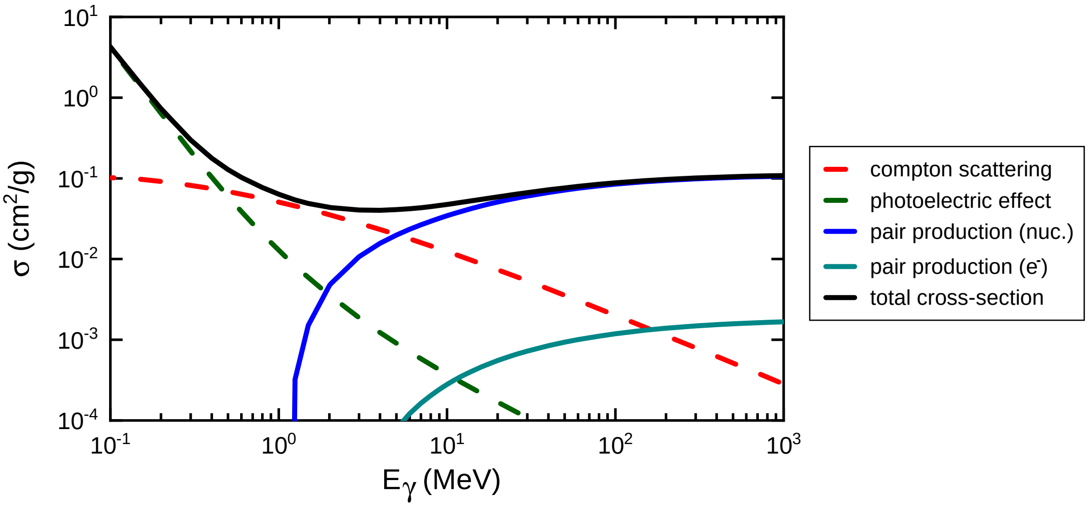

Figure 2.1. Cross-sections for the photoelectric effect, Compton scattering and pair production in tungsten. Pair production in the electric field of nuclei is dominant for energies above ~5 MeV. Data taken from [55].

Alternatively, the γ-radiation that is produced during nuclear fission in a reactor can be used for pair production. This concept is realized at the Research Institute Delft (RID) in the Netherlands [59, 60]. Another reactor-based method relies on thermal neutron capture, which triggers e.g. the nuclear reaction ^{113}Cd (n, γ) ^{114}Cd. The isotope ^{113}Cd has a large cross-section of ~26 000 barn for neutron absorption and subsequently releases the binding energy of 9.05 MeV in a cascade of prompt γ-rays, where an average of 2.3 photons has more than 1.5 MeV energy [61]. This concept has been first realized at the NEutron induced POsitron source MUniCh (NEPOMUC) at the research reactor FRM II in Garching [62, 63] and was later adapted for the positron source at the PULSTAR reactor in the USA [64]. The NEPOMUC facility is introduced in more detail in section 4.1.

There is another method that might be promising for next-generation positron sources. High-energy γ beams can be produced by inverse Compton scattering of laser photons with a relativistic electron beam. This enables the generation of a pulsed, spin-polarized positron beam with high intensity and brightness [65]. Currently, such a source is developed at the Extreme Light Infrastructure - Nuclear Physics (ELI-NP) facility in Bucharest, Romania [66, 67].

2.2. Positron moderation in solids

After β^+ decay or pair production as described in section 2.1, positrons are emitted approximately isotropically and exhibit a continuous energy spectrum up to hundreds of keV or several MeV, depending on the source [68, 69]. However, most techniques, including positron diffraction, require a directional, monoenergetic beam. In general, it is possible to use an energy selective device as filter, but this would lead to a tremendous loss of intensity. The more efficient method to form a monoenergetic beam is *positron moderation*, which is introduced in this section. In the framework of this thesis, we focus on moderation in solids and in particular in metals. Note that moderation in gases is also possible [70], which is commonly applied in buffer-gas traps [71].

2.2.1. Positron work function

Figure 2.2 shows schematically the surface potential at a metal-vacuum interface for a) electrons and b) positrons. For electrons, the chemical potential μ_- is defined by the highest occupied states at the Fermi level with respect to the crystal zero level. Due to the positive dipole barrier Δ, the electron work function Φ^- is positive. In contrast, a thermalized positron can occupy the lowest energy state in its band since there is normally no temporal overlap with other positrons [72]. The positron work function Φ^+ can be calculated as [73]

$$\Phi^+ = -\Delta - \mu_+. \tag{2.6}$$

As the dipole barrier has a negative contribution, Φ^+ can be positive or negative, depending on the material, its surface and crystallographic orientation. In the case of a negative positron work function, it is energetically favorable that positrons at the surface leave the solid. Experimentally, it has been confirmed that thermal positrons are emitted perpendicularly to the surface with an angular distribution of [74, 75]

$$\Theta_{1/2} \simeq \sqrt{\frac{k_B T}{|\Phi^+|}} \tag{2.7}$$

and a well-defined energy of $E_{kin} = -\Phi^+$ that is only thermally smeared [26]. This effect is the foundation for positron moderation and remoderation (see section 2.4) in metals.

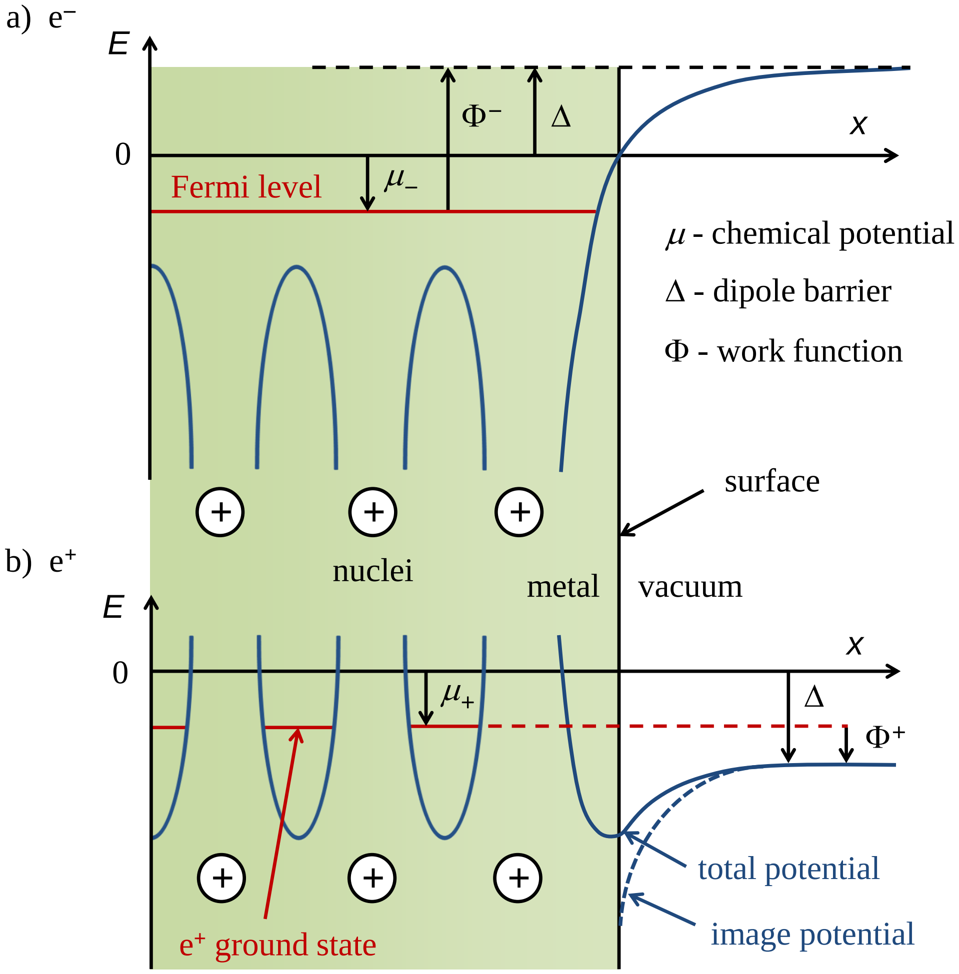

Figure 2.2. Schematic illustration of the potential near a metal surface for a) electrons and b) positrons. The dipole barrier Δ has the opposite sign for electrons and positrons. This can result in a negative positron work function, which leads to the emission of thermalized positrons from the surface. Figure inspired by reference [30].

2.2.2. Interaction in metals

At first, high-energy positrons need to lose their kinetic energy by interaction with matter. When they impinge on a solid body, a variety of phenomena can be observed, as summarized in figure 2.3 for a metal with $\Phi^+ < 0$. A certain fraction is backscattered at the surface, which depends on the positron energy and the atomic number Z of the material. Positrons that enter the metal rapidly lose their kinetic energy by emission of bremsstrahlung and inelastic scattering with core and conduction electrons. At energies in the range of $\sim 100\,\mathrm{eV}$, plasmon excitations become important and at even lower energies of eV down to thermal energy, inelastic phonon scattering is dominant [27, 76]. In metals, the complete thermalization takes place on a timescale of few ps [26]. After thermalization, the positrons scatter quasi-elastically, mainly with longitudinal acoustic phonons, which equals a random walk in the solid and is called *diffusion*. The diffusion length in defect-free crystals is typically in the range of 100 - 200 nm [77] and the timescale, determined by the bulk lifetime of the positron, is roughly 100 ps [78]. During diffusion in the crystal lattice, the positron can be described as a delocalized Bloch state.

Thermal positrons are eventually trapped in open-volume defects such as vacancies, dislocations, grain boundaries or voids, as they represent an attractive potential well [33]. As the energy scale of such defects is in the range of eV for metals, most positrons are unable to escape the trap within their lifetime. The positron wave function localizes at the defect site and the lifetime increases due to the reduced local electron density. Positrons can also be trapped in surface states, where some annihilate with core electrons from surface atoms leading to the emission of Auger electrons or characteristic X-rays. In the context of moderation, all phenomena that include trapping and annihilation are loss mechanisms. Only a small fraction of thermal positrons diffuses to the surface and, in the case of a negative positron work function, is emitted into the vacuum. These positrons can be extracted by electrostatic fields to form a monoenergetic beam. Note that epithermal, i.e. not fully thermalized positrons, can also escape the solid, but they exhibit a broad energy spectrum.

2.2.3. Moderator materials and considerations

Due to the broad energy spectrum of source positrons and depending on the geometry, many are implanted too deep or leave the moderator before complete thermalization. Therefore, the moderation efficiency is normally in the range of 10^{-4} to $5 \cdot 10^{-3}$ [30]. Metals commonly applied for moderation are tungsten ($\Phi^+_W = -3.0\,\text{eV}$ [79]), platinum ($\Phi^+_{Pt} = -1.95\,\text{eV}$ [80]) or nickel ($\Phi^+_{Ni} = -1.4\,\text{eV}$ [81]). To prevent trapping in grain boundaries, moderators are typically single crystalline or have grains that are much larger than the positron diffusion length. The surface should be as flat as possible to avoid trapping in surface states. Moreover, adsorbates have to be removed as they can change the work function locally. This can lead to a broader energy distribution or, if Φ^+ becomes positive, hinders thermal e^+ to escape the solid. An in-situ heat treatment up to $\sim 80\%$

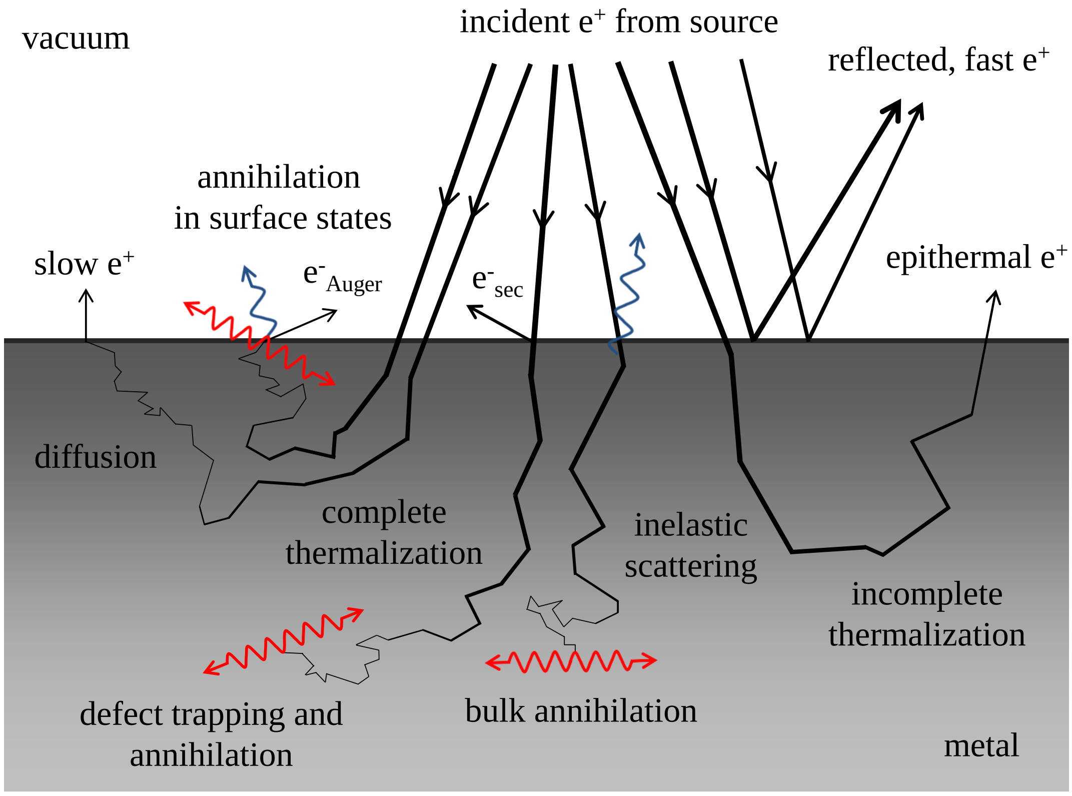

Figure 2.3. Schematic illustration of possible processes when fast positrons from a source are implanted in a metal with $\Phi^{+} < 0$ for moderation. The line width represents the respective kinetic energy, X-rays are depicted blue and γ-rays red. The majority of positrons is reflected at the surface or annihilates in the bulk, after defect trapping or in surface states. Only a small fraction leaves the metal as slow positrons with thermal energy. Note that the emission of epithermal, i.e. not completly thermalized positrons, is also possible. Electrons (secondary and Auger) as well as photons (annihilation, bremsstrahlung and deexcitation of atoms) are emitted, too. Figure inspired by [27].

of the moderator's melting temperature can anneal lattice defects and, even more important, induces the desorption of surface contaminations [27]. Ultra High Vacuum (UHV) in the range of at least 10^{-8} mbar is required to keep the moderator surface clean and decelerate its deterioration over time. During measurements, the moderator can be cooled down to enhance the energy and angular distribution of emitted positrons (see equation 2.7), while extensive condensation of gas molecules on the surface has to be prevented.

Besides metals, semiconductors and insulators can also be applied as moderators. However, due to the band gap, the cross-section for inelastic electron scattering is considerably reduced in the eV range, so that the thermalization process takes much longer [30]. In solid rare gases, positrons do not thermalize completely, but leave the solid with energies of eV despite a positive work function [82]. Compared to metal moderators, solid neon yields a better moderation efficiency, but at the expense of a broader energy distribution [83]. Other materials, such as n-type SiC ($\Phi^{+}_{SiC} \simeq -2.1\,\mathrm{eV}$ [84, 85]) or diamond ($\Phi^{+}_{C} \simeq -4\,\mathrm{eV}$ [86]) have been investigated in the context of field-assisted moderation [87, 88], where an internal electric field induces positrons to drift towards the surface.

2.3. Beam transport and positron optics

Since positrons are charged particles, their motion can be influenced by electromagnetic fields. Analogous to electrons, this can be exploited to transport, accelerate or focus the beam to meet experimental requirements. Particle, or in particular electron optics, is a very large topic that is well beyond the scope of this thesis. In this section, only the fundamental equations and techniques are briefly introduced. For further reading, the textbooks *Principles of Electron Optics* by P. W. Hawkes and E. Kasper [89] as well as *Theory and Design of Charged Particle Beams* by M. Reiser [90] are suggested.

2.3.1. Equation of motion in electromagnetic fields

As the positron density within the beam is low, mutual interactions can be neglected. In electromagnetic fields, a positron with velocity $\vec{v}$ experiences the Lorentz force

$$\vec{F}_L = e\left(\vec{E} + \vec{v} \times \vec{B}\right), \tag{2.8}$$

where $\vec{E}$ is the electric field strength and $\vec{B}$ the magnetic induction. The momentum of a relativistic positron with rest mass m_e is

$$\vec{p} = \gamma m_\mathrm{e} \vec{v} = m_\mathrm{e} \vec{v} \left(1 - \frac{v^2}{c^2}\right)^{-\frac{1}{2}}, \tag{2.9}$$

where γ denotes the Lorentz factor. The equations 2.8 and 2.9 can be combined, using Newton's second law $\vec{F} = \dot{\vec{p}}$, to obtain the equation of motion

$$\dot{\gamma}\dot{\vec{r}} + \gamma\ddot{\vec{r}} = \frac{e}{m_\mathrm{e}}\left(\vec{E} + \dot{\vec{r}} \times \vec{B}\right), \text{ with } \dot{\vec{r}} := \frac{\mathrm{d}\vec{r}}{\mathrm{d}t}. \tag{2.10}$$

In practice, a lot of systems are in good approximation rotational symmetric. Therefore, equation 2.10 is transformed to cylindrical coordinates. This leads to the following set of differential equations [90]:

$$\frac{\mathrm{d}}{\mathrm{d}t}(\gamma\dot{r}) - \gamma r\dot{\varphi}^2 = \frac{e}{m_\mathrm{e}}(E_r + r\dot{\varphi}B_z - \dot{z}B_\varphi) \tag{2.11a}$$

$$\frac{1}{r}\frac{\mathrm{d}}{\mathrm{d}t}(\gamma r^2\dot{\varphi}) = \frac{e}{m_\mathrm{e}}(E_\varphi + \dot{z}B_r - \dot{r}B_z) \tag{2.11b}$$

$$\frac{\mathrm{d}}{\mathrm{d}t}(\gamma\dot{z}) = \frac{e}{m_\mathrm{e}}(E_z + \dot{r}B_\varphi - r\dot{\varphi}B_r), \tag{2.11c}$$

which can be solved analytically only for simple cases. Moreover, to derive universal principles, the Lagrangian formalism has to be applied, which introduces generalized coordinates and potentials to be independent of the coordinate system [91].

2.3.2. Adiabatic transport by magnetic fields

Especially in large-scale facilities, the positron beam has to be transported over long distances to reach the experimental station. This is typically realized in an evacuated beamline, where slow positrons are guided adiabatically by magnetic fields.

Positron trajectory

For this specific case, where $|\vec{E}| = 0$ and $\vec{B} = B\,\vec{e_z}$, equation 2.10 simplifies to

$$\ddot{\vec{r}} = \frac{eB}{\gamma m_\mathrm{e}}\left(\dot{\vec{r}} \times \vec{e_z}\right). \tag{2.12}$$

Here, we considered $\dot{\gamma} = 0$, because static magnetic fields do not change $|\vec{v}|$. Without loss of generality, we define the coordinate system in a way that $\vec{v}(0) = v_\perp\,\vec{e_x} + v_{||}\,\vec{e_z}$. Using this initial condition, the solution to equation 2.12 can be derived as

$$\vec{v}(t) = \begin{pmatrix} v_\perp\cos(\omega_g t) \\ -v_\perp\sin(\omega_g t) \\ v_{||} \end{pmatrix} \quad \text{with} \;\; \omega_g := \frac{eB}{\gamma m_\mathrm{e}}. \tag{2.13}$$

In the plane perpendicular to $\vec{B}$, the positron thus describes a circular motion with gyration frequency ω_g and gyration radius

$$r_g = \frac{v_\perp}{\omega_g} = \frac{\gamma m_\mathrm{e} v_\perp}{eB}. \tag{2.14}$$

Superimposed by the uniform motion in field direction with velocity $v_\parallel \gg v_\perp$, the positron trajectory is a left-handed helix with the gyration length

$$l_g = \frac{2\pi}{\omega_g} v_\parallel = \frac{2\pi\gamma m_\mathrm{e}}{eB} v_\parallel. \tag{2.15}$$

Adiabatic beam guiding

In practice, the magnetic guiding field is generated by solenoid coils that are directly wrapped around the cylindrical beamline or, depending on experimental constraints, by short coils in Helmholtz-like geometry. The transport in the longitudinal magnetic field is called *adiabatic*, if $\vec{B}$ changes only very slowly along the positron trajectory. This means that

$$l_g \left| \frac{\nabla \vec{B}}{B} \right| \ll 1 \tag{2.16}$$

and r_g is essentially constant during one gyration period $T_g = 2\pi/\omega_g$ [90, 92]. Under this condition, it can be shown that the positron spirals along the field lines in a way that the magnetic flux encircled remains constant. Therefore, the physical quantity $r_g^2 B$ is an *adiabatic invariant*, i.e. a constant of motion during adiabatic variations [93, 94]. Using equation 2.14, we find that $p_\perp^2/B$ is an equivalent adiabatic invariant. Consequently, small field perturbations within the beamline do not disrupt the positron transport. Moreover, since the positrons follow the field lines, they can be guided adiabatically around bends if the radius of curvature R is sufficiently large.

Beam drift and compensation

As depicted in figure 2.4 a), weak forces perpendicular to the magnetic guiding field cause a drift of the positron's gyration center with velocity [95]

$$\vec{v}_D = \frac{\vec{F} \times \vec{B}}{eB^2}. \tag{2.17}$$

This is of particular importance in curved sections, where two different effects lead to a significant displacement of the orbit. Firstly, for geometrical reasons, the density of windings on the outer side of the bend is lower than inside, as shown in figure 2.4 b). Consequently, there is a magnetic field gradient directed towards the center of curvature, which leads to a force in the opposite direction. This gives rise to the so-called gradient drift with velocity $\vec{v}_{gr}$. Secondly, there is also the curvature drift with velocity $\vec{v}_c$ which stems from the centrifugal force that acts on the positron when it is guided along a curved path. The overall drift in a bend can be calculated as [96]

$$\vec{v}_{D,bend} = \vec{v}_{gr} + \vec{v}_c = \frac{1}{\omega_g R} \left(\frac{1}{2} v_\perp^2 + v_\parallel^2 \right) \frac{\vec{R} \times \vec{B}}{RB}, \tag{2.18}$$

with $\vec{R}$ as defined in figure 2.4 b). As usually $v_\parallel \gg v_\perp$ during adiabatic transport in the beamline, the curvature drift $\vec{v}_c \propto v_\parallel^2$ is the dominant contribution in equation 2.18.

In order to compensate this drift, correction coils are necessary, that create a magnetic field perpendicular to $\vec{B}$. Experimentally, this is typically realized by two pairs of independent saddle coils that, by superposition with the guiding field, allow to steer the beam in any direction [97]. Correction coils are usually also used in straight sections of the beamline, where they can compensate the earth's magnetic field[1] or other static perturbations. Alternatively, the beamline can be magnetically shielded by μ-metal.

2.3.3. Electrostatic positron optics

Close to the experiment, the beam can be transported electrostatically while being accelerated to the final energy. Besides acceleration, electrostatic fields can also be employed to image, or in particular focus the positron beam. In general, this can also be done magnetically. Magnetic lenses are often easier to realize experimentally, as coils can be placed outside the vacuum. On the other hand, electrostatic lenses have usually smaller aberrations and can be used for acceleration and optics simultaneously. In the scope of this thesis, the principles of electrostatic lenses are introduced, while magnetic lenses are omitted. For the sake of applications, we focus on rotational symmetric systems.

---

[1] The influence of the earth's gravitational field is much smaller and can be neglected.

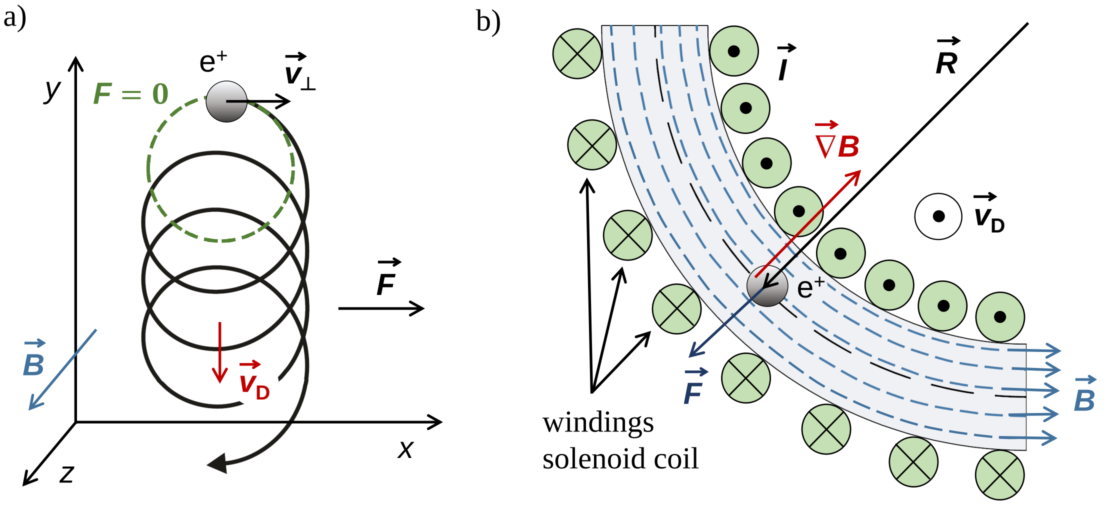

Figure 2.4. Positron drift during adiabatic beam guiding through a curved section. a) Weak forces perpendicular to the guiding field $\vec{B}$ cause a drift of the gyration center, whose direction can be determined by the right-hand rule. b) At a curved section of the beamline, the density of windings and thus the current density is larger on the inner side. This causes a field gradient that exerts a force on the positron leading to the gradient drift. The centrifugal force induces an additional, so-called curvature drift.

Comparison with light optics

In analogy to light, that is refracted at interfaces where the refractive index changes, a positron beam is deflected in a similar way when the electrostatic potential Φ changes [98]. For comparison, this is depicted in figure 2.5 a) and b), respectively. Since there is no abrupt change of the potential in free space, the positron trajectory changes continuously within the electric field as light does in a material with gradient refractive index (GRIN). For a non-relativistic beam, we find [99]

$$\frac{\sin\alpha_1}{\sin\alpha_2} = \frac{v_T/v_1}{v_T/v_2} = \frac{v_2}{v_1} = \sqrt{\frac{\Phi_2}{\Phi_1}}, \tag{2.19}$$

where the zero potential is defined as that, for which the positron is at rest ($\Phi_1, \Phi_2 < 0$). Equation 2.19 resembles Snell's law of refraction, where $\sqrt{|\Phi|}$ replaces the refractive index. Therefore, optical elements, e.g. lenses, can be realized by applying electrostatic potentials to a suitable geometry. The field gradient and thus the deflection has to be axially symmetric and must increase for beams that are further away from the optical axis. For example $F_r \propto r$, where F_r is the radial force component and r denotes the distance to the optical axis [100].

Bipotential and unipotential lens

Figure 2.5 c) depicts a so-called bipotential lens that consists of two cylindrically shaped electrodes of different potential, separated by a small gap for insulation. The optical analogue is a convex-concave lens assembly, as shown in the upper part of figure 2.5 c). The potential Φ decreases steadily along the optical axis, as plotted in figure 2.5 d), which leads to an acceleration of the positron beam. Neglecting higher order contributions, the deflecting force is proportional to the second derivative $\mathrm{d}\Phi^2/\mathrm{d}z^2$ plotted as well. At first, the beam thus experiences a deflection towards the optical axis and then away from it. As the velocity increases, the dwell time in the first section is longer. This leads to a net deflection towards the optical axis and enables to focus the positron beam [101]. For a non-relativtic beam and weak lens fields[2], we can calculate the focal length f_i on the image side as [89, 90]

$$\frac{1}{f_\mathrm{i}} = \frac{3}{16}\left|\frac{\Phi_1}{\Phi_2}\right|^{1/4} \int\limits_{-\infty}^{\infty} \left(\frac{\Phi'(z)}{\Phi(z)}\right)^2 \mathrm{d}z. \tag{2.20}$$

As expected, the focal length can be changed by adjusting the potential difference of the electrodes, which makes electrostatic lenses quite flexible. Bear in mind, that f_i also depends on the initial kinetic energy of the beam. This raises Φ_1 and Φ_2 by a constant and thus alters $\Phi(z)$ (see definition of the zero potential in the last section). However, to apply equation 2.20, we need to know $\Phi(z)$ and $\Phi'(z) = \mathrm{d}\Phi/\mathrm{d}z$, which is normally not the case for a customized lens system of arbitrary geometry. Therefore, in practice, electrostatic potentials and positron trajectories are rather directly calculated by numerical computer simulations.

A bipotential lens inherently changes the kinetic energy of the beam. In contrast, an unipotential or *Einzel lens* enables to focus the beam without changing its kinetic energy as initial and final potential are equal ($\Phi_1 = \Phi_3$). This is realized by a set of three electrodes, where the middle electrode can be either attractive ($|\Phi_2| > |\Phi_1|$) or repulsive ($|\Phi_2| < |\Phi_1|$). Weak rotational-symmetric electrostatic lenses are always converginging lenses [101]. Therefore, both configurations allow to focus the beam, but a repulsive middle electrode generates the shorter focus [102]. For reasons of symmetry, the focal length of an Einzel lens is the same on image and object side.

---

[2] *Weak* means that the focal length is much larger than the characteristinc length scale producing the field, e.g. the gap between the electrodes.

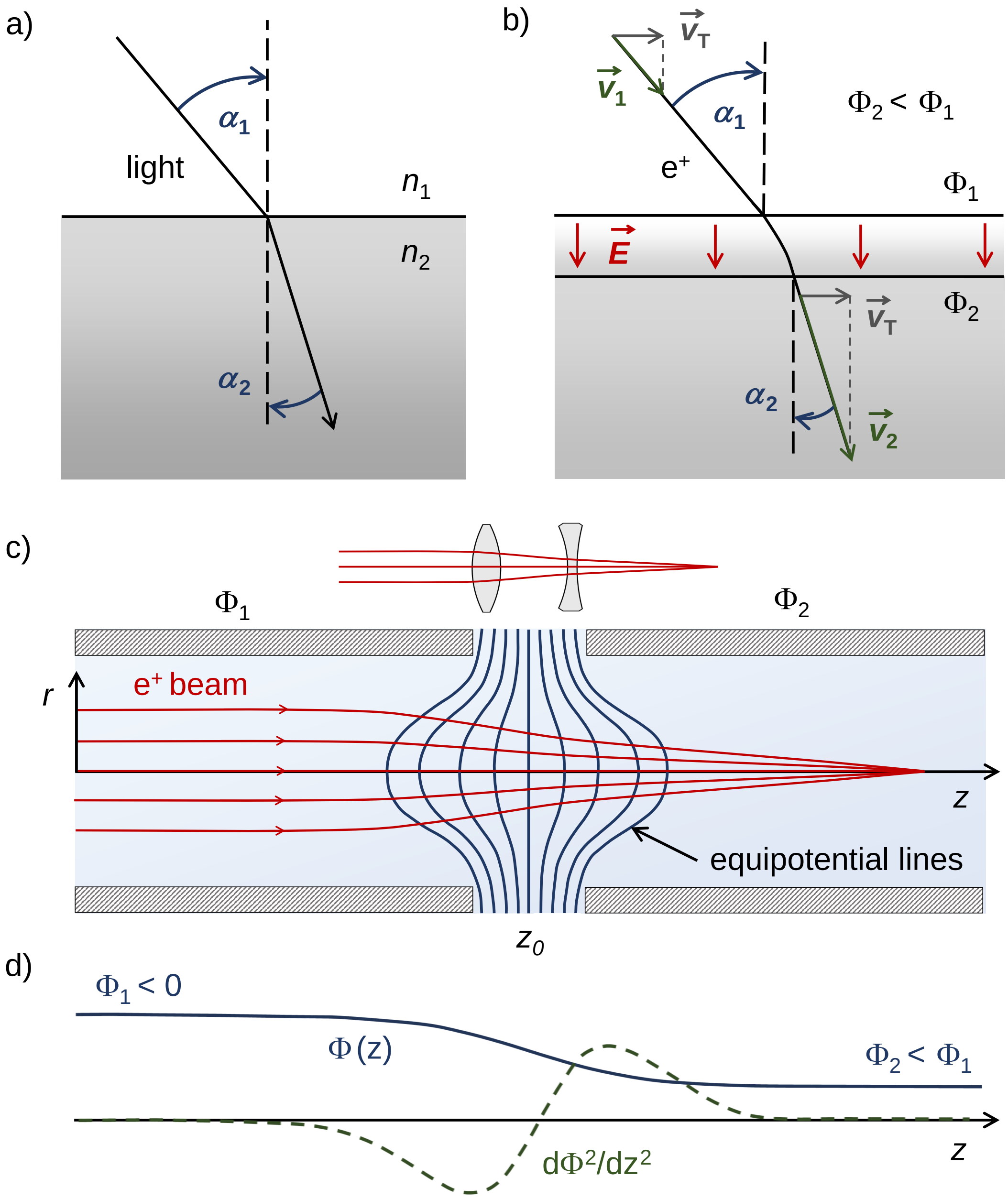

Figure 2.5. Comparison of light and electrostatic positron optics. a) Light refraction during transition into a medium that is optically denser, i.e. $n_2 > n_1$. b) A positron beam with initial velocity $\vec{v}_1$ is accelerated to $\vec{v}_2$ by an electrostatic field. This leads to a deflection that resembles the refraction of light. The beam is deflected continuously within the field, which can be best compared to the gradual light refraction in a gradient-index medium. c) Cross-sectional view of a simple bipotential lens that consists of two cylindrical tubes of different electrostatic potential. A suitable potential difference $\Delta\Phi = \Phi_2 - \Phi_1$ enables to focus the positron beam. The analogue lens system for light optics is depicted on top. d) Close to the optical axis, the potential Φ gradually decreases in z direction, which means that the kinetic beam energy increases. The second derivative $d\Phi^2/dz^2$ relates to the force, which first deflects the beam towards the optical axis and then in the opposite direction. In total, this leads to a net deflection towards the axis as the velocity increases.

Gaussian beam optics and aberrations

Within Gaussian beam optics, we only consider positron trajectories that are close to the optical axis. This means that the beam should have a radius much smaller then that of the electrostatic lenses. Moreover, this implies that the angles between positron trajectories and the optical axis are small, which allows the paraxial approximation. After series expansion of $\vec{E}$ in the vicinity of the optical axis, higher order contributions are neglected [89]. Solving the linearized equation of motion yields the cardinal elements as known from light optics. In this approximation, we observe perfectly sharp images and for weak lens fields we can calculate the beam spot as [47]

$$d_i = \frac{\alpha_o}{\alpha_i} d_o \approx \frac{d_o}{\alpha_i} \sqrt{\frac{E_\perp}{E}}. \tag{2.21}$$

Here, $d_{i/o}$ is the beam diamter on image and object side, $\alpha_{i/o}$ denotes the image and object side opening angle with respect to the optical axis and $E_\perp$ is the transverse energy of the beam. In contrast, real lens systems exhibit aberrations, which can increase the minimum beam diameter d_i when focusing the beam. Aberrations can be classified into [90, 99]

- **Spherical aberrations** that are caused by higher order contributions neglected within the paraxial approximation. In practice, spherical aberrations stem from beams that are too far away from the optical axis and thus experience an excessive deflection. This reduces the focal length of the respective beam and blurs the image.

- **Chromatic aberrations** due to the finite energy bandwidth of a monoenergetic positron beam. Faster positrons are less deflected than the slower ones, which broadens the focal point.

- **Off-axis aberrations** occur if the beam is not centered (astigmatism, distortion) or inclined (coma) with respect to the optical axis, so that the paraxial approximation is not applicable. Experimentally, this is caused by mechanical misalignment of the lens system in combination with the finite adjustment of the beam.

- **Other aberrations** can occur due to experimental imperfections, such as fluctuations (ripples) of the high voltage supply or charging of insulators. Space charge effects can be neglected as positron beam intensities are low.

Normally, spherical and chromatic aberrations are most relevant. If spherical aberrations can't be neglected, the smallest beam diameter occurs in front of the Gaussian image plane, in the so-called *plane of least confusion* [90].

2.4. Brightness enhancement by remoderation

After moderation, the positron beam is monoenergetic but often does not satisfy experimental requirements regarding beam quality, e.g. sufficiently small beam diameter, divergence or energy distribution. For example, to perform spatially resolved PALS or CDBS measurements, a beam diameter in the μm range is desired [103, 104]. In the context of positron diffraction, beam divergence and energy spread have to be small to obtain a sufficiently large coherence length [105]. The most efficient way to enhance the quality of the positron beam, i.e. its *brightness*, is by repeated stages of moderation, acceleration and focusing as suggested by A. P. Mills [106]. The moderation of a monoenergetic positron beam for brightness enhancement is called *remoderation* and is introduced in the following.

2.4.1. Definition of the brightness

Normally, the brightness B is used as a figure of merit to quantify the beam quality, which also allows to compare positron beams from different facilities. Different definitions are used in literature, for example [106]

$$B = \frac{I}{d^2\Theta^2 E_{\|}} = \frac{I}{d^2 E_{\perp}} \tag{2.22}$$

for a non-relativistic beam. Here, I denotes the intensity, d the beam diameter, Θ the angular divergence and $E_{\|} \approx E$ and $E_{\perp}$ are the components of the kinetic energy associated with the momentum parallel and perpendicular to the beam direction. We used the small-angle approximation $p_{\perp} = p_{\|} \tan\Theta \approx p_{\|}\Theta$ in the second step. This definition includes most quantities that are essential for positron diffraction, except the energy bandwidth of the beam. In the context of this work, we thus define the brightness slightly different as

$$B^{+} = \frac{I}{d^2\Theta^2 E_{\|}\Delta E_{\|}} = \frac{I}{d^2 E_{\perp}\Delta E_{\|}}, \tag{2.23}$$

which also includes the (longitudinal) energy spread $\Delta E_{\|} \approx \Delta E$. This definition has already been suggested for pulsed beams [92]. Keep in mind that there are further experimental beam properties that are more difficult to quantify, such as the beam shape [107].

2.4.2. Phase space volume and Liouville's theorem

From a theoretical perspective, the beam could be fully characterized by knowing the spatial coordinates (x, y, z) and momenta (p_x, p_y, p_z) of each positron at any time. For a given time, the beam can then be depicted in the associated six-dimensional phase space, where each positron is represented by a point [90]. Due to their large number, it is however more convenient to only consider the Phase Space Volume (PSV) that is occupied by the ensemble of positrons. Liouville's theorem states that the PSV occupied by an ensemble of non-interacting particles remains constant under the influence of conservative forces. Or in other words, the positron beam behaves like an incompressible fluid as the Phase Space Density (PSD) is invariant under these constraints [108]. This implies that the brightness of the beam is limited by the properties of the source [26]. Note that the source of a monoenergetic positron beam is in fact the moderator surface where, in combination with the extraction fields, initial PSV and PSD are defined. Using conservative forces, the beam diameter can thus only be reduced at the expense of an increased beam divergence and vice versa [109]. Additionally, we have to consider that even though the PSV remains constant, it might deform to an unfavorable shape during beam propagation. The effective PSV, defined by its envelope, usually increases during adiabatic beam transport or when applying electrostatic lenses.

How are bright electron beams produced to overcome these challenges? Firstly, electron sources, e.g. tungsten filaments that serve as hot cathode, are optimized to not only yield large intensities, but also to emit electrons from a well-defined tiny area [110]. This guarantees a small initial PSV with large PSD. Secondly, non-conservative devices such as apertures, collimators or energy filters are used to further decrease the PSV. In this way, it is possible to overcome the limitations set by Liouville's theorem. The respective transverse PSVs for a rotational symmetric system are depicted in figure 2.6 a). For illustration, we assume a homogeneous PSD within the occupied PSV.[3] By removing edge beams, the PSV can be decreased at the cost of intensity, while the PSD remains unchanged. This approach is not reasonable for positron beams because the initial PSD is too low. In comparison, remoderation is much more efficient, as it enables to reduce the occupied PSV while increasing the PSD. Brightness enhancement by remoderation is only possible for positrons, as it requires a material with negative work function (see section 2.2.1).

2.4.3. Positron remoderation

Figure 2.6 b) shows the transverse PSVs during different stages of positron remoderation in transmission geometry. The initial beam has a relatively low PSD and occupies a large PSV. When it is focused onto the remoderator, i.e. using conservative forces, the PSV changes shape but not the size. After implantation into the solid, the positrons lose their kinetic energy and thus also the momentum. This is a non-conservative process, which allows to redefine PSV and PSD. As the beam has been focused to a tiny area, which just increases marginally by the diffusion length of the positrons, its spatial extension remains small. After the re-emission of thermal positrons from an ideal remoderator surface, the transverse momentum obeys a thermal Maxwell-Boltzmann distribution. Consequently, the extension in momentum space is small as well, which leads to a significantly reduced PSV. In analogy to bright electron sources, the remoderator surface can be regarded as a new source that emits positrons from a small area with well-defined energy allowing the formation of a bright beam.

Geometry

Positron beams can be remoderated in transmission or reflection geometry, as depicted in figure 2.6 b) and c), respectively. In this context, reflection means that the brightness-enhanced beam is formed by thermal positrons which are re-emitted to the same side from where they have been implanted. Therefore, the beam guidance is more sophisticated as primary and remoderated beam have to be separated by means of electromagnetic fields or inclined incidence [27, 100]. This is naturally no issue in transmission geometry, where a thin foil is applied

---

[3] Bear in mind that the PSD is usually inhomogeneous, e.g. a Gaussian beam profile. In this case, suppressing beams from the edges of the occupied PSV can also increase the average PSD and thus the brightness of the beam, even though remoderation is still more efficient.

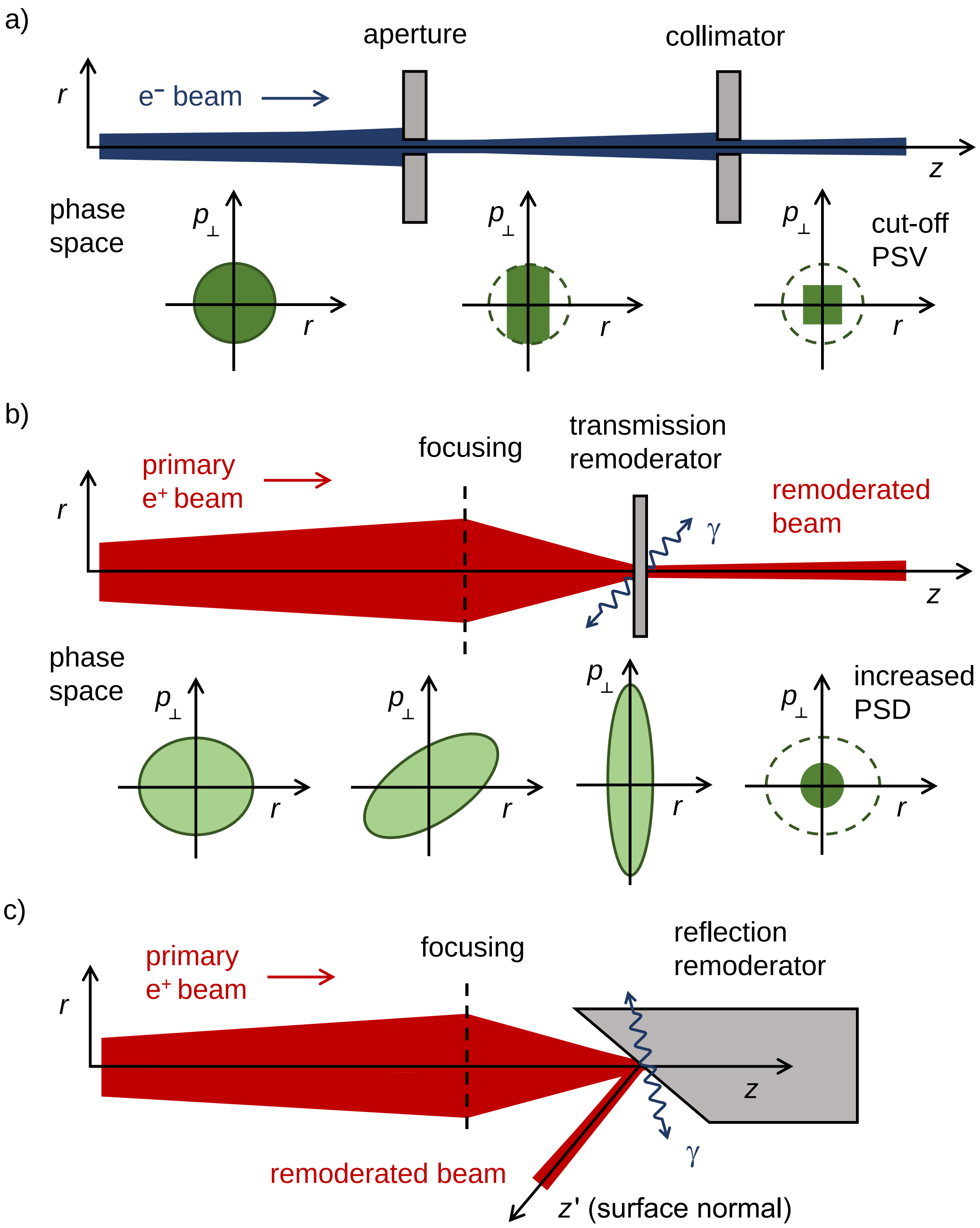

Figure 2.6. Brightness enhancement by non-conservative forces. a) For electron beams, apertures and collimators are used to decrease the PSV by removing outer trajectories and such of large transverse momentum. As the PSD remains constant, this is accompanied by a significant loss of intensity. b) For a positron beam, remoderation is the more efficient process (depicted in transmission geometry for better comparability). The beam is focused onto the remoderator, where the positrons lose their momentum during thermalization. After re-emission, the beam has a reduced PSV while the PSD has been increased. c) In reflection geometry primary and remoderated beam are on the same side of the crystal. For clarity, the angle of incidence of the primary beam is not normal to the remoderator surface. Note that this is not ideal, as it increases the beam spot on the remoderator. Figure partly inspired by [100].

as remoderator. A foil thickness in the range of the diffusion length allows that implanted positrons can reach the opposite surface. Since thermal positrons are also emitted from the entrance surface, remoderation efficiencies are normally lower than in reflection geometry. Moreover, the preparation and annealing of single-crystalline foils is more challenging [111].

Implantation of a monoenergetic beam

Remoderation efficiencies are normally in the range of $\sim$20-30% [112–114], which is much better than for initial moderation. The reason is that a slow, monoenergetic beam can be implanted into a shallow, surface-near region. Consequently, during diffusion, a much larger fraction of positrons can reach the surface to be re-emitted. Moreover, we can adjust the beam energy to optimize the implantation process, e.g. maximize the intensity of remoderated positrons while keeping the epithermal fraction low.

The implantation depth z depends on the beam energy E and is statistically distributed. It can be well described by a Makhovian profile [115, 116], as refined by Ghosh *et al.* [117]

$$P(z, E) = \frac{N_{lm}}{\bar{z}} \left(\frac{z}{c_{lm}\,\bar{z}} \right)^{l} \exp\left[- \left(\frac{z}{c_{lm}\,\bar{z}} \right)^{m} \right]. \tag{2.24}$$

The parameter l, m, N_{lm} and c_{lm} account for the material and are usually determined semi-empirically by Monte Carlo simulations. Besides m, which increases logarithmically with the beam energy E, the other parameters are approximately constant in the relevant energy range [118]. The mean implantation depth $\bar{z}$ can be estimated as

$$\bar{z} = \frac{A}{\rho} E^{n}, \tag{2.25}$$

where ρ denotes the density of the material and the parameter A and n can be obtained by simulations [118, 119] or experiments [120]. Implantation profiles for nickel and different beam energies are shown in figure 2.7. Considering a beam energy of few keV, the mean implantation depth is in the range of several nm. We also observe that the implantation profile rapidly broadens with increasing beam energy. Keep in mind that remoderator crystals are normally single crystalline, which is not explicitly considered in simulations. Therefore, effects such as channeling can increase the calculated implantation depth significantly.

Multiple remoderation and limitations

To conclude, positron remoderation enables the reduction of the beam diameter, divergence and energy spread at the expense of intensity. When only considering the transverse phase space (equation 2.22), remoderation enhances the brightness by roughly two orders of magnitude [53, 121]. It should be emphasized that the brightness B^+ relevant for diffraction increases even more. As proposed by A. P. Mills, multiple remoderation can be applied to create a positron microbeam that can be focused to a tiny spot size [106]. However, at this point, the positron diffusion length sets a natural limit to reach even smaller beam diameters by remoderation. Furthermore, with each stage of successive acceleration and thermalization, the high voltage (HV) stability of the setup becomes more challenging or, reversively, the final beam energy has to be decreased by several keV. Considering current positron sources, more than two or three remoderation stages are not reasonable as this reduces the beam intensity to an impractical level [27].

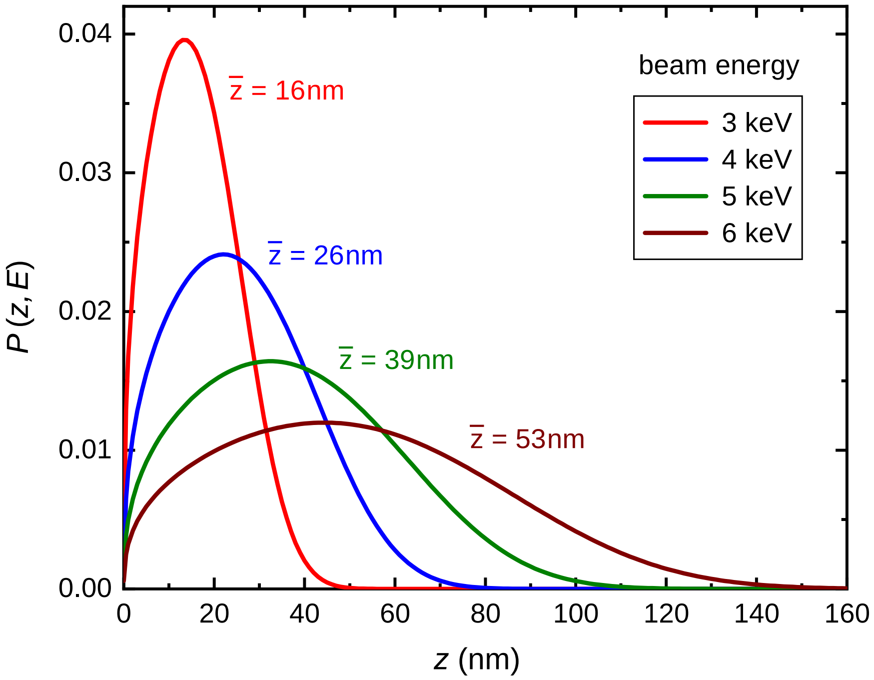

Figure 2.7. Positron implantation profiles in nickel, calculated for different beam energies using equation 2.24. The parameter l, m, N_{lm} and c_{lm} were taken from [118] and are averaged over the energy range 1- 40 keV.

3

Chapter 3.

TRHEPD for surface structure determination

In this chapter the fundamentals of surface structure analysis are summarized, relevant techniques are reviewed and Total-Reflection High-Energy Positron Diffraction (TRHEPD) is introduced, which has been employed to record the experimental data discussed in section 5.3.

3.1. Theoretical background

At first, the theoretical foundation is briefly reviewed, namely surface crystallography and the corresponding diffraction theory.

3.1.1. Surface crystallography and nomenclature

Crystalline surface structures are normally investigated in UHV in the range of 10^{-10} mbar or below, where adsorbed gas molecules can be removed during in-situ sample preparation. After that, the surface is either clean or intentionally covered by adsorbates, to form a well-ordered structure. At the surface, the three-dimensional symmetry, as present in the bulk of the crystal, is broken. The surface atoms experience a different crystal potential and form distinct chemical bonds at the interface. Therefore, even in the case of a clean (adsorbate-free) surface, the crystal structure usually differs from the bulk [122]. In the simplest case, topmost or subsurface atoms are displaced equally within their layer, which is referred to as *lattice relaxation*. This can lead to an altered, non-uniform interlayer spacing in the close vicinity of the surface [123]. In contrast, a *reconstruction* involves the rearrangement of surface atoms that changes the symmetry or periodicity of the crystal structure at the surface. Most crystals exhibit various surface reconstructions, depending on their orientation [124], external parameters such as temperature or pressure [125] and the presence of adsorbates [126]. From a thermodynamic perspective, a reconstruction is the surface phase that minimizes the free energy of the system. In general, reconstructions can include more than just the topmost atomic layer [127] and are often accompanied by relaxations of subsurface layers [128].

As a result, the lattice is only periodic parallel to the surface, i.e. it is two-dimensional. It is conventionally described with respect to the underlying substrate net specified by the surface plane of the truncated bulk lattice. The (111) surface of a fcc crystal, for example, provides an hexagonal reference net [129]. A reconstruction, especially when it comprises adsorbates, can then be regarded as a *superstructure* of the substrate net, characterized by a larger periodicity [16]. There are two established methods to label reconstructed surfaces: matrix and Wood's notation.

Matrix notation

The base vectors $\vec{b}_1$ and $\vec{b}_2$ of the reconstructed unit cell can be expressed as linear combinations of the base vectors $\vec{a}_1$ and $\vec{a}_2$ of the substrate net [122]:

$$\vec{b}_1 = m_{11}\vec{a}_1 + m_{12}\vec{a}_2, \tag{3.1}$$

$$\vec{b}_2 = m_{21}\vec{a}_1 + m_{22}\vec{a}_2. \tag{3.2}$$

As suggested by Park and Madden [130], a reconstruction and the related superstructure can thus be specified by the corresponding transformation matrix

$$\mathbf{M} = \begin{pmatrix} m_{11} & m_{12} \\ m_{21} & m_{22} \end{pmatrix}. \tag{3.3}$$

Wood's notation

The matrix notation is unambiguous and versatile, but the actual reconstruction is often not intuitive. The alternative notation, suggested by E. Wood [131], is therefore used more frequently. Consider a bulk crystal X with surface orientation characterized by the Miller indices *(hkl)*. Under the constraint [132]

$$\measuredangle\,(\vec{b}_1, \vec{b}_2) = \measuredangle\,(\vec{a}_1, \vec{a}_2), \tag{3.4}$$

we can rotate the substrate net by the angle φ so that the base vectors of the reconstruction can be expressed as

$$\vec{b}_1 = p\vec{a}_1 \text{ and } \vec{b}_2 = q\vec{a}_2. \tag{3.5}$$

The reconstruction is then labeled by

$$X\,(hkl)\text{ - }(p \times q)\; R\varphi \text{ - }Y, \tag{3.6}$$

where the chemical symbol at the end is used to indicate that the reconstruction involves adsorbates of species Y and is omitted otherwise. Figure 3.1 a) shows a square net with (1×2) reconstruction. If the base vectors of the superstructure are parallel to those of the reference net, i.e. $\varphi = 0°$, the addition $R0°$ is omitted. A centered unit cell is denoted by the symbol *c*, e.g. Ge(100) - *c*(4×2) [123]. As depicted in figure 3.1 b), Wood's notation is not unambiguous since a *c*(2×2) reconstruction could also be labeled as $(\sqrt{2} \times \sqrt{2})\,R45°$ considering a primitive unit cell [122]. Furthermore, Wood's notation is limited to reconstructions that exhibit a symmetry closely related to the reference net (see equation 3.4). It is evident that the matrix notation is more general since it contains more parameters - four (m_{11} - m_{22}) compared to just three (p, q, φ) [132]. Nevertheless, for the sake of clarity Wood's notation is used throughout this thesis.

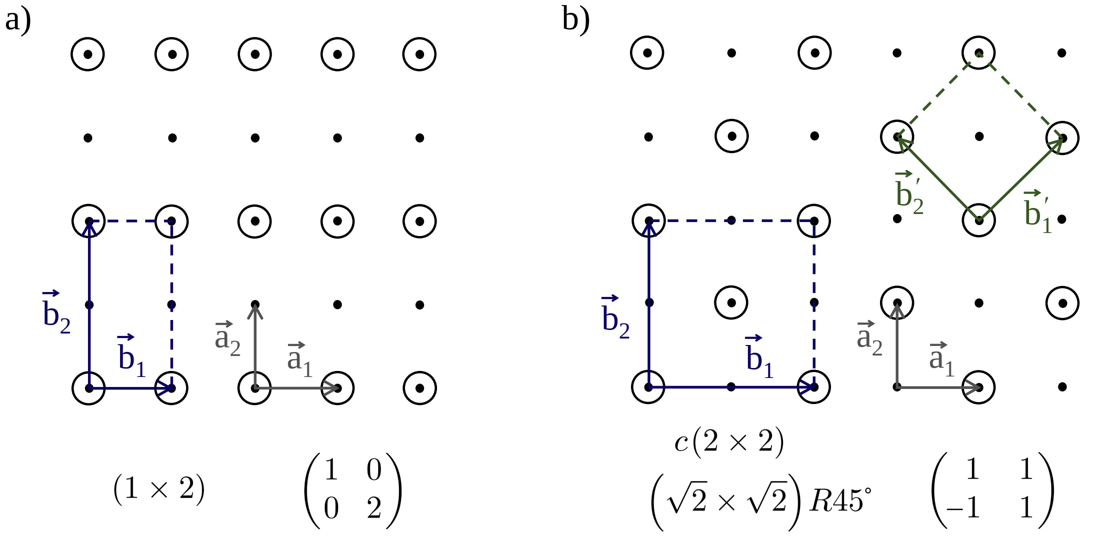

Figure 3.1. Wood's and matrix notation for two reconstructions of a square net. As indicated for b), Wood's notation is not unambiguous, even though the notation $c(2 \times 2)$, that considers a centered unit cell, is normally preferred. The matrix notation refers to the primitive unit cell [122].

3.1.2. Surface diffraction

Diffraction techniques (see sections 3.2.3, 3.2.4 and 3.3) can be employed to investigate the surface structure in reciprocal space. In this section, we discuss diffraction on an ideal two-dimensional lattice and summarize the basics of kinematic and dynamical diffraction theory.

Reciprocal lattice

As for a lattice in three dimensions, the reciprocal base vectors $\vec{a}_i^*$ $(i = 1, 2)$ of the surface net are defined by [129]

$$\vec{a}_i^* \cdot \vec{a}_j = 2\pi\, \delta_{ij}, \tag{3.7}$$

where we use the Kronecker delta δ_{ij} that is 1 for identical indices and 0 otherwise. Without loss of generality, we define the z-axis perpendicular to the surface, so that $\vec{a}_1^*$ and $\vec{a}_2^*$ can be calculated as [122]

$$\vec{a}_1^* = 2\pi \frac{\vec{a}_2 \times \vec{e}_z}{|\vec{a}_1 \times \vec{a}_2|} \text{ and } \vec{a}_2^* = 2\pi \frac{\vec{e}_z \times \vec{a}_1}{|\vec{a}_1 \times \vec{a}_2|}. \tag{3.8}$$

A translation vector in reciprocal space is thus obtained by

$$\vec{g}_n = n_1 \vec{a}_1^* + n_2 \vec{a}_2^*, \text{ with } n_1, n_2 \in \mathbb{Z}. \tag{3.9}$$

When considering surface reconstructions, the reciprocal base vectors $\vec{b}_i^*$ can be calculated analogously, i.e. replace $\vec{a}_i$ by $\vec{b}_i$ in equation 3.8. Additionally, the reciprocal vectors are connected by

$$\begin{pmatrix} \vec{b}_1^* \\ \vec{b}_2^* \end{pmatrix} = \mathbf{M}^* \begin{pmatrix} \vec{a}_1^* \\ \vec{a}_2^* \end{pmatrix}, \tag{3.10}$$

where $\mathbf{M}^* = \left(\mathbf{M}^{-1}\right)^T$ is the transpose inverse matrix of $\mathbf{M}$ (see equation 3.3) [16]. A superstructure increases the periodicity in real space, but does the reverse in reciprocal space. In this case, the matrix elements m_{ij}^* can be fractional. Effectively, this gives rise to the formation of additional reciprocal lattice points when compared to the reference net defined by $\vec{a}_1^*$ and $\vec{a}_2^*$.

Diffraction condition

Let us consider a plane, monochromatic wave incident on a surface with initial and scattered wave vectors $\vec{k}_i$ and $\vec{k}_f$, respectively. Since we are interested in elastic scattering, the condition

$$|\vec{k}_f| = |\vec{k}_i| \tag{3.11}$$

ensures conservation of energy. Both wave vectors can be decomposed into a component parallel and perpendicular to the surface, i.e. $\vec{k} = \vec{k}_{\parallel} + \vec{k}_{\perp}$. The condition for diffraction on a two-dimensional lattice is [133]

$$\Delta\vec{k}_{\parallel} = \vec{k}_{f\parallel} - \vec{k}_{i\parallel} = \vec{g}_n, \tag{3.12}$$

where $\vec{g}_n$ is a reciprocal lattice vector as defined in equation 3.9. Note that the component $\vec{k}_{\perp}$ is not conserved during this process as $\vec{k}_{f\perp}$ has to adjust to meet equation 3.11 [122]. Diffracted beams are typically labeled by the two indices $(n_1\, n_2)$ of the reciprocal lattice vector involved. We emphasize that these indices refer to the substrate net, even in the case of surface reconstruction. Additional beams due to diffraction on the superstructure are conventionally labeled by fractional indices [2, 134]. The spatial distribution of diffracted beams maps the lattice in reciprocal space and yields the periodicity of reconstructions.

Ewald sphere construction

As discussed before, there is no diffraction condition normal to the surface. Therefore, in three dimensions, an ideal 2D reciprocal lattice can be conceived as a set of *rods* rather than points. As illustrated in figure 3.2 a), each rod has an infinite extension perpendicular to the surface, where it intersects in a reciprocal lattice point [129]. To justify this concept, we can first consider a system that is also periodic normal to the surface. By increasing the lattice constant a_3 to arbitrarily large values, i.e. $a_3 \to \infty$, it converges to a 2D lattice. During this process, reciprocal lattice points move closer together along $\vec{a}_3^*$ until, in the limit, they become infinitely dense and thus form rods [122].

The concept of reciprocal lattice rods is in particular helpful when constructing the Ewald sphere, which is the graphical representation of the diffraction condition [133]. It comprises the equations 3.11 and 3.12 and is depicted in figure 3.2 b). The condition for constructive interference is met at all intersections of the Ewald sphere with a lattice rod. Within the drawing plane, this is exemplarily illustrated for the (02) rod. The beam diffracted on the (00) rod is called zeroth order or *specular reflection* as it confines the same angle with the surface as the incident beam [134]. Since the lattice rods are continuous, some always intersect the Ewald sphere, even when changing $\vec{k}_i$ slightly. This is in contrast to diffraction on a 3D lattice, where the beam needs to be tuned precisely to meet the diffraction condition for a certain reciprocal lattice point.

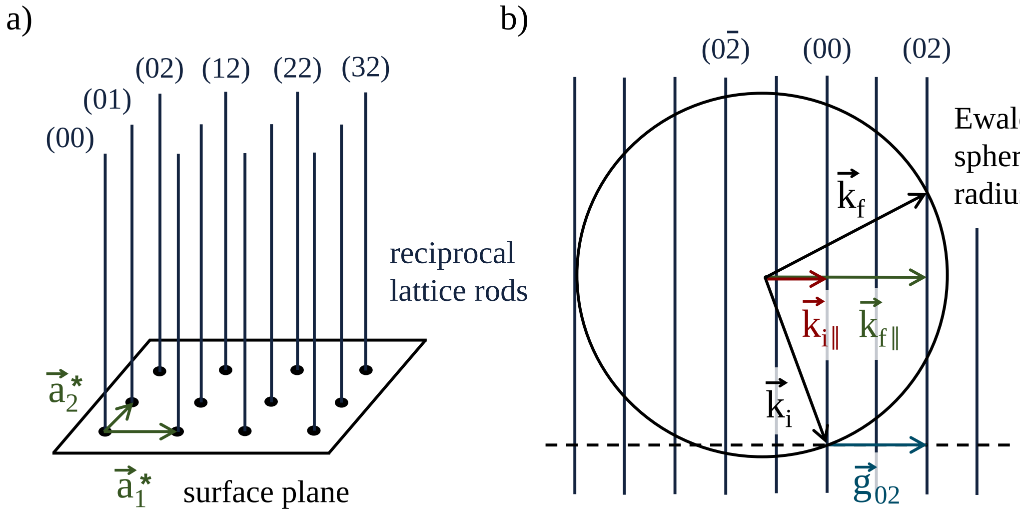

Figure 3.2. Ewald sphere construction for a 2D square lattice. a) Illustration of reciprocal lattice rods, which relate to the freedom of the wave vector normal to the surface. b) Ewald sphere for the case that $\vec{k}_{i\parallel}$ is parallel to the base vector $\vec{a}_2^*$. For clarity, only one outgoing beam is shown, diffracted on the (02) rod in the drawing plane. Note that the Ewald sphere intersects with further rods outside the drawing plane. Figure inspired by reference [122].

Intensity of diffracted beams

So far, we focused on the symmetry and periodicity of the surface structure, which is described by the lattice. The determination of the basis, i.e. the 3D arrangement of individual surface atoms within the unit cell, is considerably more challenging. In general, this information is contained in the intensity of diffracted beams and thus requires a quantitative analysis of the diffraction pattern [122]. There are two basic approaches for the necessary calculations: kinematic and dynamical diffraction theory.

Kinematic diffraction theory considers single, elastic scattering events, while multiple scattering is neglected. Implicitly, this has been assumed before and we can extend our considerations by including the basis of the lattice. The atomic positions are described by $\vec{r}_j = \vec{R}_m + \vec{u}_l$, where $\vec{R}_m = m_1\vec{a}_1 + m_2\vec{a}_2$ is the lattice vector and $\vec{u}_l$ is the position of the l^{th} base atom with respect to the unit cell. As before, we consider an incident plane wave $\psi_i = A_0 \exp(i\vec{k}_i \vec{r})$, where A_0 is a constant. Far away from the surface, the amplitude A_f of the outgoing wave ψ_f can be calculated as the coherent sum of all scattered waves. We assume weak interaction and therefore single scattering events, so that each atom contributes with a scattering factor f_j that can be calculated within the Born approximation. When taking phase differences due to different path lengths into account, we obtain [2, 135]

$$A_f = A_0 \sum_j f_j \, e^{i\Delta\vec{k}\vec{r}_j} = A_0 \underbrace{\sum_l f_l \, e^{i\Delta\vec{k}\,\vec{u}_l}}_{F(\Delta\vec{k},\,\vec{k}_i)} \cdot \underbrace{\sum_{m_1}\sum_{m_2} e^{i\Delta\vec{k}\,\vec{R}_m}}_{G(\Delta\vec{k})} . \tag{3.13}$$

By summation over l, we consider all atoms within the unit cell. The contribution of the basis is associated with the so-called structure factor F. The second factor, the summation over m_1 and m_2, is the lattice contribution G. For an ideal 2D lattice, it is non-zero only for $\Delta\vec{k}_{\|} = \vec{g}_n$, as stated in equation 3.12 [135]. In experiments, we measure the intensity, which can be calculated as

$$I = |\psi_f|^2 \propto |F|^2 \cdot |G|^2. \tag{3.14}$$

Therefore, $|G|^2$ is responsible for the formation of the diffraction pattern due to the interference of scattered waves, while $|F|^2$ modulates the intensity of each beam. Note that by specifying $\vec{g}_n$, a particular diffracted beam is chosen. Within the kinematic approach, intensity losses due to inelastic scattering can be included by adding a factor that describes absorption [133].

In contrast, *dynamical diffraction theory* also takes multiple scattering into account. This is particularly important for electron and positron diffraction, as the interaction with the sample is strong [134, 136]. Therefore, kinematic theory can only be used for qualitative predictions, such as the position of diffraction spots, but fails to yield correct beam intensities. In section 3.3.3, we outline how to perform dynamical calculations of TRHEPD beam intensities.

3.2. Conventional techniques for surface structure analysis

As introduced in section 3.1.1, many surface structures are rather complex and their precise determination, including the atomic positions within topmost and subsurface layers, is often challenging. Therefore, a simple standard technique, such as X-ray diffraction (XRD) for bulk crystallography, does not exist. Instead, it depends on the sample and the scientific question, which method is suited best. For most structures it is necessary to combine complementary techniques to obtain a comprehensive understanding [3, 137]. In this section, the main experimental techniques commonly applied for surface structure analysis are thus briefly introduced.

Since the surface consists of $\sim 10^{15}$ atoms/cm^2 compared to 10^{23} atoms/cm^3 in the bulk, an important criterion of each technique is the respective surface sensitivity [16]. Generally, we distinguish scanning probe techniques (section 3.2.1), used to investigate the local structure in real space, and diffraction techniques, that access the long-range periodic order in reciprocal space. There are various diffraction techniques, utilizing atomic (section 3.2.2), X-ray (section 3.2.3) or electron (section 3.2.4) beams of suitable wavelength. An overview is shown in figure 3.3.

3.2.1. Scanning probe techniques

In 1981, G. Binning and H. Rohrer developed Scanning Tunneling Microscopy (STM), which has been awarded with the Nobel price in 1986 [138–140]. STM is based on the quantum mechanical phenomenon of electron tunneling through a potential barrier. In practice, an atomically sharp conductive tip is scanned over the sample surface within a distance of few Å. At such close distance, the electron wavefunctions from tip and sample surface overlap and electrons can tunnel through the vacuum barrier defined by the work function [141]. By applying a bias voltage between tip and sample, it is possible to induce a net tunnel current in the order of pico- to nanoampere. As this current decreases exponentially with the distance between tip and surface, STM can be used to obtain information about the surface topography on an atomic scale, e.g. step edges, vacancies or adatoms [122].

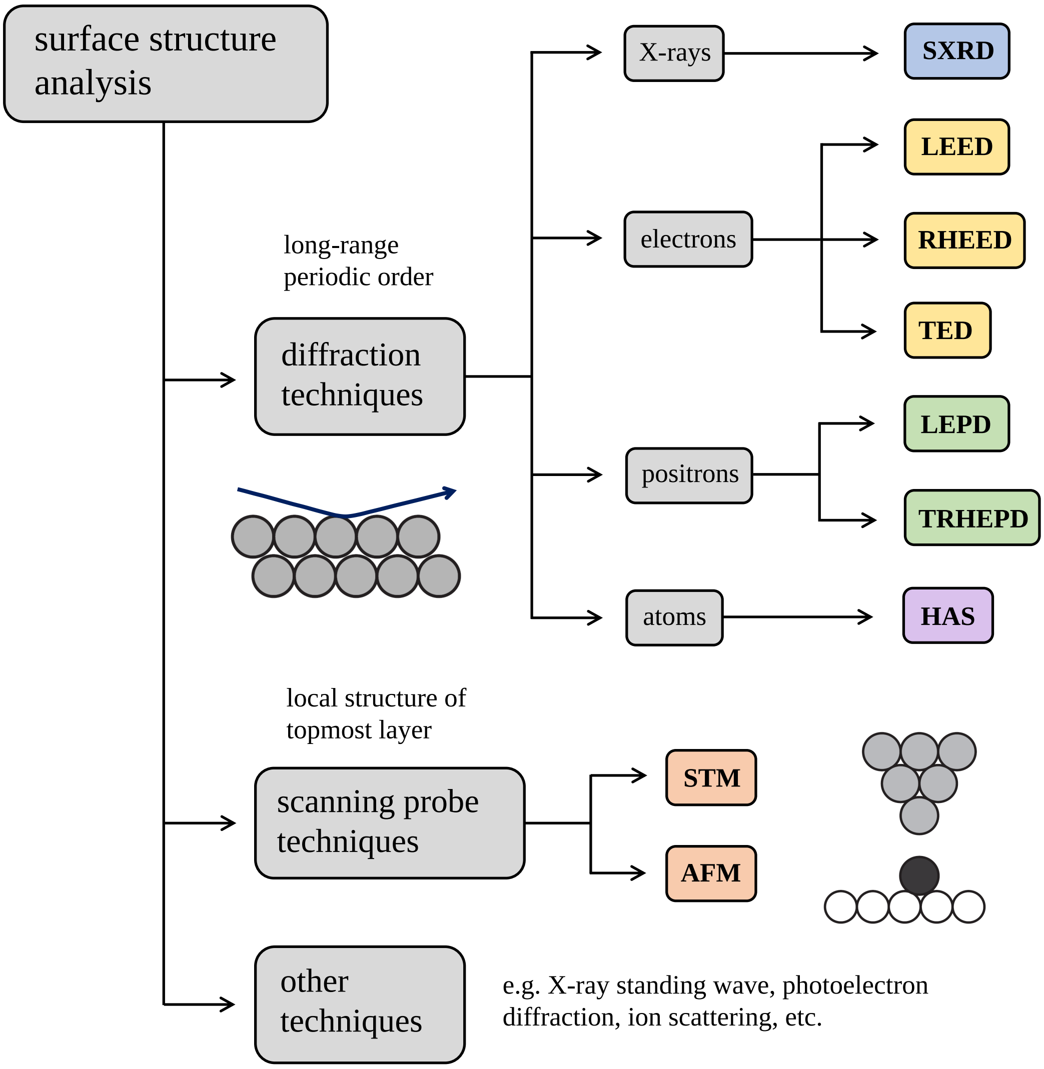

Figure 3.3. Overview of different techniques for surface structure analysis and determination. Abbreviations are introduced within the sections 3.2 and 3.3.

The quantitative analysis of the (local) surface structure is though not straightforward because the tunnel current depends on both, the topography and the electronic structure of sample and tip. This means that the signal also changes for different elements, chemical bonds or due to charge transfer. Therefore, STM images need to be interpreted carefully and don't directly relate to atomic positions [2]. Moreover, STM features ultimate surface sensitivity, but cannot probe subsurface layers. For these reasons, STM is often applied as a complementary technique to determine adsorption sites or to obtain information about complex reconstructions without the need to completely uncover them. These indications can serve as a starting point for structural models.

Also note that STM requires a conductive sample, while Atomic Force Microscopy (AFM) can be used for insulating samples as well [142]. In AFM, a sharp tip that is attached to the free end of a cantilever, is scanned over the sample surface. The forces between tip and surface atoms mechanically deflect the cantilever which can be read out in different ways [143]. Most AFMs operate however in a dynamic mode, where the cantilever oscillates close to its resonance frequency controlled by a feedback loop. The interaction with the surface leads to a change in amplitude and phase which can be measured [144].

3.2.2. Helium atom scattering

For Helium Atom Scattering (HAS), the beam energy is in the order of tens of meV, so that helium atoms are diffracted at a distance of few Å outside the actual surface. This makes the technique very surface sensitive. However, HAS only probes the corrugation of the surface potential, which is difficult to relate to the precise positions of surface atoms [2]. Besides that, helium atoms have a large cross-section for diffuse scattering on individual adatoms and defects, which can reduce the diffraction signal significantly [145]. Altogether and with regard to structure determination, HAS and related techniques are therefore only relevant for niche applications, such as the analysis of delicate adsorbate structures [146, 147].

3.2.3. Surface X-ray diffraction

Surface X-ray Diffraction (SXRD) has been developed in the early 1980s when brilliant synchrotron radiation became available [148–150]. X-rays interact only weakly with matter since the cross-section for elastic scattering on atoms is in the range of $10^{-6}\,\text{Å}^2$ [122]. In general, X-rays thus penetrate deeply into the solid. In order to enhance the surface sensitivity, SXRD is conducted in grazing incidence below or close to the critical angle of total external reflection. As the critical angle is normally in the range of only 0.2 - 0.6°, SXRD requires a very intense and highly collimated beam [151]. Due to the superimposed, much larger signal from the bulk, the detection and data evaluation concentrates on regions in reciprocal space that are surface specific, e.g. fractional order diffraction spots or the analysis of crystal truncation rods (CTR) [2, 150]. The latter are reciprocal lattice rods that contain bulk lattice points.

Since multiple scattering is negligible, SXRD can be described using kinematic diffraction theory [152]. When compared to electron diffraction, instrumentation and data acquisition are much more challenging, while the theory is relatively simple. Qualitative measurements to determine the periodicity of an unknown surface reconstruction are thus usually done with electron diffraction [150]. Besides that, SXRD is also not suitable to investigate structures, where surface atoms have low atomic numbers. In this case, the interaction and hence the signal is simply too small. In return, the weak interaction of X-rays can be exploited to study the surface structure in different environments beyond UHV, which can be relevant for applications [152].

3.2.4. Electron diffraction

Compared to X-rays, electrons have a much larger cross-section for elastic scattering, which is in the order of $1\,\text{Å}^2$ [122]. This guarantees a strong diffraction signal, while the surface sensitivity mainly stems from the large cross-section for inelastic scattering of $\sim 5\,\text{Å}^2$ [2]. Electrons that penetrate deeper into the sample are more likely scattered inelastically, which means that they lose coherence and do not contribute to the diffraction pattern. Therefore, most of the signal originates from few atomic layers and we can access the surface structure with relatively low contribution from the bulk. However, as multiple scattering is rather common, dynamical calculations are necessary for the quantitative analysis [133, 135]. When assuming a certain structural model, we can calculate the respective beam intensities and the comparison with experimental data allows the verification and adjustment of the model in an iterative process [133]. In this framework, the determination of atomic positions can be challenging, especially when the unit cell is large. An initial structural model can e.g. be established using Density Functional Theory (DFT) calculations that indicate which atomic positions are energetically favorable.

There are three well-established diffraction techniques using electrons:

- Low-Energy Electron Diffraction (LEED),
- Reflection High-Energy Electron Diffraction (RHEED) and
- Transmission Electron Diffraction (TED).

To ensure transmission, TED requires beam energies of 100 - 200 keV and samples thinner than 100 nm [122]. The most prominent success of TED was its contribution to resolve the precise structure of Si(111) - (7×7) [127]. In the following, we focus on the more relevant techniques LEED and RHEED, which are conducted in reflection geometry.

Low energy electron diffraction (LEED)

The most commonly applied technique for surface structure analysis is LEED, as it readily reveals the symmetry and periodicity of the reciprocal lattice. Its origin dates back to 1927, when C. Davisson and L. Germer investigated the wave properties of the electron [153, 154]. Figure 3.4 depicts the usual LEED setup that consists of an electron gun with optics and a hemispherical fluorescent screen to visualize the diffraction spots without angular distortion. A set of four grids in front of the screen serves as retarding field to remove secondary and inelastically scattered electrons, while the remaining electrons are accelerated towards the screen [2]. To exclude electrostatic perturbations, the last aperture of the electron gun, the sample and the first grid are grounded. The beam energy is typically in the range of 20 - 300 eV, which equals an electron wavelength of 0.7 - 2.7 Å. When raising the energy, the radius of the Ewald sphere increases and more diffraction spots can be observed on the screen. Measurements to determine the surface structure are conducted by changing the beam energy stepwise. This yields so-called *I-V* curves, where the intensity of a certain diffraction spot is plotted against cathode voltage or beam energy. The agreement between calculated and experimental *I-V* curves is used to evaluate the goodness of the proposed structure and allows an iterative refinement.

Reflection high-energy electron diffraction (RHEED)

RHEED is conducted in grazing incidence at angles of $\theta \sim 0.5 - 5^\circ$ and with a beam energy of usually 10 - 30 keV. Electron scattering is weaker in this energy range, but since the penetration depth is reduced by a factor of $\sin(\theta)$ for geometrical reasons, RHEED is still very surface sensitive and only probes a depth of few atomic layers [134]. Due to the large energy, electrons are strongly scattered in forward direction and can be detected on the opposite side of the electron gun with a fluorescent screen (often directly coated or attached to a viewport). Diffraction spots are arranged on semicircles, so-called *Laue zones*, as illustrated

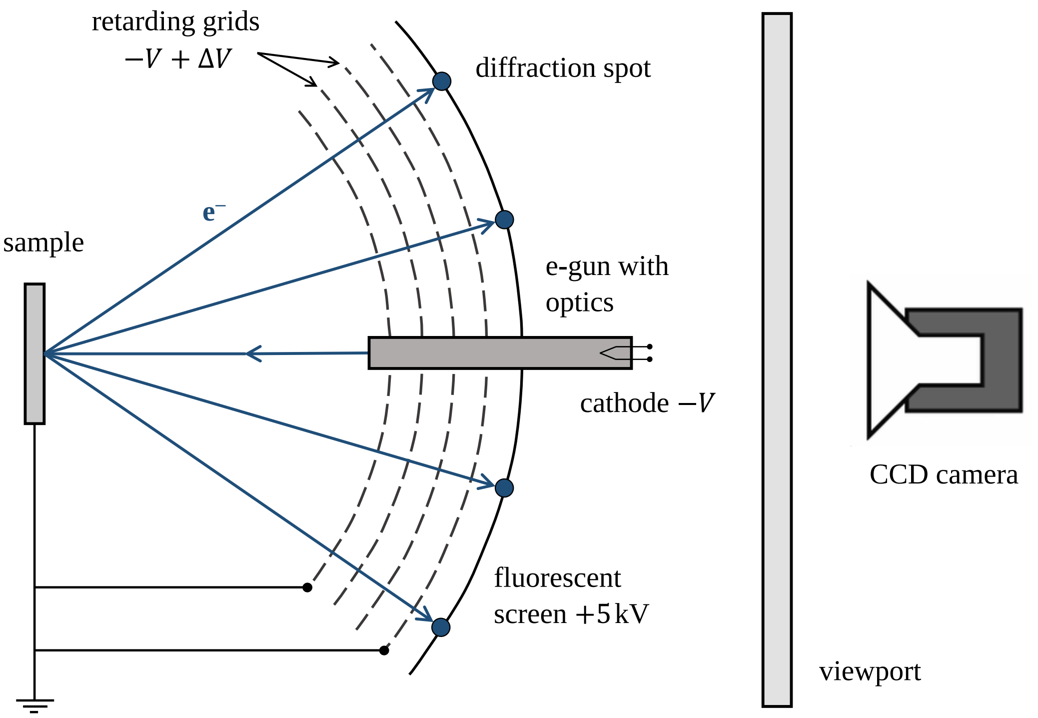

Figure 3.4. Schematic illustration of the LEED setup. After diffraction on the sample, the electrons pass a retarding field and are accelerated towards the fluorescent screen. The diffraction pattern is observed through a viewport, where it can be recorded with a CCD camera for subsequent analysis. Figure inspired by [2].

with the aid of the Ewald sphere in figure 3.5. The specular reflection is located in the middle of the zeroth order Laue zone. The RHEED pattern can be recorded from outside the vacuum using a CCD camera. In contrast to LEED, a retarding field as energy filter is usually not used, though this has been realized in specific setups [155]. When inelastically scattered electrons are not removed, so-called *Kikuchi lines* are commonly part of the RHEED pattern, too. These stem from electrons that first scatter inelastically on plasmons or phonons, where they lose a small fraction of kinetic energy and are subsequently diffracted by the crystal [133].

One advantage compared to LEED is that RHEED does not occupy the space in front of the sample surface and is compatible with complementary techniques or components necessary for thin layer growth. Therefore, it is an established standard tool to qualitatively analyze changes of the surface structure during annealing, deposition and crystal growth [156]. RHEED is also very sensitive to surface roughness, which can e.g. be exploited to precisely monitor the growth rate during molecular beam epitaxy (MBE) [157, 158].

With regard to quantitative structure determination [159, 160], RHEED faces similar challenges as LEED. For this, so-called *rocking curves* are recorded, where the glancing angle θ is varied at constant beam energy. Since the penetration depth increases with θ, rocking curves are in this sense the analogon to I-V curves in LEED, allowing an iterative adjustment of the structural model. An alternative, less established approach is the analysis of *azimuthal plots*, where θ is kept constant and the sample is rotated in-plane to vary the crystallographic orientation [161].

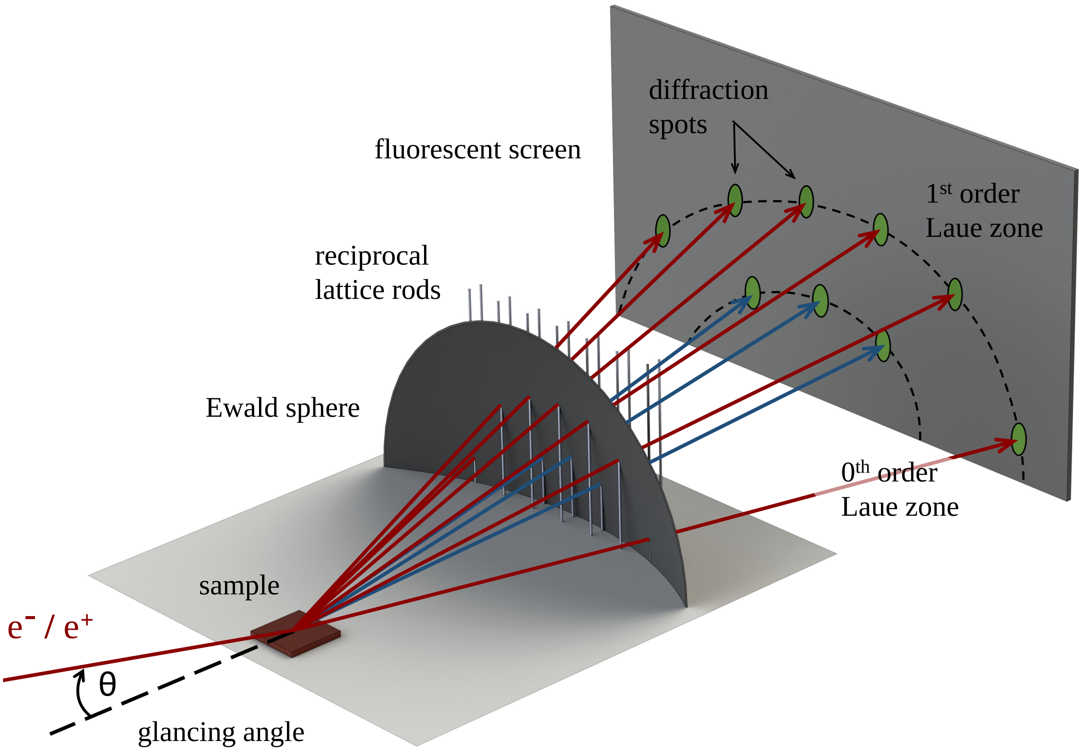

Figure 3.5. Formation of the RHEED/TRHEPD pattern after diffraction on a 2D rectangular lattice (schematic). The directions of diffracted beams are defined by the intersections of the reciprocal lattice rods with the Ewald sphere. Note that the Ewald sphere has a relatively small curvature and only the relevant part is shown. Under grazing incidence, diffraction spots are located on semicircular Laue zones (dashed lines). For better illustration, zeroth order beams are depicted in blue while first order diffracted beams are red (higher orders are not shown). Surface reconstructions can lead to the formation of further, fractional order Laue zones. Figure inspired by [162].

3.3. Total-reflection high-energy positron diffraction (TRHEPD)

In this section, the measurement technique TRHEPD is introduced in detail and advantages over conventional techniques, in particular electron diffraction, are discussed.

3.3.1. Introduction to positron diffraction

First experiments – LEPD

In the early 1980s, slow positron beams of sufficient brightness became available, enabling diffraction experiments first conducted in LEED geometry [163]. It has been demonstrated that Low-Energy Positron Diffraction (LEPD) features various advantages compared to LEED, e.g. in the energy range below 200 eV, inelastic scattering is stronger for positrons as there are no excluded final states, leading to an enhanced surface sensitivity [27]. Moreover, LEPD I-V curves yield a significantly better agreement with theory, since i) atomic scattering factors $f(\theta)$ are less anisotropic, ii) no exchange correlation has to be considered and iii) multiple scattering is less complex [164, 165].

Characteristics and advantages of TRHEPD

In 1992, the positron counterpart of RHEED, Total-Reflection High-Energy Positron Diffraction (TRHEPD)[1], has been suggested for surface studies by A. Ichimiya [167]. As for RHEED, the primary reason for the surface sensitivity is the large cross-section for inelastic scattering (see section 3.2.4), which is basically the same for electrons and positrons in this energy range [18]. However, in contrast to electrons, positrons experience a repulsive crystal potential [30]. Consequently, positrons are refracted towards the surface and are totally reflected when the glancing angle is smaller than the critical angle. This is derived in detail in section 3.3.2. As a result, TRHEPD features an outstanding surface sensitivity, which can be exploited to analyze the surface structure with less interference from the bulk [168]. Since the penetration depth of positrons is

---

[1] Initially called RHEPD, but more recently renamed to TRHEPD to emphasize the feature of total reflection [166]. Within this work, the acronym TRHEPD is used exclusively.

generally more shallow, multiple scattering is less dominant, e.g. Kikuchi lines are much less pronounced or absent in the TRHEPD pattern [166, 169]. Despite this fact, dynamical calculations are still neccesary to determine the correct beam intensities from a suggested surface structure [136]. However, the agreement between experimental and calculated rocking curves is normally better, which allows the extraction of structural parameters with smaller uncertainties [168]. The concept of dynamical calculations and the methodology to determine the surface structure are introduced in the sections 3.3.3 and 3.3.4, respectively.

First TRHEPD patterns and rocking curves have been recorded by A. Kawasuso and S. Okada in 1998 [170]. Since then, it has been demonstrated that TRHEPD is an ideal technique to determine the surface structure of topmost and immediate subsurface atomic layers [18]. The TRHEPD setup in Japan is introduced in section 3.3.5, which also includes a brief literature review.

Principle experimental considerations

As schematically shown in figure 3.6, the experimental setup is basically the same as for RHEED. A monoenergetic positron beam with a fixed energy of usually 10-20 keV and small, variable glancing angle is diffracted by the sample. As the beam intensity is much lower than in RHEED, the diffraction pattern can't be visualized directly with a fluorescent screen, but has to be amplified beforehand. This can be done by a Micro-Channel Plate (MCP), where the incident positrons produce secondary electrons that are multiplied by an array of small channel tubes [171]. Reversely, the implementation of a MCP in a RHEED or LEED system allows to decrease the beam intensity by several orders of magnitude. This is in particular interesting to reduce electron-beam-induced damage of delicate surface structures or to avoid charging of insulating samples [172]. Given this backdrop, we underline that TRHEPD can be used for the quantitative analysis of static surface structures, while electron diffraction allows time-resolved measurements on a timescale of (sub-)picoseconds as well [173–175].

3.3.2. Refraction and total reflection

The electrostatic potential V inside every material is inherently positive, which results from the point-like positive charge of the nuclei and the negatively charged electron cloud [18]. As electrons and positrons have opposite charge q,

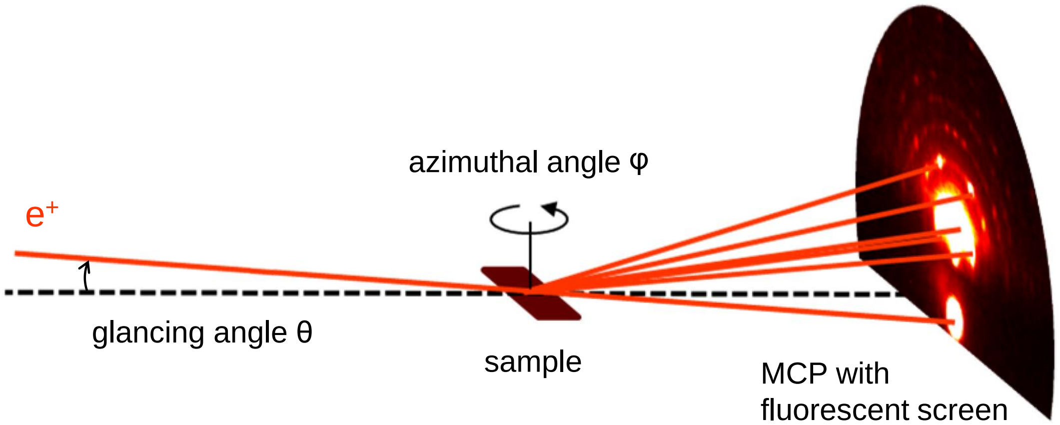

Figure 3.6. Schematic diagram of TRHEPD. To record a rocking curve, the glancing angle θ is varied (typically below 6°), while beam energy and azimuthal angle φ are fixed. The diffraction pattern can be visualized using a MCP assembly with a fluorescent screen. Figure adapted from reference [18].

the respective potential is attractive for electrons, but repulsive for positrons. This difference is crucial for diffraction in grazing incidence, as illustrated in the following. Relativistic effects are neglected as this only leads to minor corrections, but does not change the obtained results.

Refractive index

We consider an incident e^-/e^+ beam with wave vector

$$k = \frac{\sqrt{2m_e E_0}}{\hbar}, \tag{3.15}$$

where m_e is the electron mass, E_0 the kinetic energy and $\hbar$ the reduced Planck constant. The wave vector k' inside the crystal can be calculated as

$$k' = \frac{\sqrt{2m_e E}}{\hbar} = \frac{\sqrt{2m_e(E_0 - qV)}}{\hbar}, \tag{3.16}$$

where qV is the average potential energy of the e^-/e^+ in the crystal. To ensure continuity at the surface, the parallel components of the wave vector have to be equal [133]:

$$k'_{\parallel} = k_{\parallel} \Rightarrow k' \cos\theta' = k\cos\theta. \tag{3.17}$$

Here, we used the glancing angle θ and the refracted internal glancing angle θ' as defined in figure 3.7 a). We can utilize the equations 3.15 and 3.16 to replace k and k' in equation 3.17 in order to obtain

$$\sqrt{E_0}\cos\theta = \sqrt{E_0 - qV}\cos\theta'. \tag{3.18}$$

Equation 3.18 resembles Snell's law of refraction. To recognize this, first note that we defined the angles θ and θ' with respect to the surface and not to the surface normal, as it is conventionally done in optics. This simply substitutes sine by cosine. Secondly, we can identify the associated refractive index as

$$n = \sqrt{E_0 - qV}, \tag{3.19}$$

with $V_{vac} = 0$ for the potential in vacuum.[2] The refractivity at the surface is thus

$$n_{1,2} = \frac{\cos\theta}{\cos\theta'} = \sqrt{1 - \frac{qV}{E_0}}. \tag{3.20}$$

For electrons with $qV = -eV < 0$, we find that $n_{1,2} > 1$. Therefore, electrons are refracted away from the surface towards the bulk, no matter how small the glancing angle is. In contrast, for positrons with $qV = eV > 0$ we find that $n_{1,2} < 1$. Consequently, positrons are refracted towards the crystal surface. The difference is illustrated in figure 3.7 a).

Total reflection

Another implication is that positrons exhibit total external reflection for $\theta < \theta_c$, as depicted in figure 3.7 b). Total reflection takes place when the kinetic energy perpendicular to the surface is smaller than the potential energy inside the crystal [166],

$$E_{0\perp} = E_0 \sin^2\theta < eV. \tag{3.21}$$

Therefore, we can calculate the critical angle as

$$\theta_c = \arcsin\sqrt{\frac{eV}{E_0}}. \tag{3.22}$$

---

[2] Also compare this with equation 2.19, where we considered different electrostatic potentials in vacuum.

For typical parameters, such as a 10 keV positron beam incident on a Si crystal with $eV = 12\,\text{eV}$, the critical angle is approximately 2° [30]. We emphasize that the critical angle for SXRD, as introduced in section 3.2.3, is considerably smaller and thus much more difficult to access experimentally. Electrons can ony experience total internal reflection, which gives rise to surface wave resonances that can enhance Kikuchi lines and thus rather complicate the RHEED pattern [133].

Figure 3.7 c) shows the penetration depth of a 10 keV e^-/e^+ beam in relation to the glancing angle, as calculated by Fukaya *et al.* for a step-like potential of 12 V with an imaginary component of 1.2 V to account for inelastic scattering [18]. As expected, the penetration depth of positrons is lower throughout the whole angular range when compared to electrons. In the region of total reflection, the penetration depth of positrons is less than 1Å, leading to an outstanding surface sensitivity [176]. Furthermore, it is also possible to obtain information about subsurface layers by tuning the angle of incidence above θ_c.

First order Bragg reflection

The intensity of integer diffraction spots in RHEED or TRHEPD is enhanced, when the 3D Bragg condition is met, which leads to pronounced peaks in the rocking curve. The Bragg condition for surface parallel planes is

$$2d\sin(\theta') = n\lambda', \tag{3.23}$$

where d is the spacing between lattice planes, $\lambda' = 2\pi/k'$ the wavelength inside the crystal and $n \in \mathbb{N}$. By using equations 3.16 and 3.18, we can replace λ' and θ' to receive

$$E_0 \sin^2\theta = \frac{h^2 n^2}{8 m_e d^2} + qV. \tag{3.24}$$

We find that the Bragg angles for RHEED and TRHEPD are shifted in opposite directions. This is a result of refraction, as the glancing angle is effectively increased in the case of RHEED, while being decreased for TRHEPD. Let us now consider a Si crystal with $qV = 12\,\text{eV}$ and $d = 3.14\text{Å}$ [167]. For RHEED, the first order Bragg reflection is absent, since it calculates to

$$E_0 \sin^2\theta \approx (3.8 - 12)\,\text{eV} < 0, \tag{3.25}$$

which cannot be fulfilled. In contrast, first order Bragg peaks can be observed with TRHEPD as demonstrated by experiments [170].

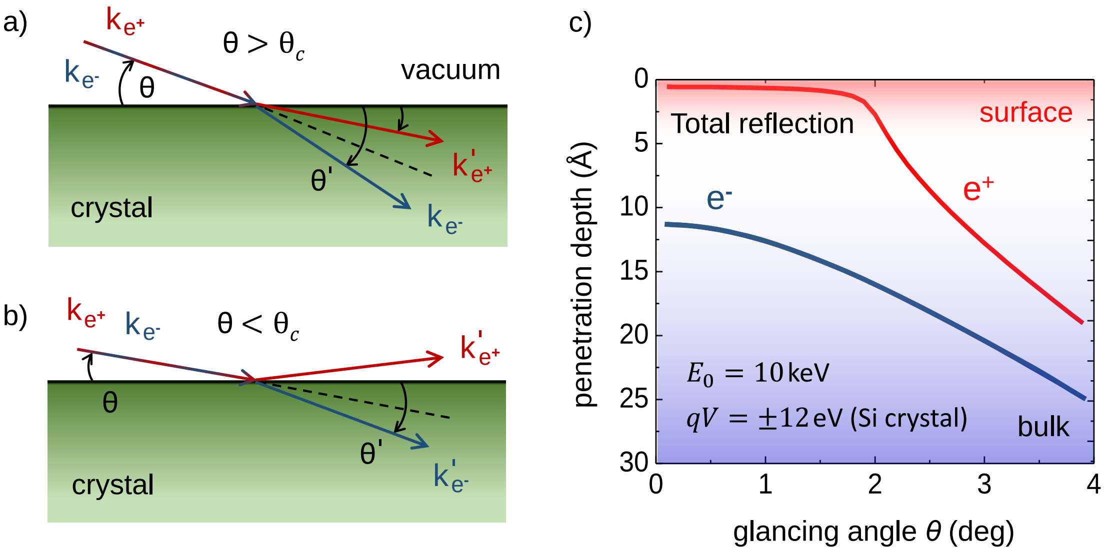

Figure 3.7. Refraction and penetration depth for electrons and positrons in grazing incidence. a) For glancing angles $\theta > \theta_c$ positrons are refracted towards the crystal surface. Due to the attractive crystal potential, electrons are always refracted into the crystal. b) For $\theta < \theta_c$ positrons are totally reflected from the crystal surface, which is not observed with electrons. Note that angles and wave vectors are sketched in a qualitative way. c) Calculated penetration depth for electrons and positrons into a silicon crystal assuming a step-like potential. Figure c) is adapted from reference [18].

3.3.3. Dynamical calculation of beam intensities

In the following, we summarize how to perform dynamical calculations of TRHEPD beam intensities, which has been adapted from RHEED. For further reading and different methods we refer to the textbook *Reflection High-Energy Electron Diffraction* by A. Ichimiya and P. I. Cohen [133].

We start with the Schrödinger equation[3] to describe positron scattering [134]

$$\left[\nabla^2 + U(\vec{r}) + k^2\right] \psi(\vec{r}) = 0, \tag{3.26}$$

where we use the wave function $\psi(\vec{r})$ and the scaled crystal potential

$$U(\vec{r}) = -\frac{2m_e e}{\hbar^2} V(\vec{r}). \tag{3.27}$$

---

[3] Relativistic effects have been considered by Fujiwara [177] and corrections are possible by simply using the relativistic expression of k_i and m_e in the equations 3.26 and 3.27.

The crystal potential $V(\vec{r})$ is determined by the atomic positions and, in this general form, takes the finite penetration depth of the positrons into account. Due to possible relaxation or reconstruction of atomic layers close to the surface, $U(\vec{r})$ is only periodic parallel to the surface. On these grounds, it can be expanded as 2D Fourier series in the following way

$$U(\vec{r}) = \sum_n U_n(z)\, e^{i\vec{g}_n \vec{r}_\parallel}, \tag{3.28}$$

where the z-axis is defined normal to the surface and $\vec{r}_\parallel$ is a vector in the surface plane. The Fourier components $U_n(z)$ depend on the atomic scattering factors f_j. These can e.g. be expressed as a sum of Gaussians, following the parameterization by Doyle and Turner [178, 179]. The wave function can then be written as 2D Bloch wave,

$$\psi(\vec{r}) = \sum_n c_n(z)\, e^{i\left(\vec{k}_\parallel + \vec{g}_n\right)\vec{r}_\parallel}. \tag{3.29}$$

By substituting equations 3.28 and 3.29 into the Schrödinger equation 3.26, we obtain the following set of coupled differential equations

$$\frac{d^2}{dz^2} c_m(z) + \Gamma_m^2 c_m(z) + \sum_n U_{m-n}(z)\, c_n(z) = 0, \tag{3.30}$$

$$\text{with } \Gamma_m^2 := k^2 - (\vec{k}_\parallel + \vec{g}_m)^2. \tag{3.31}$$

Equation 3.30 can be converted into matrix form. There are various approaches to continue, e.g. using the multi-slice method suggested by A. Ichimiya [180, 181]. Here, the crystal is divided into thin slices parallel to the surface. Within each slice, $U(\vec{r})$ is approximated to be constant in z-direction, which equals a sequence of step-like potentials. After applying appropriate boundary conditions between the slices and for the surface, the actual calculation can be done numerically. Given this framework, we can extract TRHEPD beam intensities for each lattice rod when considering a certain surface structure. However, for a correct treatment, intensity losses due to inelastic scattering (electronic and plasmon excitations) as well as thermal diffuse scattering on phonons, have to be considered. This can be done by adding an imaginary component to the crystal potential [18, 133]:

$$V = V_{elastic} + i(V_{el} + V_{pl} + V_{TDS}) \tag{3.32}$$

3.3.4. Procedure for surface structure determination

There is a well-established methodology to determine surface structures using RHEED, which can be applied for TRHEPD in the same way. Within this work, we concentrate on the standard approach, i.e. rocking curve (I-θ) analysis. Note that TRHEPD azimuthal plots (I-φ) have been recorded recently as well, but the extraction of structure parameters is more sophisticated [182].

TRHEPD rocking curves usually relate to the intensity of the specular beam, as it is the brightest diffraction spot and can be traced over the whole angular range. Moreover, the complete surface structure can be determined when only considering the specular beam. To increase the reliability, rocking curves of further (integer or fractional) diffraction spots can be included in the analysis, too. This has been done in several studies [17, 183, 184], even though such rocking curves are sometimes rather flat and lack prominent features.

One- and many-beam condition

A rocking curve depends on the beam direction with respect to the crystallographic orientation of the sample, as defined by the (fixed) azimuthal angle φ. Since the positron wavelength is much shorter than the lattice constant, the diffraction patterns and the related rocking curve are hardly affected by the atomic coordinates parallel to the beam direction [185]. When we choose $\vec{k}$ e.g. along the x-axis, the rocking curve only depends on the y and z components of the atomic positions. For a complete analysis of the surface structure, we thus have to record rocking curves in different directions, usually three, as depicted in figure 3.8 a).

Measurements along a high-symmetry direction are referred to as *many-beam condition* and when the incident beam is intentionally shifted off-axis by an appropriate angle $\Delta\varphi$, it is called *one-beam condition*. The fundamental difference is evident when comparing figures 3.8 b) and c). In the one-beam condition, each atomic layer can be considered as a homogeneous continuum. Consequently, in-plane diffraction is strongly suppressed and the main diffraction spot is the specular beam. In the one-beam approximation, the crystal potential can be averaged in the lateral directions and thus only depends on z [133]:

$$U_0(z) = \frac{1}{A} \int_{-\infty}^{\infty} \int_{-\infty}^{\infty} U(x, y, z) \, \mathrm{d}x \, \mathrm{d}y, \tag{3.33}$$

where A denotes the surface area. In fact, $U_0(z)$ can be identified as zeroth order Fourier component in equation 3.28. Since only one Fourier component is non-zero, computational times are significantly reduced. In the course of structure determination, the one-beam rocking curve is analyzed first, as it yields the atomic coordinates z_i normal to the surface, without the need to consider the in-plane coordinates [18, 133]. In the second step, we can then analyze the two many-beam rocking curves for fixed z_i to obtain the coordinates x_i and y_i.

We emphasize that, technically, it would be possible to access all necessary information with just two many-beam rocking curves. However, by inclusion of the one-beam rocking curve, the amount of free parameters can be reduced significantly in each data set. This simplifies the iterative adjustment of the structural model and ultimately leads to a faster and more reliable structure determination.

Definition of the reliability factor and iterative computation

For each beam direction, theoretical rocking curves can be calculated from an assumed structure as introduced in section 3.3.3. To quantify the agreement with experimental data, we define the reliability factor [18]

$$R = \sqrt{\sum_i \left[I_{\mathrm{exp}}(\theta_i) - I_{\mathrm{cal}}(\theta_i) \right]^2}, \tag{3.34}$$

where $I_{\mathrm{exp}}(\theta_i)$ and $I_{\mathrm{cal}}(\theta_i)$ are the experimental and calculated intensities of a certain diffraction spot at glancing angle θ_i that are normalized by

$$\sum_i I_{\mathrm{exp}}(\theta_i) = \sum_i I_{\mathrm{cal}}(\theta_i) = 1. \tag{3.35}$$

Note that the definition of the R-factor is not consistent in literature [18, 187, 188]. To optimize the structural model, we have to minimize the R-factor by iterative computation. Besides the adjustment of atomic coordinates, this can also include non-structural parameters, e.g. the vibrational amplitudes of surface atoms [2]. In practice, the optimization in this multidimensional parameter space can e.g. be realized using the Nelder-Mead algorithm [189, 190]. To exclude convergence to local minima, Tanaka *et al.* currently implement a two-stage algorithm for supercomputers, where a grid-based global search is applied prior to the local search algorithm [185, 191].

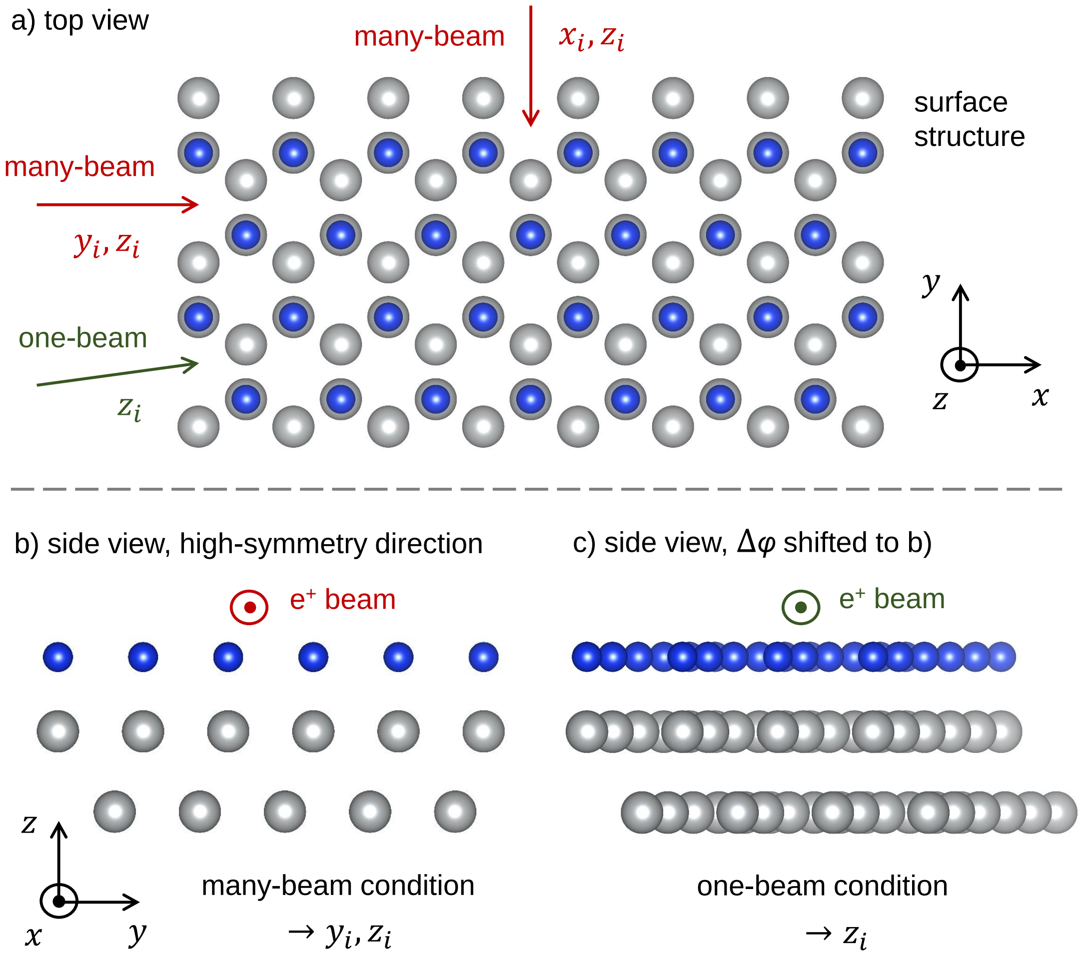

Figure 3.8. Schematic illustration of many- and one-beam condition for TRHEPD rocking curves. a) Top view: green and red arrows indicate the direction of the incident positron beam when satisfying the one- or many-beam condition. b) A rocking curve recorded along a high-symmetry direction is sensitive to the atomic coordinates perpendicular to the beam direction. This setting is called many-beam condition. c) When the incident beam is directed off any symmetry axes, the rocking curve is only sensitive to the atomic coordinates normal to the surface, which is called one-beam condition. The crystal structure has been visualized using the software VESTA [186].

Figure 3.9 summarizes the general workflow that is necessary to determine structural parameters from a single rocking curve. If the minimum value of the R-factor is not sufficiently small, the assumed model might be incorrect and the process has to be repeated for another structure [156]. Bear in mind, that the experimental conditions play a crucial role as well, e.g. an inadequate sample quality can increase the R-factor to an impracticable level.

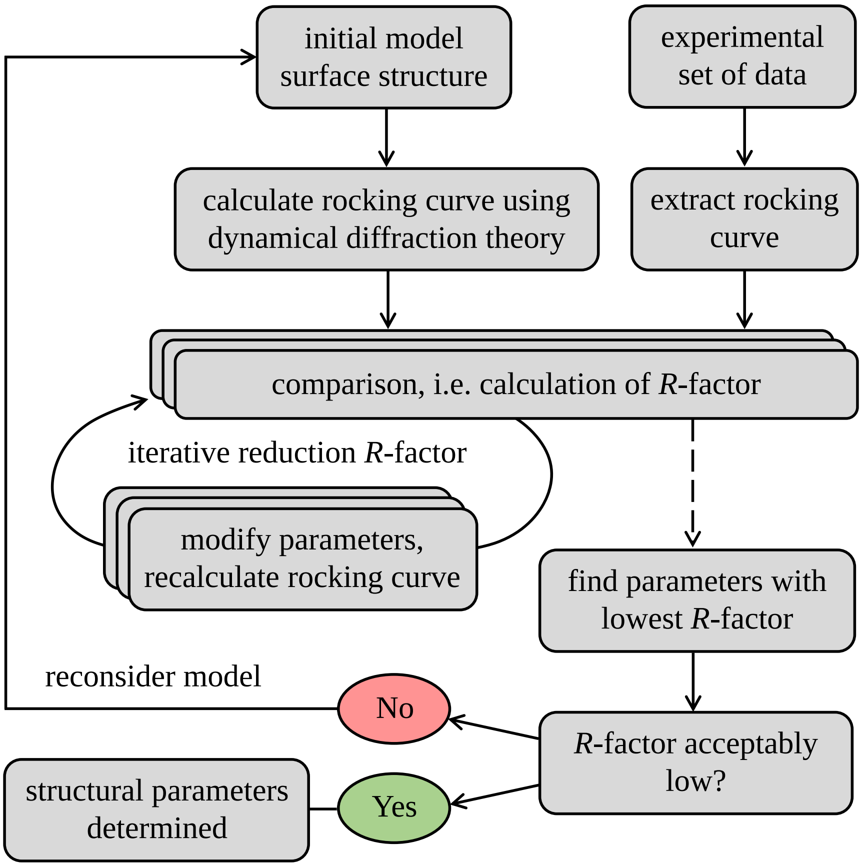

Figure 3.9. Procedure to obtain structural parameters by means of TRHEPD rocking curve analysis (flow chart). Shown are the necessary steps to analyze a single rocking curve, which are the same for one- and many-beam condition.

3.3.5. TRHEPD in Japan – a brief overview

In the following, the TRHEPD setup in Japan is introduced and the main experimental results are summarized. For a more comprehensive overview, the reviews by Fukaya *et al.* [18] and Hugenschmidt [30] are recommended.

^{22}Na-based setup and experiments on Si(111) - (1 × 1) - H

The initial TRHEPD setup was based on a ^{22}Na source, that yields a positron beam with an intensity of approximately 10^3 - 10^4 e^+/s after moderation and collimation [105, 192]. The electrostatic optics were optimized for a fixed beam energy of 20 keV that was later reduced to 10 keV in a reconstructed setup. First experiments were performed on a Si(111) - (1 × 1) hydrogen terminated surface, allowing to experimentally confirm the phenomenon of total-reflection and the presence of the first order Bragg peak in the rocking curve [170, 193]. Within the quantitative analysis, the surface could be characterized as mostly terminated by SiH, including a small fraction of SiH_3 molecules [194]. In further studies, the first order Laue zone could be resolved as well, which was achieved by the reduction of energy spread ($< 1\%$) and beam divergence ($< 0.1^\circ$) [195]. Subsequent research is summarized later (thematically ordered).

TRHEPD setup at the Slow Positron Facility at KEK

In 2010, the TRHEPD setup was transferred to the Slow Positron Facility (SPF) at KEK and later replaced by an improved, brightness-enhanced setup [121]. At the SPF, a dedicated 55 MeV electron LINAC is used to produce a pulsed positron beam with an intrinsic energy of up to 35 keV, a pulse width of 1 μs (long-pulse mode) and a repetition rate of 50 Hz. The positron production is based on a tantalum target (converter) with a structure of tungsten foils for moderation. This yields an initial beam intensity of $\sim 5 \cdot 10^7$ e^+/s in the long pulse mode [58]. After transportation to the experimental station in a magnetic field of ~ 15 mT, the beam is magnetically focused onto a 100 nm thin tungsten foil that serves as transmission remoderator. The intensity of the remoderated beam is $\sim 5 \cdot 10^5$ e^+/s [168]. It is accelerated to an energy of 10 keV and electrostatically deflected towards the grounded sample that is orientated by a fine positioning system. Compared to the previous ^{22}Na-based setup, the large intensity enhanced the signal to noise ratio significantly and enables sample orientation in real time. When slightly focused onto the MCP, the beam has a diameter of $\sim$0.5 mm (FWHM), an energy spread of $\sim$8 eV and an angular divergence of $\sim$12 mrad [121, 168]. The base pressure of the TRHEPD chamber is below $4 \cdot 10^{-10}$ mbar and the sample temperature can be adjusted between 15 and 1773 K [196].

Surface structure analysis

<ins>Si(111) - (7×7):</ins> The 1/7th - 3/7th fractional order Laue zones of Si(111) - (7×7) could already be observed in early studies [197, 198]. From rocking curve analysis of the specular beam, a mean spacing of 1.52 Å between adatom and stacking fault layers was found, which is slightly larger than predicted. This was attributed to an enhanced outward relaxation of the adatom layer [198].

Metal adatom induced superstructures on Si(111): In initial experiments, the atomic height of the uppermost Ag triangle in the Si(111) - ($\sqrt{3} \times \sqrt{3}$) - Ag structure was determined as 0.77 Å [199]. This is consistent with results from other methods and first-principle calculations. The further adsorption of a small amount of Ag, Au or also Cs atoms leads to a more complex $\sqrt{21} \times \sqrt{21}$ reconstruction, for which various models have been discussed previously. Within several TRHEPD studies [200–202], the respective height of the additional adatoms with respect to the underlying structure and their adsorption sites could be determined. Cs adatoms arrange in a large triangular structure with a side length of 10.12 Å and a height of 3.04 Å [202], which is distinct from the structure found for the noble metals Ag and Au.

Pb and Sn adsorbed on Ge(111): The deposition of 1/3 ML Pb or Sn on Ge(111) leads to a $\sqrt{3} \times \sqrt{3}$ reconstruction at room temperature that changes to 3×3 at temperatures below $\sim$ 200 K [203]. For both adsorbates, TRHEPD rocking curves indicated that the equilibrium positions are identical in both phases. It was thus concluded, that the phase transition is of order-disorder type [183, 204]. Furthermore, it was found that two adatoms are displaced downwards within the unit cell, while one is displaced upwards with a height difference of 0.51 Å in case of Pb [204] and 0.26 Å for Sn [205].

Rutile-TiO_2(110) - (1×2): After annealing at 1200 K in UHV, rutile-TiO_2(110) exhibits a (1×2) surface reconstruction [18]. The precise structure has been under debate for over 30 years and various models were suggested. By rocking curve analysis of the specular beam, Mochizuki *et al.* [188] found strong evidence for the so-called asymmetric Ti_2O_3 model. This structure was suggested by Wang *et al.* [206] and an excellent agreement was obtained after minor adjustments of the atomic positions. The study showed in particular, that TRHEPD can identify oxygen atoms on the topmost surface layer and clearly distinguish whether titanium atoms are positioned at interstitial-vertical or -horizontal sites [30].

Pt-induced nanowires on Ge(001): By sub-monolayer deposition of Pt atoms on Ge(001), 1D nanowires are formed. This leads to a (4×2) structure that changes to (4×4) for temperatures below 80 K. Using TRHEPD and comprehensive methods, Mochizuki *et al.* [207] were able to verify one of the proposed structural models. The structure essentially consist of Ge dimers at the topmost layer and buried Pt arrays. At high temperature, the dimers are flat, while they become alternately buckled normal to the surface when the temperature is decreased, hence doubling the periodicity.

2D materials: Recently, TRHEPD was applied to precisely determine the spacing between graphene and metal substrates. For Cu(111) and Co(0001), a spacing of 3.34 Å and 2.06 Å was found respectively [208]. In the case of Cu(111), this is very close to the interlayer spacing in graphite (3.35 Å), indicating that the graphene layer is only weakly bound. In contrast, the interaction with the Co(0001) substrate is strong, which is related to the hybridization of graphene p_z- and cobalt d-states, i.e. the formation of chemical bonds [176].
Further 2D materials have been investigated as well, namely silicene on Ag(111) [209] and germanene on Al(111) [210]. The experimentally obtained substrate spacings are 2.14 Å and 2.51 Å, respectively. Unlike the flat structure of graphene, silicene and germanene exhibit buckling, which could be determined as 0.83 Å and 0.94 Å, respectively. TRHEPD measurements further revealed that germanene has a 3×3 structure with asymmetric buckling, which was unlike any suggested model. Therefore, Fukaya *et al.* proposed a new structural model with only one protruding Ge atom per unit cell.

Intercalation of atoms: Most recently, Endo *et al.* [211] analyzed the structure of superconducting Ca-intercalated bilayer graphene grown on 6H-SiC(0001). Interlayer spacings (one-beam condition) and stacking structure (many-beam condition along $[1\bar{1}00]$) were determined. Furthermore, it was found that Ca atoms do not intercalate between the two graphene layers as expected, but rather between the graphene and the buffer layer.

Analysis beyond structure determination

Apart from structure determination, TRHEPD can also be applied to investigate other surface properties, such as the dipole barrier of metals [192], charge transfer [184] or surface excitations [212, 213]. Moreover, temperature-dependent TRHEPD measurements allow to analyze phase transitions [183, 214] or to precisely determine the surface Debye temperature [215]. For Si(111) - (7×7), the obtained adatom vibrational amplitude was larger than previously reported, e.g. by RHEED or SXRD [216]. This is attributed to the reduced interference from the bulk in TRHEPD.

Chapter 4.

4 Instrumentation of the positron diffractometer at NEPOMUC

Inspired by the Japanese pioneering work, which clearly demonstrates that TRHEPD is a powerful technique for surface structure analysis (section 3.3.5), we decided to develop a new diffractometer connected to the high-intensity positron source NEPOMUC. To the best of our knowledge, this is the second operational TRHEPD setup in the world. In this chapter, the instrumentation is explained in detail and the features of the new diffractometer are pointed out.

4.1. The reactor-based positron source NEPOMUC

The NEutron induced POsitron source MUniCh (NEPOMUC) provides the most intense monoenergetic positron beam in the world with an intensity of more than 10^9 e^+/s [63]. As introduced in section 2.1.2, the underlying mechanism is pair production from γ-rays that are emitted after thermal neutron capture by ^{113}Cd. The experimental realization of the in-pile source is illustrated in figure 4.1. It consist of three major components: beam tube, experimental tube and potential tube. The outer part, i.e. the beam tube (SR11), is mounted in the reactor pool, close to the fuel element.[1] The tip includes a cadmium cap, that is enriched with 80% ^{113}Cd for the (n, γ) conversion [217]. The experimental tube, which is inserted in the beam tube, is evacuated to UHV and serves as a support for the magnetic coils. A structure of Pt foils at the front of the innermost potential tube is used for both, pair production and subsequent positron moderation. The adjacent lens system is also made from Pt and contributes to the positron production. Irradiation-induced vacancies in Pt are annealed in-situ

---

[1] Note that, due to cooling constraints, the tip of the NEPOMUC beam tube is not placed in the region of maximum thermal neutron flux density.

due to γ-heating during reactor operation [53]. The NEPOMUC beam is formed by means of magnetic and electrostatic fields that extract and accelerate the moderated positrons emitted from the Pt surface. The obtained positron beam is adiabatically guided through the biological shield, which separates reactor pool and experimental hall, to reach the NEPOMUC platform.

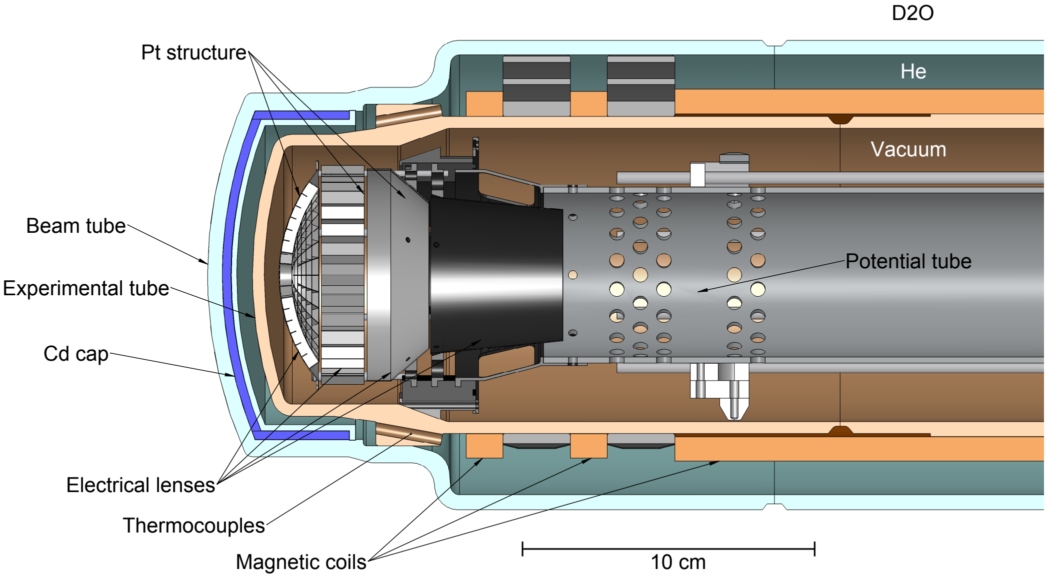

Figure 4.1. Cross-sectional view of the in-pile positron source NEPOMUC after an upgrade in 2011. Thermal neutrons from the research reactor FRM II are absorbed in a cadmium cap, which is enriched with the isotope ^{113}Cd. The subsequently emitted γ-radiation is used for pair production in a Pt structure. Moderated positrons are extracted and accelerated to form a beam. Figure taken from reference [217].

The initial positron beam from the in-pile source is referred to as *primary beam*. As described in section 2.4, the brightness of the primary beam can be enhanced via remoderation. Piochacz *et al.* [218] developed and set up an optional remoderator unit at the first accessible position downstream the beamline. Two computer-controlled magnetic switches in front and behind this section allow to quickly toggle between primary and remoderated beam [53]. For remoderation, the positron beam is magnetically focused onto a W(100) single crystal in reflection geometry outside the magnetic guiding field. Recently, the remoderator assembly has been upgraded with a movable crystal holder and a preparation chamber, which allows a convenient exchange of the remoderator crystal without breaking the beamline vacuum [219]. The properties of primary and remoderated NEPOMUC beam are summarized in table 4.1. The remoderated beam has a reduced intensity of $\sim 5 \cdot 10^7$ e$^+$/s, but is used for most experiments because of its enhanced brightness. The beam is guided in a magnetic field of typically 4 mT and is delivered to one of five different experimental stations using a central beam switch.

Beam characteristics	NEPOMUC	
	primary	remoderated
$B_{\parallel}$ (mT)	5	4
$E_{kin} \approx E_{\parallel}$ (eV)	1000	20
I (e$^+$/s)	$1.14 \cdot 10^9$	$5.0 \cdot 10^7$
d_{FWHM} (mm)	9.3	1.85
$E_{\perp}$ (eV)	50	1
$\Delta E_{\parallel}$ (eV)	90	3
B^+ (e$^+$/(mm^{2}eV^{2}s))	$2.9 \cdot 10^3$	$4.9 \cdot 10^6$

Table 4.1. Beam parameters of the NEPOMUC primary and remoderated positron beam in the magnetic guiding field $B_{\parallel}$. The data is taken from references [63, 219, 220] and the brightness B^+ was calculated using equation 2.23.

4.2. Experimental conditions and requirements

Firstly, the experimental conditions and requirements for the TRHEPD setup at NEPOMUC are discussed. The fundamental differences compared to the LINAC-based setup at the SPF in Japan are emphasized and the implications on the instrumentation are explained.

4.2.1. Positron beam properties

The key ingredient for TRHEPD measurements is naturally the positron beam. A commercial RHEED gun yields a coherent electron beam with a diameter of $\sim 100\,\mu$m and a beam current of up to $100\,\mu$A [221], which equals an intensity of more than 10^{14} e$^-$/s. When compared with the beam properties at NEPOMUC (see table 4.1), this impressively illustrates the intrinsic challenge of TRHEPD experiments. With regard to the instrumentation, we thus discuss the relevant beam parameters and how to meet the experimental requirements.

Beam intensity

The primary motivation for TRHEPD measurements at NEPOMUC is the high beam intensity. Reduced measurement times are advantageous, especially for the study of surfaces, which continuously deteriorate after preparation due to the residual gas in the UHV chamber. A large initial beam intensity also allows the application of (multiple) remoderation to adjust relevant beam parameters, namely coherence length and beam diameter. Generally, this enhances the signal-to-noise ratio of the recorded diffraction pattern, which means that fractional and higher order diffraction spots can be observed as well. Moreover, as pointed out in section 3.3.5, an adequate beam intensity is very convenient for the sample orientation because the diffraction pattern can be observed in real-time.

Coherence length

The coherence length specifies the finite distance on the surface from where scattered positrons keep their phase information and thus interfere coherently. To observe TRHEPD patterns, the coherence length of the positron beam has to be sufficiently long. This is in particular important when investigating reconstructed surfaces that have a large unit cell. The coherence length parallel and normal to the beam direction can be calculated as [133]

$$l_{\parallel} = \left[\left(\frac{\Delta\theta \, \sin\theta}{\lambda} \right)^2 + \frac{m_\mathrm{e} \, \Delta E^2}{2 h^2 E} \right]^{-\frac{1}{2}} \quad \text{and} \tag{4.1}$$

$$l_{\perp} = \frac{\lambda}{\Delta\theta}. \tag{4.2}$$

For a fixed beam energy E and a certain glancing angle θ, the coherence length is determined by $\Delta\theta$ and ΔE, i.e. angular and energy spread of the beam. Since the inherent energy spread of the remoderated NEPOMUC beam is smaller, it is much better suited for diffraction experiments than the primary beam. Note however, that the explicit calculation of $l_{\parallel}$ and $l_{\perp}$ is only meaningful for the incident beam, which has to be characterized outside the magnetic guiding field, after being accelerated and downstream the beam optics.

The importance of the beam diameter

A sufficiently small beam diameter is desirable for two main reasons. Firstly, it is more convenient regarding the beam optics. For a lens system of fixed dimension, spherical aberrations are less relevant when the beam diameter is small because the positrons are closer to the optical axis. Conversely, we would need to upscale the dimension of the lens system to compensate for a large beam diameter. Due to experimental constraints, e.g. the limited space available, this is however only possible to a certain extent.

The second reason is related to the geometry of TRHEPD, i.e. measurements in grazing incidence. As schematically depicted in figure 4.2 a), the intensity of a circular shaped beam distributes over an elliptical area in the sample plane. The semi-major axis a of the ellipse can be calculated as

$$a = \frac{d}{2\sin(\theta)}, \tag{4.3}$$

while the semi-minor axis b is just half the beam diameter d. Therefore, the eccentricity of the ellipse increases for smaller glancing angles θ. For the relevant measurement range of $\theta \sim 0.5\text{-}6^\circ$ and a typical beam diameter of few mm, we find that the ellipse exceeds by far the sample size of usually 5-10 mm. This is illustrated in figure 4.2 b) for $\theta = 4^\circ$ and $d = 2\,\mathrm{mm}$. For the primary NEPOMUC beam and $\theta = 1^\circ$, we calculate a major axis of more than 0.5 m. Consequently, only a marginal fraction of the beam intensity would actually contribute to the diffraction signal. When using the remoderated NEPOMUC beam, the geometrical losses are much lower, which can partly compensate the reduced intensity.

Also bear in mind that the fraction of the beam intensity that illuminates the sample increases with θ in the relevant range. To enable the quantitative comparison of experimental and calculated rocking curves, we have to take this effect into account. When the beam diameter is sufficiently large, the geometrical correction can be realized by a simple scaling with $1/\sin(\theta)$.[2] This is derived in detail in the appendix A.1. Both, primary and remoderated NEPOMUC beam are broad enough for this approximation. In that regard, a significant reduction of the beam diameter by further remoderation is not beneficial.

---

[2] Usually, instead of scaling the experimental intensities by $1/\sin(\theta)$, the calculated intensities are multiplied with $\sin(\theta)$ [193, 211], which is equivalent.

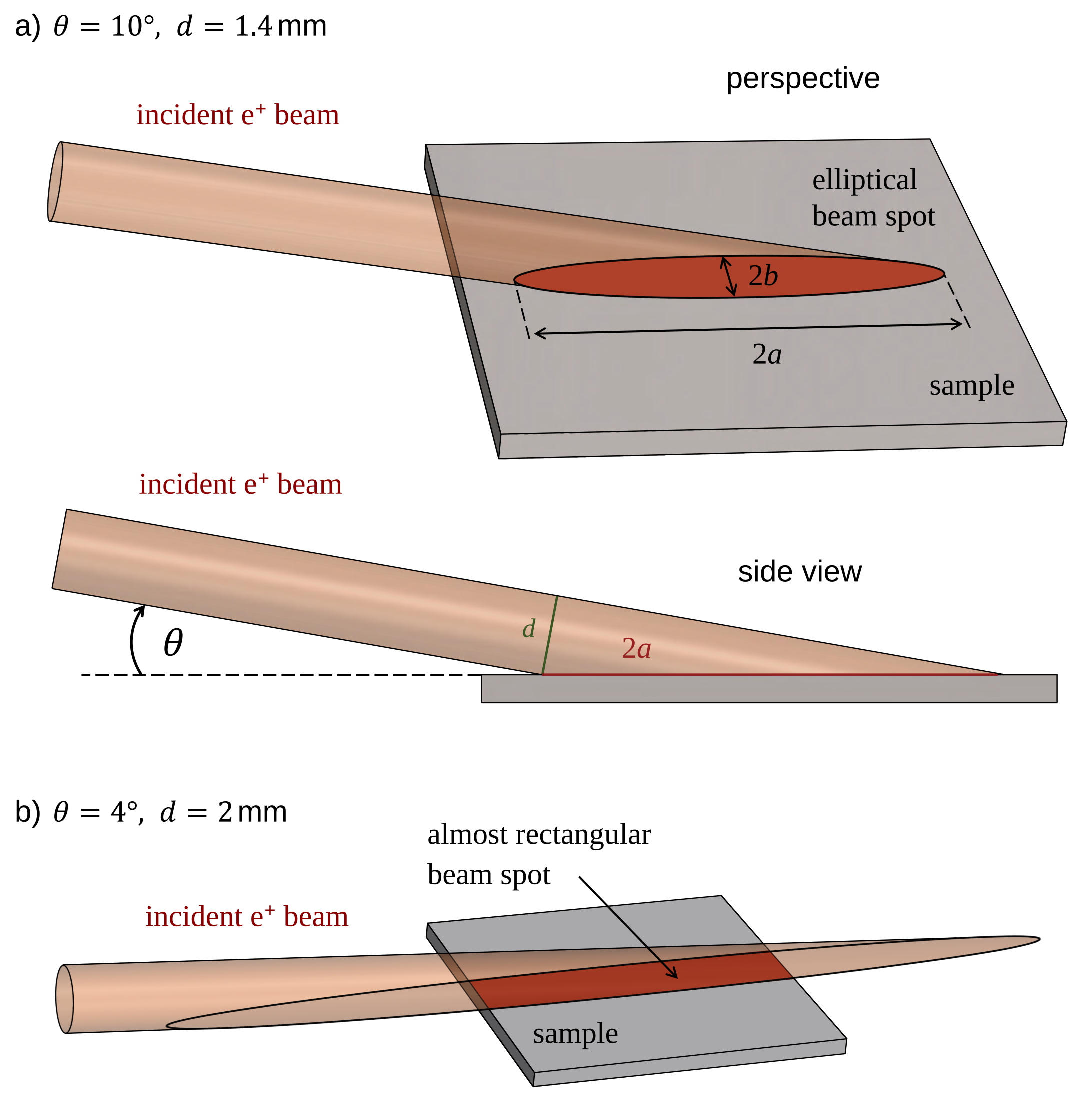

Figure 4.2. Geometrical considerations for TRHEPD. We assume a circular shaped positron beam incident on the sample with angle θ. a) When θ is large and the beam diameter d sufficiently small, the beam spot on the sample is an ellipse with semi-major axis a, which can be calculated using equation 4.3. b) In grazing incidence and for beam diameters of few mm, the ellipse is much larger than the usual sample size. This is typically the case for TRHEPD measurements. The beam spot on the sample can then be approximated as a rectangular stripe.

Increase of the beam energy

For TRHEPD, it is necessary to increase the beam energy up to several keV, which can be done by electrostatic acceleration. Consequently, the electrostatic potential must decrease from the positron source to the experiment [27]. At the

SPF, the positron source is set to a positive high voltage (HV) of 15 kV to work in a sample environment that is grounded [121]. This situation is analogous to RHEED measurements, where the HV is only applied within the electron gun. Due to the close vicinity to the reactor and the limited space available, the NEPOMUC source is however not designed to be set to such high voltages. Therefore, we have to apply a negative HV at the experimental side, which has major consequences on the instrumentation. The resulting challenges are discussed in section 4.2.2.

In general, there would be another approach to accelerate the positron beam without the need to apply HV at the experimental side. A so-called *energy elevator* allows to increase the potential energy of a pulsed beam without changing its kinetic energy or other beam parameters [222, 223]. However, for TRHEPD, it is not expedient to pulse the beam (see next section).

The advantage of a continuous positron beam

Based on the reactor operation, the NEPOMUC beam is continuous, which is in contrast to the pulsed beam from a LINAC-based source, e.g. the SPF. Since the intensity of a single pulse is far too low for time-resolved measurements on a relevant timescale, a pulsed positron beam offers no advantages for TRHEPD. In fact, a pulsed beam is unfavorable because the peak intensity is much higher, which can lead to the saturation of the MCP. This decreases the detection efficiency, but even more severe, it changes the relative intensities of the diffraction spots and is thus a systematic error when performing rocking curve analysis. To overcome this issue at the SPF, it is planned to install a pulse stretcher in the TRHEPD beamline, which increases the pulse duration from 1 μs to several ms [54, 224]. Currently, the beam intensity has to be reduced by almost one order of magnitude when conducting quantitative TRHEPD measurements [196]. Against this backdrop, a continuous positron beam, as available at NEPOMUC, is ideal for TRHEPD.

Beam stability

An adequate beam stability is a prerequisite for quantitative TRHEPD measurements. Therefore, we have to prevent time-dependent deflections, drifts or intensity fluctuations of the direct beam. This is partly related to the instrumentation, e.g. beam drifts can be caused by charging of insulators that has to be excluded. The application of a remoderator can also influence the beam stability. After the surface of the remoderator crystal has been conditioned by a heat treatment, the beam intensity naturally decreases over time since the clean surface deteriorates. Such predictable, systematic changes in intensity can however be compensated within the data evaluation.

In contrast, it is very difficult or even not possible to account for external, time-dependent perturbations. The SPF in Japan is dedicated to positron physics and while measuring TRHEPD, neighboring experiments are not in operation. External influences are thus more or less negligible. In this regard, the environment at NEPOMUC is rather problematic because the experimental hall of the FRM II accommodates a variety of neutron experiments that operate simultaneously. Known issues can occur when a nearby magnet is used for field sweeps or when the metallic heavy-duty crane moves. This affects the positron beam during the transportation in the beamline, which leads to a reduction of the intensity or a displacement of the beam on the fluorescent screen. Such influences have to be excluded during TRHEPD measurements. A relevant increase of the background due to neutron experiments is however not expected.

Conclusion and implications

When compared with the SPF in Japan, the NEPOMUC facility offers two main advantages: the larger beam intensity and the continuous beam. The drawbacks are that the sample environment has to be on HV and that special care is necessary to guarantee beam stability. As discussed in detail, it is not reasonable to use the primary NEPOMUC beam for TRHEPD, because energy spread and beam diameter are too large. The remoderated NEPOMUC beam is, in principle, much better suited, but we still have to adjust the kinetic energy and the beam divergence with an appropriate lens system to evaluate the final properties. In this context, we should also bear in mind, that a non-ideal transportation in the beamline and the termination of the magnetic guiding field can downgrade the beam properties [92, 225]. This can be even overcompensated when applying a second remoderator in front of the experiment. Besides the further reduction of energy spread and beam diameter, this yields a beam with well-defined properties. We therefore decided to integrate an additional remoderator in the setup that can be applied optionally. Alternatively, it would also be possible to use a collimator, which can be realized straightforward, but is less efficient and versatile.

4.2.2. Requirements on the setup and challenges

The high demands regarding the beam properties have a direct impact on the instrumentation. However, besides that, there are also several general requirements, e.g. concerning sample environment, in-situ preparation or characterization prior to TRHEPD. The main specifications for the experimental setup can thus be summarized as follows:

- Possibility to record TRHEPD rocking curves along different crystallographic directions as well as azimuthal plots with adequate angular precision and within acceptable measurement times
  - Optional brightness enhancement of the remoderated NEPOMUC beam in front of the experiment using a second remoderator
  - Electrostatic lens system that can be applied for both, remoderated and twofold remoderated beam, to form a coherent positron beam with variable energy of up to 30 keV (later reduced to 20 keV)
  - Sample alignment with respect to the incident beam and the capability to vary glancing and azimuthal angle with highest accuracy
  - Positron detection using a MCP assembly with fluorescent screen
- Ability to perform temperature-dependent TRHEPD measurements at elevated temperatures
- Integrated RHEED system for qualitative structure analysis and evaluation of the sample quality prior to TRHEPD
- In-situ sample conditioning to remove adsorbates, e.g. ion beam sputtering and subsequent annealing at high temperature (depending on sample)
- Vacuum chamber with a base pressure in the range of 10^{-10} mbar, as necessary for most surface studies

In fact, there would be several more demands that can eventually be realized within an upgrade, e.g. the option to conduct TRHEPD measurements at low temperatures or to grow samples in-situ. Furthermore, we decided that the setup won’t comprise a retarding field analyzer. This would be necessary to characterize the energy spread of the direct beam precisely or to investigate surface excitations. The new diffractometer is thus solely dedicated to surface structure analysis because this is the major strength of TRHEPD.

In order to realize these instrument specifications, we have to overcome different challenges. The immediate challenge is the HV, that we have to apply not only to the lens system itself (acceleration and beam optics), but also beyond the last electrode. The final potential must be preserved until the diffracted positrons are detected. Consequently, the whole beam path downstream the lens system has to be enclosed by a Faraday cage, which is biased to HV. In particular, this must also include the sample, the upper part of the positioning system and the entrance side of the MCP.

This leads to several ensuing challenges, e.g. heating the sample during TRHEPD measurements or preventing potential damage of the MCP assembly, although the applied voltages have to be raised above the normal specification. Moreover, we have to satisfy the stringent requirements regarding UHV. This is more difficult since an effective separation of the lens system and the main vacuum chamber is not possible (due to the Faraday cage). Another experimental boundary condition is the fixed geometry of the main vacuum chamber, which was originally designed for layer deposition [226] and has been recycled for the present setup.

4.3. Overview of the new diffractometer

As a major part of this work, the TRHEPD setup has been designed, assembled and put into operation. Figure 4.3 shows a cross-sectional view along the positron beam path including photos of the key components. Subsequently to the transportation in the beamline, the positron beam passes a magnetic field termination, which is described in detail in section 4.4.1. Acceleration and beam optics are realized by an electrostatic system consisting of 18 electrodes. An optional remoderator stage in transmission geometry can be inserted into the beam path to enhance the brightness of the beam. For this we use a 100 nm thin Ni(100) foil, which can be conditioned in a separate crosspiece. The remoderator and the procedure for conditioning are introduced in section 4.4.2. The design of the lens system has been refined by simulations within an iterative process. For the final geometry, we optimized the potentials of the individual electrodes to obtain a parallel beam of small diameter as necessary for diffraction. This has been done for different beam energies, as described in section 4.4.3. Downstream the lens system, i.e. when the final potential is reached, the beam is magnetically bend

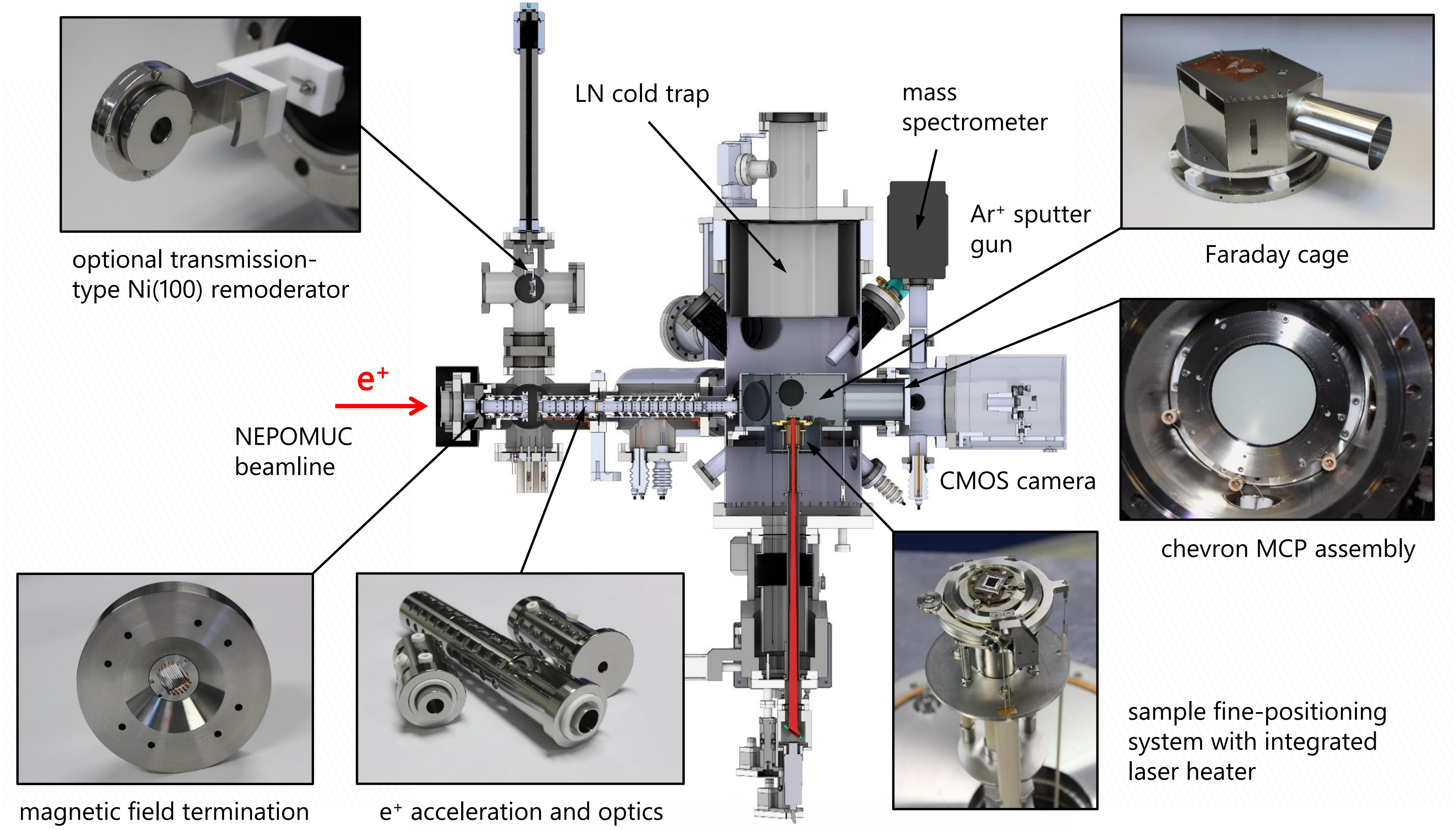

Figure 4.3. Vertical cross-sectional view of the TRHEPD setup at NEPOMUC including photos of the main components.

towards the sample by a fixed angle. For the positron detection, we use the MCP assembly *F2226-24P* from *Hamamatsu*, but collectively raise the applied potentials using a HV potentiometer. This is explained in section 4.4.4. The diffraction pattern is recorded with a CMOS camera (*Basler acA1920-50gm*) through a viewport and processed by a Python script. The camera is attached to a kinematic mirror mount to allow a precise alignment. To reduce the background produced by visible light, camera and viewport are shielded by an aluminum cap. The interior of the cap is wrapped by black velour to suppress back reflections of the image.

Within a first beamtime, we characterized the direct beam with and without applied remoderator (see section 4.6). This confirmed the results from the simulations and the electrostatic system was fine-tuned manually. Although the assembled setup has been tested with voltages up to 20 kV, so far we only worked with beam energies of 10 or 15 keV. This has two main reasons. Firstly, a reduced beam energy increases the critical angle for total reflection and thus the surface sensitivity of the measurements (compare equation 3.22). Secondly, this also minimizes the risk of HV flashovers, which could damage the MCP or other components.

A second cross-sectional view of the TRHEPD setup is shown in figure 4.4. The axes for TRHEPD and RHEED are indicated, which confine an angle of approximately 135 °. To prevent electrostatic charging, the Faraday cage has to be grounded during RHEED measurements. The electron diffraction pattern is visualized by a conventional fluorescent screen and recorded with a second CMOS camera. Inside the Faraday cage, the sample can be orientated by a customized fine positioning system, which is equipped with a laser for contactless sample heating. Five axes allow to precisely adjust the position of the sample (x, y, z), the crystallographic orientation (rotation φ) and the glancing angle of the positron beam (tilt θ). This system was supplied by the company *Surface systems and technology* and is further discussed in section 4.5.1. The base pressure of the UHV chamber is below $2 \cdot 10^{-9}$ mbar, which increases slightly during the measurements. Since the UHV chamber is not baked yet, we are optimistic to reach a final pressure in the range of $5 \cdot 10^{-10}$ mbar after the bake-out. Further aspects of the vacuum system are described in section 4.5.3. Two photos of the TRHEPD setup at NEPOMUC are shown in the appendix A.2.2.

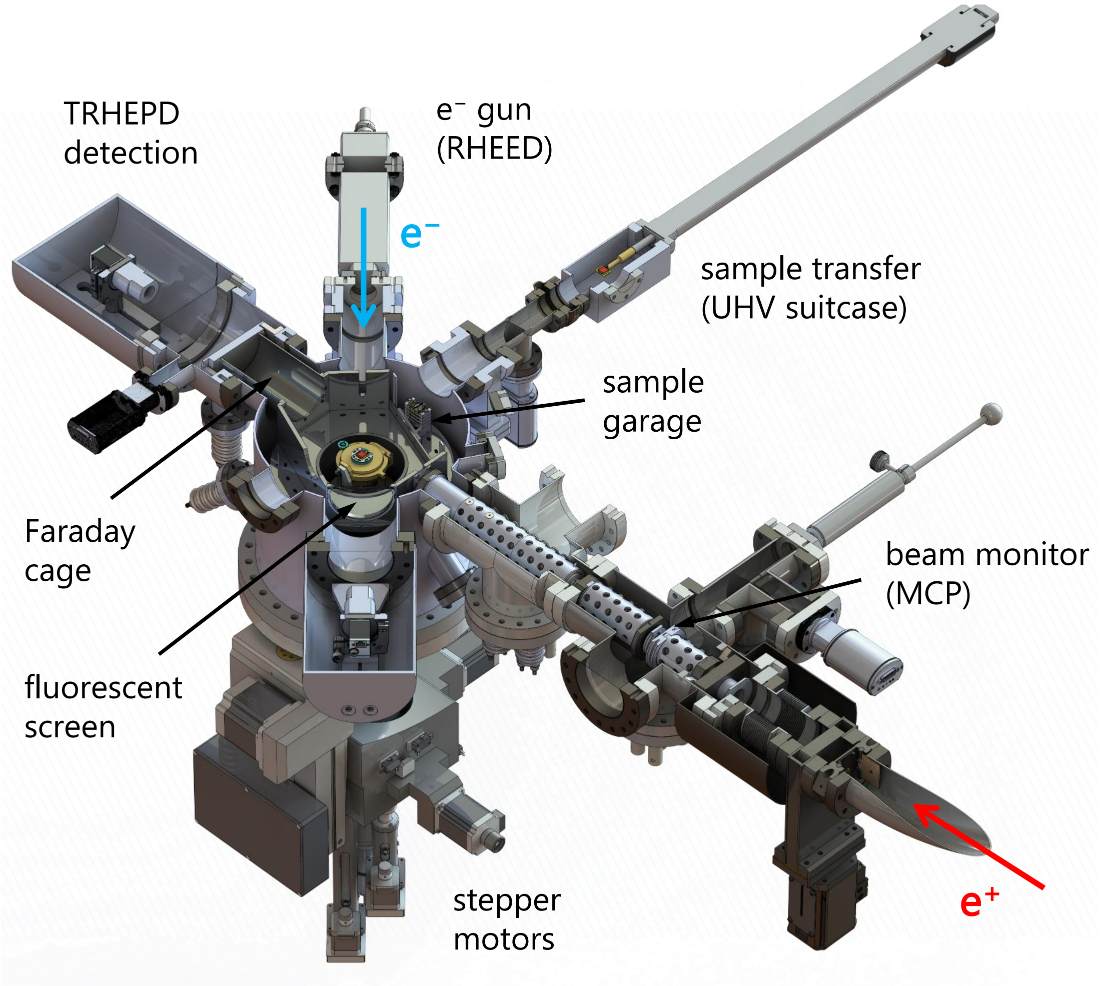

Figure 4.4. Cross-sectional view of the TRHEPD setup at NEPOMUC. TRHEPD and RHEED axes are indicated by red and blue arrows, respectively. To visualize the RHEED pattern, we use a commercial fluorescent screen attached to the Faraday cage.

4.4. Positron beam adaption and detection

As the space on the NEPOMUC platform is very limited, the TRHEPD setup has been connected to the so-called SuSpect beamline. For this, we disconnected the PAES setup and modified the beamline downstream the central beam switch. In the newly assembled section, we checked the strength and direction of the magnetic guiding field using a Hall probe. As the beamline vacuum is typically in the range of only 10^{-8} mbar, we add a narrow beam tube to enhance the decoupling of beamline and experiment. In the following, we introduce the individual components that are necessary to adapt the positron beam after the transportation in the beamline.

4.4.1. Magnetic field termination

At the experimental setup, the magnetic guiding field needs to be terminated as the beam is transported electrostatically from here on. It is crucial to reduce the influence of stray fields and prevent that positrons follow the diverging field lines since this would increase their mean transverse momentum. Consequently, the magnetic field in beam direction has to end abruptly so that the extraction is highly non-adiabatic. This is a well-known issue and various field terminations have been developed within the NEPOMUC research group in the past [218, 227, 228]. A possible approach is the utilization of a μ-metal aperture that picks up the magnetic fields lines, which are then directed outwards to be fed back to the beamline by a μ-metal sheet. More sophisticated designs may include very thin ferromagnetic stripes in the beam path that guarantee an even more abrupt transition. To minimize the geometrical shadowing and related intensity losses, this requires a precise alignment. Moreover, the material and the size of the stripes has to be considered carefully, so that the magnetic flux density does not saturate. The field termination for the TRHEPD setup is based on the previous experience.

We use a structure of 25 μm thin metallic glass stripes[3] that guide the field lines outwards, away from the optical axis, to a conical μ-metal ring. The configuration is shown in figure 4.5 a) and b). The metallic glass stripes are mechanically clamped in a venetian blind geometry using a Cu frame that is screwed to a μ-metal support. The gaps between adjacent stripes are 1 mm, which leads to a theoretical transparency of 97.5 %. Originally, it was planned to attach the stripes directly to the μ-metal support, e.g by laser spot welding. A welding test revealed that this is generally possible, but difficult to realize, as each stripe would need to be spot-welded multiple times on both sides while ensuring parallel alignment. Additionally, we considered to fix the stripes using special ceramic adhesive, which resulted in an inclined and rather fragile bond. Other adhesives, such as conductive silver paste, are not suitable for UHV. Mechanical clamping is therefore the most reliable and accurate approach. As it is necessary to bake-out the whole experiment at 150 °C for several days, we further examined the temperature behavior of the metallic glass in an external furnace. When baking at 300 °C for several hours, the magnetic properties are not affected, which is reasonable as the metallic glass has a Curie temperature of 415 °C [229].

---

[3] Amorphous alloy Fe78/B13/Si9, purchased from *Goodfellow* and cut to stripes.

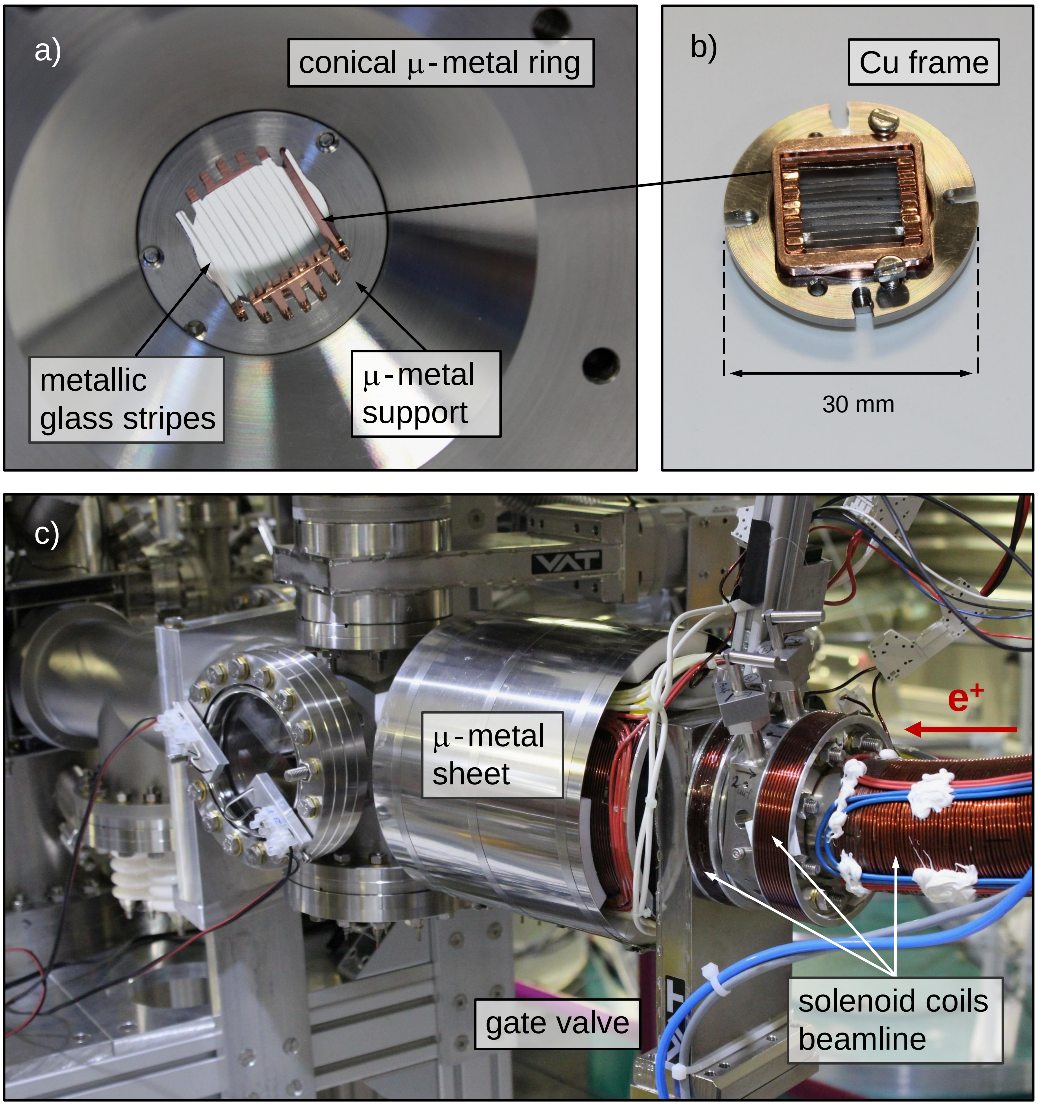

Figure 4.5. Magnetic field termination. a) 12 metallic glass stripes are used to guide the magnetic field lines outwards to the μ-metal support. b) The stripes are clamped in a frame to be orientated as parallel as possible. c) Outside the vacuum, the magnetic field lines are guided back to the beamline using a μ-metal sheet. It covers the last solenoid coil, which is operated with a reduced current. A pneumatic gate valve separates beamline and electrostatic lens system.

There are two further aspects to improve the decoupling from the magnetic guiding field. Firstly, faster positrons are generally much less affected by the field termination. Before they pass, we thus increase the beam energy from 20 eV up to $\sim$ 1.5 - 2.5 keV. As a second measure, we also reduce the magnetic guiding field in front of the field termination. This can be done gradually, i.e. by applying an *adiabatic decompression line* [53]. Instead, we decided to simply reduce the current of the last solenoid coil, that indeed has a slightly positive effect on the beam quality. The end of the beamline with the outer part of the field termination is shown in figure 4.5 c).

4.4.2. Optional transmission-type remoderator

Figure 4.6 a) depicts the electrostatic lens system adjacent to the field termination, where the optional remoderator can be applied. The remoderator stage can be inserted into the beam path from above and a spherical fit at the top ensures that it is positioned concentrically to the lens system. This also excludes any inclined alignment, so that the remoderator surface is perpendicular to the optical axis. To monitor the beam and adjust the focus onto the remoderator foil, we can alternatively insert a MCP from the side. A photo of this section with applied remoderator is shown in figure 4.6 b). As the majority of positrons annihilate in the remoderator foil, the possible influence of γ-radiation has to be considered. However, as the distance to the MCP at the end of the Faraday cage is over 80 cm and the quantum efficiency for γ-rays is rather low, we do not expect a significant increase of the background. This has also been confirmed experimentally.

Mainly due to geometrical constraints, we decided to employ a transmission-type remoderator. For this, tungsten [230] or nickel thin foils [104, 111] are usually used, which yield efficiencies of up to 20% as reported in early studies [79, 114]. The advantages of nickel are the easier preparation, the lower annealing temperature and the narrower energy distribution, while the disadvantages are its ferromagnetic nature and the reduced chemical stability of the surface. Since the energy distribution is most relevant in our case, we use a 100 nm thin single crystalline Ni(100) foil as remoderator, which is shown in figure 4.6 c). The nickel foil is attached to a support with a 3 mm pinhole and has been purchased from the University of Aarhus.

As discussed in section 2.2.3, it is crucial to reduce surface roughness and impurities to a minimum, which requires regular conditioning of the nickel foil. Typical impurities are carbon and oxygen, which can be removed by high temperature annealing in hydrogen atmosphere, as pointed out by Fujinami *et al.* [111]. This was experimentally investigated in more detail by Gigl *et al.*, who directly measured the chemical composition of the nickel surface [104]. It was found that an in-situ heat treatment at $\sim 500\,^\circ\mathrm{C}$ already removed the majority of adsorbates and improved the remoderation efficiency by a factor of four. The supplementary treatment with (molecular) hydrogen further enhanced the efficiency by a factor of almost three due to the chemical reduction of oxides. On this basis, we built the heater which is shown in figure 4.6 d). It consists of a commercial 250 W halogen light bulb with a spherical mirror to enhance the efficiency. We apply a light bulb instead of a bare filament to prevent tungsten evaporation onto the nickel foil, which turned out to be an issue at the CDBS heater designed by M. Thalmayr [231, 232]. Although the light bulb is filled with inert gas and a small amount of halogen, it is suitable for UHV application as only glass, ceramic and metal parts are exposed [233]. To maximize the solid angle, the heater can be manually moved close to the remoderator using an edge welded bellow. For the temperature measurement, we use a thermocouple attached to the mirror. The calibration curve is shown in figure 4.6 e). As the nickel foil is much thinner than the support, we assume that the actual temperature might be even higher. The hydrogen flow can be adjusted with a leak valve and should be set to reach a pressure between 10^{-4} and 10^{-3} mbar. The efficiency of the remoderator after annealing in hydrogen atmosphere could not be determined yet, as explained in section 4.7.

4.4.3. Positron acceleration and beam optics

The electrostatic system for acceleration and beam optics plays a decisive role as it has a major impact on the final beam properties. Furthermore, it must also be versatile since it has to adapt to the optional remoderation and different beam energies. The complete system is depicted in a cross-sectional view in figure 4.7 a). It is crucial to adjust the beam concentric to the lens system, which can be done with the last correction coils in the beamline. A single electrode is used to pre-accelerate the beam within the magnetic guiding field. The subsequent section with three electrodes is dedicated to adjust the focus onto the remoderator foil while the implantation energy is defined by the potential of the remoderator stage. The remaining electrodes are basically used for acceleration and to counteract the beam divergence. This section is rather long because the system was originally designed for beam energies of up to 30 keV. The last, elongated electrode serves as potential tube, which is connected to the Faraday cage. It also contains two apertures (one exchangeable).

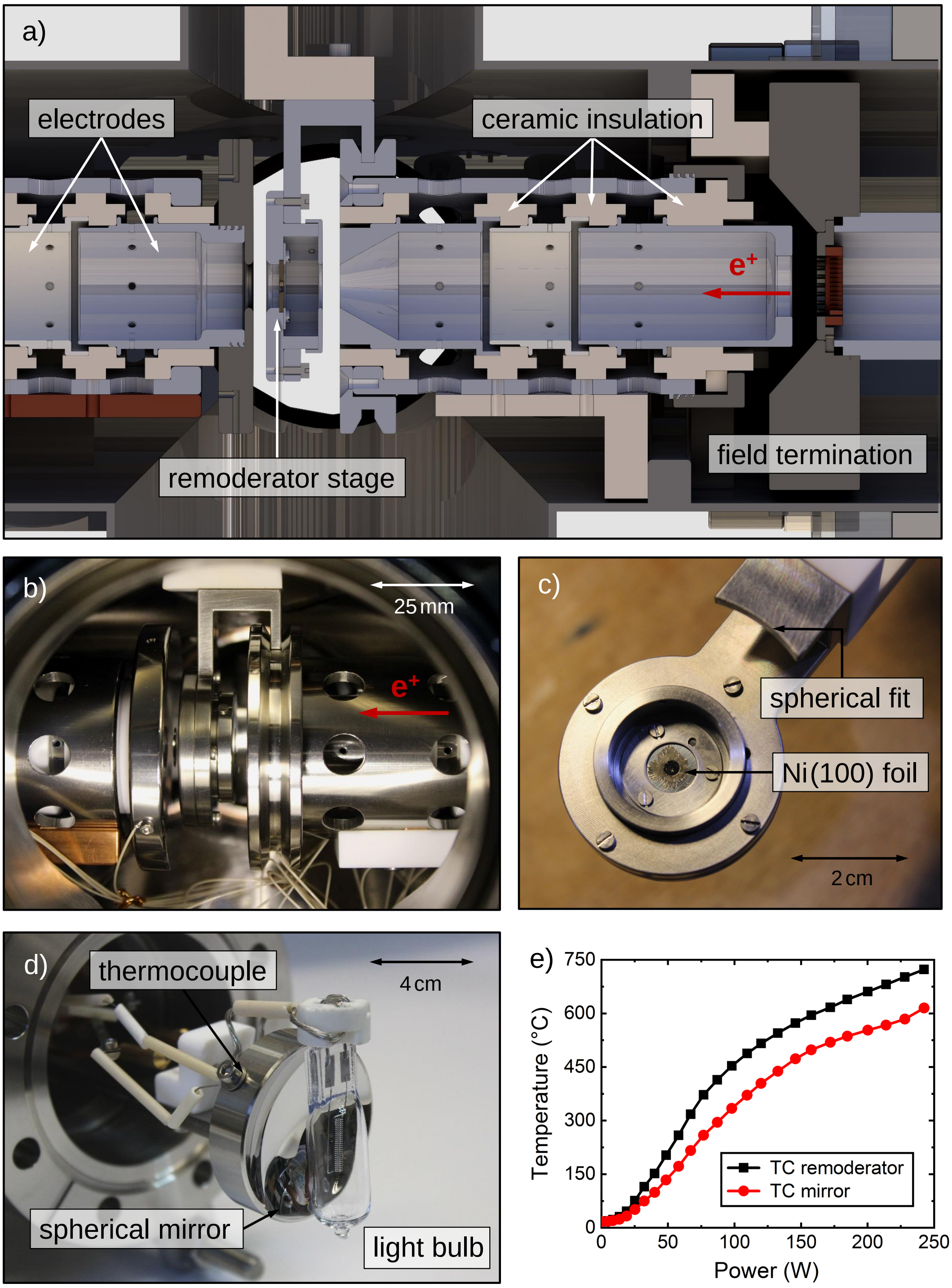

Figure 4.6. Optional transmission-type remoderator that can be conditioned in-situ. a) Cross-sectional view and b) photo of the electrostatic lens system around the remoderator. A spherical fit on the top ensures concentric alignment with respect to the lens system. c) We employ a 100 nm thin, free-standing Ni(100) foil as remoderator. d) A radiation heater is used to anneal the remoderator foil in hydrogen atmosphere, which is done in a separate cross piece. e) Temperature calibration of the thermocouple that is attached to the heater.

Experimental implementation

The individual electrodes are stacked with Macor (glass ceramic) insulators in three support tubes, which are mounted in two UHV cross pieces. To prevent inherent aberrations, special care was taken to ensure concentric alignment. The electrodes are designed in a way that they slightly overlap, which guarantees that the positron beam is not disrupted by charging of insulators. The electrical contacting from outside the support tube is realized with a screw, as depicted in figure 4.7 b). For the connection to the HV feedthrough, we use PEEK insulated wires, although this is not ideal for UHV [234]. Ceramic beads or tubes alone wouldn't provide sufficiently long creepage distances. As the PEEK wires are only specified for voltages of up to 10 kV, they are fixed with Kapton foil and ceramic tubes where necessary. A photo of this assembly is shown in figure 4.7 c).

We extensively tested and improved the HV stability of the Faraday cage and the electrostatic system, which is summarized in section A.3 of the appendix. The final assembly is suitable for voltages of up to 20 kV in the last section (no leak currents) and up to 5 kV can be applied between adjacent electrodes. Besides that, we also considered the thermal expansion of the Macor-steel system when the setup is baked. This was explicitly tested with a stacked support tube in an external furnace - no cracks or other issues were observed.

Simulation of positron trajectories

Before the mechanical components were fabricated, the configuration and the geometry of the electrodes have been optimized by comprehensive simulations with *COMSOL Multiphysics*. For the final geometry, further simulations were performed to determine the ideal potentials for different beam energies. The goal is to obtain a parallel beam of small diameter at the sample position and the MCP. To facilitate the calculations, the system has been approximated as rotational symmetric, i.e. we neglect the metallic glass strips of the field termination and the extension of the remoderator stage that guarantees the concentric alignment. The equations 2.11a, 2.11b and 2.11c were applied in a non-relativistic form to compute the positron trajectories in the magnetic guiding field and during the electrostatic acceleration using the finite elements method (FEM). To compromise between accuracy and computation time, we refined the mesh in the vicinity of the optical axis. The beam is represented by a set of individual

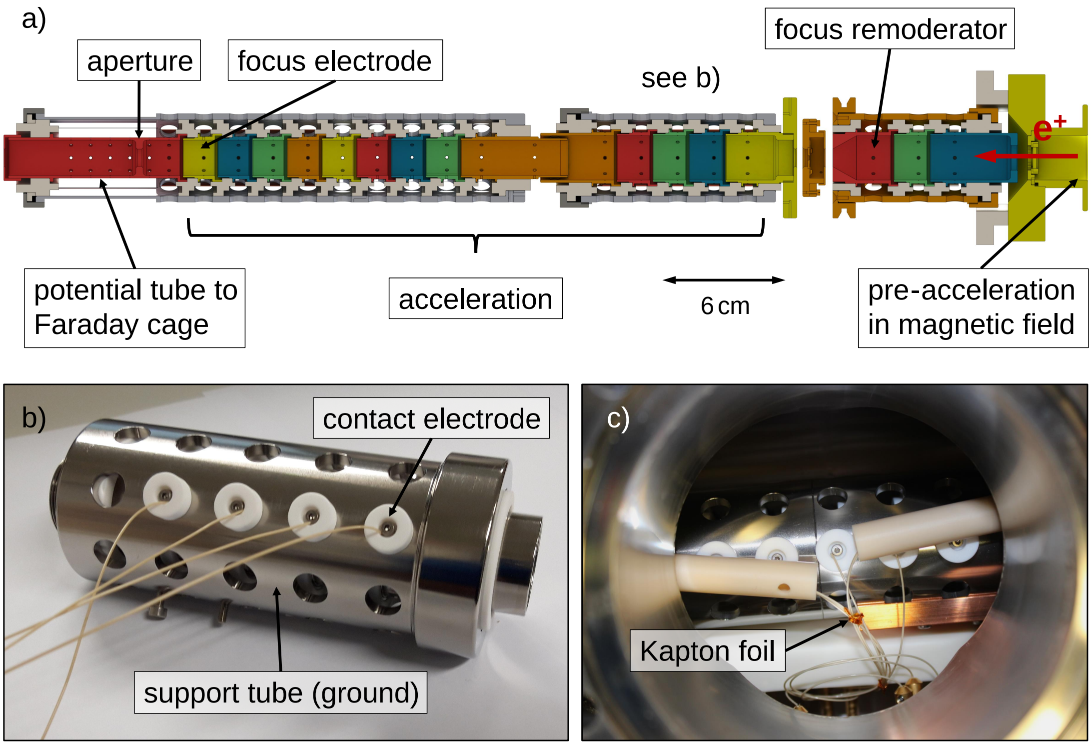

Figure 4.7. Electrostatic system for acceleration and beam optics. a) Cross-sectional view of the entire system that consists of 18 electrodes. All colored components are on HV. b) Grounded support tube to fix and align five electrodes that are contacted with a screw. c) Installation in the UHV cross piece, special measures were necessary to exclude HV flashovers at the wires.

positrons with different starting conditions, e.g. axial position z, distance to the optical axis r as well as longitudinal and transverse momentum. Note, that subsequently to the magnetic transportation in the beamline the exact beam properties are unknown and have to be estimated. For this, the values stated in table 4.1 can serve as first approach, although the recent upgrade of the NEPOMUC remoderator further improved the beam properties [219]. On these grounds, we estimate the beam diameter as $d = 2$ mm at FWHM and consider transverse energies $E_\perp$ of up to 0.2 - 0.5 eV. The influence of the energy bandwidth ($\Delta E = 3$ eV assumed) was found to be rather small. In the following, we present and discuss selected results.

Influence of the gyration motion: During the magnetic transport with an initial beam energy of 20 eV, each positron gyrates around its center of motion. The beam as a whole consists of a multitude of positrons, so that the actual beam diameter increases to $d' = d + 2r_g$. To enable a realistic simulation, we considered

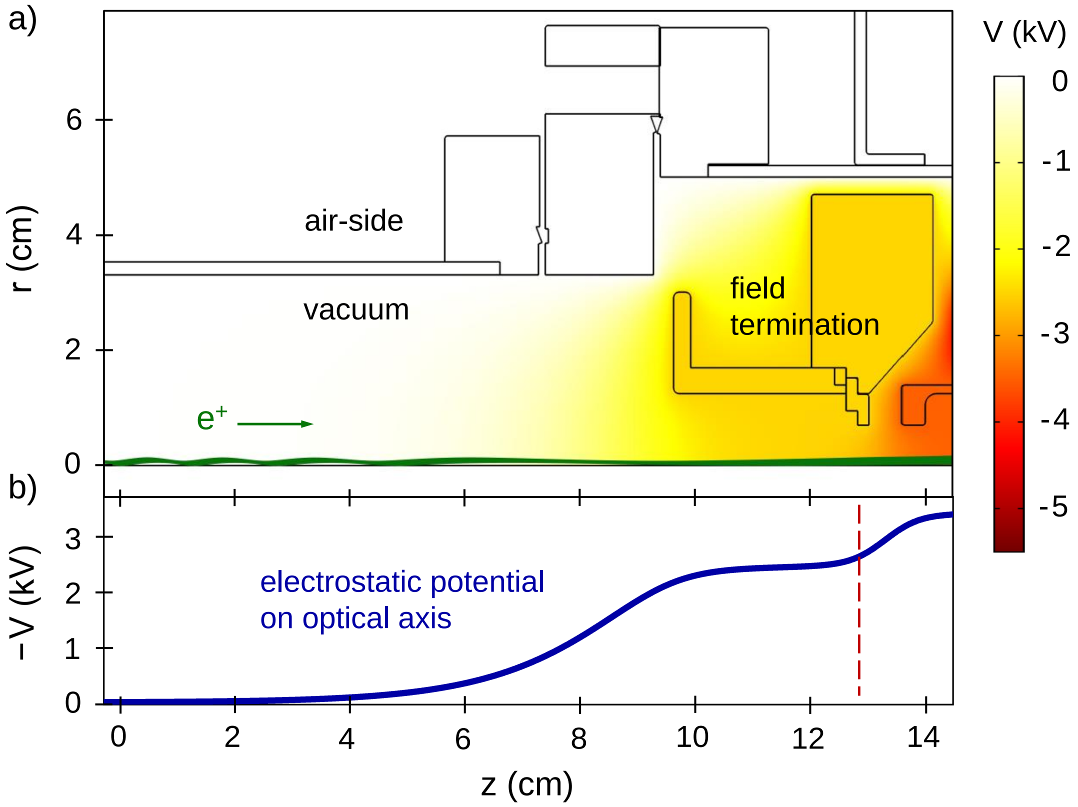

Figure 4.8. Numerical simulation of the electrostatic potential and the positron trajectories (green) during acceleration in the magnetic guiding field and when passing the field termination. a) As the positrons have a finite transverse momentum, they gyrate in the magnetic guiding field (depicted for $E_\perp = 0.5\,\mathrm{eV}$). When being accelerated, the gyration length increases, while the gyration radius is not affected. b) On the optical axis, the electrostatic potential increases steadily up to around 2.7 kV before the magnetic field is terminated (dashed line).

different axial starting positions z far upstream the first electrode. Figure 4.8 a) shows the calculated electrostatic potential and specific positron trajectories ($E_\perp = 0.5\,\mathrm{eV}$, green) when being accelerated in the magnetic guiding field. The positrons are equally separated over the beam radius and for clarity, only trajectories that start at $z = -25\,\mathrm{cm}$ are shown. The magnetic guiding field on the optical axis far away from the field termination is 6.4 mT. This leads to an initial gyration length of around 1.5 cm in the simulation, which agrees well with the value calculated using equation 2.15. Figure 4.8 b) shows the the electrostatic potential on the optical axis, which increases steadily when the beam approaches the field termination. As the velocity raises, the gyration length increases noticeably. Positrons that start from other z-positions exhibit the same trend, but are in a different state of the gyration motion when passing the field termination, which leads to varying trajectories. For meaningful results, it is thus crucial to include all possible beams.

Remoderated NEPOMUC beam: When the optional transmission-type remoderator is not applied, the positron beam has to pass a gap of 2 cm. The corresponding section of the simulation is shown in figure 4.9 a). The remoderator stage is moved up by approximately 25 cm and has no effect on the beam. To reduce the possible influence of the wires or the grounded surrounding, the two electrodes have a large outer diameter of 6.8 cm, which is limited by the dimension of the CF100 crosspiece. This geometry corresponds to a plate capacitor and thus results in a relatively homogeneous field close to the optical axis. To form a parallel beam, the simulation suggests a potential difference of 2.5 kV to accelerate the beam within the gap.
Downstream this section, we can obtain a parallel, slightly converging beam by further successive acceleration. This was originally simulated for different beam energies of up to 30 keV. In the range of 10-20 keV and after reaching the final energy, the parallel beam is maintained by inclusion of repulsive electrodes that form a suitable optics. The last electrode, where we can adjust the beam, has a distance of 22 cm to the sample stage and 47 cm to the MCP, respectively. For a final energy of 15 keV, the simulation yields a very small beam divergence of less than 1 mrad while the beam diameter is kept below 4 mm over the whole path. A slightly smaller diameter is possible when focusing the beam. Considering the additional parameter $\Delta E \sim 3\,\text{eV}$ and $\theta \sim 2^\circ$, we can use equations 4.1 and 4.2 to estimate the coherence lengths $l_{\|} \sim 90\,\text{nm}$ and $l_{\perp} \sim 10\,\text{nm}$, respectively. These values are adequate for the investigation of surface reconstructions with large unit cells.

Twofold remoderated beam: When the additional remoderator is applied, we have to divide the simulation into two parts: i) the focus onto the remoderator foil and ii) the acceleration of the emitted slow positrons. As shown in figure 4.9 b), we use a set of three electrodes to accelerate and focus the beam onto the remoderator. The focal point can be adjusted by changing the potential of the repulsive electrode. For $d = 3\,\text{mm}$ and $E_{\perp} = 0.2\,\text{eV}$, the beam is focused to a spot with a minimum diameter of less than 0.6 mm. To optimize the configuration, we also considered positrons outside the FWHM of the intensity distribution or with a larger transverse momentum. Qualitatively, different parameters lead to the same result, but affect the minimum diameter and slightly shift the common focal point due to the onset of spherical aberrations.

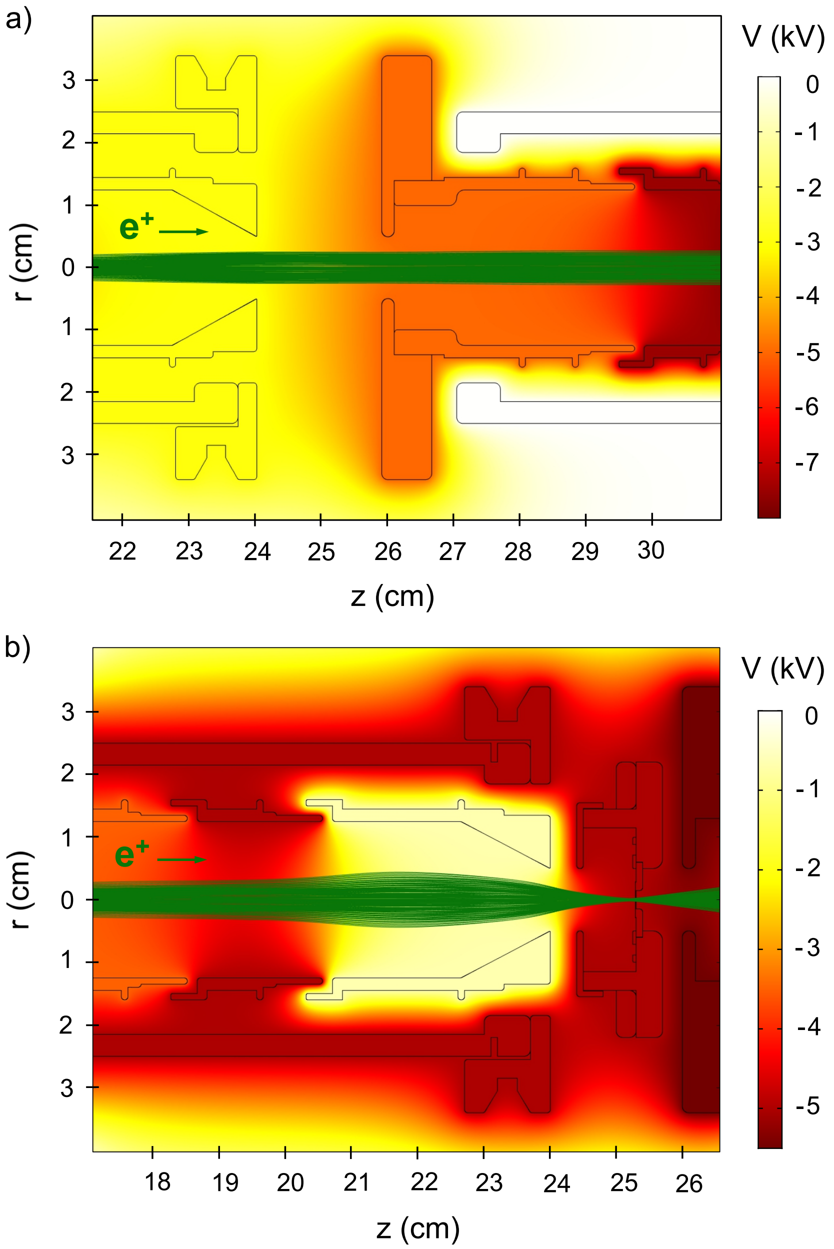

Figure 4.9. Simulation of the positron trajectories in the section where the optional remoderator can be applied. a) Without remoderator, the beam has to pass a gap and is successively accelerated ($d = 2\,\mathrm{mm}$ and $E_\perp = 0.2\,\mathrm{eV}$). b) Focus onto the remoderator foil. For $d = 3\,\mathrm{mm}$ and $E_\perp = 0.2\,\mathrm{eV}$, we expect a beam diameter of less than 0.6 mm at the focal point.

For remoderation, the positrons are implanted with an energy of 5 keV, which is a trade-off between a high remoderation yield and a low epithermal positron fraction [104]. To optimize the energy bandwidth of the beam at the expense of a reduced intensity, it can however be reasonable to decrease the implantation energy to 3 - 4 keV at a later stage (compare figure 2.7). Simulations suggest that the system works for a wide range of implantation energies, which just requires to marginally adjust the focal point.

In the second part of the simulation, the remoderator foil can be conceived as a new source, i.e. the positrons start from the surface and have well-defined properties. The beam diameter is specified by the result of the previous simulation and we can estimate $E_{\|} = |\Phi^{+}_{Ni}| \approx 1.4\,\mathrm{eV}$ [81] and $E_{\perp} = 25\,\mathrm{meV}$ (thermal energy), assuming a perfect alignment of the remoderator. A simulation of the positron trajectories after remoderation is shown in figure 4.10. The geometry of the extraction electrode has been modified, so that the positrons experience a strong electric field in axial direction immediately after being emitted, which was found to be beneficial. Due to the very low initial energy, the acceleration results in a focal point approximately 9 mm downstream the remoderator. The focal point can be shifted by few mm in z when changing the extraction voltage, but it is always present, independent of the electrode geometry. The gradual acceleration by the subsequent electrodes allows the formation of a parallel beam. For a final energy of 10 keV, we expect a beam diameter of $\sim$1.2 mm at the position of the sample and the MCP.

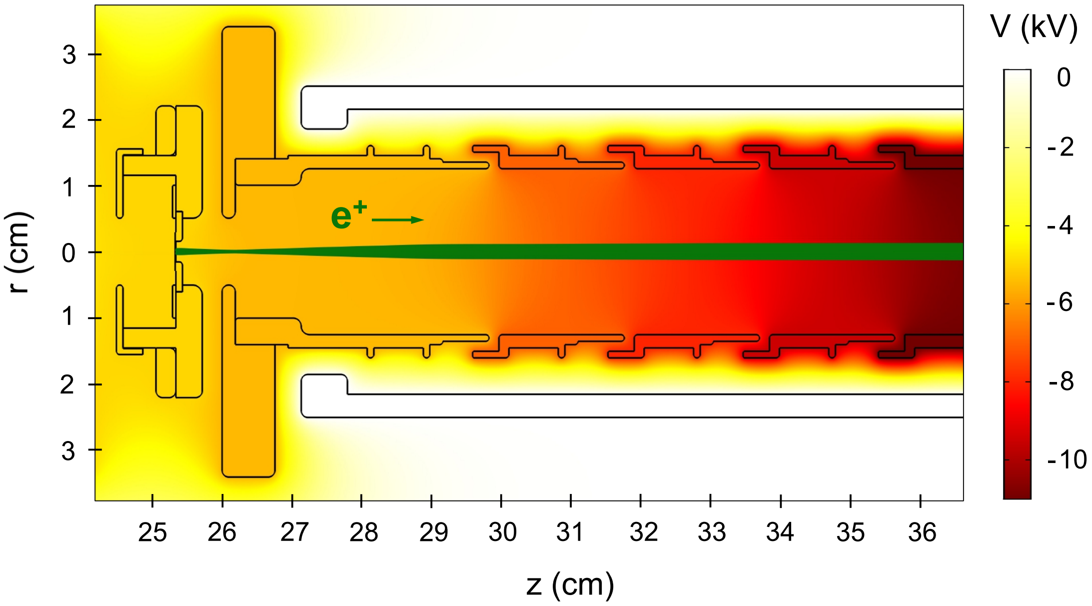

Figure 4.10. Simulation of the positron trajectories after remoderation ($d = 0.6\,\mathrm{mm}$, $E_{\perp} = 25\,\mathrm{meV}$). When being accelerated, the beam exhibits a focal point in the close vicinity of the remoderator. The subsequent electrodes are used to form a parallel beam.

4.4.4. MCP assembly and HV potentiometer

To visualize the diffraction pattern, we use a two-stage (chevron) MCP assembly with a standard P43 fluorescent screen. The diameter of the active area is 77 mm and the chevron configuration allows to amplify the signal by a factor of up to 10^6. The installed MCP assembly with the electrical contacts is shown in figure 4.11 a). According to the user manual [235], the maximum potential difference across the MCP ($|V_{MCP,in} - V_{MCP,out}|$) is 2 kV, while up to 4 kV can be applied between MCP and fluorescent screen ($|V_{MCP,out} - V_{screen}|$). As discussed before, the entrance side of the MCP must be connected with the Faraday cage, which defines the potential $|V_{MCP,in}| \geq 10\,\mathrm{kV}$, depending on the final beam energy. Since we can't exceed the specifications, we have to raise the potentials $V_{MCP,out}$ and V_{screen} as well. This approach is particularly critical because HV flashovers, e.g. at the Faraday cage, would only reduce $V_{MCP,in}$ which can lead to secondary flashovers across the MCP. It is most important to prevent such flashovers as this can damage the electronics of the MCP.

On this basis, we decided to provide all three potentials by a single channel of the HV source using a home-built potentiometer, which is shown in figure 4.11 b) and d). If there is a HV flashover, the MCP potentials decrease collectively, which significantly reduces the risk to damage the MCP. The potentiometer consists of seven HV resistors and two commercial potentiometers (*POC-400* from *Metallux*), which are arranged as schematically depicted in figure 4.11 c). The two potentiometers can be rotated with a grounded knob from outside the housing to adjust the MCP gain and the acceleration towards the screen. To modify the circuit for different beam energies, i.e. potentials of the Faraday cage, we apply a bypass that can be inserted at four positions. This allows to conduct TRHEPD measurements with discrete beam energies in 5 keV steps. Other energies would require the exchange of HV resistors. When using the bypass, the voltage drop at the commercial potentiometers and the current through the circuit is the same in all positions. The measured current of 199.4 μA at 15 kV (blue bypass in the block diagram) agrees reasonably well with the calculated value of 200 μA. The high current is necessary to guarantee stable potentials, as we have to continuously recharge the MCP channels during detection and compensate possible leak currents as well.

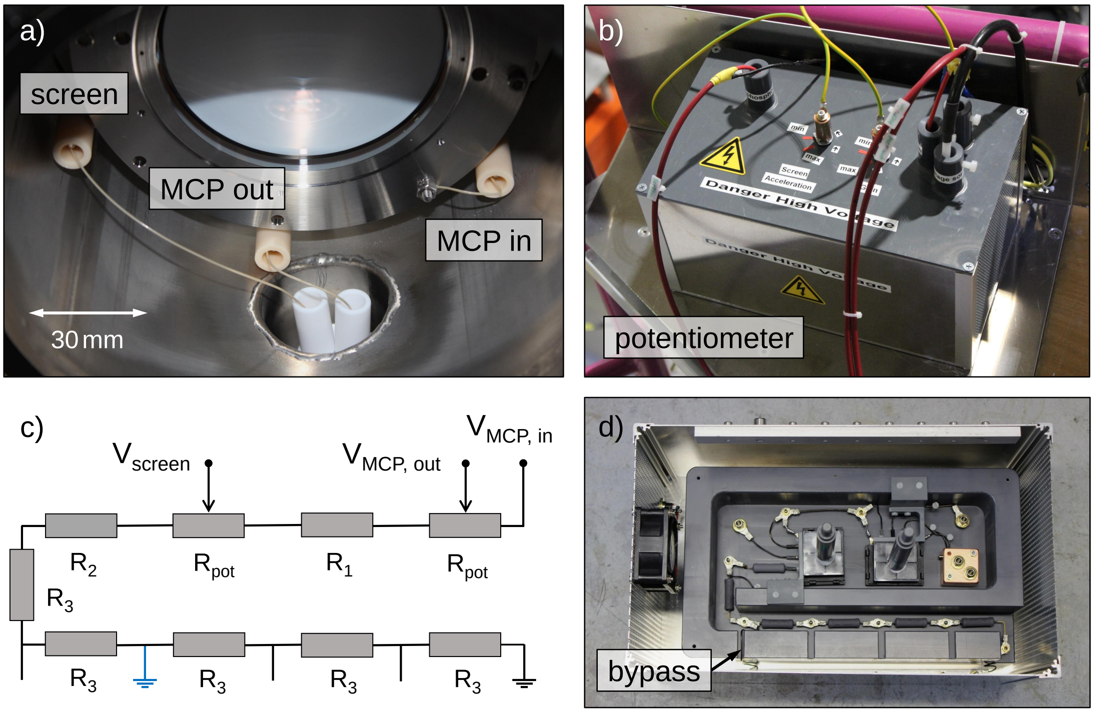

Figure 4.11. MCP assembly and HV potentiometer. a) To integrate the MCP in the TRHEPD setup, we have to raise the potentials by a constant offset that depends on the beam energy. b) Housing of the HV potentiometer. Two grounded knobs allow to safely set the gain of the MCP and the acceleration towards the fluorescent screen while the HV is applied. c) Block diagram and d) photo of the HV potentiometer. The resistors $R_3 = 25\,\text{M}\Omega$ can be bypassed at four positions to adjust the circuit for different beam energies. The blue bypass in the block diagram corresponds to a beam energy of 15 keV.

4.5. Further aspects of the instrumentation

Besides the properties of the positron beam, the sample quality and its precise orientation relative to the beam are most important to perform TRHEPD measurements. Therefore, in this section, we discuss the positioning system and further commercial components that are necessary to condition and characterize the sample in-situ. Additionally, we introduce the vacuum system and details about the sample transfer, storage and carrier design. Note that all these components were tested with a first setup outside the experimental hall of the FRM II, which is described in section A.2.1 of the appendix.

4.5.1. Positioning system with integrated laser heater

Considerations sample positioning

Most important regarding sample alignment is the ability to vary the glancing angle of the incident positron beam, which is realized by tilting the sample stage along the TRHEPD axis. In principle, the glancing angle could also be adjusted by magnetic (or electrostatic) deflection of the beam, which is however rather imprecise and thus, in practice, only used to bend the beam towards the sample. Since the angular step size for TRHEPD rocking curves is typically 0.1°, the glancing angle has to be set very accurately to minimize the uncertainty. If we want to conduct azimuthal plots in the future, the same holds true for the in-plane rotation, while the accuracy of the x-, y- and z-motion is not critical for the measurements. Hence, we initially considered to realize tilt and rotation with piezo motors, which utilize the inverse piezoelectric effect and thus enable an excellent accuracy and repeatability. However, commercial solutions could only carry a very limited weight and were not compatible with the requirements regarding HV insulation, sample heating or angular range [236]. Therefore, we decided to purchase a customized system that employs stepper motors for the motion of all five axes, while the sample can be heated using an integrated infrared (IR) laser.

Resolution, accuracy and repeatability

Besides x-, y- and z-alignment in the range of mm, this system enables to tilt the sample stage by $\pm 10°$ and to rotate by more than 360°. For tilt and rotation, we experimentally determined the accuracy and repeatability by measurements under atmosphere, and later for the evacuated system as well. The procedure and related experimental uncertainties are described in detail in the appendix A.4. Firstly, we found that small angular steps of 0.01° can still be clearly resolved and result in a measurable tilt or rotation of the sample stage. For angular steps of 0.1°, we obtained an accuracy of $\Delta\,\theta < 0.02°$. Although the uncertainties can accumulate to slightly larger values after several steps, the overall accuracy is still much better than the step size (compare table A.1), which is sufficient. To minimize the influence of the bearing clearance, the sample should be tilted continuously in one direction when recording rocking curves. For such unidirectional operation, the repeatability for tilt and rotation is approximately $\pm 0.1°$ and $\pm 0.2°$, respectively.

Contact-less sample heating

Apart from the sample alignment, the positioning system must also be compatible with the requirements regarding sample heating. Most samples that are transferred to the UHV chamber have to be conditioned by a heat treatment to remove adsorbates, which enhances the quality of the diffraction pattern significantly. Conventionally, this is realized by electron bombardment or resistive heating of the sample or its support, which allows to reach relatively high temperatures. Besides that, temperature control during TRHEPD measurements is also important, e.g. to induce surface reconstructions. Since the sample stage is on HV standard methods are not applicable. Instead, contact-less sample heating is a possible approach, as demonstrated by Reiner *et al.*, who applied a halogen lamp with water-cooled Cu reflector [237]. However, since radiation heat is naturally emitted in all directions, the maximum sample temperature is rather limited while the overall heat input to the UHV system is substantial. A customized reflector can increase the solid angle, but also occupies a lot of space in the close vicinity of the sample stage. To overcome these issues, we use an IR laser ($\lambda = 938\,\text{nm}$, $P_{\text{max}} = 140\,\text{W}$) for sample heating. The safety precautions for the laser operation in the experimental hall of the FRM II are summarized in the appendix A.5.

Laser heater, alignment and temperature measurement

The laser itself is placed outside the vacuum, which is convenient for cooling reasons. After the transportation in an optical fiber, the laser beam is introduced to the UHV chamber with an appropriate optics through a quartz viewport. The defocused beam is used to heat the backside of the sample carrier. Alternatively, the sample can also be heated directly, but this is only possible if it is opaque for the IR laser light. In general, direct heating allows to reach higher temperatures at the expense of a larger thermal gradient along the sample surface. The design of the respective sample carriers is discussed in detail in section 4.5.4.

The temperature of the sample carrier (or the backside of the sample) is measured contact-less with a pyrometer from below. The field of view can be changed by two adjustment screws, while being indicated with an aiming light, i.e. an integrated laser pointer. For the adjustment under atmosphere, we can place a piece of paper with a cross-hair at the sample position, as shown in figure 4.12 a). Since the adjustment of the pyrometer must be repeated after the bake-out of

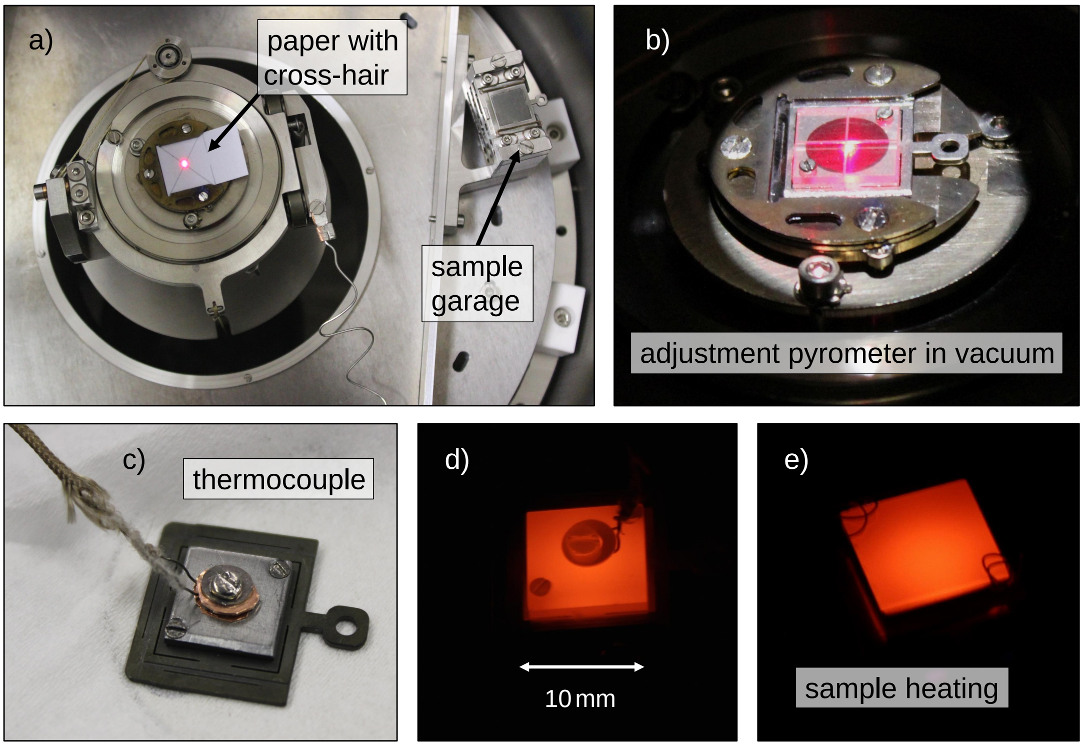

Figure 4.12. Pyrometer adjustment and calibration of the sample temperature. a) Pyrometer adjustment under atmosphere: a paper with cross-hair is used to indicate the center of the sample position. b) Pyrometer adjustment in vacuum: instead of the paper, we use a thin glass plate mounted onto a sample carrier with hole. c) Black oxidized sample carrier with attached thermocouple for the temperature calibration. Thermal radiation d) during the calibration and e) while heating a Si(111) sample at 900 °C.

the UHV chamber, we considered a second approach that is suitable for the evacuated system as well. For this purpose, we use a thin glass plate with a cross-hair that is screwed to a sample carrier with a central hole as depicted in figure 4.12 b). To enhance the diffuse scattering of the aiming light the glass surface is roughened. Besides the pyrometer, the laser beam must also be adjusted to minimize the required power and thus the heat input to the system. The best method for the fine-tuning is to observe the heat glow of an empty sample carrier at elevated temperatures to center the laser beam.

Prior to the final assembly, the sample temperature was calibrated with a thermocouple as shown in figure 4.12 c) and d). For indirect sample heating, the emissivity of the pyrometer is set to $\epsilon = 0.8$ as we use black oxidized sample carriers. This allows to reach sample temperatures of up to 850 °C (with $\sim 60\%$ of the laser power) while the backside of the sample carrier has approximately

1000 °C. This value is in good agreement with the results from direct sample heating, where we obtained sample temperatures slightly below 1000 °C. However, bear in mind that during TRHEPD measurements the sample temperature is rather limited by the background of the diffraction pattern, which increases significantly at elevated temperatures due to the thermal radiation of the sample and the diffusely scattered IR light from the laser.

4.5.2. RHEED system and Ar^+ sputter gun

To assess the sample quality after the transfer or heat treatment, we use a commercial RHEED system. The fluorescent screen that visualizes the diffraction pattern is mounted to the Faraday cage. We emphasize that this system is only used for qualitative measurements since neither the setup nor the electron gun are optimized for quantitative RHEED, e.g. the sample can't be tilted along the RHEED axis. Beam rocking as well as vertical and horizontal deflection are realized by a set of internal coils. In the present setup, we add an additional (external) pair of coils in Helmholtz-like geometry to bend the beam towards the sample, which is required for energies above 15 keV. Further details and experimental parameters are mentioned in the appendix A.6.1.

First RHEED measurements on α-Al_2O_3 (0001) (sapphire), $SrTiO_3$ (100) and (110) were conducted in the framework of a master thesis to test the system [238]. These surfaces are rather stable and can be investigated before the UHV chamber is baked out, i.e. a pressure in the range of 10^{-8} to 10^{-9} mbar is adequate. The sapphire samples were cleaned with alcohol and deionized water in an ultrasonic bath and annealed in an external furnace (1 h, 1300 °C, $\sim 10^{-5}$ mbar), before being quickly introduced to the UHV chamber. Subsequently, they were heated in-situ up to 850 °C for 30 min to remove adsorbates. Typical RHEED patterns obtained after this procedure are shown in figure 4.13 a) and b). Kikuchi lines and diffraction spots are clearly visible, which could also be traced when changing the crystallographic orientation of the sample with respect to the incident beam. In agreement with literature [239], we observe a (1×1) structure, i.e. no surface reconstruction. Higher order Laue zones are well resolved and we assigned the respective diffraction spots as indicated in figure 4.13 b). For more details, we refer to the thesis from A. Elovskii [238].

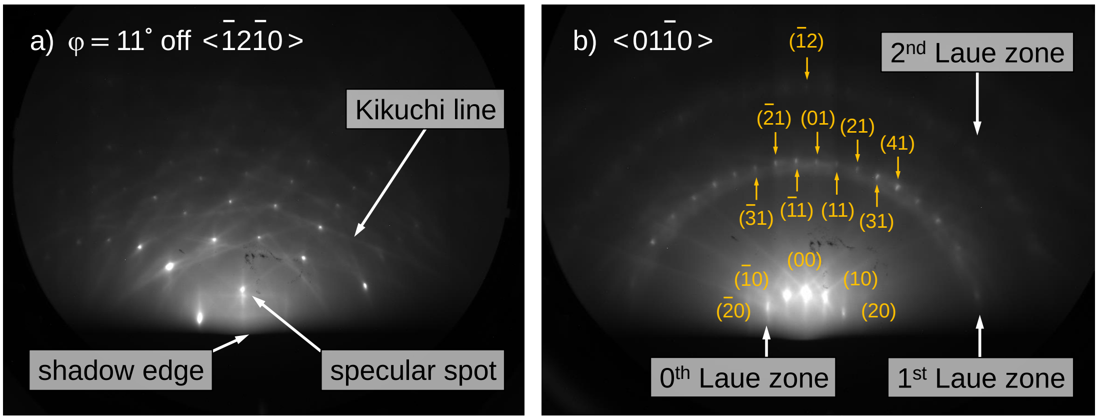

Figure 4.13. RHEED pattern from α-Al_2O_3 (0001) - (1×1), recorded with $E = 15\,\mathrm{keV}$ and for $\theta = 3.6\,°$. a) A clear diffraction pattern indicates a clean and ordered surface. b) The individual diffraction spots can be assigned to reciprocal lattice rods.

A common approach to remove different layers of strongly (chemically) bound adsorbates or impurities is Ar-ion sputtering, which is used in combination with high-temperature annealing to subsequently restore the crystalline surface structure. For this purpose, the setup comprises a commercial sputter gun (*IQE 11/35* from *SPECS*) that is placed outside the Faraday cage, in a distance of ∼12 cm to the sample. To protect the MCP from deposition, we use a shutter that is manually moved by a push-pull feedthrough. The argon gas flow can be adjusted precisely by a leak valve, which increases the pressure of the UHV chamber to 10^{-6} - 10^{-5} mbar during Ar^+ sputtering. For a first sputter test, we used a vanadium foil. As shown in figure 4.14, it is possible to remove the natural oxide layer in a uniform way, which confirms that geometry and diameter of the ion beam are appropriate. Further sputter tests were conducted with a sapphire sample and evaluated with RHEED. Although the diffraction pattern could be restored after a heat treatment, better results were obtained following the preparation sequence mentioned before.

4.5.3. Ultra-high vacuum and residual gas

Apart from the sample quality, which can be optimized within the preparation procedure, meaningful surface structure analysis is only possible if the vacuum is sufficiently good. An overview of the vacuum system is shown in figure A.10 in the appendix A.6.3. For the main UHV chamber, we use a Turbo Molecular Pump (TMP) in combination with a Non-Evaporable Getter (NEG) pump, which

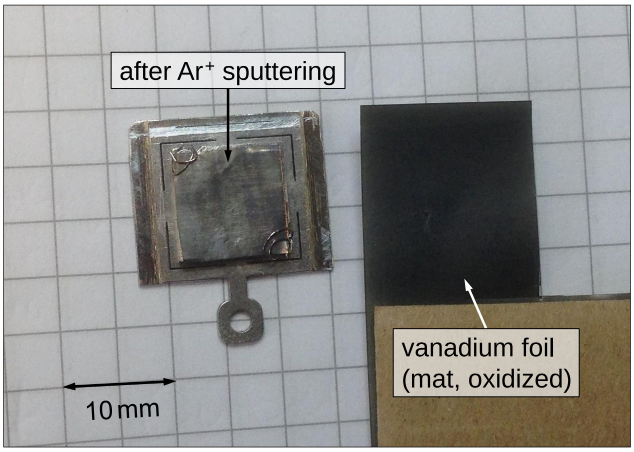

Figure 4.14. Vanadium foil before (right) and after (left, on sample carrier) Ar^+ sputtering to remove the natural oxide layer. Sputter parameters: emission current $I = 10\,\mathrm{mA}$, $E_{\mathrm{ion}} = 3\,\mathrm{keV}$, $p_{\mathrm{Ar}} = 10^{-5}\,\mathrm{mbar}$ and $t = 10\,\mathrm{min}$.

is very efficient to reduce the partial pressure of H_2 [240]. We do not apply ion pumps as they are known to increase the background considerably. A mass spectrometer is used to analyze the composition of the residual gas. The spectrum shown in figure 4.15 a) confirms that water desorption from inner surfaces is the dominant contribution. Subsequently to this work, it is thus envisaged to bake out the entire experiment at a temperature of 150 °C for several days. Besides that, the base pressure of currently $2{\cdot}10^{-9}\,\mathrm{mbar}$ can be further reduced by a home-built cryogenic pump, which is essentially a cold trap filled with liquid nitrogen. As shown in figure 4.15 b), the cryogenic pump particularly decreases the partial pressure of H_2O and CO_2.

4.5.4. Sample handling

In the following, we discuss the features of the sample carrier and the realization of transfer and storage in the TRHEPD setup.

Sample carrier design

Since the beam spot in grazing incidence is typically larger than the sample length (see section 4.2.1) we also have to consider the fate of positrons that miss the sample. This can be quite a substantial fraction, which could potentially increase the background of the diffraction pattern. In particular, we thus want

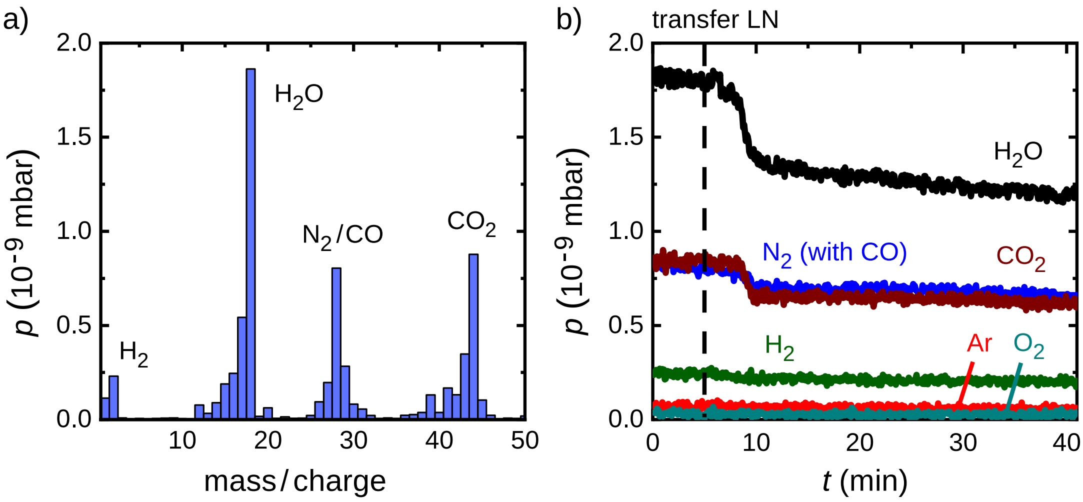

Figure 4.15. Analysis of the residual gas. a) The mass spectrum before bake-out reveals that water is the predominant component and that minor contaminations are present, e.g. the signal next to the main peaks can partly be assigned to fragments of hydrocarbons. b) Decrease of individual partial pressures after transfer of liquid nitrogen (LN) into the cooling trap.

to exclude that positrons are scattered by adjacent components of similar height, e.g. the accommodation of the sample carrier. Therefore, the sample must be slightly elevated on the carrier to effectively shadow its surrounding. Besides that, the sample carrier must be well adapted to the laser heater. To minimize the heat conduction towards the accommodation, we use a structure of 150 μm thin laser cuts, as shown in figure 4.16 a). The carrier is 0.8 mm thin and made from non-magnetic stainless steel. To enhance the absorption of the IR laser light, the carriers are black oxidized by a standardized heat treatment in an external furnace. The best results were obtained when heating for 10 min at 1000 °C (ramp speed 4 °C/min) in a 3 mbar oxygen atmosphere, as depicted in figure 4.16 b) in the middle. To elevate the sample, we use a molybdenum support that is screwed to the carrier and thereby guarantees a good thermal contact.

There are two promising approaches to fix the sample: a bond with high-temperature, UHV compatible ceramic adhesive or mechanical clamping. The main advantage of ceramic adhesive is the flexibility regarding the sample size. Following the preparation reported by Duncan *et al.* [241], the adhesive was blended with graphite powder (ratio 20:1) to enhance the electrical and thermal conductivity. Although different products have been tested (*Aremco Ceramabond 503*, *516* and *571*) the results were not convincing. After the in-situ

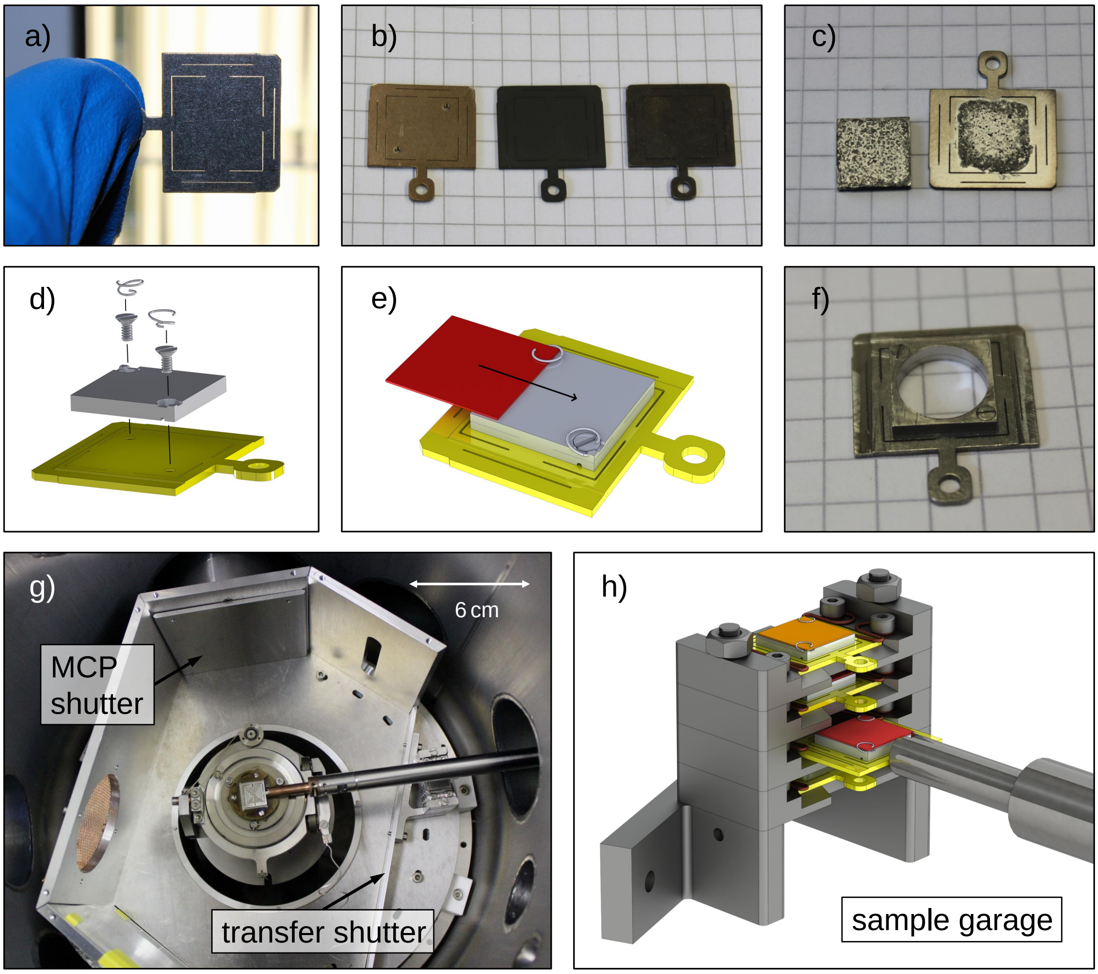

Figure 4.16. Sample carrier design and transfer. a) The sample carriers feature a structure of 150 μm thin laser cuts to reduce the heat conduction towards the side. b) The carriers are black oxidized to increase the IR absorption during laser heating. Different heat treatments were tested: 2 h at 400 °C in air (left) and 1 h (right) as well as 10 min (middle, best result) at 1000 °C in 3 mbar oxygen atmosphere. c) Ceramic adhesive does not provide a reliable bond as it becomes brittle after in-situ heating. d) A molybdenum support is screwed to the carrier to elevate the sample. e) Two bent steel wires, tightened by the screw heads, serve as clamp to fix the sample. f) Sample carrier with a hole in the middle for direct sample heating (only possible if the sample absorbs the IR laser light). g) A shutter allows to open the Faraday cage (lid removed in the photo) for the sample transfer. h) The shutter also comprises a sample garage that can accommodate up to four samples.

heat treatment, the bond became very brittle, which makes it break easily. Besides that, it is rather challenging to mount the sample perfectly plane on the support, which could lead to a slight misalignment. On these grounds, we decided to mechanically clamp the sample, which is realized by two steel springs as illustrated in figure 4.16 d) and e). The sample carriers are designed for 10×10 mm sized substrates of flexible thickness. A second type of carrier design that enables direct sample heating is shown in figure 4.16 f). These carriers are not oxidized and the corresponding support is made from steel instead of molybdenum because of the lower thermal conductivity.

Sample transfer and UHV suitcase

For the sample transfer, the Faraday cage can be opened with a dedicated shutter as shown in figure 4.16 g). A home-built sample garage that is connected with the shutter allows to store up to four samples in the main UHV chamber. Since in-situ sample growth is not possible with the current setup we built an UHV suitcase to transport air-sensitive samples from nearby experiments on the campus. Several UHV transport systems are reported in literature [242–244], which are able to maintain a pressure in the range of low 10^{-9} mbar down to 10^{-11} mbar. During transportation, such systems can either be pumped by a battery-powered ion pump or using a NEG pump as recently demonstrated by Firpo *et al.* [244]. We decided to apply a NEG pump which is less spacious and requires no continuous power supply, but doesn't pump inert gases. After the bake-out, the main residual gas is thus expected to be argon, which is no issue for most samples. A buffer crosspiece enables the transfer without the need to vent the main UHV chamber.

4.6. Experimental characterization of the direct positron beam

After the final assembly of the TRHEPD setup, the magnetic transport and the positron beam optics were tested and optimized during beamtime. The results from the simulations (see section 4.4.3) were used for the initial setting of the electrostatic potentials. The subsequent manual fine-tuning of individual coils and electrodes was based on the size, shape and intensity of the beam spot on the MCP assembly. Besides that, we also monitor the count rate of the annihilation radiation from the MCP, which is measured with a collimated BGO scintillation detector. This allows the comparison of the beam intensity for different MCP gains. The experimental adjustments were validated by the simulation to ensure that the positron beam is still parallel. The optimized currents of the correction coils and the potentials of the electrodes are listed in the appendix in table A.4 and A.5, respectively. Since the system has a lot of parameters it might be possible to further improve the settings, e.g. by an automated numerical optimization as demonstrated by T. Schmidt for CDBS [107]. However, for TRHEPD, this would be more sophisticated as we also need to consider the beam divergence, which is not directly accessible during the experiment but has to be retrieved from simulations.

Figure 4.17 a) shows the beam profile and the intensity distribution along major and minor axis of the 15 keV remoderated NEPOMUC beam. The positron beam has an elliptical shape with a diameter (FWHM) of 3.9 mm and 2.7 mm, respectively. Compared to the simulation, the experimentally determined diameter is slightly smaller than expected which could be explained by the rather conservative estimate of the starting conditions or the better transition through the magnetic field termination. To exclude that the distortion of the beam is related to the applied optics we used the beam monitor downstream the first remoderator to confirm that the elliptical shape is already present in the beamline. This is consistent with the observation from Piochacz *et al.* [245]. It is therefore assumed, that the distortion might stem from the non-ideal transport through the magnetic switch. In general, an elliptical beam could be used for diffraction, as long as it is parallel. However, with regard to rocking curve analysis, it can be expedient to revise the magnetic switch or use a suitable aperture.

The beam profile of the 10 keV twofold remoderated beam and the intensity distribution along two perpendicular axes is shown in figure 4.17 b). The beam shape is almost perfectly circular, which is validated by the identical distribution along both axes. The intensity of the beam spot saturates in the middle, so that a precise determination of the beam diameter is difficult. Nevertheless, we can evaluate that $d < 1.3$ mm at FWHM, which is close to the value obtained in the simulation. The beam has also been slightly focused onto the MCP, which can enhance the resolution of the diffraction pattern on the fluorescent screen, as known from RHEED [133].

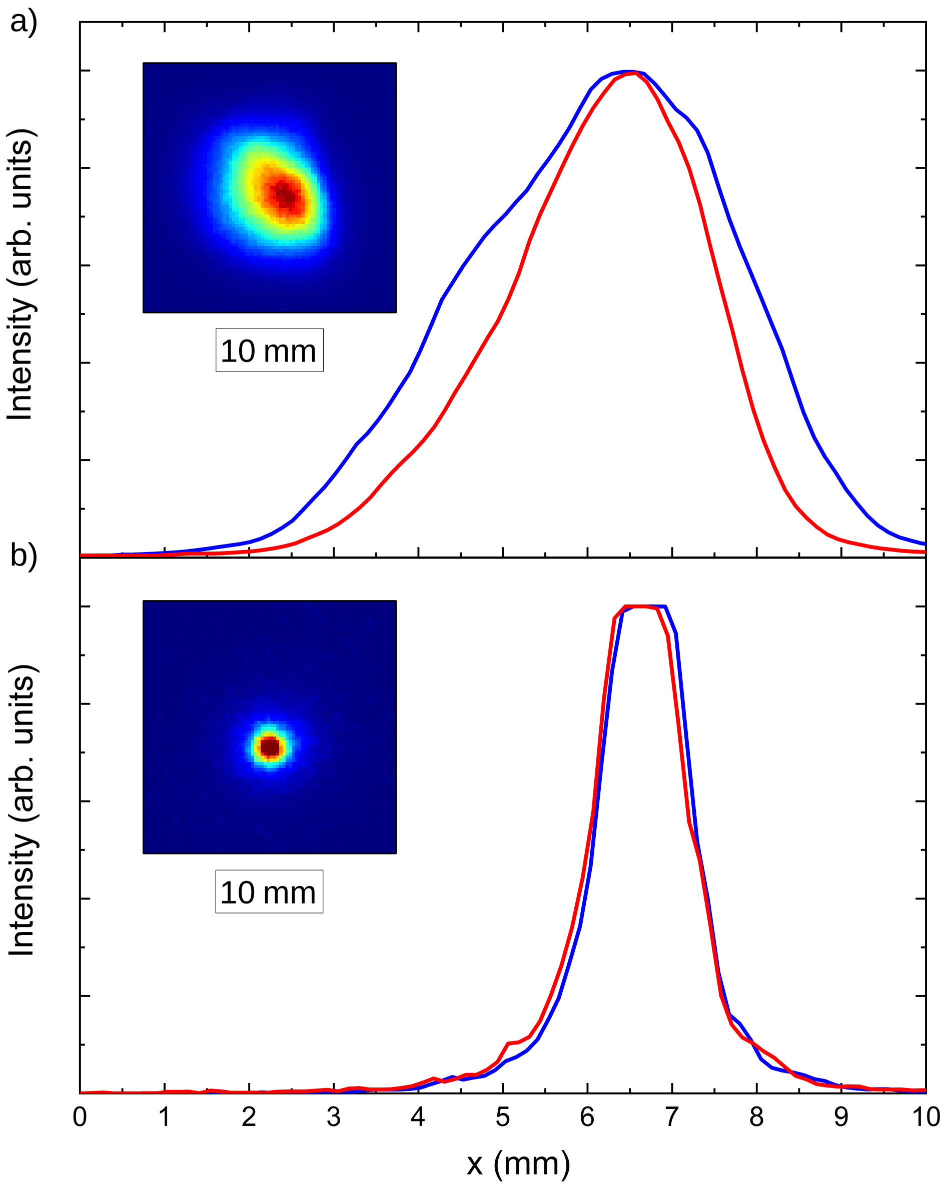

Figure 4.17. Experimentally determined profile of the direct positron beam. a) Elliptical beam shape of the 15 keV remoderated NEPOMUC beam on the MCP (linear color scale) and intensity distribution along minor and major axis. b) Circular beam shape of the 10 keV twofold remoderated beam. The intensity distribution along different axes is almost identical and the beam diameter is $d < 1.3\,\mathrm{mm}$ at FWHM. Note that the color scale in a) and b) does not allow a direct comparison of the beam intensities because the MCP gain was increased in b).

4.7. Concluding remarks

We successfully built up the TRHEPD setup at NEPOMUC and adapted the positron beam for diffraction experiments. The beam profiles of the 15 keV remoderated and the 10 keV twofold remoderated beam have been investigated during a first beamtime in February 2020. The comprehensive results from the experiment and the simulations are promising, even though further optimization might be possible. Since then, there was no reactor operation due to unexpected technical problems and the restart has been postponed for an indefinite period (status summer 2021). Therefore, it was not possible to accurately determine the final beam intensity and the efficiency of the transmission-type remoderator. Most serious is however that this incident also prevented us from recording first diffraction patterns, which was planned for the beamtime initially scheduled for May 2020.

Subsequently to this work, it is thus envisaged to obtain diffraction patterns from a relatively stable and less complex surface: hydrogen terminated Si(111) - (1×1) [246]. This surface structure is well-known and has been comprehensively investigated by different techniques, including TRHEPD [170, 194]. It can thus serve as a reference to benchmark the setup and further tune the electrostatic system, if necessary. Si(111) samples were already etched jointly with D. Vogl from the group of Prof. Brandt (WSI), but can not be stored on such long timescale without degradation. Apart from that, two graphene samples similar to those introduced in section 5.2.1 were also prepared, pre-characterized and are still stored in the TRHEPD chamber for the upcoming beamtime. After successful measurements, the UHV chamber will be baked out to pave the way for the determination of unknown surface structures with highest accuracy.

5

Chapter 5.

TRHEPD measurements on graphene/6H-SiC(0001)

In this chapter we discuss the results from TRHEPD measurements on epitaxially grown graphene on 6H-SiC(0001). Two different samples were prepared and pre-characterized by our co-workers from the group of Prof. Seyller (TU Chemnitz). The subsequent TRHEPD measurements were conducted at the SPF in Japan in collaboration with Prof. Mochizuki and Prof. Hyodo (Institute of Material Structure Science, KEK). The iterative comparison of experimental and calculated rocking curves allowed the extraction of structural parameters, i.e. the interlayer spacings of the graphene and buffer layer to the silicon carbide (SiC) substrate.

5.1. Epitaxial graphene on 6H-SiC(0001)

In the beginning, we briefly introduce the material graphene and the growth mechanism on SiC, which specifies the structure of the system.

5.1.1. Graphene – a unique two-dimensional material

Graphene is an allotrope of carbon that crystallizes in a two-dimensional honeycomb lattice, as shown in figure 5.1 a). The Bravais lattice is hexagonal and the unit cell comprises two atoms with a bond length of $a_{\mathrm{CC}} \approx 1.42\,\text{Å}$ [247]. As illustrated in figure 5.1 b), the carbon atoms are sp^2-hybridized, which leads to strong covalent σ-bonds, while the remaining p_z-orbitals form covalent π-bonds. Given this structure, graphene can be regarded as the basic building block of other carbon allotropes, e.g. it could be stacked to form a 3D graphite crystal, rolled up to a 1D carbon nanotube or, when considering an appropriate shape, wrapped to fullerenes [248]. Figure 5.1 c) depicts the band structure

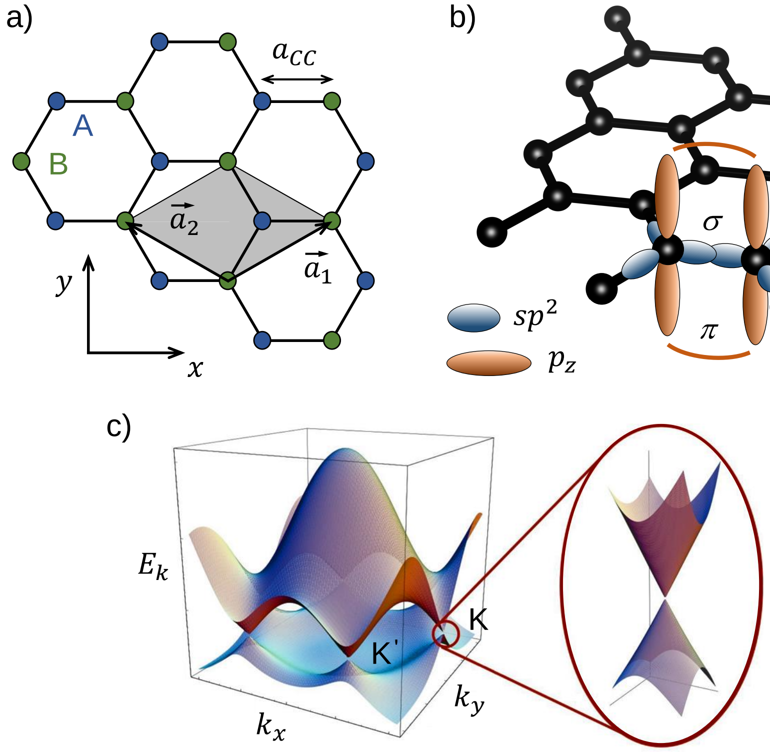

Figure 5.1. a) The honeycomb crystal structure of graphene consists of two equivalent sublattices, indicated by A and B. The 2D hexagonal Bravais lattice has a unit cell with a basis of two atoms (shaded in gray) and is spanned by the vectors $\vec{a}_1$ and $\vec{a}_2$. b) The carbon atoms in graphene are sp^2-hybridized, forming covalent σ- and π-bonds. c) Band structure of graphene with linear dispersion of the π bands around the K and K′ points in the Brillouin zone (Dirac points). Figure c) is adapted from reference [247].

of graphene, which is a zero-gap semiconductor as valence and conduction band touch. The most striking feature is however the linear dispersion of the π-bands in the vicinity of the K (K′) points. Hence, the electrical transport can essentially be described by the relativistic Dirac equation [249], giving rise to massless charge carriers with unusual behaviour in tunneling, confinement or magnetotransport [247].

Although the first theoretical description of graphene dates back to 1947, when P. R. Wallace calculated the band structure of graphite [250], free-standing graphene was assumed to be thermodynamically unstable [251]. It thus served as a theoretical model until 2004, when Novoselov *et al.* isolated and characterized graphene for the first time [6]. Since then, graphene revealed remarkable properties such as exceptionally high charge carrier mobility [252], thermal conductivity [7] and mechanical strength [8, 9] while being extremely flexible and impermeable to gases [253] at the same time. This combination of supreme properties is very promising for a variety of applications, e.g. in electronics, energy storage, photonics or for sensors [254].

5.1.2. Synthesis of large-area graphene on SiC(0001)

The actual properties of graphene heavily depend on the preparation procedure and the interaction with the substrate. Among different approaches to produce graphene on an industrial scale, we focus on the synthesis on SiC [255, 256]. This is particularly promising in the context of electronic applications because single or multilayer graphene can be directly grown on a semi-insulating substrate that is compatible with the existing technology.[1] In the following, we review the crystal structure of SiC before introducing the growth process of graphene.

Bulk crystal structure of silicon carbide

The atoms in SiC are sp^3-hybridized to form bonds with the respective other element in a tetrahedral configuration, as shown in figure 5.2 a). Since carbon has a higher electronegativity than silicon, the covalent bonds have a slightly ionic character. Figure 5.2 b) and c) depict the basic building block of the crystal structure, which is a SiC bilayer with hexagonal symmetry. The crystal is built up by the periodic stacking of such bilayers and the interlayer spacing is determined by the Si-C bond length of 1.89 Å [257].

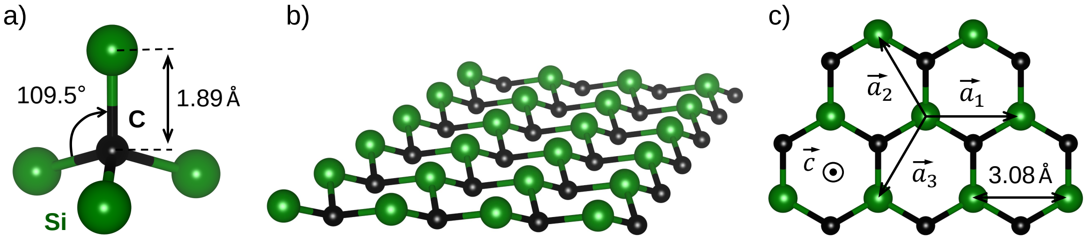

Figure 5.2. a) Tetrahedral bond of a sp^3-hybridized carbon atom with four silicon atoms. b) Perspective view of a SiC bilayer, which represents the basic building block of the bulk crystal. c) The top view on the bilayer visualizes the hexagonal structure (lattice constant $a_{\text{SiC}} \approx 3.08$ Å). The unit vectors within the basal plane obey $\vec{a}_3 = -(\vec{a}_1 + \vec{a}_2)$. Graphic created with VESTA [186], structure parameters obtained from [258].

---

[1] Competing techniques, such as chemical vapor deposition (CVD) on metals, require the graphene transfer to a suitable substrate [254].

When considering the tetrahedral geometry of the bonds, there are two possibilities to orientate two bilayers with respect to each other: either atoms of different species are aligned along the *c*-axis (eclipsed) or they are rotated by 60° (staggered). These two configurations are illustrated in figure 5.3 a). The eclipsed arrangement of consecutive bilayers leads to a hexagonal wurtzite structure (2H-SiC), while the staggered arrangement establishes a cubic zinc blende structure (3C-SiC) [259]. Besides that, mixed stacking orders of different periodicity are possible as well, which results in a multitude of distinct crystal structures, so-called *polytypes*. In fact, almost 250 SiC polytypes have already been reported [260]. They are commonly denoted using the Ramsdell notation [261], which indicates the periodicity of bilayers in *c*-direction and the true lattice symmetry (C - cubic, H - hexagonal, R - rhombohedral). In the context of this work, we focus on the polytype 6H-SiC, which is shown in figure 5.3 b) along the $(11\bar{2}0)$ plane. When considering the lateral positions of the Si atoms, the stacking order can be described by the sequence ABCACB, where the uppermost bilayer is labeled with the letter A. However, bear in mind that any other bilayer within this sequence can also be the actual surface layer. Furthermore, we need to distinguish the Si-terminated (0001) and the C-terminated $(000\bar{1})$ surfaces, which have an opposite polarity and exhibit different surface reconstructions [257].

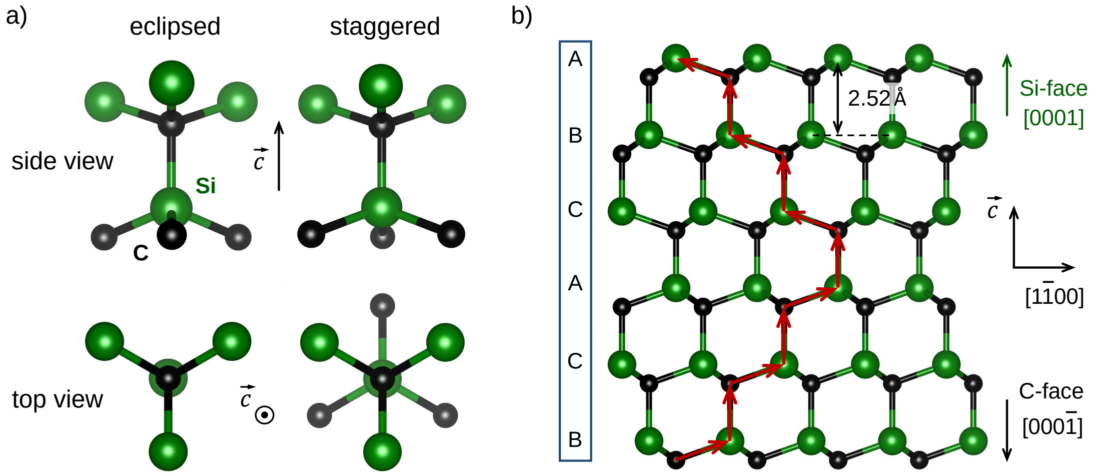

Figure 5.3. a) Possible mutual stacking orientations of SiC bilayers. The denotations *eclipsed* and *staggered* refer to the view along the *c*-direction (top view). b) Crystal structure of 6H-SiC along the $(11\bar{2}0)$ plane. The stacking order is indicated by the red arrows that connect atoms in the same plane. 6H-SiC has a stacking sequence of ABCACB, where identical letters are used when the Si atoms have the same lateral position. Figure inspired by [259].

$(6\sqrt{3} \times 6\sqrt{3})\,R30^\circ$ reconstruction and graphene growth on 6H-SiC(0001)

When being annealed at elevated temperatures, SiC experiences surface graphitization, which was already known before the discovery of graphene [262, 263]. This process is based on the thermal decomposition at the surface and the subsequent sublimation of Si atoms, which is related to the higher vapor pressure of Si compared to C. The remaining C atoms form thin graphitic films down to monolayer (ML) graphene, which are preferentially orientated parallel to the basal plane of hexagonal SiC. The growth on the C-terminated $(000\bar{1})$ surface is relatively fast and typically comprises domains of different rotational orientation. This is in contrast to the (0001) surface, where the growth is *epitaxial*, i.e. the graphene layer has a well defined azimuthal orientation with respect to the substrate [260]. In the following, we introduce the underlying process.

As a precursor to the graphene growth, 6H-SiC(0001) exhibits a characteristic $(6\sqrt{3} \times 6\sqrt{3})\,R30^\circ$ surface reconstruction [262, 264]. This reconstruction is related to the excess carbon atoms that rearrange in a graphene-like structure, the so-called *buffer layer*. However, in contrast to graphene, the buffer layer is covalently bound to the SiC substrate and thus has a corrugated structure [265, 266]. This also influences the electronic properties, e.g. the buffer layer has no pronounced π-bands and is electronically inactive [267]. At higher annealing temperatures, further Si atoms sublimate, which results in the formation of a new buffer layer at the interface to the substrate. At the same time, the bonds to the previous buffer layer break, which makes it rehybridize and transform into a graphene layer. This mechanism is also responsible for the epitaxial growth: since each graphene layer evolves from a buffer layer, their orientation is effectively dictated by the initial bonds to the substrate [268, 269].

As illustrated in figure 5.4, a $(6\sqrt{3} \times 6\sqrt{3})\,R30^\circ$ reconstruction on the SiC(0001) surface lattice almost coincides with a 13×13 graphene superstructure, although both lattices are incommensurate. When considering the topmost SiC bilayer, the $(6\sqrt{3} \times 6\sqrt{3})\,R30^\circ$ unit cell covers 108 Si and 108 C atoms, while the graphene superstructure comprises 169 graphene unit cells or 338 C atoms [264]. The carbon density of the buffer/graphene layer is therefore approximately three times larger than in a SiC bilayer, i.e. around three bilayers have to be decomposed to form a graphene ML. Moreover, when assuming that the Si surface atoms are rather flexible regarding bond length and angle, we can estimate that every third C atom of the buffer layer is covalently bound to the substrate [268].

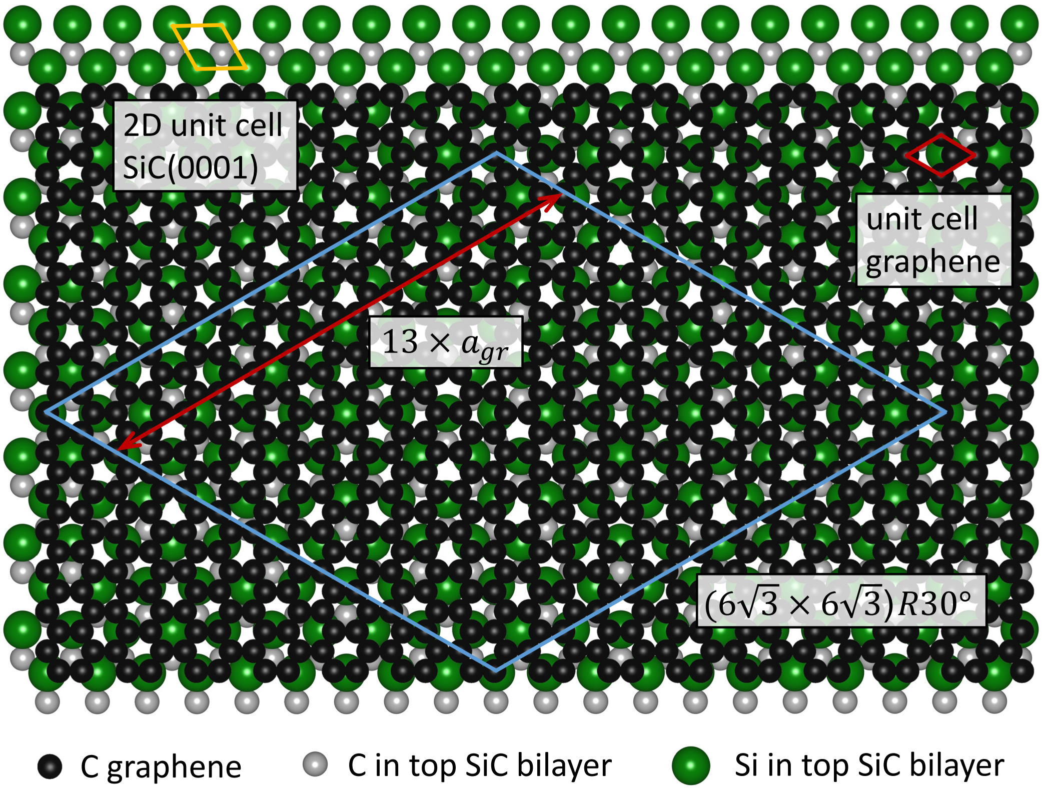

Figure 5.4. Aligned graphene monolayer on top of a bulk truncated SiC(0001) surface (only topmost bilayer shown). The dimension of the $(6\sqrt{3} \times 6\sqrt{3})\,R30^\circ$ unit cell is indicated, which almost coincides with a 13×13 graphene superstructure. Figure inspired by [259].

Hydrogen intercalation

A single graphene layer on top of the buffer layer is called Monolayer Graphene (MLG) in the following. Although the MLG is only bound by van der Waals interaction, it is still affected by the morphology of the buffer layer. This leads to an intrinsic n-doping, a long-range corrugation in the density of states and a reduced charge carrier mobility [270], which is adverse with regard to possible applications. A better decoupling from the substrate can be obtained by intercalation of hydrogen atoms, as demonstrated by Riedl *et al.* [267]. During annealing in a hydrogen atmosphere at temperatures above $\sim 500°\mathrm{C}$ [271], hydrogen atoms migrate below the buffer layer, break the covalent bonds to the substrate and saturate the dangling bonds of the topmost Si atoms. Within this process, the buffer layer is decoupled from the substrate and converted into a graphene layer that resides on the H-terminated SiC(0001) surface. Since the interaction with the substrate is almost negligible and the electronic properties are closer to that of pristine graphene [267, 272, 273], this structure was named Quasi-Free-Standing Monolayer Graphene (QFMLG). In a similar way, MLG can be converted into (quasi-free-standing) bilayer graphene. Apart from hydrogen, the intercalation of oxygen [274] and various other elements [275–279] has been demonstrated as well. However, depending on the atomic species, the decoupling can be accompanied by a rather large doping of the graphene layer.

5.2. Samples and pre-characterization

Two samples were investigated within our study: MLG and hydrogen intercalated QFMLG grown on 6H-SiC(0001). The samples were prepared and comprehensively pre-characterized by P. Richter and P. Schädlich from the group of Prof. Seyller (TU Chemnitz). As part of the present work, the experimental data was evaluated and analyzed in more detail to provide as much information as possible. In the following, we introduce further sample details and discuss the results from the analysis prior to TRHEPD.

5.2.1. Sample details

Both samples have the dimension of $4.8 \times 10 \times 0.33\,\mathrm{mm}^3$ (width × length × thickness) and were cut along the <$\bar{1}$100> and <11$\bar{2}$0> directions from a nitrogen n-doped 6H-SiC(0001) wafer purchased from the company *PAM-Xiamen*. The Si-terminated surface has been finished by an industrial-grade chemical-mechanical polishing (CMP) procedure, leading to a marginal surface roughness of less than 0.5 nm. Additional hydrogen etching, as reported in other studies (e.g. [271]), was therefore not necessary. Due to the finite manufacturing accuracy, on-axis aligned SiC wafers have a small miscut, which typically leads to a stepped terrace structure on the surface [257]. For this specific wafer, the miscut angle with respect to the (0001) surface is specified to be smaller than 0.5°.

Buffer and graphene layer were synthesized using the state-of-the-art Polymer-Assisted Sublimation Growth (PASG) technique [19]. As the name implies, prior to the annealing, the samples were covered by polymer adsorbates, which serve as an external source of carbon. This accelerates the formation of the buffer layer and leads to a smoother surface morphology. Further details on the sample preparation can be found in the appendix A.7.

5.2.2. Contaminations and average graphene coverage

Within the sample characterization, X-ray Photoelectron Spectroscopy (XPS) was applied to exclude possible contaminations and evaluate the thickness of the graphene layer. XPS is based on the photoelectric effect on core electrons and can be used to analyze the elementary composition and the chemical bonds at the surface [16]. When measuring the kinetic energy E_{kin} of the emitted photoelectrons, the respective binding energies E_{B} can be calculated by

$$E_{\mathrm{B}} = \hbar\omega - (E_{\mathrm{kin}} + \Phi_{\mathrm{spec}}), \tag{5.1}$$

where $\hbar\omega$ is the energy of the incident photons and Φ_{spec} is the work function of the spectrometer. Bear in mind that the photoelectrons can also scatter inelastically, although this is not included in equation 5.1.

Figure 5.5 a) shows the XPS spectra of the MLG sample, the buffer layer before hydrogen intercalation and the QFMLG sample. On this scale, the spectra look very similar and the main peaks can be assigned to the carbon 1s and the silicon 2s and 2p core levels [280]. The adjacent minor peaks stem from plasmon excitations and are not further relevant. More important is however the absence of additional peaks in the spectra, e.g. we do not observe an oxygen 1s peak at $\sim$533 eV [280]. Consequently, there are no significant contaminations and we can particularly exclude the partial intercalation of oxygen for both samples.

Further information can be obtained from the chemical shifts of E_{B} within the C-1s peak. The different surface structures are schematically depicted on the left side of figure 5.5 b) - d) while the corresponding XPS spectra are shown on the right. The spectrum of the buffer layer exhibits a large peak with a side lobe at higher binding energy and can be fitted with three components. Most of the signal stems from the C atoms in the substrate while the side lobe is composed of the components S_1 and S_2 that are assigned to the buffer layer [268]. The spectrum of MLG contains an additional component which can be assigned to the graphene layer. Following the approach from K. Emtsev [259], we used the overlayer-substrate attenuation model[2] to estimate the thickness of the graphene layer from the respective intensities (peak areas fit). This yields an average graphene coverage of 1.2 ± 0.1 monolayer for the MLG sample.

---

[2] The combination of buffer and graphene layer can be conceived as an overlayer, which attenuates the signal of the SiC substrate in the C-1s peak due to the inelastic scattering of photoelectrons.

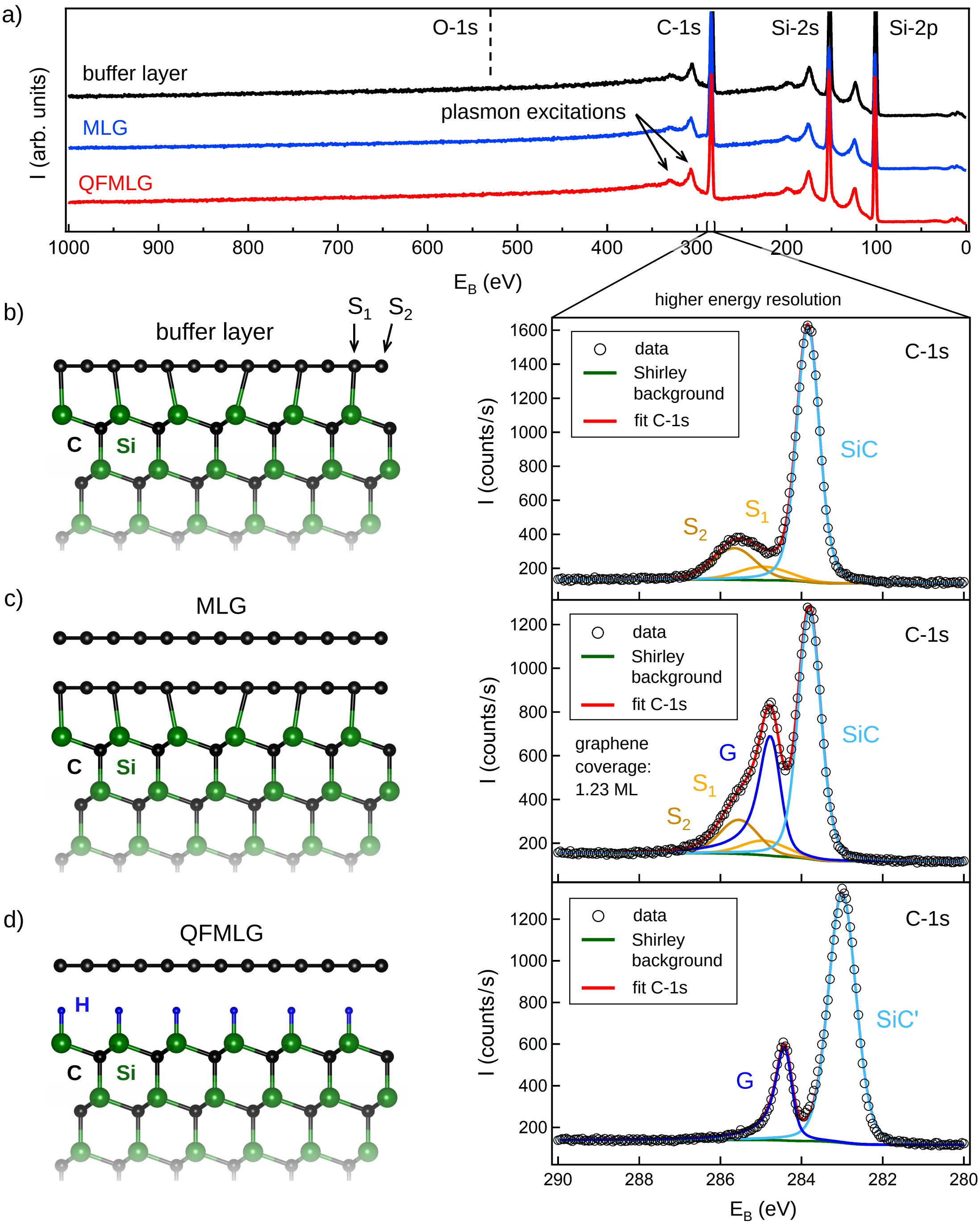

Figure 5.5. XPS characterization of the graphene samples. a) For clarity, the spectra are shifted vertically. The three distinct peaks are related to C or Si core levels and there are no indications of contaminations. b) - d) Left: illustration of the respective structure (schematic). Right: related high-resolution XPS spectra of the C-1s peak. The indicated components were fitted by a standard routine considering a Voigt line shape and a Shirley background. b) The components S_1 and S_2 can be assigned to the buffer layer, while the large peak corresponds to the C atoms of the substrate [268]. c) The additional component in MLG can be assigned to graphene and the relative intensities yield an average graphene coverage of around 1.2 ± 0.1 ML. d) For QFMLG, the buffer layer components S_1 and S_2 are absent.

As shown in figure 5.5 d), the XPS spectrum of QFMLG can be well fitted by two components and there is no significant contribution from S_1 and S_2. We can thus conclude that the hydrogen intercalation successfully converted the buffer layer into QFMLG. When compared with the other spectra, the SiC and graphene peaks are slightly shifted to lower binding energies. This can be explained by the different doping of the graphene layer and the larger surface band bending after intercalation [272]. The coverage of the QFMLG sample is assumed to be close to one monolayer. This is related to the fact that the growth of the first graphene layer on top of the buffer layer requires much higher annealing temperatures (compare table A.7), thus leading to a negligibly small bilayer fraction in QFMLG.

5.2.3. Surface topography and structure

The samples were further characterized by Atomic Force Microscopy (AFM) and Low-Energy Electron Diffraction (LEED) to evaluate the surface topography and structure, respectively.

Stepped terrace structure and substrate miscut

A typical AFM image of the MLG sample is shown in figure 5.6 a). On a scale of μm we find minor defects and irregular regions which might be caused by a non-uniform polymer adsorption during the preparation. The stepped terrace structure of the surface is most evident in the phase image shown in figure 5.6 b). The contrast of the image is related to the phase shift of the oscillating cantilever, which highlights the edges of the terraces. Besides that, this also visualizes regions of different graphene coverage, i.e. bare buffer or bilayer domains. Since the average layer thickness is above 1 monolayer, the darker areas are most likely bilayer graphene.

Two AFM images of the QFMLG sample are shown in figure 5.6 c) and d). The topography changes within the sample and also differs from the MLG sample. For a quantitative comparison we consider two height profiles perpendicular to the terrace steps along the green and blue paths, which are plotted in figure 5.6 e). The steps along the blue path are relatively small and although the respective heights are different, most correspond to either 2 or 3 SiC bilayers. In contrast, the step heights along the green path are very inhomogeneous:

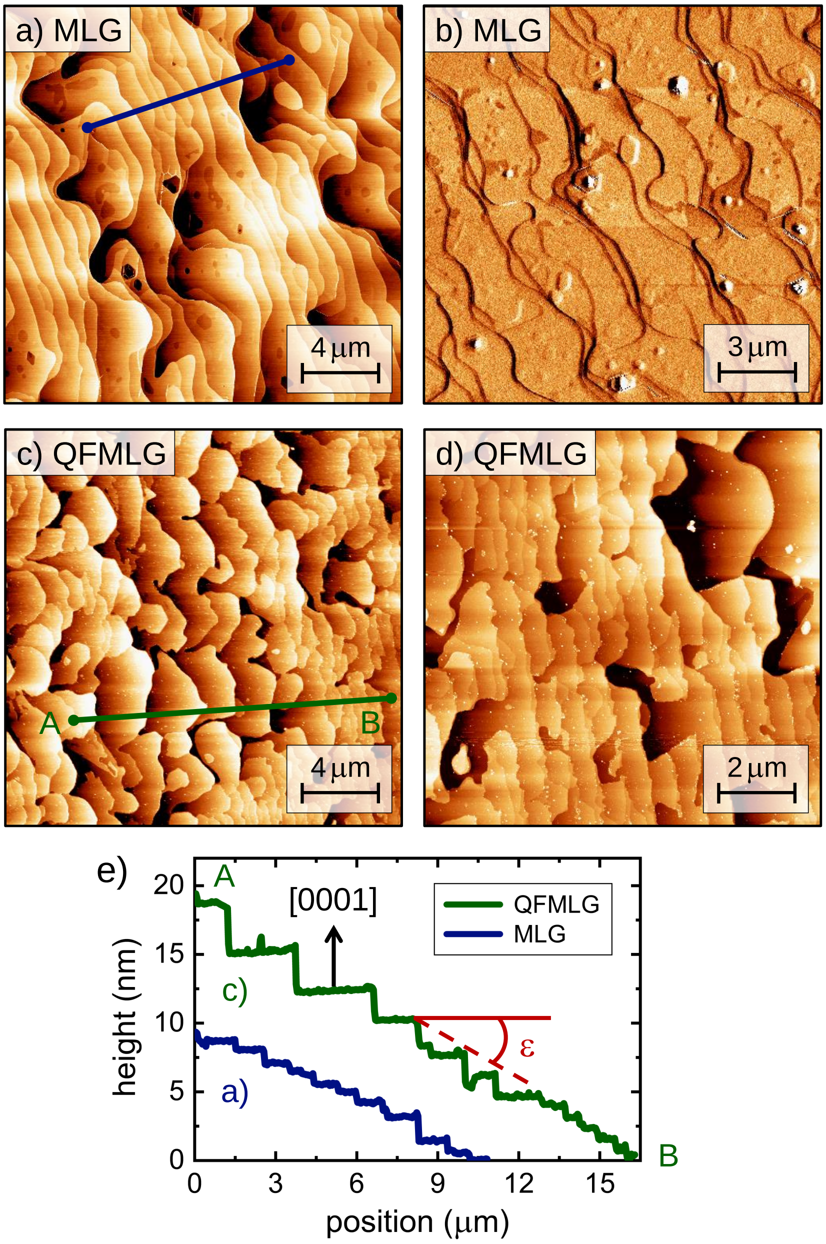

Figure 5.6. AFM analysis graphene samples. a) Topography and b) phase image of the MLG sample (obtained from two different positions). The surface is characterized by a stepped terrace structure with a few defects. c), d) The images of the QFMLG sample indicate a rather inhomogeneous arrangement of the terraces. e) This is confirmed by the height profiles along the green and blue paths, which reveal several large steps for the QFMLG sample. The wafer miscut angle ε is calculated to $\sim 0.07^\circ$.

there are relatively large steps of more than 2 SiC unit cells close to the point A, while the steps are similar to those along the blue path when approaching point B. The coalescence of several small steps into a single step of greater height is known as *step bunching* [281] and should usually be less pronounced in PASG [19, 282]. However, with regard to the TRHEPD measurements, larger steps are not considered to be a problem. Conversely, many very small steps can affect the diffraction pattern when the terrace width becomes smaller than the coherence length of the beam [156], but this is not the case either. The height profiles can be further utilized to determine the (local) miscut angle ε of the SiC(0001) substrate. Referring to the sketch in figure 5.6 e), the calculation is straightforward and has been done for four different profiles which yields $\varepsilon \approx 0.07°$. The actual miscut is therefore well below the company specification of less than $0.5°$.

Long-range periodic order

Additionally, qualitative LEED measurements were carried out to characterize the surface structure. As shown in figure 5.7 a) and b), both samples exhibit a clear diffraction pattern for $E_{e^-} = 140\,\mathrm{eV}$. We can thus conclude that the surface has a long-range periodic order and that the sample quality is sufficiently good for TRHEPD measurements. The presence of the $(6\sqrt{3} \times 6\sqrt{3})\,R30°$ reconstructed buffer layer in MLG is clearly evident by the large amount of additional diffraction spots, although not all of them are visible. The graphene peaks have a high intensity and are surrounded by six distinct satellite spots that can be assigned to the buffer layer. The magnification shown in figure 5.7 c) further reveals that the two satellite spots on the inside have a significantly higher intensity than the other four spots. Interestingly, these spots can also be resolved for QFMLG, where we do not expect the presence of a buffer layer (compare XPS data). Besides that, QFMLG exhibits several further diffraction spots that do not correspond to single integer graphene or SiC reciprocal lattice vectors. Some are exemplary encircled in red in figure 5.7 b).

The presence of these additional spots in QFMLG can be attributed to multiple diffraction on both, the graphene and the SiC 2D lattice [263]. This is illustrated in figure 5.7 d). The integer first order diffraction spots are represented by green and red dots, respectively. By the linear combination of a graphene and a SiC reciprocal lattice vector (green and dashed red line) we reach the point A, which is thus a (mixed) second order diffraction spot. When considering all second and third order spots (blue and brown dots), the diffraction pattern of QFMLG can indeed be well reproduced. Since both pairs of lattice vectors coincide with the $(6\sqrt{3} \times 6\sqrt{3})\,R30°$ grid, the higher order diffraction spots are

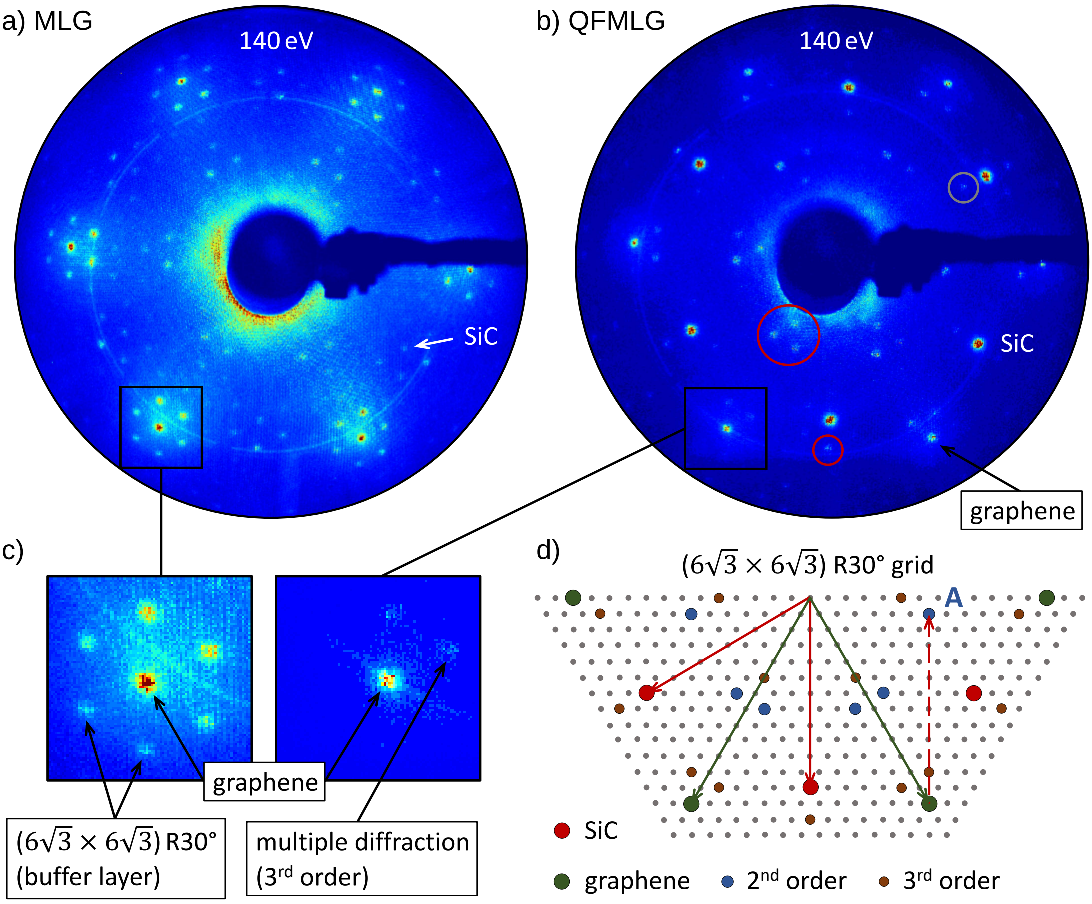

Figure 5.7. LEED pattern and interpretation. The color is a linear measure for the intensity. a) The MLG sample exhibits a variety of diffraction spots arranged on a $(6\sqrt{3} \times 6\sqrt{3})\,R30^\circ$ grid, which is a clear indication for the presence of the buffer layer. b) For QFMLG, we observe pronounced diffraction spots that can be assigned to the SiC substrate and the graphene layer, respectively. Further spots of reduced intensity are encircled in red and gray. c) The satellite spots around the graphene peak in MLG exhibit a striking feature: the two spots on the inside have a much higher intensity than the other four spots. The intensity of these spots is enhanced by the combined third order diffraction on the graphene and the SiC 2D lattice. Therefore, both spots can also be observed for QFMLG. d) Reciprocal lattice vectors of graphene (green) and SiC (red) on a $(6\sqrt{3} \times 6\sqrt{3})\,R30^\circ$ grid. The linear combinations of both vectors specify the location of (mixed) higher order diffraction spots, as illustrated for the second order spot A. When third order diffraction is included as well, the low intensity spots encircled in red in b) can be well reproduced.

located at the same positions as the fractional order spots of the buffer layer. This makes a strict separation of the signal from possibly remaining buffer layer domains almost impossible. The presence of the very faint diffraction spot encircled in gray in figure 5.7 b) could e.g. be interpreted as fifth order spot or as indication of a tiny fraction of buffer layer. Although the XPS data in figure 5.5 d) indicates the absence of the buffer layer, such small fraction could simply be compensated by the fit. On the other hand, we note that this particular spot is also not very pronounced in the diffraction pattern of MLG, which makes it unlikely to be exclusively related to the buffer layer. Since the overall contribution is negligibly small in either case, the QFMLG sample can be considered as completely intercalated for the further analysis.

5.3. Surface structure analysis with TRHEPD

The TRHEPD measurements were carried out at the SPF at the research center KEK in Japan. The key features of the experimental setup are introduced in section 3.3.5. We point out that there have been two previous TRHEPD studies of graphene on 6H-SiC(0001) [211, 283]. In an early study, Kawasuso *et al.* investigated the surface graphitization and structure of few-layer graphene on 6H-SiC(0001) [283]. However, since then not only the theoretical understanding of the material system and the sample preparation improved significantly, but also the positron beam quality available for TRHEPD. Most recently, Endo *et al.* investigated pristine and Ca-intercalated bilayer graphene grown on 6H-SiC(0001) [211]. To the best of our knowledge, the present study is thus the first analysis of MLG and hydrogen intercalated QFMLG using TRHEPD. In the following, we discuss the experimental procedure, the obtained diffraction pattern and the results from the rocking curve analysis.

5.3.1. Experimental procedure

Subsequently to the pre-characterization, both samples were stored and transported in air. This is possible because the Si dangling bonds are saturated either by the buffer layer or the hydrogen atoms. The graphene layer is chemically inert as well, so that there is only physisorption at the surface. After the transfer to the UHV chamber, the clean surface can be restored by an appropriate in-situ heat treatment, which is discussed in more detail in section 5.3.4. All TRHEPD measurements were conducted at room temperature and the sample quality was checked by RHEED beforehand.

Following a standard routine, the sample position was adjusted with respect to the positron beam to maximize the intensity of the specular spot on the fluorescent screen. To reduce the background, all viewports were covered and the pressure gauges were switched off during the measurements. Additionally, the MCP gain was increased to the maximum. The crystallographic orientation of the sample was adjusted by eye until a symmetric TRHEPD pattern was observed, as necessary for the many-beam condition. For the one-beam condition, the azimuthal angle was set to $\varphi = 7.5^\circ$ off the <1$\bar{1}$00> or <11$\bar{2}$0> directions, respectively, which yields equivalent curves [196]. To obtain a set of rocking curve data, diffraction patterns were recorded for glancing angles from 0.3° to 6.5° with a step size of 0.1°. The images were acquired with 25 fps and during post-processing, the brightness values are added pixel-wise for each θ. The individual integration time was $t_{\theta_i} = 40\,\mathrm{s}$ so that the acquisition time for each rocking scan was a bit more than 40 min. This is sufficient for the rocking curve analysis of the specular spot, which contains the full structural information. For a few selected glancing angles we further recorded diffraction patterns with a significantly longer integration time of $t_{\theta_i} = 40\,\mathrm{min}$. Due to the enhanced statistics, this allowed us to resolve weaker diffraction spots as well.

5.3.2. Positron diffraction patterns

In the following, we discuss the observed TRHEPD patterns and assign the respective diffraction spots.

Quasi-free standing monolayer graphene

For small glancing angles within the region of total reflection, we only observe the specular spot. This is shown in figure 5.8 a) and c) for the high-symmetry directions of QFMLG. To enable a precise rocking curve analysis down to very small glancing angles of $\sim 0.3^\circ$, it is crucial to cover the direct beam that misses the sample. Figure 5.8 b) and d) display the TRHEPD patterns along the <11$\bar{2}$0> and <1$\bar{1}$00> directions for a larger glancing angle of 5.5°. Apart from the specular spot, we observe several additional diffraction spots that greatly differ in intensity. In figure 5.8 d) we can further identify very faint Kikuchi lines. When compared with the RHEED pattern, the contribution of Kikuchi lines is significantly reduced for TRHEPD, which is related to the shallower probing depth of positrons (see section 3.3.2).

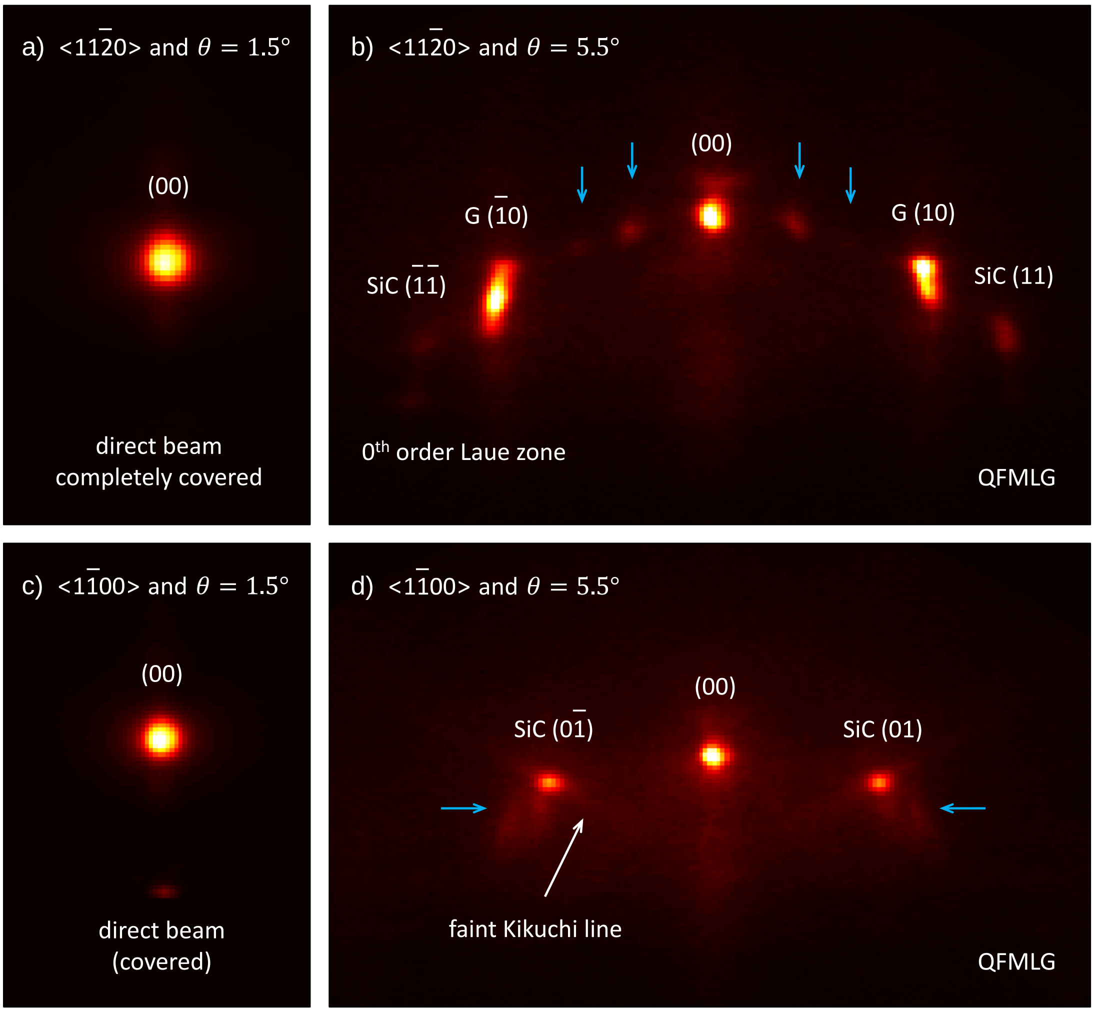

Figure 5.8. TRHEPD patterns of QFMLG along the high-symmetry directions (integration time 40 min, linear color scale). a), c) When the glancing angle θ is small, only the specular reflection is observed. b) For $\theta = 5.5°$, the diffraction spots along <11$\bar{2}$0> vary greatly in intensity and the brightest ones are assigned to the graphene lattice. The turquoise arrows indicate the spots that are attributed to third and fourth order diffraction on both lattices as indicated in figure 5.9 a). Only the zeroth order Laue zone is resolved. d) The two additional spots along <1$\bar{1}$00> can be assigned to the SiC lattice. Kikuchi lines are present as well, although their intensity is very low.

Based on the preceding LEED analysis (section 5.2.3), we expect the TRHEPD pattern of QFMLG to be composed of diffraction spots from graphene and SiC, which are superimposed by further spots that stem from multiple diffraction on both lattices. Since the lattices of graphene and SiC are rotated by 30° with respect to each other, the main diffraction spots are observed along different crystallographic directions. Due to the different lattice constants, the spacing of the graphene spots on the Laue semicircle has to be greater than for SiC [284]. Therefore, we can assign the two bright spots in figure 5.8 b) to graphene and the pronounced spots in figure 5.8 d) to SiC. The ratio of the respective horizontal spacings is approximately 1.29, which agrees reasonably well with the inverse ratio of the lattice constants that calculates to ~ 1.25. The small deviation can be attributed to the experimental uncertainty, e.g. it might be related to a slight misalignment of the sample. Additionally, we find that the intensity of the graphene spots is much larger than for SiC, although only the topmost surface layer is composed of graphene. This can be explained by the exceptional surface sensitivity of TRHEPD, even at such large glancing angle. For a comparison, we refer back to the LEED pattern shown in figure 5.7 b), where the SiC spots are more pronounced thus indicating a deeper mean probing depth.

For the assignment of the remaining diffraction spots, we refer to figure 5.9 a), which is a map of reciprocal space including (mixed) higher order spots. The zeroth order Laue zones of both high-symmetry directions are marked by the dashed red and green line, respectively. The turquoise arrows indicate the relevant mixed order diffraction spots that coincide with the zeroth Laue zones. For the measurement along <$11\bar{2}0$>, all four spots are clearly resolved and the relative intensities of third and fourth order also support this assignment. With respect to the SiC lattice, these spots are located at $\pm(5/18, 5/18)$ and $\pm(8/18, 8/18)$, respectively. Since the two mixed second order spots between third and fourth order are located on fractional Laue zones (compare figure 5.9 b)), their intensity is considerably reduced and they are not resolved in the diffraction pattern of QFMLG. The two minor spots further outside on the Laue semicircle in figure 5.8 b) can be assigned to the (11) and ($\bar{1}\bar{1}$) reflections of SiC. The additional faint spot close to the shadow edge on the left side is most likely of (mixed) fifth order.

For the measurement along <$1\bar{1}00$>, we expect to see the two (mixed) third order spots next to the SiC (01) and ($0\bar{1}$) reflections. In the diffraction pattern of figure 5.8 d), these spots are however kind of smeared out so that it is difficult to determine their exact location. It even looks like there might be another spot in the close vicinity, but this could not be confirmed by the RHEED pattern. The two fourth order spots in the zeroth Laue zone are located too close to the much brighter specular spot to be resolved in the experiment.

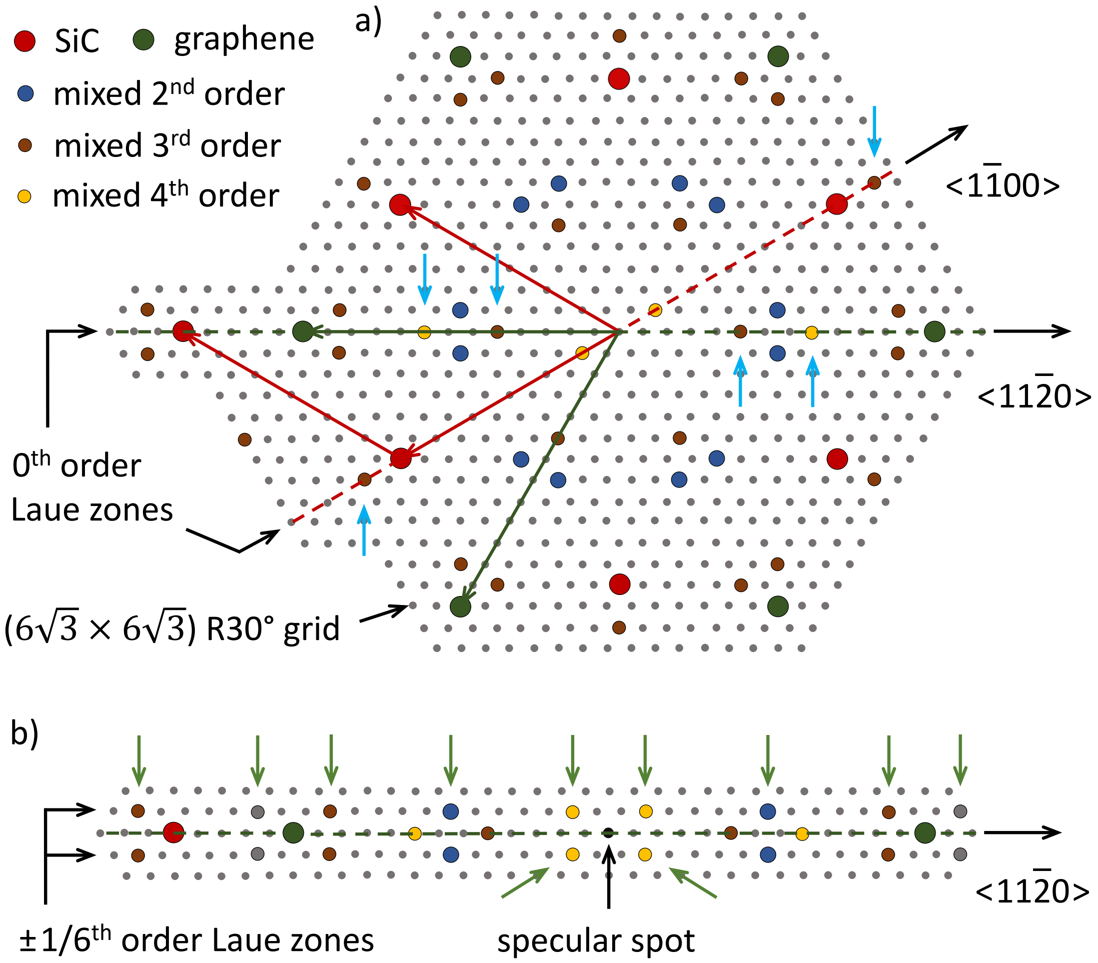

Figure 5.9. a) Reciprocal space: $(6\sqrt{3} \times 6\sqrt{3})\,R30°$ grid with SiC (red) and graphene (green) lattice vectors and points. Higher order diffraction spots that stem from the combined diffraction on both lattices are marked in blue, brown and yellow. Note that not all fourth order spots are shown, but only those located in the zeroth Laue zones. The turquoise arrows indicate the mixed higher order spots that are observed in figure 5.8 b) and d), respectively. The crystallographic directions on the right side refer to the SiC lattice. b) Higher order diffraction spots in the $1/6^{\text{th}}$ and $-1/6^{\text{th}}$ order Laue zones for the measurement along <11$\bar{2}$0>. The green arrows indicate the diffraction spots that are experimentally observed for MLG, as shown in figure 5.10 b).

Monolayer graphene

Figure 5.10 a) shows the diffraction pattern of MLG along <1$\bar{1}$00> and for $\theta = 5.5°$. We identify the (01) and (0$\bar{1}$) reflections of SiC that were also observed for QFMLG, but the background is considerably larger. As quantified in section 5.2.2, the MLG sample has an average graphene coverage of around 1.2

monolayer, while QFMLG corresponds to almost exactly one monolayer. The higher background can thus be attributed to the larger surface roughness, which increases the diffuse scattering of positrons in grazing incidence. Diffraction spots from the buffer layer might be present, but the signal-to-noise ratio is too low to clearly resolve them. The additional intensity below the specular spot could originate from a fractional Laue zone, but could also be interpreted as transmission spot. Since the latter explanation would agree well with the picture of a rough surface, we restrain from a definite assignment.

The TRHEPD pattern of MLG along <11$\bar{2}$0> is shown in figure 5.10 b). Despite the large diffuse background, we can resolve several additional diffraction spots that are not observed for QFMLG (green arrows). These spots can thus be associated with the $(6\sqrt{3} \times 6\sqrt{3})\,R30^\circ$ reconstructed buffer layer present in MLG. Using the software *RHEED SIM* [285], we clarified that the spots are unambiguously located in the $\pm 1/6^{\text{th}}$ order Laue zones. The two visible spots in the $-1/6^{\text{th}}$ zone can be assigned to the $(-1/6, 0)$ and $(0, 1/6)$ reflections. By comparison with figure 5.9 b), we recognize that the two innermost spots of the $-1/6^{\text{th}}$ Laue zone are not resolved in the diffraction pattern. This is in agreement with the results from the LEED analysis (section 5.2.3), where it was also not possible to observe all diffraction spots expected from a $(6\sqrt{3} \times 6\sqrt{3})\,R30^\circ$ reconstruction. In general, it is more likely to observe those spots that coincide with a mixed higher order enhancing the intensity. This might also explain why we did not resolve any additional spot along <1$\bar{1}$00>: the adjacent fractional Laue zones do not include higher orders.

Our first approach to identify the visible spots of the $1/6^{\text{th}}$ Laue zone is hence based on the comparison with the location of mixed higher orders in figure 5.9 b). The two innermost spots are therefore assigned to $(0, -1/6)$ and $(1/6, 0)$, which coincide with the fourth orders. Additionally, these spots are on the same horizontal positions as those of the $-1/6^{\text{th}}$ Laue zone, which further supports our assignment. Further outside on the semicircle, we expect to see the two spots that coincide with the second orders. As shown in figure 5.10 c), both spots can indeed be resolved. The relative intensity of the second and fourth order spots is a clear indication that most of the signal can be attributed to the diffraction on the reconstructed buffer layer, as expected. Apart from that, we observe at least four additional minor peaks in figure 5.10 c), as indicated by the gray arrows. Since their arrangement is symmetric, it is most likely that these peaks correspond to diffraction spots of the buffer layer as well.

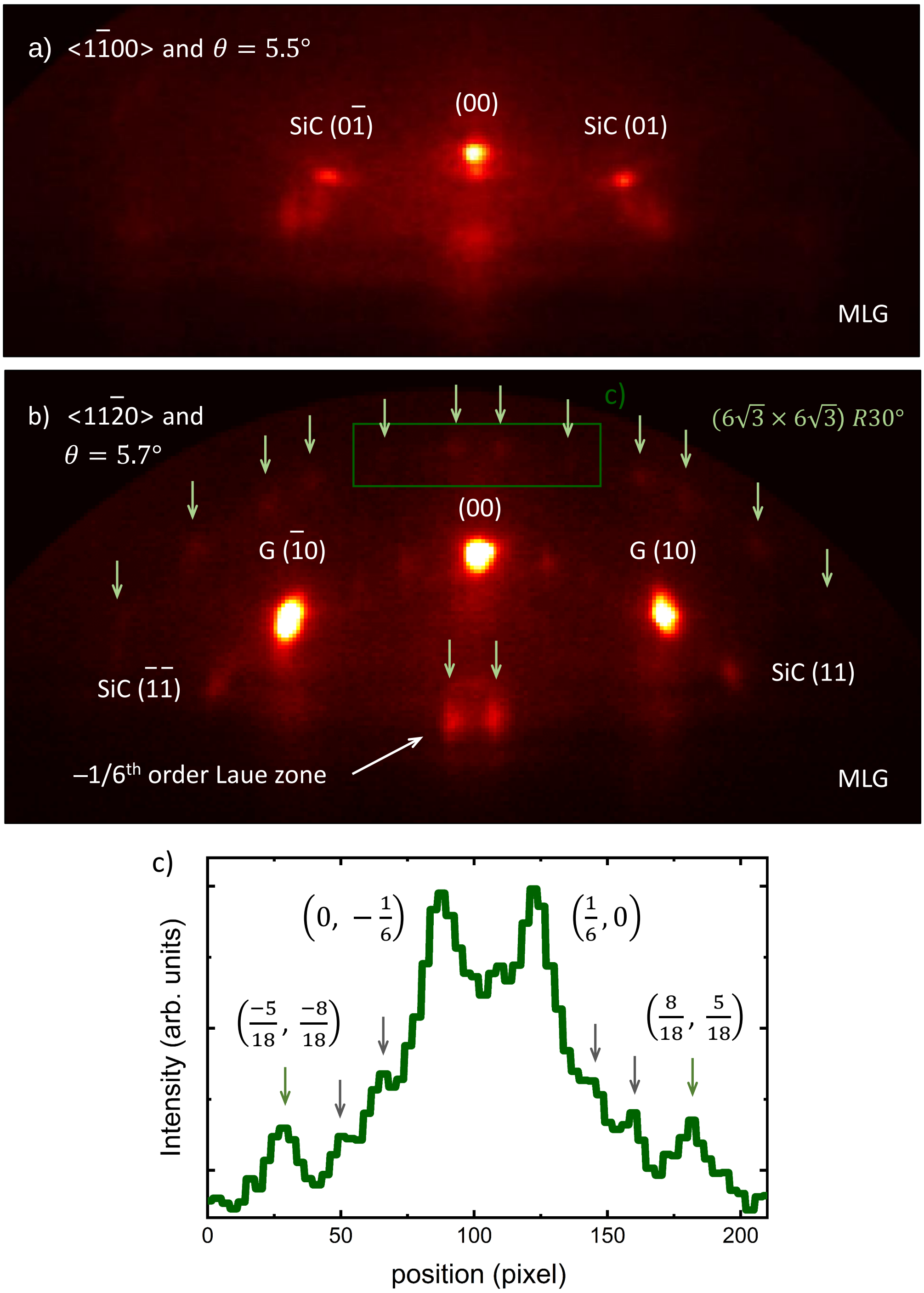

Figure 5.10. TRHEPD patterns of MLG along the high-symmetry directions (integration time 40 min, linear color scale). a) Along <1$\bar{1}$00> and for $\theta = 5.5°$, we identify the same diffraction spots as for QFMLG, i.e. it was not possible to resolve any spot related to the buffer layer. b) For the measurement along <11$\bar{2}$0>, we observe a multitude of additional spots located in the $\pm 1/6^{\text{th}}$ order Laue zones (green arrows). These spots are assigned to the $(6\sqrt{3} \times 6\sqrt{3})\ R30°$ reconstruction of the buffer layer. c) Intensity plot of each pixel column within the green rectangular box shown in b). At least four further diffraction spots are resolved, as indicated by the gray arrows.

Further outside on the 1/6th Laue semicircle in figure 5.10 b), the next two spots on each side are located on the height of the graphene spots. Consequently, these spots are identified as two of the six satellite spots present in the LEED pattern (see figure 5.7 c), left side). Considering both directions, the four spots are located at $(-13/18, -16/18)$, $(-10/18, -13/18)$, $(13/18, 10/18)$ and $(16/18, 13/18)$, respectively. The remaining satellite spots are not observed, since they are either below the shadow edge or located in the 1/3th Laue zone. The next two spots on the 1/6th Laue semicircle are on the height of the $(\bar{1}\bar{1})$ and (11) SiC reflections. Using *RHEED SIM*, we find that they are located at $(-1, -21/18)$ and $(21/18, 1)$, respectively and thus coincide with the third order spots shown in figure 5.9 b). A comparison with the LEED pattern was not possible in this case, because for $E_{e^-} = 140\,\mathrm{eV}$, these spots are already outside the screen. The outermost visible spots of the 1/6th Laue semicircle are located at $(-23/18, -26/18)$ and $(26/18, 23/18)$, respectively. Although not shown in figure 5.9 b), they coincide with a fourth order spot as well.

5.3.3. Further data processing

Figure 5.11 a) shows the specular spot of QFMLG recorded along $<1\bar{1}00>$ and for $\theta = 3.6^\circ$. Despite the relatively short integration time of only 40 s, the signal-to-noise ratio is sufficiently good. In a first step, we recalculate θ from the position of the (00) spot, which was done for each glancing angle of the rocking scan. This allowed to verify the experimental setting and confirm that the angular steps are equidistant within the experimental uncertainty.

To obtain the experimental rocking curve, we have to extract the intensity of the specular spot from each diffraction pattern for all glancing angles θ_i. This must be done in a standardized way to ensure comparability, although the shape and size of the spot varies slightly. For a specific θ_i, the intensity of each pixel can be defined as the sum of its brightness values over all frames recorded. Furthermore, we define the center of the specular spot by the pixel with highest intensity, which is unambiguous since there is no saturation. It is most natural to include several pixels around the center and add up the respective intensities to obtain a measure for the (00) spot intensity. Following the established procedure at the SPF, we considered square-shaped pixel arrays of different size, as illustrated in figure 5.11 b) for 7×7 and 11×11 pixels. After the normalization (equation 3.35), both approaches yield very similar rocking

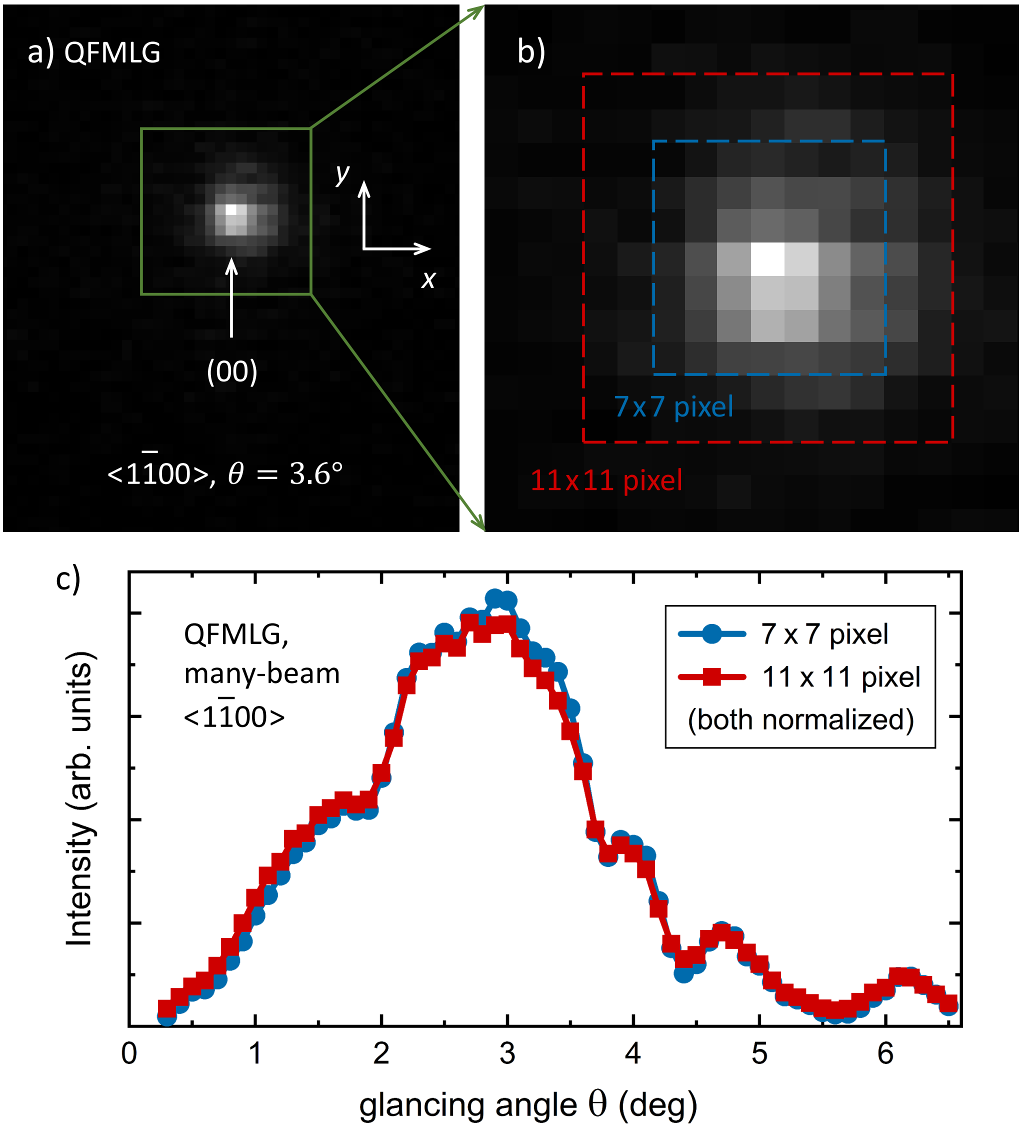

Figure 5.11. Extraction of the (00) spot intensity. a) Specular spot of QFMLG, recorded along <1$\bar{1}$00>, for $\theta = 3.6°$ and with an integration time of 40 s. b) Magnification of the green area in a), revealing the intensity of individual pixels. The center of the (00) spot can be defined by the brightest pixel. There are different possibilities to quantify the spot intensity, e.g. by adding up the brightness values of a 7×7 or 11×11 pixel array around the center. c) Both approaches result in a similar rocking curve, but the features are slightly more pronounced when considering only $7 \times 7 = 49$ pixels. For better comparability, the curves were normalized following equation 3.35.

curves, as shown in figure 5.11 c). Although the curves exhibit the same features, peaks and valleys are slightly less pronounced when including more pixels. This is attributed to the fact that outer pixels have a worse signal-to-noise ratio and thus increase the average contribution of the diffuse background. On the other hand, including more pixels increases the statistics and can therefore reduce the influence of death pixels or dust on camera and MCP. For the quantitative analysis, we decided to consider both approaches as this also yields information about the associated uncertainty. Obviously, there are various other possibilities to extract the intensity and a fixed procedure could potentially cause a systematic error. Alternatively, one could e.g. consider diamond-shaped pixel arrays, but this approach yields very similar rocking curves, too [196]. On these grounds, we do not expect that the chosen method has a significant influence on the obtained results.

5.3.4. Evaluation of the heat treatment

As mentioned in section 5.3.1, both samples were annealed in-situ, which is necessary to obtain a clean, adsorbate-free surface. This step is particularly critical for QFMLG because the hydrogen intercalation is known to be unstable for elevated temperatures [270, 286]. Consequently, the annealing temperature has to be sufficiently low – otherwise we would simply restore the buffer layer. Riedl *et al.* reported that QFMLG is stable up to 700°C [267]. This temperature should however be regarded as upper limit since it marks the onset of the Si-H bond breaking [287]. To exclude hydrogen desorption from the interface, we thus started with a rather low annealing temperature of 300°C. Subsequently, the temperature and/or duration of the heat treatment were successively increased. The cool-down time after each step was at least 30 min and the TRHEPD patterns were recorded at room temperature.

Figure 5.12 a) shows the obtained rocking curves of QFMLG along <1$\bar{1}$00> (many-beam condition) and for $T_{\mathrm{anneal}} \leq 400^\circ\mathrm{C}$. As plotted on the left side, the absolute intensity of the specular spot increases steadily when extending the heat treatment, which holds true for the entire angular range. This is a clear indication that the surface is not fully conditioned yet. After the normalization (right plot), we further find that the increase in intensity is not completely uniform, i.e. the shape of the rocking curve changes slightly. As indicated by the brown arrow, the shoulder at around $\theta = 1.6^\circ$ becomes more pronounced with higher temperature. Based on the extensive experience of our collaborators, annealing at 400°C should not affect the structure of QFMLG and we can particularly exclude the desorption of hydrogen [288]. A possible explanation might be that positrons in total reflection are much more affected by the surface roughness

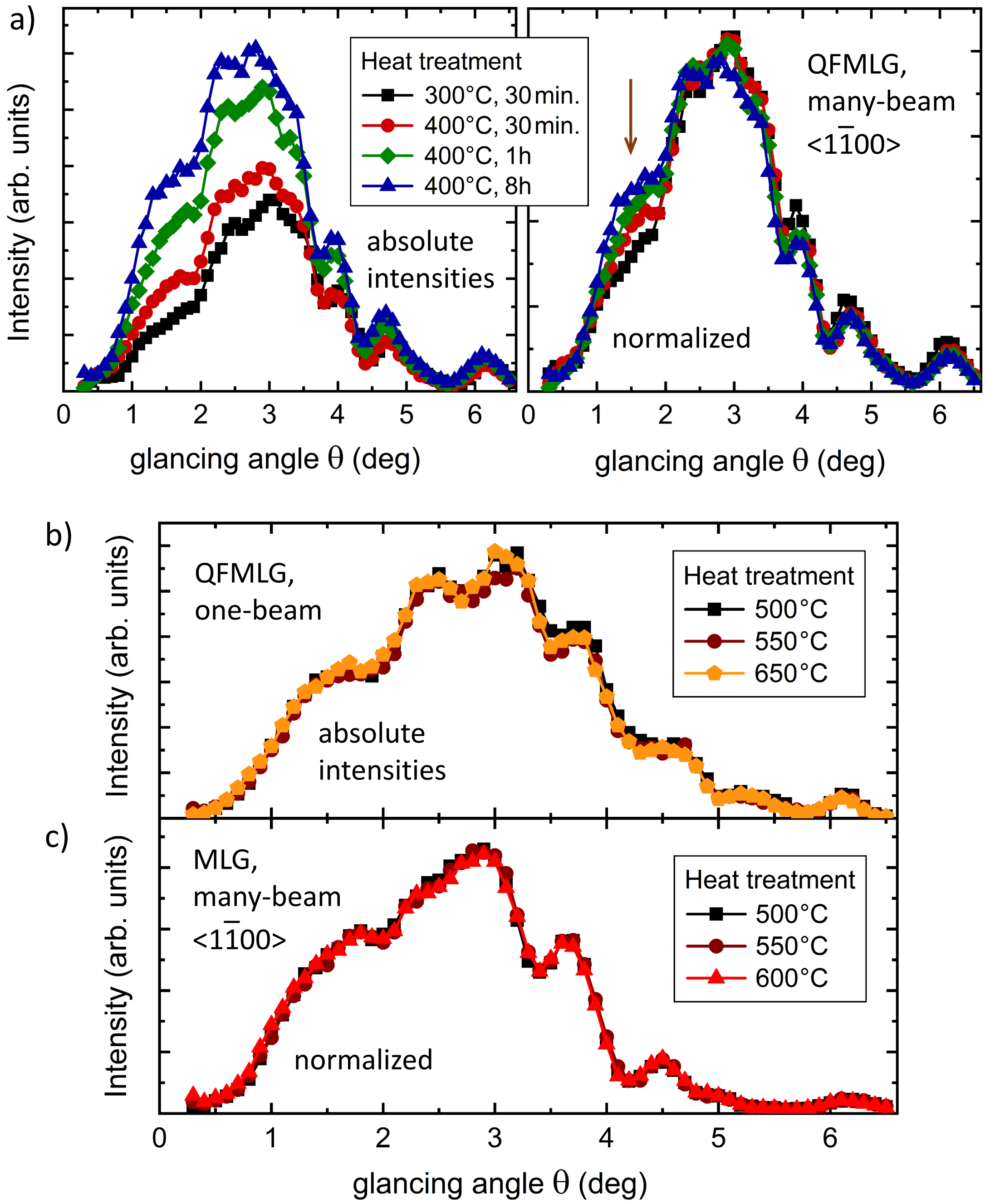

Figure 5.12. Effect of the heat treatment prior to TRHEPD at room temperature. Intensities of the (00) spot were obtained from 7 × 7 pixel arrays and equation 3.35 was used for normalization. a) Extracted (left) and normalized (right) rocking curves of QFMLG along <1$\bar{1}$00> and for $T_{\text{anneal}} \leq 400°\text{C}$. The increase of the absolute intensity reveals that the surface is not completely clean yet. Moreover, the normalized rocking curve changes slightly (brown arrow). b) Rocking curves of QFMLG (one-beam condition) after additional, step-wise annealing at higher temperatures (30 min each). There is no further increase in intensity, i.e. we obtained a clean surface. c) Normalized rocking curves of MLG along <1$\bar{1}$00> after annealing at $T_{\text{anneal}} \leq 600°\text{C}$. The curve is perfectly reproducible, i.e. there are no structural changes and we expect a clean surface as well.

due to adsorbates, effectively leading to a disproportionate increase of intensity in this angular range. It could be interesting to test this hypothesis with other (less complex) samples, which was however not possible within the scope of this work. Upon further annealing at temperatures of up to 650°C no more changes were observed. In fact, the rocking curve can be well reproduced, as shown in figure 5.12 b) for the one-beam condition. We can conclude that annealing at $\sim$ 500°C is already sufficient to remove adsorbates, which is reasonable since they are only weakly bound by van der Waals interaction. This is in agreement with the degassing procedure reported by Emery *et al.* [289]. Moreover, even when annealing at 650°C, we find no indication for hydrogen desorption, which is consistent with the results from Riedl *et al.* [267]. For the quantitative analysis of QFMLG (section 5.3.5), we used the data obtained after annealing at 500°C, averaged over three separate rocking scans.

The heat treatment of MLG is uncritical since there is no intercalated hydrogen. Figure 5.12 c) shows the normalized rocking curves for different annealing temperatures along <$1\bar{1}00$>, which are almost identical. We conclude that annealing at 500°C for 30 min is already sufficient to condition the surface. This is in agreement with our observation for QFMLG. For the quantitative analysis of MLG (section 5.3.6), we used the data recorded after annealing at 600°C averaged over three scans as well.

5.3.5. Determination of the spacing between QFMLG and SiC

TRHEPD rocking curve intensities were calculated based on the full dynamical diffraction theory, as introduced in section 3.3.3. The actual calculations were done numerically using an existing Fortran code originally developed for RHEED by T. Hanada and A. Ichimiya [185, 290]. The corresponding software utilizes the multi-slice method and we set the slice thickness to 0.01 Å. To account for the experimental resolution, the calculated rocking curves are convoluted with a Gaussian which has a FWHM of 0.3°. Moreover, we considered the geometrical correction by scaling the calculated intensities with a factor of $\sin\theta$ (compare appendix A.1).

The iterative adjustment of the structural parameters was done by minimizing the R-factor of the fit (equation 3.34) using the Nelder-Mead algorithm. Since all calculations were performed on a normal computer, we restricted our study to a local search around the values predicted by theory and confirmed by other measurement techniques [1, 289]. The precisely known bulk lattice parameters of SiC were fixed while we considered the possible relaxation of the uppermost Si and C layer.

One-beam analysis

In practice, the information obtained from the one-beam analysis can be used to determine the separation of atomic layers when we include their mean occupation and composition [133]. As the structure of QFMLG is already known and we do not expect buckling [1], our particular aim was thus to precisely determine the spacing between the graphene layer and the SiC substrate.

In a first step, we manually fine-adjusted the crystal potential of SiC and graphene so that the distinct Bragg peaks of calculated and experimental rocking curve coincide. The crystal potential of graphene was set to 11.5 eV [208]. For SiC, we adjusted the crystal potential to 17.1 eV, which is close to the rough value of 17 eV reported by Kawasuso *et al.* [197]. Using equation 3.24 with the lattice spacing $d_{\text{SiC}} \approx 2.52\,\text{Å}$, we calculate the first to fourth order Bragg reflections to 2.7°, 3.7°, 4.8° and 6.1°. Since the penetration depth of positrons increases with θ, the average contribution of SiC in the signal increases with θ as well and the intensity of higher orders is enhanced accordingly. The experimentally observed peaks at 3.8° and 6.1° (compare figure 5.12 b)) can be clearly identified as second and fourth order Bragg reflections. The shoulder at around 4.6 - 4.7° is most likely caused by the third order reflection. The first order reflection is superimposed by the strong structural features from the graphene layer and can thus not be assigned unambiguously to the peak at 2.5°.

For SiC, the imaginary part of the crystal potential[3] was set to 15% of the real part, which is the empirical value normally used for 10 keV positrons [196]. Within the analysis, it was found that the agreement between calculation and experimental data improves significantly when reducing the imaginary part of the crystal potential for graphene, $V_{\text{gr,im}}$. This is shown in figure 5.13 for different values of

$$\kappa := \frac{V_{\text{gr,im}}}{V_{\text{gr,real}}}. \tag{5.2}$$

---

[3] The imaginary crystal potential governs inelastic scattering, see equation 3.32

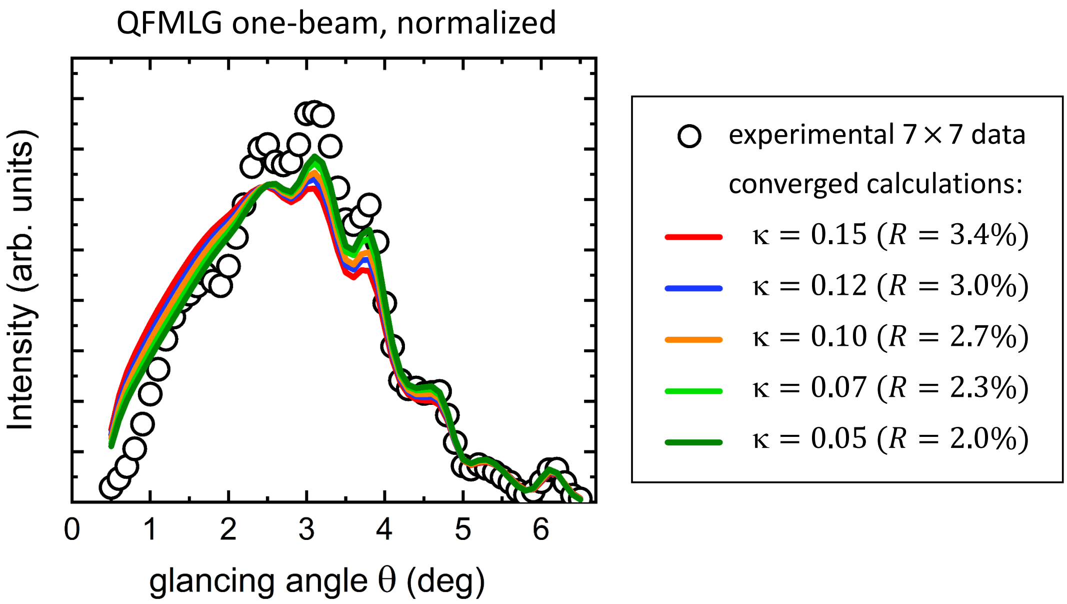

Figure 5.13. Adjustment of the imaginary crystal potential of graphene. The parameter κ is defined in equation 5.2. The structural model used for the calculations considers one complete layer QFMLG without bilayer fraction. The spacings of hydrogen and graphene layer were flexible with respect to the topmost Si layer of the substrate and have been optimized individually for each value of κ.

The calculations were first done for a relatively simple model assuming a fully occupied graphene layer without bilayer fraction or surface roughness. When reducing κ to 5%, the R-factor decreases continuously from 3.4% to 2.0%. A further reduction of κ decreases the R-factor only slightly and was not considered since it visibly worsens the agreement of the observed features and has no physical meaning. In the first instance, it is unclear why the inelastic scattering on the graphene layer should be reduced to such extent. On the other hand, we emphasize that the proportionality of real and imaginary scattering factors is just an approximation without physical background [133]. Moreover, we did not apply an energy filter, which means that inelastically scattered positrons are detected as well. These positrons thus contribute to some extent to the rocking curve, which might effectively lead to an underestimation of the inelastic scattering factor, in particular of the uppermost layer. After refinement of the structural model as explained in the following, we found that the experimental data can be best reproduced with κ in the range of 5 - 8%.

The optimized calculations shown in figure 5.13 describe the experimental data (7×7 pixel array) very well in the angular range above $\sim 3.5°$. However, the model fails to reproduce the shoulder at 1.6°, which was already discussed in the context of the heat treatment in section 5.3.4. This feature is located in the region of total reflection, as the critical angle can be estimated to $1.94^\circ < \theta_c < 2.36^\circ$ using equation 3.22 with the respective crystal potentials. At the same position, Kawasuso *et al.* observed a more pronounced dip structure, which was essentially attributed to atomic-scale surface roughness [167, 193, 197]. Within our analysis, we found that the shoulder can be reproduced by a small fraction of bilayer graphene with a low occupation of 5 - 10%. This is shown in figure 5.14 a), where we included the bilayer occupation, its spacing to the substrate and the occupation of QFMLG as additional parameters in the optimization.[4] The R-factor decreases to 1.7%, which is below the threshold of 2% commonly defined for the correct structure in TRHEPD [196]. Moreover, as shown in figure 5.14 b), the experimental data extracted from an 11×11 pixel array can be fitted with an even lower R-factor of 1.5%. The parameter κ was set to a fixed value of 7%. The spacing d_{QFMLG} between QFMLG and the substrate obtained from both fits is almost identical, i.e. 4.21 Å and 4.18 Å, respectively.

The fit still deviates from both experimental data sets for very small glancing angles below 1°. In this angular range, the intensity decreases significantly and a precise measurement is sophisticated for geometrical reasons. On these grounds, we extracted the structural parameters from a fit restricted to 1 - 6.5°, i.e. the red curve shown in figure 5.14 c). The obtained parameters are listed in table 5.1 and the structure is schematically illustrated in figure 5.14 d). We emphasize that the calculated rocking curve is particularly sensitive to the parameter d_{QFMLG}. When we reduce the optimum value by e.g. only 0.18 Å, the shoulder at $\sim$4.6° changes to a distinct peak (compare figure 5.14 c) red and dashed blue curve). For this specific example, the R-factor would increase from 1.1% to 1.7% or, if all other parameters are readjusted, to at least 1.5%. The strong influence on the rocking curve thus allows us to determine d_{QFMLG} with highest precision. In fact, already with the first, simplified structural model (without bilayer occupation) and even for different κ, we obtain very consistent results: The fits shown in figure 5.13 yield e.g. values of d_{QFMLG} between 4.16 Å and 4.21 Å. Considering systematic errors as well, we thus estimate the uncertainty to be $\Delta d_{\mathrm{QFMLG}} = 0.06$ Å.

In contrast, the uncertainties of the other parameters are significantly higher. The TRHEPD signal generally tends to be more sensitive to heavier atoms, which is due to their increased atomic scattering factors [191, 224]. In agreement with

---

[4] We excluded the potential buckling of QFMLG as further parameter to prevent overfitting.

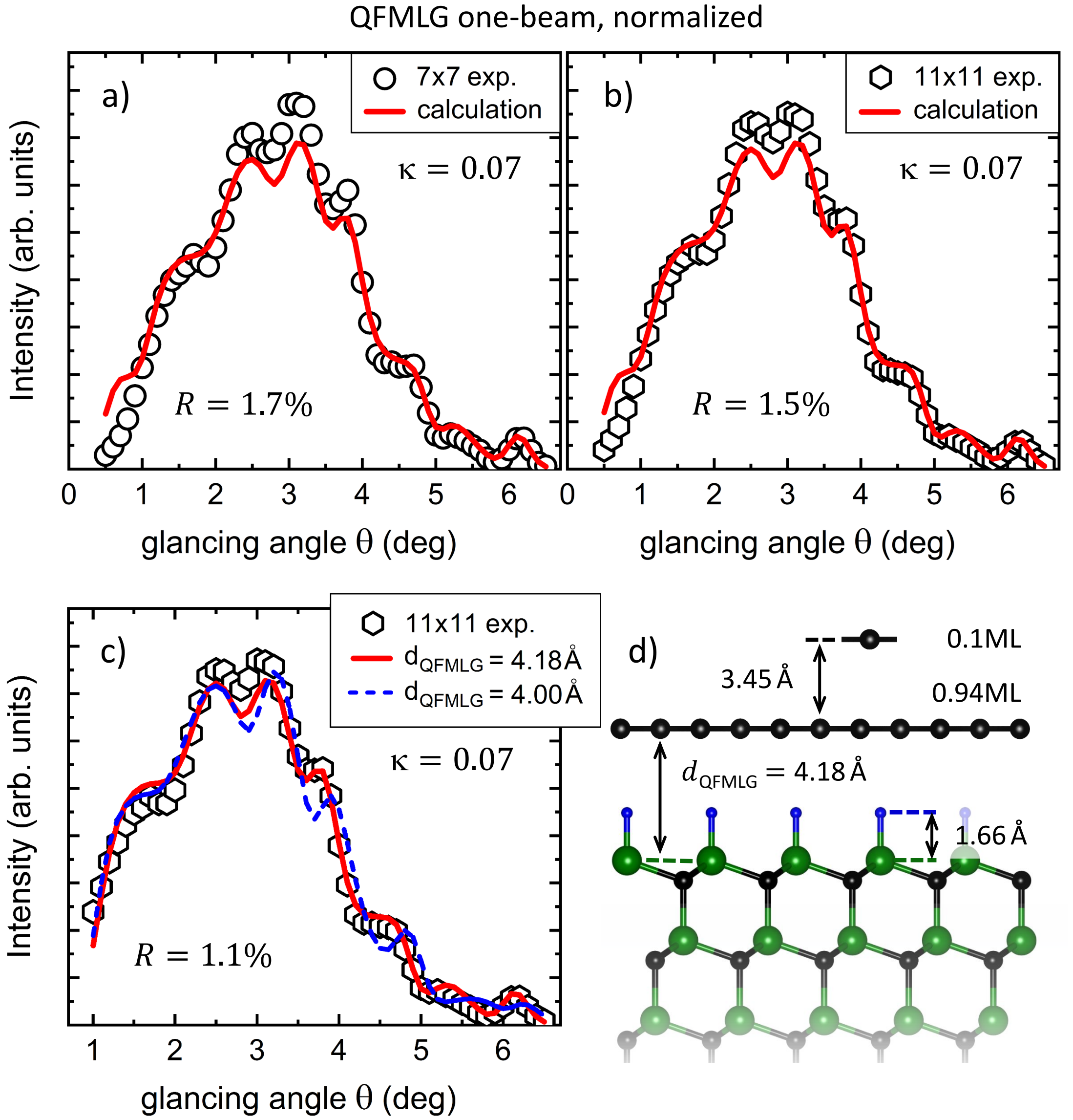

Figure 5.14. TRHEPD one-beam rocking curve analysis for QFMLG. Open symbols in a) and b) represent different experimental data, extracted from a 7×7 and an 11×11 sized pixel array, respectively. The calculation is based on the structure depicted in d), including six fit parameters, i.e. occupations and spacings of QFMLG and graphene bilayer, the spacing of the hydrogen atoms and the lattice relaxation of the top Si layer. The better agreement was obtained using the 11×11 data set, as evident by the lower R-factor of the fit in b). The structural parameters were extracted from the fit in c) (red curve), excluding the angular range below 1°. The fit is very sensitive to the spacing d_{QFMLG}: when detuned by 0.18 Å, the R-factor increases from 1.1% to 1.7% and the features change significantly (dashed blue curve).

bilayer fraction		QFMLG		hydrogen	top Si layer
occupation	d_{BL} (Å)	occupation	d_{QFMLG} (Å)	d_{H} (Å)	Δz_{Si} (Å)
9.8%	7.63 ± 0.20	93.9%	4.18 ± 0.06	1.66 ± 0.25	-0.01 ± 0.05

Table 5.1. Determined structural parameters of the QFMLG sample grown on 6H-SiC(0001). The values were extracted from the fit shown in figure 5.14 c) (red curve). The spacings d_{QFMLG}, d_{BL} and d_{H} are defined with respect to the position of the top Si layer (relaxed by Δz_{Si}). The uncertainties are based on the influence of the respective parameter on the fit, the differences when evaluating 7×7 and 11×11 rocking curves and the results for different imaginary crystal potentials of graphene. Systematic errors were considered as well.

this, we observe that the spacing of the hydrogen layer has very little effect on the rocking curve. Consequently, the uncertainty $\Delta d_{\mathrm{H}} \approx 0.25$ Å is relatively high and there are other measurement techniques that are better suited to precisely determine the Si-H bond length, such as IR spectroscopy. The literature value for the bond length of the $\mathrm{SiH_4}$ molecule is e.g. 1.48 Å [291], while DFT calculations yield 1.50 Å for the spacing of intercalated hydrogen bound to SiC(0001) [1]. These values are well within the estimated uncertainty range.

Since the occupation of bilayer graphene is rather low and the contribution is superimposed by other effects of surface roughness (e.g. step edges), the uncertainty of d_{BL} is estimated to be 0.20 Å. We emphasize that the calculation did not explicitly consider bilayer domains, but individual C atoms that are distributed over the surface. Together with the reduced occupation of the QFMLG layer, this can be interpreted as surface roughness that might, e.g. originate from a slightly uneven polymer coating during the sample preparation or intrinsic defects. The best fit was obtained for a bilayer spacing of 3.45 Å with respect to the QFMLG layer. This is only slightly larger than the interlayer spacing of graphite, which is roughly 3.35 Å [292].

Many-beam analysis

The calculation of the rocking curves along <11$\bar{2}$0> and <1$\bar{1}$00> (many-beam condition) is computationally much more demanding. In contrast to the one-beam analysis, we have to include several Fourier components in equations 3.28 and 3.29 to calculate the correct intensities of the (00) spot. Moreover, due to the incommensurate structure of QFMLG we must consider a very large unit cell that is almost commensurate with the SiC substrate. The stepped terrace structure of the surface (see section 5.2.3) leads to different stacking terminations of 6H-SiC(0001) [257, 282]. This has practically no effect in the one-beam analysis of QFMLG because the vertical spacings are the same for all stacking orders, but it must be considered in the many-beam analysis. Apart from these challenges, we emphasize that the in-plane coordinates of pristine graphene are already known precisely and since the interaction with the SiC substrate is relatively weak, we do not expect further insights on the structure. Given this backdrop, we used the many-beam data for a counter-check to verify the results obtained from the one-beam analysis.

The calculations were performed for fixed parameters, i.e. without using the Nelder-Mead algorithm. We tested the influence of different Fourier components and the final computation for <11$\bar{2}$0> and <1$\bar{1}$00> was done considering 15 and 33 components, respectively. Additionally, we checked the effect of a slight misalignment by $\Delta\varphi$, but this did not improve the fit. The comparison between calculated and experimental rocking curves is shown in figure 5.15. The overall agreement is good for both directions and we obtain R-factors of 1.8% and 1.7%, respectively. As already discussed for the one-beam data, the fit deviates for small glancing angles below 1° for experimental reasons (low intensity in combination with a broadening of the (00) spot on the screen). The shoulder at $\sim 1.6^\circ$ is well reproduced by the bilayer occupation that was determined before. Interestingly, the agreement in the angular range above $\sim 4^\circ$ is noticeably worse than for the one-beam data. This is most likely related to the presence of different stacking terminations of the SiC substrate, as associated with terrace steps of different heights. Since step bunching is less pronounced for graphene samples prepared by PASG [282], the TRHEPD signal from different (non-equivalent) stacking terminations is superposed. In the calculations, on the other hand, we only considered a specific stacking order due to computational constraints.

Altogether, the many-beam data support our results from the one-beam analysis. The presence of surface roughness associated with a small fraction of bilayer graphene and the determined graphene spacing d_{QFMLG} describe the experimentally observed features along <11$\bar{2}$0> and <1$\bar{1}$00> reasonably well. In particular, we can also confirm the adjustment made for the imaginary crystal potential of graphene (see figure 5.13). If we set $\kappa > 8\%$, the fit deteriorates noticeably for all data sets.

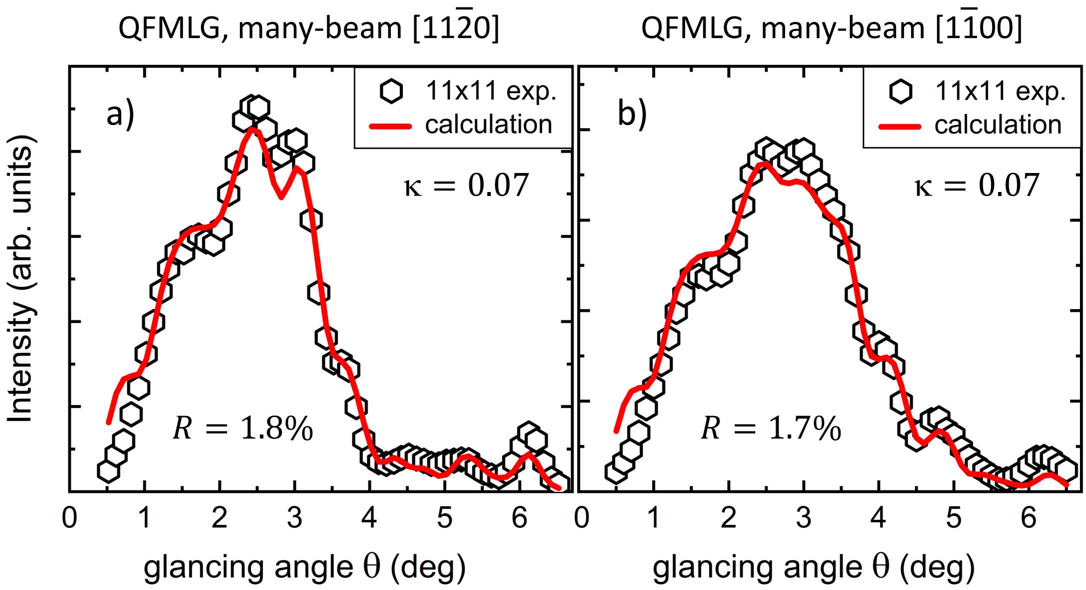

Figure 5.15. TRHEPD many-beam rocking curve analysis of QFMLG along a) <11$\bar{2}$0> and b) <1$\bar{1}$00>. The calculations were done for the structural parameters obtained from the one-beam analysis (see table 5.1) and the literature values for the in-plane coordinates of graphene and SiC [258].

Comparison with theoretical predictions and other studies

To facilitate DFT calculations, the large unit cell is often approximated by a reduced periodicity, e.g. $(\sqrt{3} \times \sqrt{3})\,R30°$ combined with a slight stretch of the graphene lattice constant. Following this approach, Markevich *et al.* [293] performed DFT calculations using the Local Density Approximation (LDA) for the exchange-correlation potential. For hydrogen intercalated QFMLG on 4H-SiC[5] they obtained a graphene spacing of 2.59 Å with respect to the hydrogen layer. Compared to our experimental value, this leads to a small discrepancy of approximately 0.1 Å when we account for the nominal Si-H bond length. More accurate DFT calculations were performed by Sforzini *et al.* [1], who considered the full $(6\sqrt{3} \times 6\sqrt{3})\,R30°$ supercell of QFMLG on 6H-SiC(0001). Within the Generalized Gradient Approximation (GGA) they used the Perdew-Burke-Ernzerhof (PBE) functional with a correction for van der Waals effects, which yields $d_{\mathrm{QFMLG,\,DFT}} = 4.16$ Å. Our experimental result of (4.18 ± 0.06) Å is in excellent agreement with this value. For the reduced $(\sqrt{3} \times \sqrt{3})\,R30°$ periodicity, Sforzini *et al.* also tested the influence of the exchange correlation functional.

---

[5] The influence of the SiC polytype on the calculation is small, i.e. in the range of 0.02 Å (compare supplementary material of ref. [1]).

When they apply a more sophisticated theory, i.e. using the Heyd-Scuseria-Ernzerhof (HSE) hybrid functional and incorporating many-body effects in the van der Waals correction, this only leads to a negligible difference of 0.01 Å.

To the best of our knowledge, there were two previous experimental studies to determine the spacing of QFMLG on 6H-SiC(0001). Sforzini *et al.* [1] applied the Normal Incidence X-ray Standing Wave (NIXSW) technique, i.e. combined dynamical X-ray diffraction and photoelectron spectroscopy. They found a spacing of $d_{\mathrm{QFMLG,Sfo}} = (4.22 \pm 0.06)$ Å, which is slightly larger than predicted by their DFT calculations and just overlaps within the uncertainty range. Moreover, we note that the obtained surface relaxation of the substrate layers is particularly large, which is not consistent with the calculation. Emery *et al.* [289] performed synchrotron-based high-resolution X-ray Reflectivity (XRR) measurements to investigate the structure of hydrogen intercalated few-layer graphene. Their analysis suggests that the bottom graphene layer is $4.22^{+0.06}_{-0.08}$ Å above the top Si layer of the substrate. Assuming a negligible effect of the additional graphene layers, both studies yield exactly the same value, most likely slightly overestimating the actual spacing. In contrast, the result obtained in our study agrees much better with the predicted value, highlighting the strength of TRHEPD rocking curve analysis.

5.3.6. Quantitative structure analysis of MLG

It is evident that the structure of MLG is more complex than that of QFMLG. Due to the covalent bonds with the substrate and the incommensurate structure, the buffer layer exhibits a long-range periodic corrugation that is superimposed by a local buckling [265, 294]. In fact, the precise atomic coordinates of the buffer layer are still unknown. Apart from that, we have to consider the buckling of the graphene and the substrate layers as well. The DFT calculations performed by Sforzini *et al.* [1] suggest that the interface may lead to a significant relaxation of the top three SiC bilayers. In conjunction with the large unit cell, this leads to a lot of free parameters, making the quantitative structure analysis of MLG rather challenging. Moreover, the recent study by Sinterhauf *et al.* [295] on the local sheet resistance of MLG implies that the different stacking terminations of 6H-SiC(0001) give rise to distinct vertical spacings between graphene layer and substrate.

Against this background, we restrict our study to the one-beam analysis to investigate the average spacing and buckling of graphene and buffer layer. For the calculations, we used the same crystal potentials of SiC and graphene as for QFMLG (with $\kappa = 7\%$). Analogous to before, we employed the Nelder-Mead algorithm to minimize the R-factor of the fit.

One-beam analysis

A general issue was the integration of bilayer graphene in the calculation. As already mentioned for QFMLG, the bilayer is included as overlayer with a small occupation, but not as individual (local) domains that are fully occupied. We tried to artificially realize the latter by performing calculations with 0% and 100% bilayer occupation, which are subsequently added proportionate to compose the signal. However, this approach would require that the actual bilayer fraction is known precisely, which was not the case. Furthermore, this does not allow to fully utilize the optimization algorithm. On these grounds, the only feasible approach was to treat the bilayer domains as an overlayer of individual C atoms, thereby compromising a possible systematic error.

Apart from this, a major difficulty was the large amount of parameters. Initially, we thus tested the influence of particular parameters on the fit, e.g. the buckling of individual layers or the relaxation of deeper substrate bilayers. Figure 5.16 a) shows the experimental 11×11 data set together with an initial and a converged calculation when buckling is completely neglected. The parameter space of the fit includes the spacings and occupations of mono- and bilayer graphene, as well as the spacings of the buffer layer and the top Si layer. The calculated rocking curves exhibit two peaks in the angular range above 4° that are much more pronounced than in the experimental data. This is plausible: the buckling present at the interface alters the regular periodicity perpendicular to the surface, thus decreasing the intensity of associated features, e.g. the third order Bragg reflection at $\sim 4.7^\circ$.

For the one-beam analysis, the average buckling of a certain layer can be included by splitting it into two (or more) sublayers that are vertically displaced by a small variable distance [196]. When we include the buckling of MLG, buffer layer and top Si layer as further parameters, the experimental data can be well fitted, as depicted in figure 5.16 b). To limit the parameter space and reduce the risk of overfitting, we did not consider the relaxation of deeper substrate

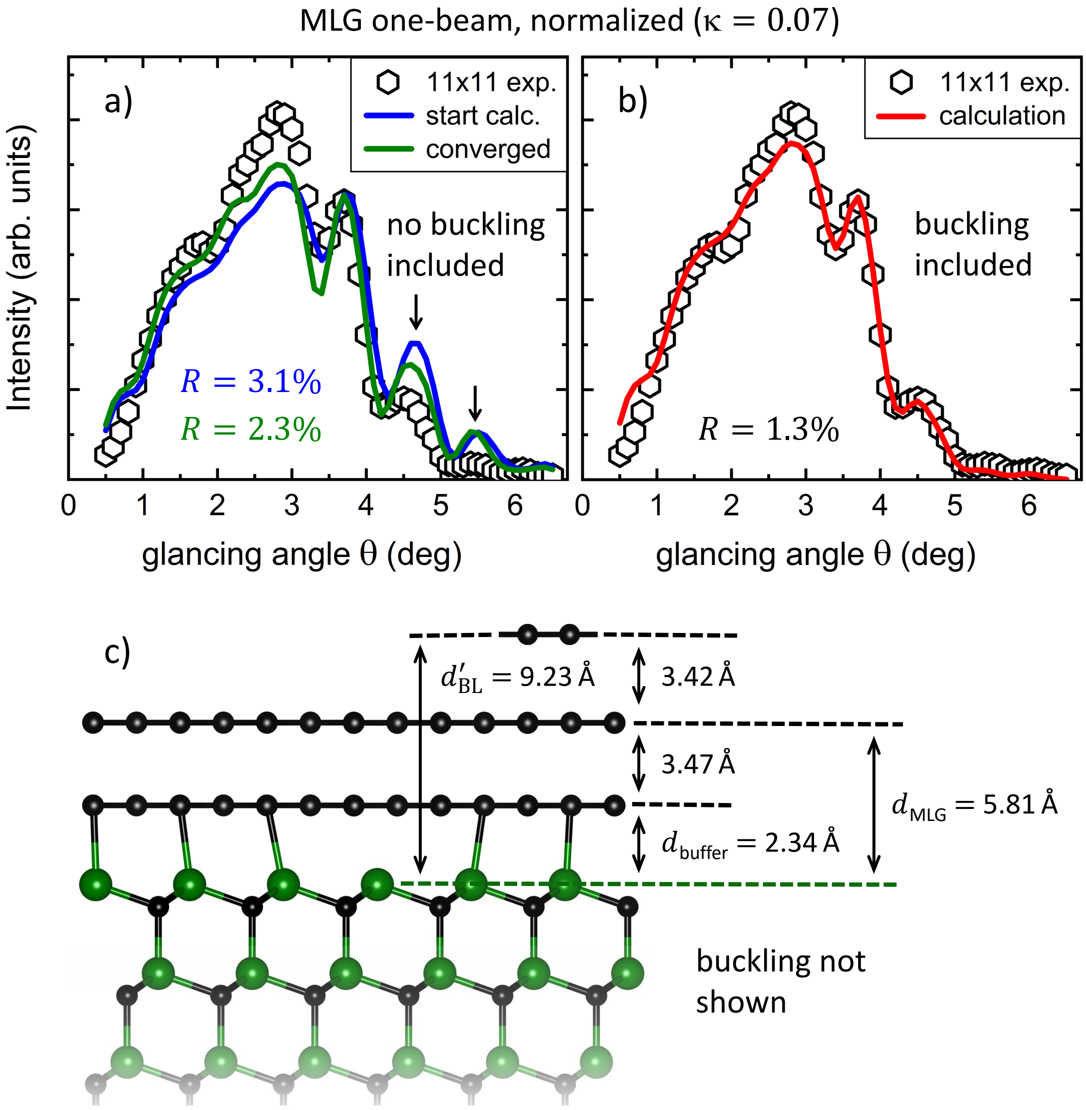

Figure 5.16. TRHEPD one-beam rocking curve analysis of MLG. The open hexagons represent the experimental data that has been extracted from an 11 × 11 sized pixel array (compare section 5.3.3). a) The calculations within a limited parameter space, where the buckling of individual layers has been neglected, particularly overestimate the intensity of the peaks in the angular range above 4° (see arrows). b) An excellent agreement with $R = 1.3\%$ was obtained when the buckling of MLG, buffer layer and top Si layer is included. The related structural parameters are listed in table 5.2 and the respective spacings are visualized in c) (buckling not shown).

layers. There are two considerations for this decision. Firstly, even above the critical angle TRHEPD is very surface sensitive, so that the overall contribution of deeper layers is small. Secondly, the experimental rocking curve is relatively flat above 5°, which makes it more difficult to fine-tune the fit in this range.

Altogether, we find that the TRHEPD rocking curve is not very sensitive to relaxations of the substrate and can thus already be well described when only adjusting the top Si layer. Given this context, the obtained parameters for the Si layer should however not be over-interpreted.

Figure 5.16 c) illustrates the individual layer spacings as obtained from the fit (buckling not shown). Additionally, the respective spacings are listed in table 5.2 together with the other structural parameters. We find that the bilayer occupation is a bit smaller than determined from the XPS characterization (see section 5.2.2), which is most likely related to the inaccurate treatment as overlayer. Besides that, it is worth mentioning that the gradient of the R-factor is very flat in the vicinity of the minimum. For example, when the R-factor increases only slightly from 1.2451% to 1.2458%, the obtained graphene and buffer layer spacings change by roughly 0.04 Å. For comparison and to get a better estimate of the uncertainty, we also evaluated the experimental 7×7 data set and the results from the fit are listed in table 5.2, too. As already observed for QFMLG, the R-factor is noticeably larger and the best fit only yields $R = 1.6\%$. However, the results for both data sets are very consistent, e.g. the respective graphene spacings d_{MLG} are 5.81 Å and 5.84 Å with respect to the top Si layer. Restricting the fit to the angular range above 1° yields similar results for both data sets as well. The stated uncertainties are based on these considerations and include systematic errors that may result from the experimental setup itself or the approximations made for the calculations, e.g. neglecting the relaxation of deeper substrate layers or not explicitly including bilayer domains.

Comparison with theory and other studies

The results obtained from the 11×11 data set were compared with DFT calculations performed by Sforzini *et al.* [1]. We find a very good agreement for the graphene and buffer layer spacings and the calculated values are well within the experimental uncertainty range of ± 0.08 Å (compare table 5.2). On the other hand, the determined buckling of both layers is significantly smaller than predicted by theory. This could be attributed to our simplified approach approximating the buckling by two vertically displaced sublayers. In contrast, Sforzini *et al.* defined the magnitude of buckling by the width of the calculated electron distribution. Interestingly, the results from other experimental studies also indicate a lower buckling, although the magnitude is very different [289, 294].

Parameter		TRHEPD		DFT	other experimental studies			
		7×7	11×11	PBE+vdW [1]	XSW-XPS [298]	XRR [289]	PED [294]	NIXSW [297]
bilayer	occupation	8.4%	7.8%	-	45%	48%	-	-
	d'_{BL} (Å)	9.24	9.23 ± 0.20	-	9.16	9.17	-	-
MLG	occupation	100%	99.6%	-	86%	100%	-	-
	d_{MLG} (Å)	5.84	5.81 ± 0.08	5.76	5.82	5.75	5.91	5.67
	buckling (Å)	0.32	0.31	0.45	0.21	0.15	0	-
buffer layer	d_{buffer} (Å)	2.38	2.34 ± 0.08	2.36	$2.32^{\star}$	$2.36^{\star}$	2.16	2.37
	buckling (Å)	0.38	0.42	0.86	$0.7^{\star}$	$0.5^{\star}$	0.09	-
top Si layer substrate	$\Delta z'_{\mathrm{Si}}$ (Å)	0.02	-0.01	-0.06	-0.05 ± 0.05	-	-0.05	0
	buckling (Å)	0.25	0.21	0.78	0.3 ± 0.1	-	-	-

Table 5.2. Structural parameters obtained from TRHEPD measurements on MLG grown on 6H-SiC(0001) compared with DFT calculations and results from other analysis techniques. The spacings d'_{BL}, d_{MLG} and d_{buffer} are defined with respect to the top Si layer (relaxed by $\Delta z'_{\mathrm{Si}}$), as shown in figure 5.16 c). The fits of the 7×7 and 11×11 data sets yield R-factors of 1.6% and 1.3%, respectively. Since the R-factor is lower for the 11×11 data, the estimated uncertainties are listed with the final results of our TRHEPD analysis in the corresponding column. The determined layer spacings are in good agreement with DFT calculations by Sforzini *et al.* and the results from different synchrotron-based techniques, although the buckling is significantly smaller than predicted by theory. Emery *et al.* [289, 298] fitted the buffer layer by two separate components S_1 and S_2 (compare section 5.2.2). Therefore, we calculated the spacing d_{buffer} as weighted mean value from both components and the buckling from the respective distribution widths (indicated by $\star$).

Previous studies on the MLG interlayer spacing were based on synchrotron-related measurement techniques such as SXRD [296], NIXSW [297], X-ray Standing Wave (XSW) [298], XRR [289, 299] or Photoelectron Diffraction (PED) [294]. The XRR study by Emery *et al.* [289] yields layer spacings that are almost identical to the theoretical values, although they actually measured on few-layer graphene and they fitted the data by considering the contribution of five layers. Moreover, in the preceding work they found slightly different values using XSW-excited XPS in conjunction with XRR [298]. In their first study they further observed that the top Si layer of the substrate was depleted by 15%, which was attributed to a growth artifact from Si sublimation. In contrast, Conrad *et al.* [299], who observed a slightly larger depletion, raised the question whether the top Si layer of the substrate is bulk-terminated or reconstructed. However, without specific structural model and due to the high surface sensitivity of TRHEPD, we did not investigate this further. It could thus be interesting to analyze the structure of the buffer layer itself without additional graphene layer on top in a subsequent study. To cope with the large amount of parameters and evaluate the many-beam data as well, it would be vital to perform rocking curve analysis on a supercomputer allowing a global search, as suggested by Hoshi *et al.* [191]. Additionally, more theoretical work on the interface structure would be necessary to clarify whether the top Si layer is reconstructed or not.

6 Chapter 6.

Conclusion and outlook

In the framework of this thesis, we designed and set up a new positron diffractometer at the high-intensity positron source NEPOMUC and adapted the beam to enable diffraction experiments in grazing incidence. In addition, we determined the interlayer spacings of Monolayer Graphene (MLG) and hydrogen intercalated Quasi-Free-Standing Monolayer Graphene (QFMLG) grown on 6H-SiC(0001) using Total-Reflection High-Energy Positron Diffraction (TRHEPD) for the first time. In the following, the main results of the instrumentation and the TRHEPD measurements are summarized separately including a brief outlook.

Instrumentation at NEPOMUC

Based on the Japanese pioneering work [18, 167, 170], we have developed a new positron diffractometer tailored to the distinct experimental conditions at NEPOMUC. When compared with the LINAC-based setup at the SPF in Japan, the diffractometer at NEPOMUC benefits from the continuous positron beam of larger (yet to be quantified) intensity. This is a major advantage, since it will reduce the measurement time considerably or allow the resolution of weaker diffraction spots. On the other hand, the TRHEPD setup at NEPOMUC required a more sophisticated instrumentation. This comprises the possibility to apply voltages of several kV on the sample stage and the MCP detector, which are connected to a Faraday cage necessary to preserve the electrostatic potential after acceleration to the final positron beam energy.

The instrument was set up in the experimental hall of the FRM II and connected to the SuSpect beamline, which was redesigned downstream the central beam switch. In order to enhance the brightness and coherence length of the remoderated NEPOMUC beam after the adiabatic transport in the beamline, we developed an optional transmission-type remoderator stage that can be inserted into the beam path. The remoderator, a 100 nm thin Ni(100) foil, can be conditioned in-situ in a separate section of the UHV chamber using a dedicated radiation heater. For the acceleration and optics of the positron beam, we have developed an electrostatic lens system that consists of 18 electrodes and allows beam energies of up to 20 keV. The geometry of the lens system was optimized in an iterative process by comprehensive simulations of the positron trajectories to obtain a parallel positron beam of small diameter. For this, we considered both, the remoderated and the twofold remoderated beam, as well as different beam energies.

The new TRHEPD setup allows sample alignment with respect to the incident positron beam by a customized fine-positioning system along five axes, contactless sample heating up to 1000 °C using an IR laser and pre-characterization with an integrated RHEED system. The UHV chamber has a base pressure of less than $2 \cdot 10^{-9}$ mbar and we expect to reach a final pressure of at least $5 \cdot 10^{-10}$ mbar after bake-out.

During a first beamtime, we fine-tuned the lens system and characterized the direct positron beam with and without additional remoderation. For the twofold remoderated beam of 10 keV energy, we achieved a beam diameter of less than 1.3 mm at FWHM, which agrees well with the simulation. Altogether, we thus demonstrated that the beam properties are well suited for positron diffraction experiments. Unexpected technical problems of the research reactor FRM II and its long downtime, however, prevented us from recording first diffraction patterns. This has to be done subsequently to this work to benchmark the new instrument.

In the future, we further plan to move the TRHEPD experiment to the Neutron Guide Hall East where it will be integrated in the instrument SuSpect. This will provide a unique experimental station that enables structural and chemical surface analysis using positrons in combination with conventional techniques. In addition, SuSpect allows in-situ sample preparation and layer growth [40, 300].

TRHEPD study of MLG and hydrogen intercalated QFMLG

To investigate the surface structure of MLG and hydrogen intercalated QFMLG epitaxially grown on 6H-SiC(0001), we conducted TRHEPD measurements at the SPF in Japan. The samples were comprehensively pre-characterized by XPS, AFM, LEED and RHEED to evaluate the quality and exclude the presence of surface contaminations. To condition the graphene samples after exposure to air, adsorbates can be removed efficiently by in-situ annealing at 500°C, which was explicitly confirmed by TRHEPD measurements. Furthermore, for

QFMLG, we find no indication of hydrogen desorption, even when increasing the annealing temperature up to 650°C, which is consistent with the observations from Riedl *et al.* [267].

For a glancing angle of $\theta = 5.5^\circ$, we observed several diffraction spots and also identified faint Kikuchi lines, which are much less pronounced than in RHEED. Although only the zeroth order Laue zone was resolved for QFMLG, we find at least nine diffraction spots along <11$\bar{2}$0> and three along <1$\bar{1}$00>. The individual diffraction spots were assigned to graphene, SiC or higher order spots that stem from multiple diffraction on both lattices. In contrast to LEED or RHEED, the graphene spots in the TRHEPD patterns are much brighter than those associated with SiC, which is explained by the greater surface sensitivity of positrons. For MLG, we also resolved the $-1/6^{\text{th}}$ and $1/6^{\text{th}}$ order Laue zones and identified at least 27 diffraction spots along <11$\bar{2}$0> and three along <1$\bar{1}$00>. The additional spots have been attributed to the buffer layer present in MLG, even though the intensity of most spots is enhanced by multiple diffraction.

For the quantitative analysis, we extracted the beam intensities of the specular spot from the TRHEPD patterns to obtain the experimental rocking curves, which were compared with the curves calculated from the respective structure models. The numerical calculations were based on the full dynamical diffraction theory and we employed the Nelder-Mead algorithm to minimize the R-factor of the fit. It was found that the experimental rocking curves exhibit a characteristic shoulder at $\theta = 1.6^\circ$, which could be well reproduced by including a small fraction of bilayer graphene in the model. In combination with the reduced occupation of the graphene layer, this can also be interpreted as surface roughness that might stem from the sample preparation or intrinsic defects. Under the one-beam condition, the rocking curve of QFMLG is particularly sensitive to the spacing between the graphene layer and the SiC substrate, which was determined to be $d_{\text{QFMLG}} = (4.18 \pm 0.06)\,\text{Å}$. This value is in excellent agreement with DFT calculations by Sforzini *et al.*, yielding $d_{\text{QFMLG, DFT}} = 4.16\,\text{Å}$ [1]. Moreover, we emphasize that previous experimental studies showed a worse agreement, i.e. a slight overestimation of the graphene spacing.

The parameter space for fitting the rocking curve of MLG is significantly larger than for QFMLG, which is due to the presence of the buffer layer and the associated buckling. In this context, it was found that the relaxation of deeper substrate layers can be neglected for the TRHEPD analysis because the overall contribution is sufficiently small. The best fit of MLG was obtained by including nine parameters, yielding average graphene and buffer layer spacings of $d_{\mathrm{MLG}} = (5.81 \pm 0.08)\,\text{Å}$ and $d_{\mathrm{buffer}} = (2.34 \pm 0.08)\,\text{Å}$ with respect to the top Si layer of the substrate. These values are in good agreement with the results from DFT calculations and complementary experimental studies. However, the magnitude of buckling was found to be significantly smaller than predicted by theory. Qualitatively, other experimental studies suggest a reduced buckling of MLG as well, although the magnitude varies greatly among different measurement techniques.

To be more sensitive to the structure at the SiC interface, it could be interesting to perform subsequent TRHEPD measurements on samples with a bare buffer layer. Moreover, to cope with the large amount of parameters and enable a global search, the rocking curve analysis should be carried out on a supercomputer, as already suggested by Hoshi *et al.* [191]. This would also facilitate the evaluation of the many-beam data, which can yield valuable information, e.g. about the stacking order.

A Appendix A.

Appendix

A.1. Geometrical correction for TRHEPD rocking curve analysis

For TRHEPD rocking curve analysis, it is crucial to consider the fraction of the beam intensity that illuminates the sample. An ideal, circularly shaped beam leads to an elliptical spot that is usually much longer than the sample, as discussed in section 4.2.1. When we increase the glancing angle θ, the eccentricity of the elliptical spot decreases and a larger fraction of the beam contributes to the diffraction pattern. In the following, we want to estimate this fraction.

A.1.1. Initial approach

In a first approach, we include several simplifications and assume that:

(i) the intensity within the FWHM of the beam diameter is constant, i.e. we neglect the intensity distribution,

(ii) the beam shape is perfectly circular and

(iii) the beam diameter d is sufficiently large, i.e. $d \gg L \sin\theta$, where L is the dimension of the sample in beam direction.

In this case, the complete beam intensity distributes over an elliptical area

$$A_{tot} = \pi ab = \frac{\pi d^2}{4 \sin\theta}\,, \tag{A.1}$$

where we used equation 4.3 to substitute the semi-major axis a. As we assume that $d \gg L \sin\theta$, the beam spot on the sample can be approximated as a rectangular stripe with area

$$A_{rec} = dL\,. \tag{A.2}$$

The fraction of the beam intensity that illuminates the sample is therefore

$$\eta = \frac{A_{rec}}{A_{tot}} = \frac{4L\sin\theta}{\pi d}\,. \tag{A.3}$$

As d and L are constant, the geometrical correction can be realized by scaling the experimental rocking curve with $1/\sin\theta$.

A.1.2. Small beam diameter

Let us now consider the effect of a reduced beam diameter, for which equation A.2 is not a good approximation. This situation is illustrated in figure A.1, where the elliptical spot is just slightly larger than the sample. The illuminated area of the sample can be calculated as

$$A_{ill} = 4\int\limits_0^{L/2} y(x)\,\mathrm{d}x = 2d\int\limits_0^{L/2}\sqrt{1-\frac{4x^2}{d^2}\sin^2\theta}\;\mathrm{d}x, \tag{A.4}$$

where $y(x)$ is the parametrization of the ellipsis, which is

$$\frac{4y^2}{d^2}+\frac{4x^2}{d^2}\sin\theta^2 = 1 \implies y = {\scriptstyle(}\pm{\scriptstyle)}\,\frac{d}{2}\sqrt{1-\frac{4x^2}{d^2}\sin^2\theta}\,. \tag{A.5}$$

To solve the integral in equation A.4, we can substitute

$$\sin\zeta = \frac{2x\sin\theta}{d} \tag{A.6}$$

which yields

$$A_{ill} = \frac{d^2}{\sin\theta}\int\limits_0^{u}\cos^2\zeta\,\mathrm{d}\zeta, \tag{A.7}$$

with the upper integration limit

$$u = \arcsin\left(\frac{L\sin\theta}{d}\right). \tag{A.8}$$

The integration of equation A.7 is straightforward, e.g. by using the trigonometric formula $2\cos^2 x = 1+\cos 2x$, and after simplification we obtain

$$A_{ill} = \frac{d^2}{2\sin\theta}\left[\arcsin\left(\frac{L\sin\theta}{d}\right)+\frac{L\sin\theta}{d}\cdot\sqrt{1-\left(\frac{L\sin\theta}{d}\right)^2}\,\right]. \tag{A.9}$$

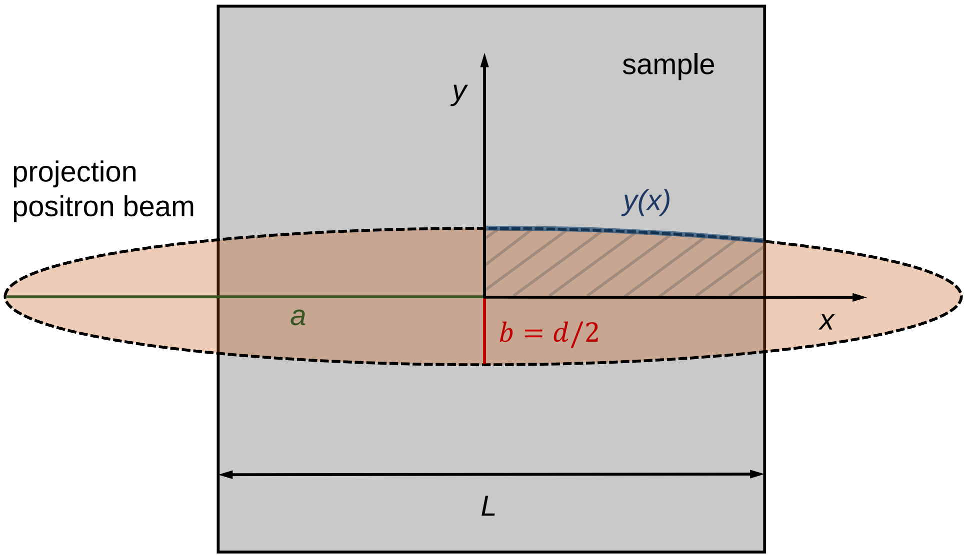

Figure A.1. Illumination of the sample by the positron beam (top view). The area can be divided into four equal quadrants, one shaded in gray, which are calculated by integration of the elliptical function $y(x)$.

To counter-check this result, we can consider the limit $d \gg L\sin\theta$ to approximate equation A.9. This allows to Taylor expand arcsine and neglect higher orders, i.e. $\arcsin(x) = x + \mathcal{O}(x^3)$ [301]. Moreover, we can also neglect the quadratic correction underneath the square root. These two approximations lead to the same expression we found earlier (equation A.2), which validates our result. Analogous to equation A.3, we find

$$\eta' = \frac{A_{ill}}{A_{tot}} = \frac{2}{\pi}\left[\arcsin\left(\frac{L\sin\theta}{d}\right) + \frac{L\sin\theta}{d}\cdot\sqrt{1-\left(\frac{L\sin\theta}{d}\right)^2}\right]. \tag{A.10}$$

We can utilize the equations A.9 and A.10 to estimate the error of the initial approximation and to evaluate in which range it is meaningful. For a sample size of $L = 10\,\text{mm}$ and a beam diameter of $d = 2\,\text{mm}$, the corrections are rather small, as displayed in figure A.2 a) and b). Even for $\theta = 6°$, the beam spot is roughly twice as long as the sample and the deviation from the rectangular approximation is less than 5%. In contrast, for a beam diameter of $d = 1\,\text{mm}$, the approximation is not valid anymore, as shown in figure A.2 c) and d). The deviation is obvious and for $\theta = 6°$, the beam spot is completely on the sample (assuming no intensity outside the FWHM). For the intermediate range, we could apply equation A.10 for correction, but this is not ideal as we didn't consider the intensity distribution of the beam.

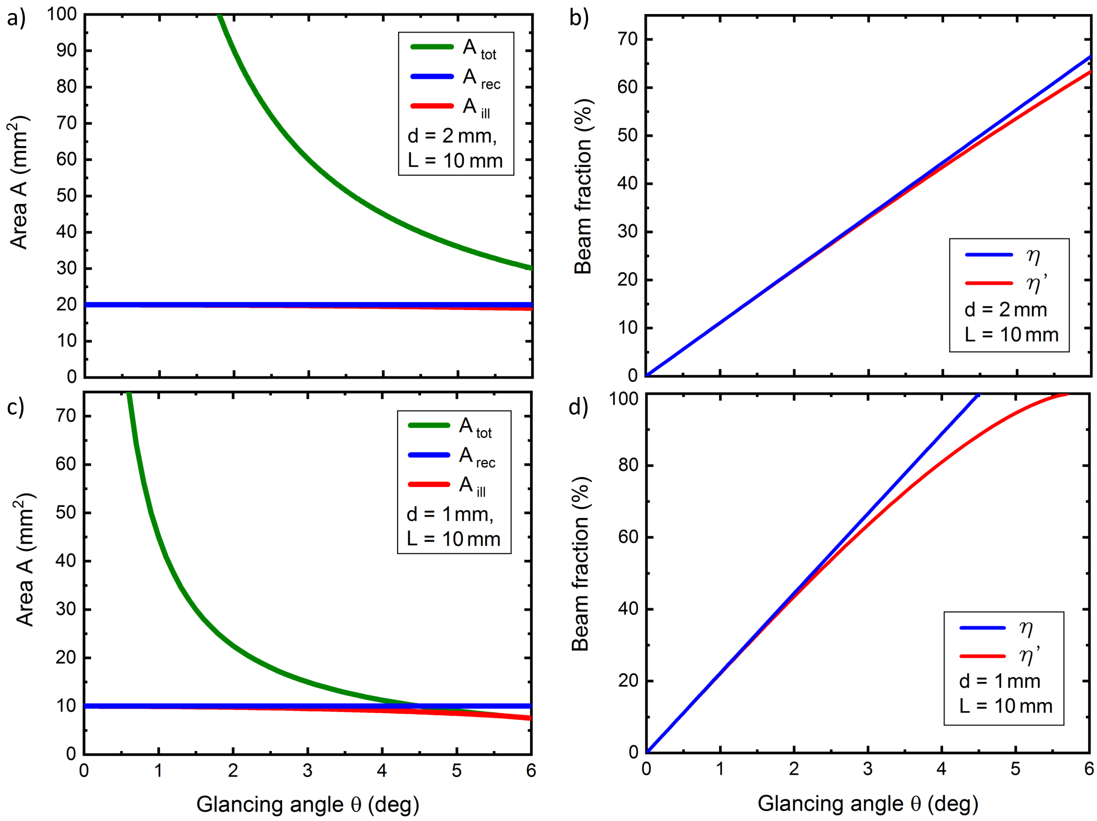

Figure A.2. Sample illumination for different beam diameter. a) For $d = 2\,\mathrm{mm}$, the difference between A_{rec} and A_{ill} is only marginal. b) Smaller deviations of the ratios $\eta = A_{rec}/A_{tot}$ and $\eta' = A_{ill}/A_{tot}$ can be observed for $\theta > 3^\circ$ and less than 70% of the beam intensity (within the FWHM) contributes to the diffraction pattern. c), d) For $d = 1\,\mathrm{mm}$, we have to account for the elliptical shape of the beam spot. In the case of large glancing angles, the entire beam would contribute to the diffraction pattern, which complicates the geometrical correction for rocking curve analysis.

A.1.3. Gaussian intensity distribution

The intensity profile of the positron beam could be assumed as Gaussian distribution

$$\rho(x,y) = \frac{I_{tot}}{2\pi\,\sigma_x\sigma_y}\exp\left(-\frac{x^2}{2\,\sigma_x^2} - \frac{y^2}{2\,\sigma_y^2}\right), \tag{A.11}$$

where σ_x and σ_y are the standard deviations in x and y direction and

$$I_{tot} := \int\limits_{-\infty}^{\infty}\int\limits_{-\infty}^{\infty}\rho(x,y)\,\mathrm{d}x\,\mathrm{d}y. \tag{A.12}$$

For a circularly shaped beam in grazing incidence, the intensity distribution in the sample plane is elongated along the x direction, which can be described as

$$\sigma = \sigma_y = \sin\theta\, \sigma_x. \tag{A.13}$$

The standard deviation is related to the FWHM of the beam diameter by

$$\sigma = \frac{d}{2\sqrt{2\,\ln 2}}. \tag{A.14}$$

We can calculate the intensity that illuminates the sample as

$$I_{ill} = 4 \int\limits_0^{L/2} \int\limits_0^{L/2} \rho(x,y)\, \mathrm{d}x\, \mathrm{d}y = \frac{2\, I_{tot} \sin\theta}{\pi\sigma^2} \int\limits_0^{L/2} e^{-\frac{y^2}{2\sigma^2}}\, \mathrm{d}y \int\limits_0^{L/2} e^{-\frac{x^2 \sin^2\theta}{2\sigma^2}}\, \mathrm{d}x. \tag{A.15}$$

In the following, we utilize the error function [302]

$$\mathrm{erf}(x) = \frac{2}{\sqrt{\pi}} \int\limits_0^x e^{-t^2}\, \mathrm{d}t \tag{A.16}$$

and after the change of variables in both integrals we find

$$I_{ill} = I_{tot} \cdot \mathrm{erf}\left(\frac{L}{2\sqrt{2}\,\sigma}\right)\, \mathrm{erf}\left(\frac{L\sin\theta}{2\sqrt{2}\,\sigma}\right). \tag{A.17}$$

Furthermore, we can use equation A.14 to replace σ, which leads to

$$\eta'' = \frac{I_{ill}}{I_{tot}} = \mathrm{erf}\left(\sqrt{\ln 2}\, \frac{L}{d}\right)\, \mathrm{erf}\left(\sqrt{\ln 2}\, \frac{L}{d}\, \sin\theta\right). \tag{A.18}$$

Note that only the second error function in equation A.18 is relevant for the geometrical correction, as it depends on the glancing angle θ. Moreover, for $L = 10\,\mathrm{mm}$ and a typical beam diameter of $d < 4\,\mathrm{mm}$, the argument of the first error function is large, so that it can be approximated as 1. Due to the additional factor $\sin\theta$, the argument of the second error function is much smaller and the calculation has to be done numerically, using the series expansion [302]

$$\mathrm{erf}(x) = \frac{2}{\sqrt{\pi}} \sum_{n=0}^{\infty} \frac{(-1)^n}{(2n+1)\, n!}\, x^{2n+1}. \tag{A.19}$$

In agreement with the previous considerations, we find that the leading term ($n = 0$) is proportional to $\sin\theta$. Figure A.3 confirms that the linear approximation of $\mathrm{erf}(x)$ is valid for small arguments, i.e. when d is sufficiently large. When d is small, equation A.18 can be used for the geometrical correction. In practice, this is however rather inconvenient as it requires the precise determination of the beam diameter at the sample position and deviations from an ideal Gaussian distribution can cause systematic errors.

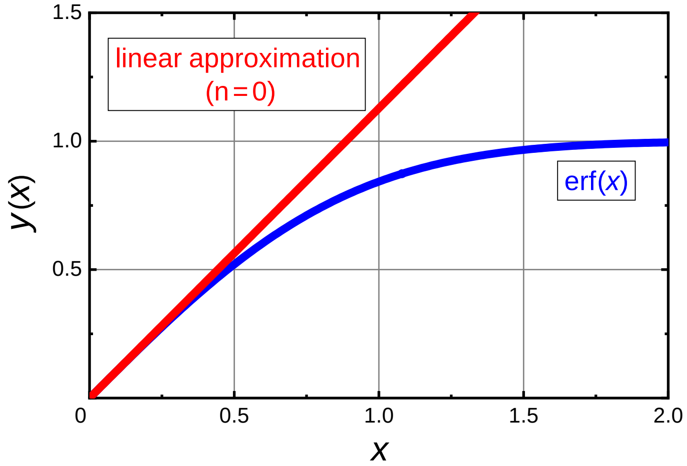

Figure A.3. Linear approximation of the error function considering only the zeroth order ($n = 0$) of equation A.19.

A.1.4. Beam shape

During experiments, the intensity distribution might be asymmetric, e.g. the positron beam could have an elliptical shape (compare section 4.6). For a correct description, we would need to adjust equation A.11 and recalculate the intensity that illuminates the sample, which is not feasible for arbitrary beam shapes. Small distortions can be caused during non-ideal transport in the beamline and are particularly relevant if the beam is not remoderated afterwards. However, in this case, the beam spot is relatively large. Therefore, slight distortions have no significant influence on the geometrical correction, because the beam is extremely elongated in beam direction.

A.2. Initial and final experimental setup

A.2.1. Test setup and relocation to the FRM II

Initially, the experimental setup has been assembled in our laboratory at the Max-Planck-Institute for Plasma Physics (IPP) in Garching, where we can perform tests outside the radiation protected area. Here, we also checked the functionality of commercial components, e.g. regarding HV stability, vacuum compatibility or other specifications. Two photos of the test setup are shown in figure A.4. After the successful commissioning of all commercial components including the RHEED gun and the positioning system, the setup has been relocated to the NEPOMUC platform at the research reactor FRM II. Since the heavy-duty crane in the experimental hall was out of service for several months in 2019/20, it was necessary to move the UHV chamber by a manual pulley, as depicted in figure A.5 c) and d).

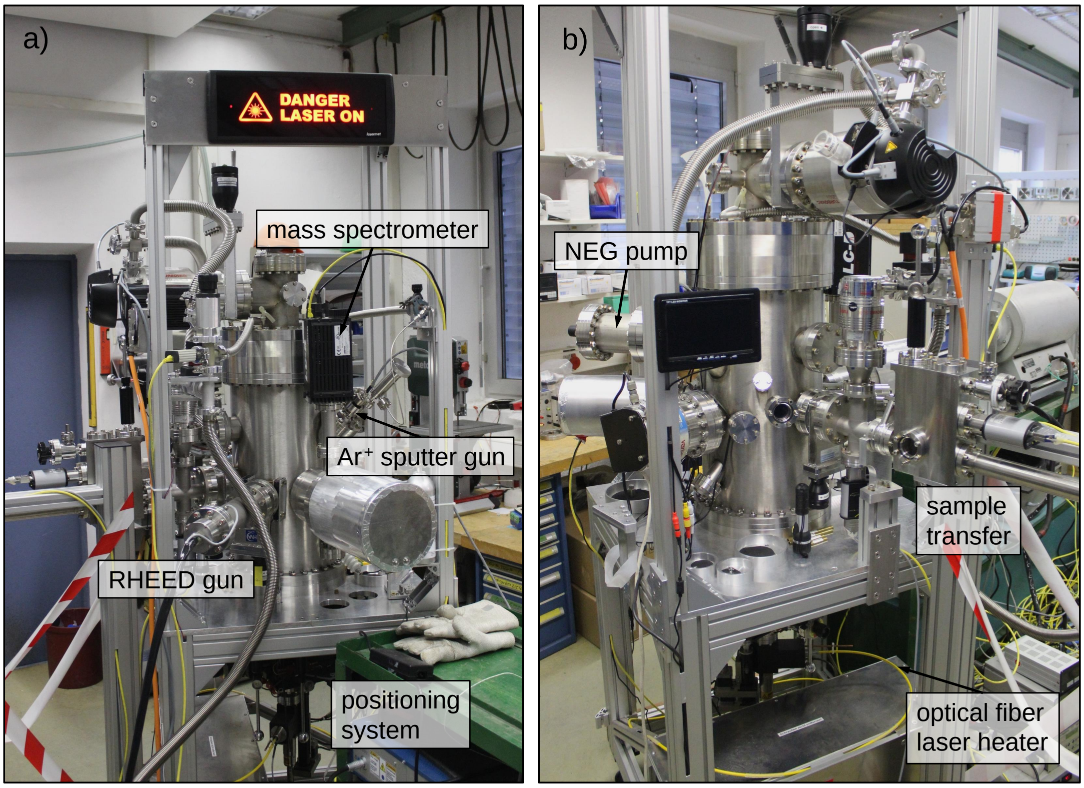

Figure A.4. First setup to test commercial and self-constructed components outside the radiation protected area of the FRM II. The main elements are labeled.

Figure A.5. Relocation of the TRHEPD setup to the NEPOMUC platform. a), b) Transportation of the main vacuum chamber to the FRM II. c), d) In the experimental hall, a manual pulley was used to lift the setup over the existing experiments because the heavy-duty crane was out of service.

A.2.2. TRHEPD setup at NEPOMUC

All components related to the positron beam, e.g. the remoderator or the electrostatic lens system, were assembled and tested with the final setup at NEPOMUC. Figure A.6 shows the TRHEPD experiment that is connected to the SuSpect beamline. Two walls of lead panels and bricks are used to shield the γ-radiation that stems from annihilation events at the remoderator and the MCP.

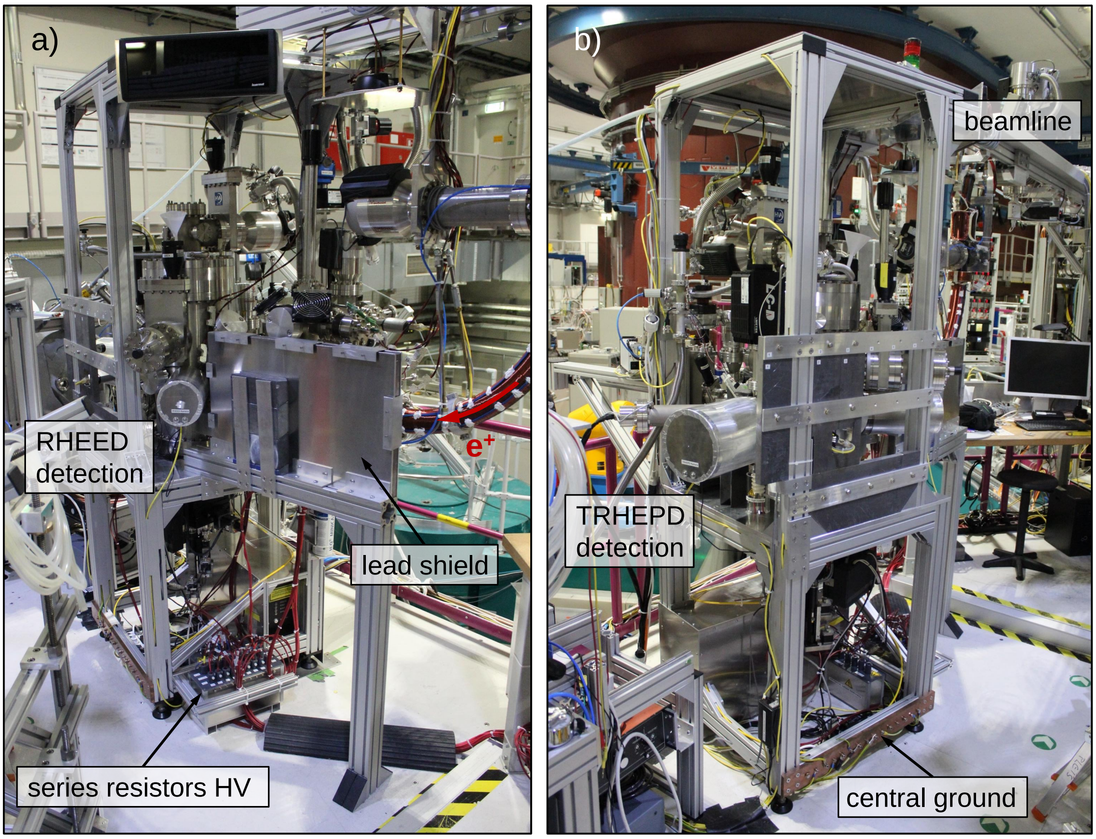

Figure A.6. TRHEPD setup at the NEPOMUC platform in the experimental hall of the FRM II. The experiment is connected to the SuSpect beamline.

A.3. High voltage stability

The HV stability of the setup is essential for operation. In this regard, the fixed geometry of the UHV chamber was a major challenge, as it restricts the design, e.g. limits the space for insulation. HV flashovers in vacuum can be identified with the pressure gauges, which is based on the instantaneous increase of pressure after a spark due to local evaporation. Firstly, we only tested the Faraday cage with and without installed positioning system and for voltages of up to 30 kV. During these tests, it was found that the amount of flashovers significantly increases when the positioning system is moved to a specific side. As depicted in figure A.7 a), flashovers occurred in bunches and on a sub-minute timescale. This was caused by charging of a Kevlar rope, as revealed in figure A.7 b). This issue could be solved by replacing the Kevlar rope by a ceramic rod (upper part) combined with a steel rope (lower part). Figure A.7 c) shows the experimental data (pressure, voltage and leak current) subsequently to the modification and further improvements. After conditioning, flashovers occur occasionally on a time-scale of several hours, which might be acceptable. Another problem is however the fluctuating leak current of roughly 1.5 μA. This leads to a local heat input and thus unnecessarily increases the pressure. Leak currents were only observed for voltages above 26 kV.

Further tests were conducted in the experimental hall, after including the electrostatic system for positron acceleration and beam optics. We emphasize that the geometry of the Macor insulators is optimized, e.g. we maximized the creepage distance and rounded all edges [303]. Furthermore, all ceramic insulators were cleaned in an ultrasonic bath with organic solvents, sodium hydroxide (NaOH) and deionized water to remove grease, metallic contamination and dust. Initial problems related to the wiring on the vacuum side could be solved and the assembly was successfully tested up to 23 kV. In a last step we installed the MCP, which can be easily damaged by HV flashovers. Therefore, the complete system was only tested up to 20 kV, where a stable operation without leak currents is possible.

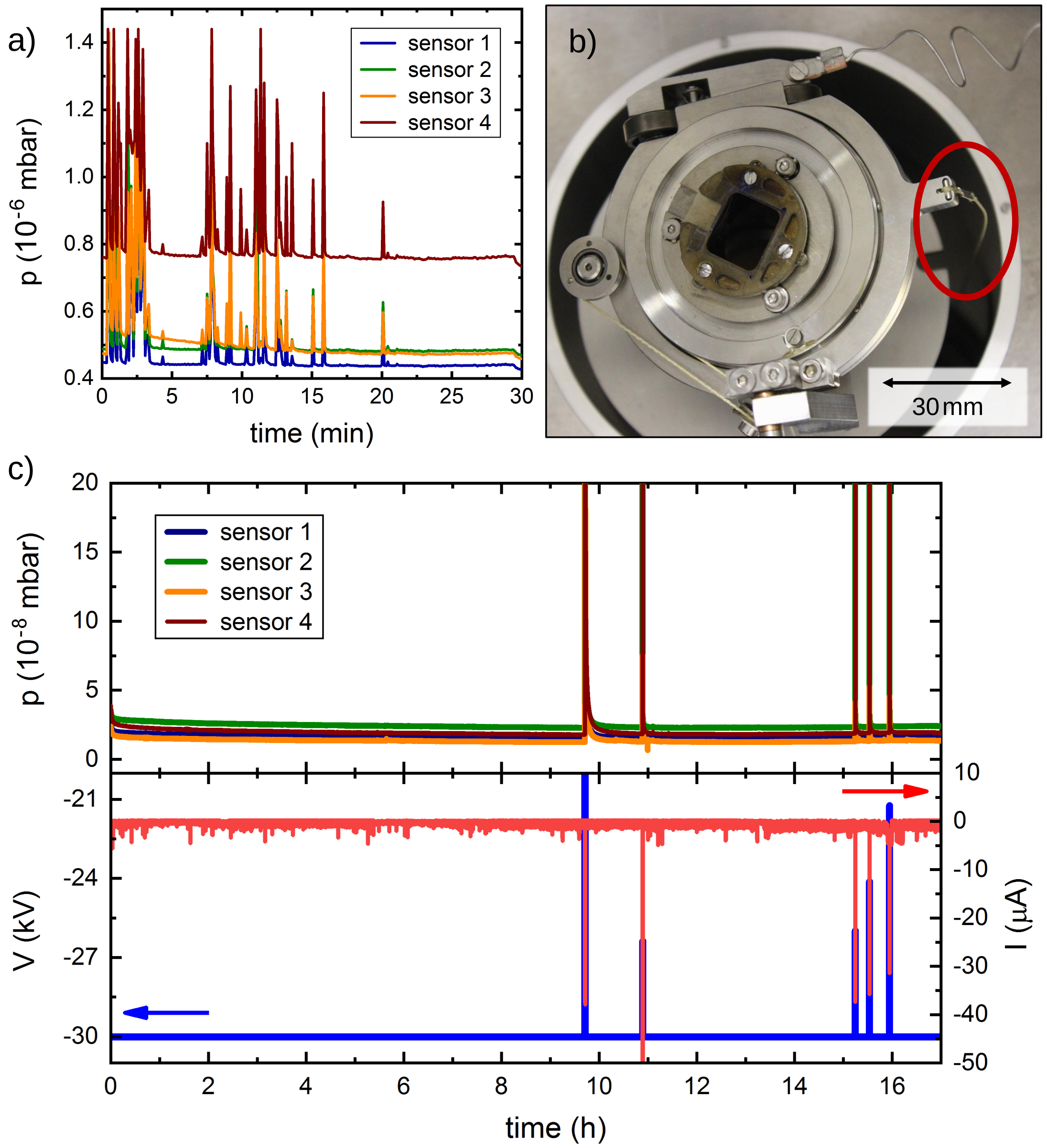

Figure A.7. Testing the HV stability of the positioning system and the Faraday cage. a) When the sample stage is located in a specific side position, the system exhibits many HV flashovers (substantially more then in the middle). b) This was related to the charging of a Kevlar rope that bent towards the side (red circle). c) After the modification, the amount of HV flashovers is significantly reduced. However, one issue remained: the leak current of approximately 1.5 μA at 30 kV.

A.4. Determination of the positioning accuracy

To enable precise TRHEPD measurements, the accuracy of tilt (rocking curves) and rotation axis (azimuthal plots) is crucial. Therefore, we extensively tested the positioning system prior to the final assembly.

A.4.1. First tests (atmosphere)

First tests were performed under atmospheric conditions, i.e. before the positioning system was connected with the UHV chamber. The experimental setup to investigate the accuracy and repeatability of the rotation axis is shown in figure A.8 a) and b). A Si wafer is mounted to an angle piece to serve as a mirror that reflects the red light from a laser pointer. A similar setup with different mirror geometry was used to test the tilt motion as well. When the sample stage is rotated by a small angle $\Delta\theta$ ($\Delta\varphi$), the laser spot on a screen in distance s is vertically (horizontally) displaced by $\Delta y = s \tan(2\,\Delta\theta)$ ($\Delta x = s \tan(2\,\Delta\varphi)$). This allows to compare the experimentally determined and the set value of $\Delta\theta$ ($\Delta\varphi$). To resolve smallest angular increments and enhance the precision, the distance between mirror and screen was set to $s = 7.92\,\mathrm{m}$ (measured using a laser rangefinder). On atmosphere, the tilt axis exhibits a reproducible jump at around $-7.8°$, which is most likely caused by the relaxed edge welded bellow and the motion screw that could have changed the flank. After this observation, we decided that meaningful measurements can only be conducted when the system is evacuated.

A.4.2. Tests in UHV

A photo along the TRHEPD (tilt) axis through the viewport of the UHV chamber is shown in figure A.8 c). At the sample position we attached a 45° mirror to reflect the laser beam towards the screen outside the vacuum. The setup is schematically depicted in figure A.8 d). For the given geometry, two additional angle pieces were necessary to investigate the entire tilt range from $-10°$ to $10°$. As before, we measured the deflection of the laser spot on the screen by Δy (Δx) due to the tilt (rotation) of the sample stage. In contrast to the previous measurements on atmosphere, no jumps were observed with the evacuated system. Moreover, we found that the two axis are well decoupled. Typical

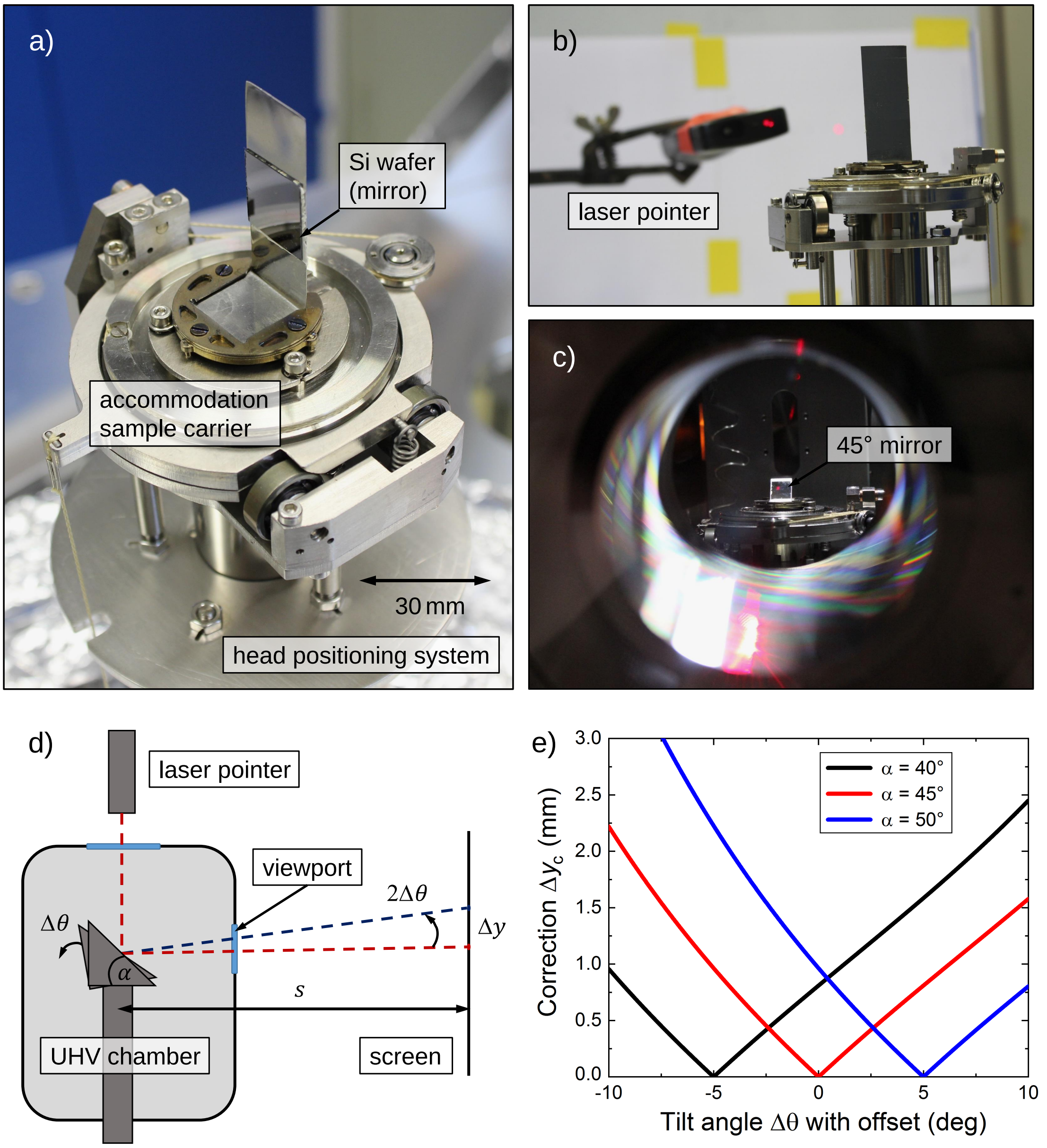

Figure A.8. Setup and considerations to determine the accuracy of the positioning system. a), b) Test of the rotation axis on atmosphere. We emphasize that the distance to the screen has been increased for subsequent measurements to enhance the resolution. c) Test of tilt and rotation in vacuum, view along the TRHEPD axis through the viewport. d) Schematic illustration of the setup for measurements in vacuum. Three different angle pieces with $\alpha = 40^\circ$, 45° and 50° were used to access the complete tilt range. e) Systematic errors stem from the refraction through the second viewport and the offset of the angle piece to the actual rotation plane. These effects were calculated to estimate the experimental uncertainty and allow corrections.

experimental data is listed in table A.1, as measured for the tilt from $-4.6°$ to $-6.2°$ with a step size of $0.1°$ and fixed rotation angle ($\Delta\varphi = 0$).

The measurement of Δy comprises several uncertainties, e.g. due to the finite size of the laser spot on the screen that makes it more difficult to accurately mark the position. Additionally, the deflection was measured manually, so that we estimate the statistical uncertainty of Δy to $\sim 2\,\text{mm}$. Besides that, the setup contains inherent systematic errors, e.g. induced by the refraction of the laser beam through the viewport. Another issue is the height of the angle piece, which leads to a reflection slightly above the actual tilt plane of the system. These two effects were considered within the data evaluation, but the respective corrections are rather small, as shown in figure A.8 e).

Δy (mm)	$\Delta\theta_{exp}$ (°)	$\Delta\theta_{set}$ (°)	$\lvert\Delta\theta_{exp} - \Delta\theta_{set}\rvert$ (°)	$\Delta\theta_{exp}$ each step (°)
29	0.105	0.1	0.005	0.105
57	0.206	0.2	0.006	0.101
85	0.307	0.3	0.007	0.101
113	0.409	0.4	0.009	0.102
140	0.506	0.5	0.006	0.097
171	0.618	0.6	0.018	0.112
200	0.723	0.7	0.023	0.105
228	0.824	0.8	0.024	0.101
255	0.922	0.9	0.022	0.098
285	1.03	1.0	0.03	0.108
310	1.121	1.1	0.021	0.091
336	1.215	1.2	0.015	0.094
361	1.305	1.3	0.005	0.09
386	1.395	1.4	0.005	0.09
414	1.496	1.5	0.004	0.101
441	1.594	1.6	0.006	0.098

Table A.1. Experimental data when tilting the sample stage from $-4.6°$ to $-6.2°$ in angular steps of $0.1°$ (set value). The measured deflection Δy of the laser spot on the screen allows to calculate the tilt angle as $\Delta\theta_{exp} = 0.5\arctan(\Delta y/s)$. All calculated values were rounded to four digits (systematic errors not compensated).

A.5. Safety concept laser heater

The commercial laser system used for in-situ sample heating includes several internal interlocks:

- To start the laser, a key must be inserted and turned in the laser controller.
- If the optical fiber is not attached to the optics at the viewport, an interlock prevents the laser from being started.
- During operation, the communication between software and controller is checked regularly, if it breaks down, the laser switches off automatically.
- Humidity, temperature and cooling water flow of the laser are monitored. If a threshold value is exceeded, the controller displays an errors message and the laser switches off automatically.

Since the IR laser can be categorized into class IV, additional safety measures are necessary for the operation at NEPOMUC. In collaboration with the laser safety officer M. Antic, we thus developed a detailed concept - the key points are summarized in the following.

In the UHV chamber, the incident laser beam is shielded by a metal tube up to the sample carrier. Via multiple reflections, laser light could leave the Faraday cage and potentially reach one of the viewports. Therefore, each viewport has to be covered with a laser safety fabric, which is supported by a protective cap made from aluminum. These protective caps are fastened with specially designed nuts that have a seven-fold symmetry, as shown in figure A.9 a). Moreover, the nuts are sunken in the cap, so that they can only be removed with the associated tool, as depicted in figure A.9 b). Consequently, unauthorized persons can't remove the safety fabric and no laser light can escape from the UHV chamber. Further safety aspects are:

- A warning light that indicates when the laser is in operation, as shown in figure A.4 a).
- Two laser safety goggles used for alignment work (optical density 8 for the corresponding wavelength).
- An additional housing, which is screwed to the experimental setup to guarantee that the laser controller is not accessible.

- The optical fiber is installed below the setup, so that nobody can trip over it or step on it.
- Only the responsible person has the tool to remove the special nuts and the key to start the laser.
- If the TRHEPD experiment opens for user access in the future, all users must receive a laser safety instruction prior to their beamtime.

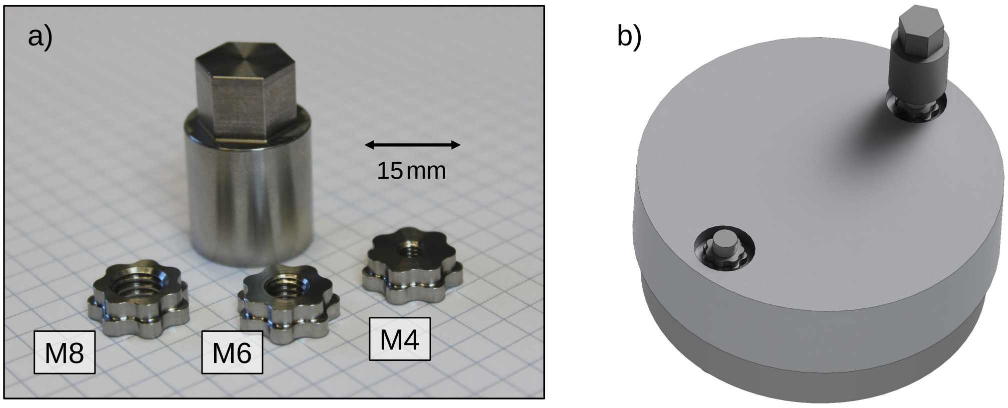

Figure A.9. Customized solution to prevent unauthorized people from removing the cover of the viewports during laser heating. a) Special nuts with a seven-fold symmetry and the associated tool. b) Fixing the protective cap that covers the viewport.

A.6. Experimental parameters and remarks

To facilitate the subsequent research with the TRHEPD setup at NEPOMUC, relevant experimental details are shared in the following.

A.6.1. RHEED system

During RHEED measurements, the Faraday cage must be connected to ground, while the transfer shutter can either be open or closed. We emphasize that the RHEED system, although specified for energies of up to 30 keV, should not be operated above 25 keV due to HV issues. Moreover, it is essential to increase the anode voltage[1] V_A stepwise and re-adjust the focus voltage V_F accordingly to prevent HV flashovers. The ideal values of V_F for different beam energies are listed in table A.2. We found that the beam properties are better for higher energies, e.g. the spot size on the screen is smaller. The beam intensity can be varied by the repulsive potential V_G1 of the Wehnelt cap. For beam alignment, it was set to $-83\,\mathrm{V}$ and decreased to around $-77\,\mathrm{V}$ during RHEED measurements, when the direct beam is covered by the sample. The acquisition time of the camera was set to 5-10 s, which allows to measure with a reduced beam intensity. The angle of incidence θ can be adjusted by the external deflection coil and the z-position of the sample stage, which was usually set to 35 - 44 mm.

V_A (kV) or E_{e^-} (keV)	10	15	20	25
V_F (V)	2900	4350	5750	7250

Table A.2. Experimentally determined focus voltages (V_F) for the present RHEED geometry and different beam energies E_{e^-} (defined by the anode voltage V_A).

A.6.2. Sample transfer and Ar$^+$ sputter position

The settings of the positioning system for sample transfer and Ar-ion sputtering are listed in table A.3. The transfer position is also saved in the *LabView* software and can be approached directly.

---

[1] In accordance with the RHEED controller/manual, we refer to the anode voltage. However, technically, the anode is grounded while the cathode (filament) is on negative HV.

position sample transfer				
x (mm)	y (mm)	z (mm)	rotation (°)	tilt (°)
5.00	8.00	5.00	152.25	0.00

position Ar-ion sputtering				
x (mm)	y (mm)	z (mm)	rotation (°)	tilt (°)
5.00	5.00	15.00	arbitrary	0.00

Table A.3. Determined sample position for transfer and Ar-ion sputtering.

A.6.3. Vacuum system

The vacuum system of the TRHEPD setup is schematically shown in figure A.10. The scroll pump and all TMPs are connected to an uninterruptible power supply (UPS) to bridge announced power shutdowns at the FRM II, which are related to periodic inspections. Before the UHV chamber is baked out, we obtain $p_3 = 1.9 \cdot 10^{-9}$ mbar, $p_4 = 2.4 \cdot 10^{-9}$ mbar, $p_5 = 4.1 \cdot 10^{-9}$ mbar and $p_6 = 1.4 \cdot 10^{-8}$ mbar (all gate valves closed). Using the cryogenic pump, the pressure of the main UHV chamber can be further reduced to $p_3' \approx 1.0 \cdot 10^{-9}$ mbar, which lasts for more than 12 h without refilling liquid nitrogen. The sensors p_1 and p_2 are typically in the range of low 10^{-8} mbar, which depends on the last sample transfer.

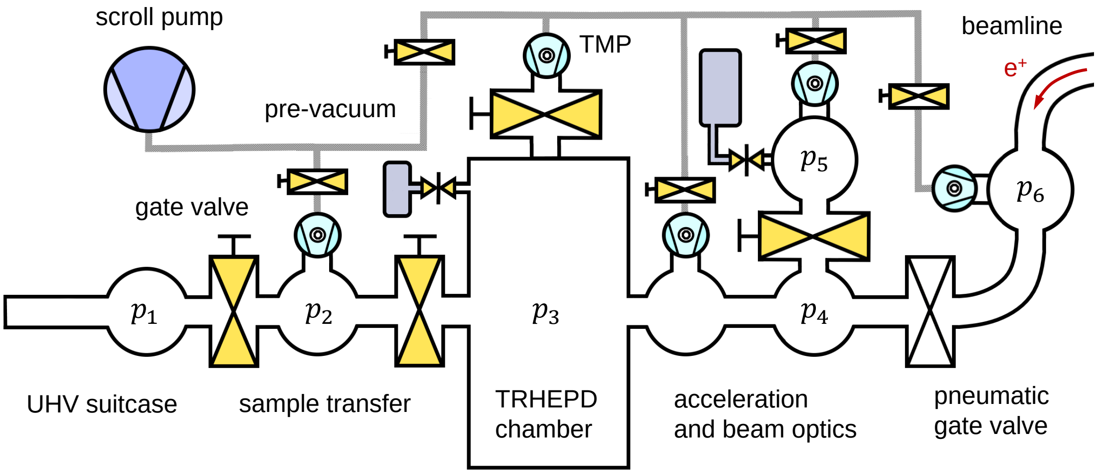

Figure A.10. Schematic illustration of the TRHEPD vacuum system. A pneumatic gate valve separates the setup from the SuSpect beamline.

A.6.4. Magnetic transport beamline

Figure A.11 schematically depicts the newly assembled SuSpect beamline downstream the central beam switch at NEPOMUC. Magnetic guiding coils (F53-F70) and correction coils (KP25-KP30) are assigned. In this section of the beamline, most guiding coils were operated with $I = 7\,\mathrm{A}$, except F65 ($I_{65} = 10\,\mathrm{A}$) and F70 ($I_{70} = 6\,\mathrm{A}$). The experimentally optimized currents of the correction coils are listed in table A.4.

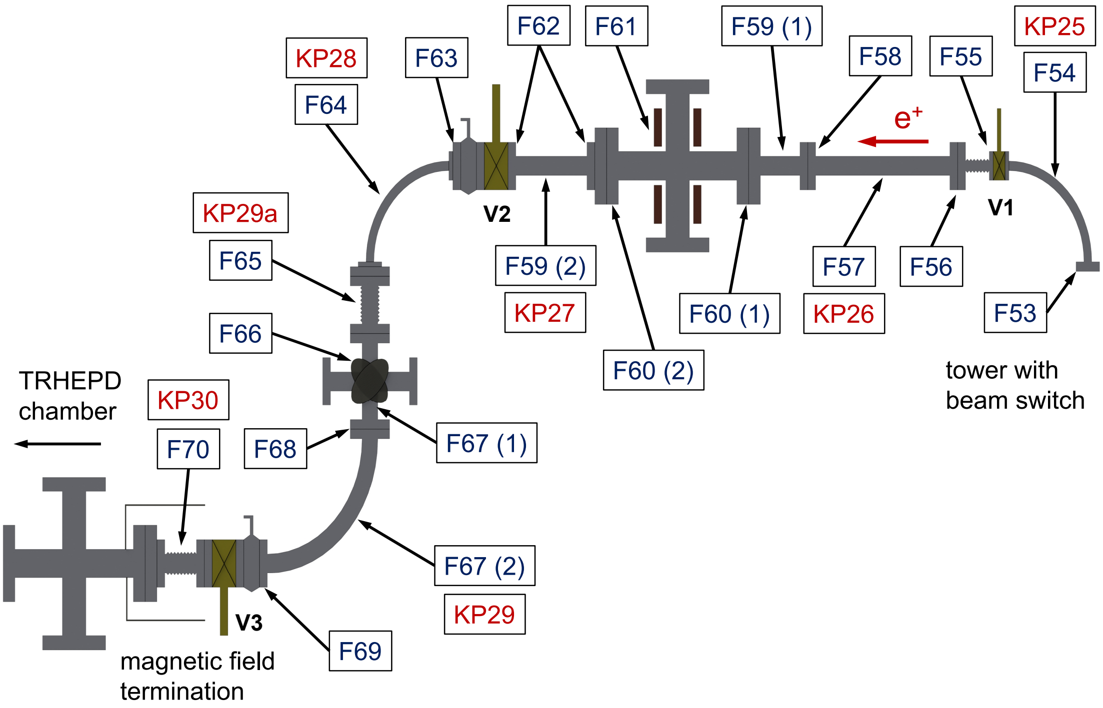

Figure A.11. SuSpect beamline downstream the central beam switch at NEPOMUC (schematic). Magnetic guiding coils (blue), correction coils (red) and pneumatic gate valves (V1-V3) are labelled.

A.6.5. Electrostatic acceleration and optics

The experimentally adjusted settings of the electrostatic system are listed in table A.5. Before applying HV, close the transfer shutter of the Faraday cage, set the gain of the HV potentiometer to minimum and check that all HV cables are connected, in particular the one to the Faraday cage as it is removed regularly, e.g. for RHEED measurements or Ar-ion sputtering. To prevent HV flashovers, it

label	horizontal I (mA)	vertical I (mA)
KP25	−1180	354
KP26	906	−48
KP27	−858	3368
KP28	−1153	−2190

label	horizontal I (mA)	vertical I (mA)
KP29a	−1000	400
KP29	700	−200
KP30	−2000	−400
	-500^*	-600^*

Table A.4. Optimized currents of the correction coils for the SuSpect beamline. Left: KP25-KP28, controlled by the central NEPOMUC system and numerically optimized with a Nelder-Mead algorithm that also considered coils and electrodes upstream the beam switch. Right: KP29a-KP30, manually optimized, based on the intensity and shape of the positron beam. Note that the determined currents of the last correction coils KP30 are different when applying the optional Ni(100) remoderator ($*$).

is essential that all voltages are increased simultaneously, i.e. do not apply more than 5 kV between adjacent electrodes. If the UHV chamber has been vented and re-evacuated, it is most important to carefully ramp up the voltage while watching out for HV flashovers or the onset of leak currents.

label	HV module	15 keV remod. beam V (kV)	10 keV twofold remod. beam V (kV)	beam monitor (MCP) V (kV)
V_{01}	iseg 030	-1.6	-2.5	-2.5
V_{02}	iseg 031	-2.5	-3.5	-3.5
V_{03}	iseg 032	-4.5	-5	-5
V_{04}	iseg 033	-3	-1.1	-0.8
V_{05}	iseg 034	-3	-5	-5
V_{BM1}	iseg 036	0	0	-4.4
V_{BM2}	iseg 037	0	0	-1.5
V_{06}	iseg 035	-5	-5.5	-1.5
V_{07}	iseg 023	-7.5	-7	-1.0
V_{08}	iseg 022	-9	-8	-0.5
V_{09}	iseg 021	-10	-9.5	0
V_{10}	iseg 020	-11	-11	0
V_{11}	iseg 010	-13	-13	0
V_{12}	iseg 013	-15	-15	0
V_{13}	iseg 011	-11	-12	0
V_{14}	iseg 013	-15	-15	0
V_{15}	iseg 012	-13	-15	0
V_{16}	iseg 013	-15	-15	0
V_{17}	FuG	-15	-15	0
V_{18}	iseg 000	-11.8	-12.1	0
V_{cage}	FuG	-15	-15	0

Table A.5. Experimentally adjusted voltages of the electrostatic system for measurements with the remoderated and twofold remoderated beam or when using the beam monitor. The electrodes are numbered consecutively in beam direction, see figure 4.7 a) for illustration.

A.7. Preparation parameters graphene samples

Here, we briefly list the parameters of the sample preparation. Table A.6 summarizes the standardized cleaning procedure, which was employed in the first step to remove organic and inorganic contaminations. In the next step, the samples were coated with polymer adsorbates as necessary for PASG. For this, the photoresist *AZ5214E* was used and the process parameters were adapted from reference [19]. After rinsing in isopropyl alcohol, the excess polymer was removed with a spin coater (100 rps). Subsequently, the samples were successively annealed at different temperatures and environments, as summarized in table A.7. Note that step 4 was only carried out for the MLG sample, while the hydrogen intercalation in step 5 was only necessary for the QFMLG sample.

step	solvents/chemicals	ratio	T (°C)	t (min)
1	acetone	-	50 (ultrasonic bath)	10
2	isopropyl alcohol	-	50 (ultrasonic bath)	10
3	H_2SO_4 and H_2O_2	4:1	180 (hot plate)	10
4	H_2O, H_2O_2 and HCl	4:1:1	80 (hot plate)	10

Table A.6. Cleaning procedure of the SiC samples prior to the graphene growth. The samples were rinsed in deionized water after each step and blown dry with nitrogen gas in the end.

step	atmosphere	T (°C)	t (min)	purpose
1	UHV	900	30	polymer decomposition
2	Ar (1 bar)	1200	10	rearrangement/healing
3	Ar (1 bar)	1400	5	growth buffer layer
(4)	Ar (1 bar)	1700	5	growth MLG
(5)	H_2 (930 mbar)	550	90	hydrogen intercalation

Table A.7. Parameters for PASG and hydrogen intercalation. For heating up, the temperature ramp was set to 3 K/s. The samples were cooled down naturally after step 1 and 3/4, respectively. The Ar atmosphere in the steps 2-4 limits the Si sublimation, which allows annealing at higher temperatures than in UHV and thus leads to an enhanced ordering kinetics [256]. During the hydrogen intercalation in step 5, the H_2 flow rate was set to 15.2 mbar · l/s.

Abbreviations

ACAR	Angular Correlation of Annihilation Radiation
AFM	Atomic Force Microscopy
CCD	Charge-Coupled Device
CDBS	Coincident Doppler Broadening Spectroscopy
CMOS	Complementary Metal–Oxide–Semiconductor
DFT	Density Functional Theory
fcc	Face-Centered Cubic
FRM II	Forschungsreaktor München II
FWHM	Full Width at Half Maximum
GGA	Generalized Gradient Approximation
HAS	Helium Atom Scattering
HV	High Voltage
IR	Infrared
LDA	Local Density Approximation
LEED	Low-Energy Electron Diffraction
LEPD	Low-Energy Positron Diffraction
LINAC	Linear Accelerator
MBE	Molecular Beam Epitaxy
MCP	Micro-Channel Plate
ML	Monolayer
MLG	Monolayer Graphene
NEG	Non-Evaporable Getter
NEPOMUC	NEutron induced POsitron source MUniCh
NIXSW	Normal Incidence X-ray Standing Wave

PAES	Positron annihilation induced Auger Electron Spectroscopy
PALS	Positron Annihilation Lifetime Spectroscopy
PASG	Polymer-Assisted Sublimation Growth
PBE	Perdew-Burke-Ernzerhof
PED	Photoelectron Diffraction
PSD	Phase Space Density
PSV	Phase Space Volume
QFMLG	Quasi-Free-Standing Monolayer Graphene
RHEED	Reflection High-Energy Electron Diffraction
SiC	Silicon Carbide
SPF	Slow Positron Facility
STM	Scanning Tunneling Microscopy
SuSpect	Surface Spectrometer
SXRD	Surface X-ray Diffraction
TED	Transmission Electron Diffraction
TMP	Turbo Molecular Pump
TRHEPD	Total-Reflection High-Energy Positron Diffraction
UHV	Ultra High Vacuum
XPS	X-ray Photoelectron Spectroscopy
XRR	X-ray Reflectivity
XSW	X-ray Standing Wave

Publications

- M. Dodenhöft, I. Mochizuki, P. Richter, P. Schädlich, T. Seyller, T. Hyodo and C. Hugenschmidt: Precise determination of the spacing between hydrogen-intercalated quasi-free-standing monolayer graphene and 6H-SiC(0001) using total-reflection high-energy positron diffraction, *in preparation*.
- M. Dodenhöft, S. Vohburger and C. Hugenschmidt: Total-reflection high-energy positron diffractometer at NEPOMUC - Instrumentation, simulation and first measurements, *Rev. Sci. Instrum.*, 92(11):115103, 2021.
- M. Dodenhöft, S. Vohburger and C. Hugenschmidt: Development of a new reflection high-energy positron diffractometer at NEPOMUC, *AIP Conf. Proc.*, 2182(1):040003, 2019.

Parts of this thesis have been published in the above stated references

Bibliography

[1] J. Sforzini, L. Nemec, T. Denig, B. Stadtmüller, T. L. Lee, C. Kumpf, S. Soubatch, U. Starke, P. Rinke, V. Blum, F. C. Bocquet, and F. S. Tautz. Approaching truly freestanding graphene: the structure of hydrogen-intercalated graphene on 6H-SiC(0001). *Phys. Rev. Lett.*, 114(10):106804, 2015.

[2] D. P. Woodruff. *Modern Techniques of Surface Science*. Cambridge University Press, 3rd edition, 2016.

[3] J. C. Vickerman and I. S. Gilmore, editors. *Surface Analysis - The Principal Techniques*. John Wiley and Sons Ltd., 2nd edition, 2009.

[4] W. Huang and W. Li. Surface and interface design for heterogeneous catalysis. *Phys. Chem. Chem. Phys.*, 21(2):523–536, 2019.

[5] R. J. MacDonald, E. C. Taglauer, and K. R. Wandelt, editors. *Surface Science - Principles and Current Applications*. Springer Verlag Berlin Heidelberg, 1996.

[6] K. S. Novoselov, A. K. Geim, S. V. Morozov, D. Jiang, Y. Zhang, S. V. Dubonos, I. V. Grigorieva, and A. A. Firsov. Electric field effect in atomically thin carbon films. *Science*, 306(5696):666–669, 2004.

[7] A. A. Balandin, S. Ghosh, W. Bao, I. Calizo, D. Teweldebrhan, F. Miao, and C. Ning Lau. Superior thermal conductivity of single-layer graphene. *Nano Lett.*, 8(3):902–907, 2008.

[8] C. Lee, X. Wei, J. W. Kysar, and J. Hone. Measurement of the elastic properties and intrinsic strength of monolayer graphene. *Science*, 321(5887):385–388, 2008.

[9] K. Cao, S. Feng, Y. Han, L. Gao, T. Hue Ly, Z. Xu, and Y. Lu. Elastic straining of free-standing monolayer graphene. *Nat Commun.*, 11:284, 2020.

[10] A. K. Geim and I. V. Grigorieva. Van der Waals heterostructures. *Nature*, 499:419–425, 2013.

[11] T. Seyller. Science and Technology of Graphene. *Ann. Phys. (Editorial)*, 529(11):1700322, 2017.

[12] Y. Cao, V. Fatemi, S. Fang, K. Watanabe, T. Taniguchi, E. Kaxiras, and P. Jarillo-Herrero. Unconventional superconductivity in magic-angle graphene superlattices. *Nature*, 556:43–50, 2018.

[13] H. Li, S. Li, E. C. Regan, D. Wang, W. Zhao, S. Kahn, K. Yumigeta, M. Blei, T. Taniguchi, K. Watanabe, S. Tongay, A. Zettl, M. F. Crommie, and F. Wang. Imaging two-dimensional generalized Wigner crystals. *Nature*, 597:650–654, 2021.

[14] S. Lisi, X. Lu, T. Benschop, T. A. de Jong, P. Stepanov, J. R. Duran, F. Margot, I. Cucchi, E. Cappelli, A. Hunter, A. Tamai, V. Kandyba, A. Giampietri, A. Barinov, J. Jobst, V. Stalman, M. Leeuwenhoek, K. Watanabe, T. Taniguchi, L. Rademaker, S. J. van der Molen, M. P. Allan, D. K. Efetov, and F. Baumberger. Observation of flat bands in twisted bilayer graphene. *Nat. Phys.*, 17:189–193, 2021.

[15] E. Li, J.-X. Hu, X. Feng, Z. Zhou, L. An, K. T. Law, N. Wang, and N. Lin. Lattice reconstruction induced multiple ultra-flat bands in twisted bilayer WSe_2. *Nat. Commun.*, 12(5601), 2021.

[16] H. Lüth. *Solid Surfaces, Interfaces and Thin Films*. Springer Berlin Heidelberg, 5th edition, 2010.

[17] Y. Fukaya, M. Hashimoto, A. Kawasuso, and A. Ichimiya. Surface structure of Si(111) - (8×2) - In determined by reflection high-energy positron diffraction. *Surf. Sci.*, 602(14):2448–2452, 2008.

[18] Y. Fukaya, A. Kawasuso, A. Ichimiya, and T. Hyodo. Total-reflection high-energy positron diffraction (TRHEPD) for structure determination of the topmost and immediate sub-surface atomic layers. *J. Phys. D: Appl. Phys.*, 52(1):013002, 2019.

[19] M. Kruskopf, D. M. Pakdehi, K. Pierz, S. Wundrack, R. Stosch, T. Dziomba, M. Götz, J. Baringhaus, J. Aprojanz, C. Tegenkamp, J. Lidzba, T. Seyller, F. Hohls, F. J. Ahlers, and H. W. Schumacher. Comeback of epitaxial graphene for electronics large-area growth of bilayer-free graphene on SiC. *2D Mater.*, 3:041002, 2016.

[20] P. A. M. Dirac. The quantum theory of the electron. *Proc. Roy. Soc. A*, 117(778):610–624, 1928.

[21] P. A. M. Dirac. A theory of electrons and protons. *Proc. Roy. Soc. A*, 126(801):360–365, 1930.

[22] P. A. M. Dirac. Quantised singularieties in the electromagnetic field. *Proc. Roy. Soc. A*, 133(821):60–72, 1931.

[23] C. D. Anderson. Energies of cosmic-ray particles. *Phys. Rev.*, 41(4):405–421, 1932.

[24] C. D. Anderson. The positive electron. *Phys. Rev.*, 43(6):491–494, 1933.

[25] E. Bellotti, M. Corti, E. Fiorini, C. Liguori, A. Pullia, A. Sarracino, P. Sverzellati, and L. Zanotti. A new experimental limit on electron stability. *Phys. Lett. B*, 124(5):435–438, 1983.

[26] P. J. Schultz and K. G. Lynn. Interaction of positron beams with surfaces, thin films and interfaces. *Rev. Mod. Phys.*, 60(3):701–779, 1988.

[27] P. G. Coleman, editor. *Positron Beams and their Applications*. World Scientific Publishing Co. Pte. Ltd., 2000.

[28] P. Hautojärvi, editor. *Positrons in Solids*. Springer-Verlag Berlin Heidelberg New York, 1979.

[29] R. Krause-Rehberg and H. S. Leipner. *Positron Annihilation in Semiconductors*. Springer-Verlag Berlin Heidelberg, 1999.

[30] C. Hugenschmidt. Positrons in surface physics. *Surf. Sci. Rep.*, 71(4):547–594, 2016.

[31] M. Eldrup. Positron methods for the study of defects in bulk materials. *Journal de Physique IV Colloque*, 05(C1):93–109, 1995.

[32] J. Banhart, M. D. H. Lay, C. S. T. Chang, and A. J. Hill. Kinetics of natural aging in Al-Mg-Si alloys studied by positron annihilation lifetime spectroscopy. *Phys. Rev. B*, 83(1):014101, 2011.

[33] J. Čížek. Characterization of lattice defects in metallic materials by positron annihilation spectroscopy: A review. *J. Mater. Sci. Technol.*, 34(4):577–598, 2018.

[34] F. Tuomisto and I. Makkonen. Defect identification in semiconductors with positron annihilation: Experiment and theory. *Rev. Mod. Phys.*, 85:1583, 2013.

[35] M. Reiner, A. Bauer, M. Leitner, T. Gigl, W. Anwand, M. Butterling, A. Wagner, P. Kudejova, C. Pfleiderer, and C. Hugenschmidt. Positron spectroscopy of point defects in the skyrmion-lattice compound MnSi. *Sci. Rep.*, 6(29109), 2016.

[36] A. Dupasquier and A. P. Mills, editors. *Positron Spectroscopy of Solids*. Proceedings of the International School of Physics "Enrico Fermi" 125, IOS Press, 1995.

[37] J. A. Weber, A. Bauer, P. Böni, H. Ceeh, S. B. Dugdale, D. Ernsting, W. Kreuzpaintner, M. Leitner, C. Pfleiderer, and C. Hugenschmidt. Spin-resolved Fermi surface of the localized ferromagnetic Heusler compound Cu_2MnAl measured with spin-polarized positron annihilation. *Phys. Rev. Lett.*, 115(20):206404, 2015.

[38] A. Weiss, R. Mayer, M. Jibaly, C. Lei, D. Mehl, and K. G. Lynn. Auger-electron emission resulting from the annihilation of core electrons with low-energy positrons. *Phys. Rev. Lett.*, 61:2245, 1988.

[39] A. H. Weiss, S. Yang, H. Q. Zhou, E. Jung, and S. Wheeler. Auger line shape measurements using positron annihilation induced Auger electron spectroscopy. *J. Electron Spectros. Relat. Phenomena*, 72:305–309, 1995.

[40] J. Mayer, C. Hugenschmidt, and K. Schreckenbach. Direct observation of the surface segregation of Cu in Pd by time-resolved positron-annihilation-induced Auger electron spectroscopy. *Phys. Rev. Lett.*, 105:207401, 2010.

[41] S. Zimnik, C. Piochacz, S. Vohburger, and C. Hugenschmidt. Time-dependent investigation of sub-monolayers of Ni on Pd using positron-annihilation induced Auger electron spectroscopy and XPS. *Surf. Sci.*, 643:178–182, 2016.

[42] S. Zimnik, C. Piochacz, S. Vohburger, and C. Hugenschmidt. Comparative study of time-dependent PAES and XPS on a Ni/Pd surface. *Trans. Tech. Publications, Ltd.*, 373:313–316, 2017.

[43] C. S. Wu, E. Ambler, R. W. Hayward, D. D. Hoppes, and R. P. Hudson. Experimental test of parity conservation in beta decay. *Phys. Rev.*, 105(4):1413, 1957.

[44] K. Wada, A. Miyashita, M. Maekawa, S. Sakai, and A. Kawasuso. Spin-polarized positron beams with ^{22}Na and ^{68}Ge and their applications to materials research. *AIP Conf. Proc.*, 1970:040001, 2018.

[45] B. Straßer, C. Hugenschmidt, and K. Schreckenbach. Set-up of a slow positron beam for Auger spectroscopy. *Mater. Sci. Forum*, 363-365:686–688, 2001.

[46] M. Maekawa and A. Kawasuso. Development of pulsed positron beam line with compact pulsing system. *Nucl. Instrum. Meth. B*, 270:23–27, 2012.

[47] M. Dickmann. *Radio Frequency Energy Elevation and Characterization of a Pulsed Positron Microbeam*. PhD thesis, TU München, 2017.

[48] K. G. Lynn, A. P. Mills, R. N. West, S. Berko, K. F. Canter, and L. O. Roellig. Positron or positroniumlike surface state on Al(100)? *Phys. Rev. Lett.*, 54(15):1702, 1985.

[49] G. R. Gilmore. *Practical Gamma-Ray Spectroscopy*. John Wiley & Sons Ltd., 2nd edition, 2008.

[50] C. Leroy and P. G. Rancoita. *Principles of Radiation Interaction in Matter and Detection*. World Scientific Publishing Co. Pte. Ltd., 2nd edition, 2009.

[51] W. Demtröder. *Experimentalphysik 4 Kern-, Teilchen- und Astrophysik*. Springer-Verlag Berlin Heidelberg, 3rd edition, 2010.

[52] A. van Veen, F. Labohm, H. Schut, J. de Roode, T. Heijenga, and P. E. Mijnarends. Testing of a nuclear-reactor-based positron beam. *Appl. Surf. Sci.*, 116:39–44, 1997.

[53] C. Hugenschmidt, C. Piochacz, M. Reiner, and K. Schreckenbach. The NEPOMUC upgrade and advanced positron beam experiments. *New J. Phys.*, 14:055027, 2012.

[54] T. Hyodo, I. Mochizuki, K. Wada, N. Toge, and T. Shidara. Slow positron applications at Slow Positron Facility of Institute of Materials Structure Science, KEK. *AIP Conf. Proc.*, 1970:040004, 2018.

[55] Website National Institute of Standards and Technology. Photon cross section data for a single element, compound, or mixture. https://physics.nist.gov/PhysRefData/Xcom/html/xcom1.html, accessed 21.08.2020.

[56] R. Krause-Rehberg, G. Brauer, M. Jungmann, A. Krille, A. Rogov, and K. Noack. Progress of the intense positron beam project EPOS. *Appl. Surf. Sci.*, 255(1):22–24, 2008.

[57] T. Hyodo, K. Wada, A. Yagishita, T. Kosuge, Y. Saito, T. Kurihara, T. Kikuchi, A. Shirakawa, T. Sanami, and M. Ikeda. KEK-IMSS Slow Positron Facility. *J. Phys. Conf. Ser.*, 262:012026, 2011.

[58] K. Wada, T. Hyodo, A. Yagishita, M. Ikeda, S. Ohsawa, T. Shidara, K. Michishio, T. Tachibana, Y. Nagashima, Y. Fukaya, M. Maekawa, and A. Kawasuso. Increase in the beam intensity of the linac-based slow positron beam and its application at the Slow Positron Facility, KEK. *Eur. Phys. J. D*, 66:37, 2012.

[59] A. van Veen, H. Schut, J. de Roode, F. Labohm, C. V. Falub, S. W. H. Eijt, and P. E. Mijnarends. Intense positron sources and their applications. *Mater. Sci. Forum*, 363-365:415–419, 2001.

[60] H. Schut, A. van Veen, J. de Roode, and F. Labohm. Long term performance of the reactor based positron beam POSH. *Mater. Sci. Forum*, 445-446:507–509, 2004.

[61] C. Hugenschmidt, G. Kögel, R. Repper, K. Schreckenbach, P. Sperr, B. Straßer, and W. Triftshäuser. Intense positron source at the Munich research reactor FRM-II. *Appl. Phys. A*, 74:295–297, 2002.

[62] C. Hugenschmidt, K. Schreckenbach, M. Stadlbauer, and B. Straßer. Low-energy positrons of high intensity at the new positron beam facility NEPOMUC. *Nucl. Instrum. Meth. A*, 554(1-3):384–391, 2005.

[63] C. Hugenschmidt, H. Ceeh, T. Gigl, F. Lippert, C. Piochacz, M. Reiner, K. Schreckenbach, S. Vohburger, J. Weber, and S. Zimnik. Positron beam characteristics at NEPOMUC upgrade. *J. Phys. Conf. Ser.*, 505:012029, 2014.

[64] A. I. Hawari, D. W. Gidley, J. Xu, J. Moxom, A. G. Hathaway, B. Brown, and R. Vallery. The intense slow positron beam facility at the NC State University PULSTAR reactor. *AIP Conf. Proc.*, 1099(1):862–865, 2009.

[65] C. Hugenschmidt, K. Schreckenbach, D. Habs, and P. G. Thirolf. High-intensity and high-brightness source of moderated positrons using a brilliant γ beam. *Appl. Phys. B*, 106:241–249, 2012.

[66] N. Djourelov, A. Oprisa, and V. Leca. Source of slow polarized positrons using the brilliant gamma beam at ELI-NP. Converter design and simulations. *Nucl. Instrum. Meth. A*, 806:146–153, 2016.

[67] N. Djourelov, D. Dinescu, and V. Leca. An overview of the design of ELIPS - A new slow positron beam line. *Nucl. Instrum. Meth. A*, 934:19–25, 2019.

[68] B. T. Wright. Spectrometer measurement on the high energy positrons of sodium 22. *Phys. Rev.*, 90(1):159, 1953.

[69] B. Krusche and K. Schreckenbach. Intense positron sources by pair creation with neutron capture γ-rays. *Nucl. Instrum. Meth. A*, 295(1-2):155–171, 1990.

[70] B. Löwe, K. Schreckenbach, and C. Hugenschmidt. Positron remoderation by gas cooling within an electric drift field. *Nucl. Instrum. Meth. B*, 268(5):529–532, 2010.

[71] C. M. Surko, G. F. Gribakin, and S. J. Buckman. Low-energy positron interactions with atoms and molecules. *J. Phys. B*, 38(6):R57–R126, 2005.

[72] B. Barbiellini, M. J. Puska, T. Korhonen, A. Harju, T. Torsti, and R. M. Nieminen. Calculation of positron states and annihilation in solids: a density-gradient-correction scheme. *Phys. Rev. B*, 53(24):16201, 1996.

[73] C. H. Hodges and M. J. Stott. Work functions for positrons in metals. *Phys. Rev. B*, 7(1):73, 1973.

[74] C. A. Murray and A. P. Mills. Narrow beam emission of slow positrons from negative affinity surfaces. *Solid State Commun.*, 34(10):789–794, 1980.

[75] D. A. Fischer, K. G. Lynn, and D. W. Gidley. High-resolution angle-resolved positron reemission spectra from metal surfaces. *Phys. Rev. B*, 33(7):4479, 1986.

[76] J. Oliva. Inelastic positron scattering in an electron gas. *Phys. Rev. B*, 21:4909, 1980.

[77] B. Bergersen, E. Pajanne, P. Kubica, M. J. Stott, and C. H. Hodges. Positron diffusion in metals. *Solid State Commun.*, 15(8):1377–1380, 1974.

[78] R. N. West. Positron studies of condensed matter. *Adv. Phys.*, 22(3):263–383, 1973.

[79] D. M. Chen, K. G. Lynn, R. Pareja, and B. Nielsen. Measurement of positron reemission from thin single-crystal W(100) films. *Phys. Rev. B*, 31(7):4123, 1985.

[80] C. Hugenschmidt, G. Kögel, R. Repper, K. Schreckenbach, P. Sperr, and W. Triftshäuser. First platinum moderated positron beam based on neutron capture. *Nucl. Instrum. Meth. B*, 198(3-4):220–229, 2002.

[81] E. M. Gullikson, A. P. Mills, and C. A. Murray. Dependence of the positron reemission probability on the positron work function of a metal surface. *Phys. Rev. B*, 38(3):1705, 1988.

[82] E. M. Gullikson and A. P. Mills. Positron dynamics in rare-gas solids. *Phys. Rev. Lett.*, 57(3):376, 1986.

[83] A. P. Mills and E. M. Gullikson. Solid neon moderator for producing slow positrons. *Appl. Phys. Lett.*, 49(17):1121, 1986.

[84] J. Störmer, A. Goodyear, W. Anwand, G. Brauer, P. G. Coleman, and W. Triftshäuser. Silicon carbide: a new positron moderator. *J. Phys. Condens. Matter*, 8(7):L89–L94, 1996.

[85] J. Kuriplach, M. Šob, G. Brauer, W. Anwand, E. M. Nicht, P. G. Coleman, and N. Wagner. Positron affinity in semiconductors: Theoretical and experimental studies. *Phys. Rev. B*, 59(3):1948, 1999.

[86] G. R. Brandes, A. P. Mills, and D. M. Zuckermann. Positron workfunction of diamond C(100) surfaces. *Mater. Sci. Forum*, 105-110:1363–1366, 1992.

[87] K. G. Lynn and B. T. A. McKee. Some investigations of moderators for slow positron beams. *Appl. Phys.*, 19:247–255, 1979.

[88] C. D. Beling, S. Fung, Li Ming, M. Gong, and B. K. Panda. A theoretical search for possible high efficiency semiconductor based field assisted positron moderators. *Appl. Surf. Sci.*, 149(1-4):253–259, 1999.

[89] P. W. Hawkes and E. Kasper. *Principles of Electron Optics, Volume 1 Basic Geometrical Optics*. Academic Press, 1996.

[90] M. Reiser. *Theory and Design of Charged Particle Beams*. Wiley Weinheim, 2nd edition, 2008.

[91] W. Nolting. *Grundkurs Theoretische Physik 2 - Analytische Mechanik*. Springer Spektrum, 9th edition, 2014.

[92] C. Piochacz. *Generation of a High-Brightness Pulsed Positron Beam for the Munich Scanning Positron Microscope*. PhD thesis, TU München, 2009.

[93] H. Goldstein, C. P. Poole, and J. L. Safko. *Klassische Mechanik*. John Wiley & Sons, 3rd edition, 2012.

[94] F. S. Crawford. Elementary examples of adiabatic invariance. *Am. J. Phys.*, 58(4):337, 1990.

[95] U. Stroth. *Plasmaphysik Phänomene, Grundlagen und Anwendungen*. Springer Spektrum Berlin Heidelberg, 2nd edition, 2018.

[96] A. Piel. *Plasma Physics - An Introduction to Laboratory, Space and Fusion Plasmas*. Springer Verlag Berlin Heidelberg, 2nd edition, 2017.

[97] T. Gigl. *New Brightness Enhanced Positron Microbeam for Spatially Resolved Doppler Broadening Spectroscopy at NEPOMUC*. PhD thesis, TU München, 2018.

[98] P. Grivet, P. W. Hawkes, and A. Septier. *Electron Optics*. Pergamon Press, Oxford and New York, 2nd edition, 1972.

[99] D. W. O. Heddle. *Electrostatic Lens Systems*. CRC Press, 2nd edition, 2000.

[100] C. Hugenschmidt. Lecture notes *Physik mit Positronen I*, WS 2013/14.

[101] J. Großer. *Einführung in die Teilchenoptik*. Vieweg Teubner Verlag, 1983.

[102] T. Kalvas. Beam Extraction and Transport. *CERN yellow report*, 007:537–564, 2013.

[103] J. Mitteneder, M. Dickmann, G. Kögel, W. Egger, P. Sperr, and G. Dollinger. Micrometer positron beam characterization at the Scanning Positron Microscope Interface. *J. Phys. Conf. Ser.*, 791:012006, 2017.

[104] T. Gigl, L. Beddrich, M. Dickmann, B. Rienäcker, M. Thalmayr, S. Vohburger, and C. Hugenschmidt. Defect imaging and detection of precipitates using a new scanning positron microbeam. *New J. Phys.*, 19:123007, 2017.

[105] A. Kawasuso, T. Ishimoto, M. Maekawa, Y. Fukaya, K. Hayashi, and A. Ichimiya. A coherent positron beam for reflection high-energy positron diffraction. *Rev. Sci. Instrum.*, 75:4585, 2004.

[106] A. P. Mills. Brightness enhancement of slow positron beams. *Appl. Phys.*, 23:189–191, 1980.

[107] T. Schmidt. *Automated Positron Beam Adjustment and new Detector Readout at the Coincident Doppler Broadeing Spectrometer*. Master Thesis, TU München, 2019.

[108] F. Schwabl. *Statistical Mechanics*. Springer-Verlag Berlin Heidelberg, 2nd edition, 2006.

[109] K. F. Canter and A. P. Mills. Slow positron beam design notes. *Can. J. Phys.*, 60(4):551–557, 1982.

[110] Private communication with Dr. G. Gassler, May 2018.

[111] M. Fujinami, S. Jinno, M. Fukuzumi, T. Kawaguchi, K. Oguma, and T. Akahane. Production of a positron microprobe using a transmission remoderator. *Anal. Sci.*, 24(1):73–79, 2008.

[112] F. M. Jacobsen, M. Charlton, J. Chevallier, B. I. Deutch, G. Laricchia, and M. R. Poulsen. The effect of laser annealing of thin W(100) films on positron transmission reemission properties. *J. Appl. Phys.*, 67:575, 1990.

[113] R. J. Wilson and A. P. Mills. Positron and positronium emission from tungsten (111). *Phys. Rev. B*, 27(7):3949, 1983.

[114] P. J. Schultz, E. M. Gullikson, and A. P. Mills. Transmitted positron reemission from a thin single-crystal Ni(100) foil. *Phys. Rev. B*, 34(1):442, 1986.

[115] A. F. Makhov. The penetration of electrons into solids, II the distribution of electrons in depth. *Sov. Phys. Solid State*, 2:1942–1944, 1961.

[116] S. Valkealahti and R. M. Nieminen. Monte Carlo calculations of keV electron and positron slowing down in solids II. *Appl. Phys. A*, 35:51–59, 1984.

[117] V. J. Ghosh, D. O. Welch, , and K. G. Lynn. Monte Carlo studies of positron implantation in elemental metallic and multilayer systems. *AIP Conf. Proc.*, 303:37, 1994.

[118] J. Dryzek and P. Horodek. GEANT4 simulation of slow positron beam implantation profiles. *Nucl. Instrum. Meth. B*, 266(18):4000–4009, 2008.

[119] M. J. Puska and R. M. Nieminen. Theory of positrons in solids and on solid surfaces. *Rev. Mod. Phys.*, 66(3):841, 1994.

[120] J. Algers, P. Sperr, W. Egger, G. Kögel, and F. H. J. Maurer. Median implantation depth and implantation profile of 3-18 keV positrons in amorphous polymers. *Phys. Rev. B*, 67(12):125404, 2003.

[121] M. Maekawa, K. Wada, Y Fukaya, A. Kawasuso, I. Mochizuki, T. Shidara, and T. Hyodo. Brightness enhancement of a linac-based intense positron beam for total-reflection high-energy positron diffraction (TRHEPD). *Eur. Phys. J. D*, 68:165, 2014.

[122] K. Oura, V. G. Lifshits, A. Saranin, A. V. Zotov, and M. Katayama. *Surface Science - An Introduction*. Springer-Verlag Berlin Heidelberg, 2003.

[123] H. Ibach. *Physics of Surfaces and Interfaces*. Springer Berlin Heidelberg, 1st edition, 2006.

[124] B. C. Russell and M. R. Castell. Reconstructions on the polar $SrTiO_3$ (110) surface analysis using STM, LEED and AES. *Phys. Rev. B*, 77(24):245414, 2008.

[125] I. W. Yeu, J. Park, G. Han, C. S. Hwang, and J. Choi. Surface reconstruction of InAs(001) depending on the pressure and temperature examined by density functional thermodynamics. *Sci. Rep.*, 7:10691, 2017.

[126] M. J. Harrison, D. P. Woodruff, J. Robinson, D. Sander, W. Pan, and J. Kirschner. Adsorbate-induced surface reconstruction and surface-stress changes in Cu(100)/O: experiment and theory. *Phys. Rev. B*, 74:165402, 2006.

[127] K. Takayanagi, Y. Tanishiro, M. Takahashi, and S. Takahashi. Structural analysis of Si(111) - 7×7 by UHV-transmission electron diffraction and microscopy. *J. Vac. Sci. Technol. A*, 3(3):1502, 1985.

[128] A. Mikkelsen, S. V. Hoffmann, J. Jiruse, and D. L. Adams. Surface reconstruction and relaxation of Al(110) - c (2×2) - Na. *Phys. Rev. B*, 61(20):13988, 2000.

[129] C. Kittel. *Introduction to Solid State Physics*. John Wiley and Sons, Inc., 8th edition, 2004.

[130] R. L. Park and H. H. Madden. Annealing changes on the (100) surface of palladium and their effect on CO adsorption. *Surf. Sci.*, 11(2):188–202, 1968.

[131] E. A. Wood. Vocabulary of Surface Crystallography. *J. Appl. Phys.*, 35:1306, 1964.

[132] M. Hermann. *Crystallography and Surface Structure - An Introduction for Surface Scientists and Nanoscientists*. Wiley-VCH, 2nd edition, 2016.

[133] A. Ichimiya and P. I. Cohen. *Reflection High Energy Electron Diffraction*. Cambridge University Press, 2004.

[134] W. Braun. *Applied RHEED - Reflection High-Energy Electron Diffraction During Crystal Growth*. Springer-Verlag Berlin Heidelberg, 1st edition, 1999.

[135] M. A. Van Hove, W. H. Weinberg, and C.-M. Chan. *Low-Energy Electron Diffraction - Experiment, Theory and Surface Structure Determination*. Springer-Verlag Berlin Heidelberg, 1986.

[136] K. Hayashi, Y. Fukaya, A. Kawasuso, and A. Ichimiya. Kinematical and dynamical analyses of reflection high-energy positron diffraction (RHEPD) patterns from Si(111) 7×7 surfaces. *Appl. Surf. Sci.*, 237(1-4):34–39, 2004.

[137] A. Zangwill. *Physics at Surfaces*. Cambridge University Press, 1988.

[138] G. Binnig, H. Rohrer, C. Gerber, and E. Weibel. Surface studies by scanning tunneling microscopy. *Phys. Rev. Lett.*, 49:57, 1982.

[139] G. Binnig, H. Rohrer, C. Gerber, and E. Weibel. 7×7 reconstruction on Si(111) resolved in real space. *Phys. Rev. Lett.*, 50:120, 1983.

[140] G. Binnig and H. Rohrer. Scanning tunneling microscopy - from birth to adolescence. *Rev. Mod. Phys.*, 59:615, 1987.

[141] C. J. Chen. *Introduction to Scanning Tunneling Microscopy*. Oxford University Press, 2nd edition, 2007.

[142] G. Binnig, C. F. Quate, and C. Gerber. Atomic force microscope. *Phys. Rev. Lett.*, 56(9):930, 1986.

[143] S. V. Kalinin and A. Gruverman. *Scanning Probe Microscopy*. Springer-Verlag New York, 2007.

[144] F. J. Giessibl. AFM's path to atomic resolution. *Mater. Today*, 8(5):32–41, 2005.

[145] F. Traeger. Helium atom scattering from oxide surfaces. *Chem. Phys. Chem.*, 7(5):1006–1013, 2006.

[146] G. N. Robinson, N. Camillone III, P. A. Rowntree, G. Liu, J. Wang, and G. Scoles. Low energy helium diffraction studies of CH_3Br overlayers physisorbed on C(0001), NaCl(001), and LiF(001) surfaces. *J. Chem. Phys.*, 96(12):9212, 1992.

[147] J. P. Toennies, F. Traeger, J. Vogt, and H. Weiss. Low-energy electron induced restructuring of water monolayers on NaCl(100). *J. Chem. Phys.*, 120(24):11347, 2004.

[148] P. Eisenberger and W. C. Marra. X-ray diffraction study of the Ge(001) reconstructed surface. *Phys. Rev. Lett.*, 46:1081, 1981.

[149] I. K. Robinson. Crystal truncation rods and surface roughness. *Phys. Rev. B*, 33:3830, 1986.

[150] R. Feidenhans'l. Surface structure determination by X-ray diffraction. *Surf. Sci. Rep.*, 10(3):105–188, 1989.

[151] M. V. Kovalchuk, A. Yu Kazimirov, and S. I. Zheludeva. Surface-sensitive X-ray diffraction methods: physics, applications and related X-ray and SR instrumentation. *Nucl. Instrum. Meth. B*, 101(4):435–452, 1995.

[152] H. Tajiri. Progress in surface X-ray crystallography and the phase problem. *Jpn. J. Appl. Phys.*, 59:020503, 2020.

[153] C. Davisson and L. H. Germer. The scattering of electrons by a single crystal of nickel. *Nature*, 119:558–560, 1927.

[154] C. Davisson and L. H. Germer. Diffraction of electrons by a crystal of nickel. *Phys. Rev.*, 30:705, 1927.

[155] Y. Horio, Y. Hashimoto, and A. Ichimiya. A new type of RHEED apparatus equipped with an energy filter. *Appl. Surf. Sci.*, 100-101:292–296, 1996.

[156] S. Hasegawa. Reflection High-Energy Electron Diffraction. In: E. N. Kaufmann (editor) *Characterization of Materials*, John Wiley and Sons Inc., 2nd edition, 2002.

[157] J. J. Harris, B. A. Joyce, and P. J. Dobson. Oscillations in the surface structure of Sn-doped GaAs during growth by MBE. *Surf. Sci.*, 103:90–96, 1981.

[158] J. H. Neave, B. A. Joyce, P. J. Dobson, and N. Norton. Dynamics of film growth of GaAs by MBE from RHEED observations. *Appl. Phys. A*, 31:1–8, 1983.

[159] Y. Shigeta and Y. Fukaya. Structural phase transition and thermal vibration of surface atoms studied by reflection high-energy electron diffraction. *Appl. Surf. Sci.*, 237:21–28, 2004.

[160] W. Voegeli, T. Aoyama, K. Akimoto, A. Ichimiya, Y. Hisada, Y. Mitsuoka, and S. Mukainakano. Structure of the SiC(0001) - $\sqrt{3} \times \sqrt{3}$ - R30° surface after initial oxidation. *Surf. Sci.*, 604(19-20):1713–1717, 2010.

[161] Z. Mitura and P. A. Maksym. Analysis of reflection high energy electron diffraction azimuthal plots. *Phys. Rev. Lett.*, 70(19):2904–2907, 1993.

[162] U. W. Pohl. *Epitaxy of Semiconductors - Physics and Fabrication of Heterostructures*. Springer International Publishing, 2nd edition, 2020.

[163] I. J. Rosenberg, A. H. Weiss, and K. F. Canter. Low-energy positron diffraction from a Cu(111) surface. *Phys. Rev. Lett.*, 44(17):1139, 1980.

[164] X. M. Chen, K. F. Canter, C. B. Duke, A. Paton, D. L. Lessor, and W. K. Ford. Low-energy positron diffraction from the (110) surfaces of GaAs and InP. *Phys. Rev. B*, 48(4):2400, 1993.

[165] S. Y. Tong. Why is the positron an ideal particle for studying surface structure? *Surf. Sci.*, 457(3):L432–L436, 2000.

[166] T. Hyodo, Y. Fukaya, M. Maekawa, I. Mochizuki, K. Wada, T. Shidara, A. Ichimiya, and A. Kawasuso. Total reflection high-energy positron diffraction (TRHEPD). *J. Phys. Conf. Ser.*, 505:012001, 2014.

[167] A. Ichimiya. Reflection high-energy positron diffraction (RHEPD). *Solid State Phenom.*, 28-29:143–148, 1992.

[168] Y. Fukaya, M. Maekawa, A. Kawasuso, I. Mochizuki, K. Wada, T. Shidara, A. Ichimiya, and T. Hyodo. Total reflection high-energy positron diffraction: An ideal diffraction technique for surface structure analysis. *Appl. Phys. Express*, 7(5):056601, 2014.

[169] Z. Mitura. Comparison of azimuthal plots for reflection high-energy positron diffraction (RHEPD) and reflection high-energy electron diffraction (RHEED) for Si(111) surface. *Acta Cryst. A*, 76:328–333, 2020.

[170] A. Kawasuso and S. Okada. Reflection high energy positron diffraction from a Si(111) surface. *Phys. Rev. Lett.*, 81:2695, 1998.

[171] J. L. Wiza. Microchannel plate detectors. *Nucl. Instrum. Meth.*, 162(1-3):587–601, 1979.

[172] K. Saiki, T. Kono, K. Ueno, and A. Koma. Highly sensitive reflection high-energy electron diffraction measurement by use of micro-channel imaging plate. *Rev. Sci. Instrum.*, 71(9):3478, 2000.

[173] M. Aeschlimann, E. Hull, J. Cao, C. A. Schmuttenmaer, L. G. Jahn, Y. Gao, H. E. Elsayed-Ali, D. A. Mantell, and M. R. Scheinfein. A picosecond electron gun for surface analysis. *Rev. Sci. Instrum.*, 66(2):1000, 1995.

[174] T. Frigge, B. Hafke, T. Witte, B. Krenzer, C. Streubühr, A. Samad Syed, V. M. Trontl, I. Avigo, P. Zhou, M. Ligges, D. von der Linde, U. Bovensiepen, M. Horn-von Hoegen, S. Wippermann, A. Lücke, S. Sanna, U. Gerstmann, and W. G. Schmidt. Optically excited structural transition in atomic wires on surfaces at the quantum limit. *Nature*, 544:207–211, 2017.

[175] S. Vogelgesang, G. Storeck, J. G. Horstmann, T. Diekmann, M. Sivis, S. Schramm, K. Rossnagel, S. Schäfer, and C. Ropers. Phase ordering

of charge density waves traced by ultrafast low-energy electron diffraction. *Nat. Phys.*, 14:184–190, 2018.

[176] Y. Fukaya. Structure analysis of two-dimensional atomic sheets by Total-Reflection High-Energy Positron Diffraction. *e-J. Surf. Sci. Nanotechnol.*, 16:111–114, 2018.

[177] K. Fujiwara. Relativistic dynamical theory of electron diffraction. *J. Phys. Soc. Jpn.*, 16(11):2226–2238, 1961.

[178] P. A. Doyle and P. S. Turner. Relativistic Hartree-Fock X-ray and electron scattering factors. *Acta Cryst.*, A24:390–397, 1968.

[179] S. L. Dudarev, L. M. Peng, and M. J. Whelan. On the Doyle-Turner representation of the optical potential for RHEED calculations. *Surf. Sci.*, 330(1):86–100, 1995.

[180] A. Ichimiya. Many-beam calculation of reflection high energy electron diffraction (RHEED) intensities by the multi-slice method. *Jpn. J. Appl. Phys.*, 22:176, 1983.

[181] A. Ichimiya. Correction to many-beam calculation of RHEED intensities by the multi-slice method. *Jpn. J. Appl. Phys.*, 24(10R):1365, 1985.

[182] I. Mochizuki. *Recent Studies of Surface Structure Analysis with Total Reflection High-Energy Positron Diffraction (TRHEPD) at Slow-Positron Facility, KEK*, Invited Talk at the 15th International Workshop on Slow Positron Beam Techniques and Applications (SLOPOS-15), Sept. 2019.

[183] Y. Fukaya, A. Kawasuso, and A. Ichimiya. Order-disorder phase transition of Sn/Ge(111) surface studied by reflection high-energy positron diffraction. *e-J. Surf. Sci. Nanotechnol.*, 4:435–438, 2006.

[184] Y. Fukaya, I. Mochizuki, and A. Kawasuso. Charge transfer and structure of K/Si(111) - $2\sqrt{3} \times 2\sqrt{3}$ - B surface studied by reflection high-energy positron diffraction. *Phys. Rev. B*, 86(3):035423, 2012.

[185] K. Tanaka, T. Hoshi, I. Mochizuki, T. Hanada, A. Ichimiya, and T. Hyodo. Development of data-analysis software for total-reflection high-energy positron diffraction (TRHEPD). *Acta Phys. Pol. A*, 137:188, 2020.

[186] K. Momma and F. Izumi. VESTA 3 for three-dimensional visualization of crystal, volumetric and morphology data. *J. Appl. Cryst.*, 44:1272–1276, 2011.

[187] A. Ichimiya. RHEED intensity analysis of Si(111) 7×7 at one-beam condition. *Surf. Sci.*, 192(2-3):L893–L898, 1987.

[188] I. Mochizuki, H. Ariga, Y. Fukaya, K. Wada, M. Maekawa, A. Kawasuso, T. Shidara, K. Asakura, and T. Hyodo. Structure determination of the rutile - TiO_2(110) - (1×2) surface using total-reflection high-energy positron diffraction (TRHEPD). *Phys. Chem. Chem. Phys.*, 18:7085–7092, 2016.

[189] J. A. Nelder and R. Mead. A simplex method for function minimization. *Comput. J.*, 7(4):308–313, 1965.

[190] Manual TRHEPD analysis software 2DMAT. Website University of Tokyo. https://www.pasums.issp.u-tokyo.ac.jp/2dmat/en/, accessed 29.11.2020.

[191] T. Hoshi, D. Sakata, S. Oie, I. Mochizuki, S. Tanaka, T. Hyodo, and K. Hukushima. Data-driven sensitivity analysis in surface structure determination using total-reflection high-energy positron diffraction (TRHEPD). *Comput. Phys. Commun.*, 271:108186, 2021.

[192] A. Kawasuso, S. Okada, and A. Ichimiya. Development and application of reflection high-energy positron diffraction. *Nucl. Instrum. Meth. B*, 171(1-2):219–230, 2000.

[193] A. Kawasuso, K. Kojima, M. Yoshikawa, H. Itoh, and K. Narumi. Effect of hydrogen etching on 6H SiC surface morphology studied by reflection high-energy positron diffraction and atomic force microscopy. *Appl. Phys. Lett.*, 76(9):1119, 2000.

[194] A. Kawasuso, M. Yoshikawa, K. Kojima, S. Okada, and A. Ichimiya. Rocking curves of reflection high-energy positron diffraction from hydrogen-terminated Si(111) surfaces. *Phys. Rev. B*, 61:2102, 2000.

[195] A. Kawasuso, T. Ishimoto, S. Okada, H. Itoh, and A. Ichimiya. Reflection high-energy positron diffraction at solid surfaces by improved electrostatic positron beam. *Appl. Surf. Sci.*, 194(1-4):287–290, 2002.

[196] Private communication with Prof. I. Mochizuki, Dec. 2020.

[197] A. Kawasuso, T. Ishimoto, Y. Fukaya, K. Hayashi, and A. Ichimiya. Top most surface studies by total reflection positron diffraction. *e-J. Surf. Sci. Nanotechnol.*, 1:152–157, 2003.

[198] A. Kawasuso, Y. Fukaya, K. Hayashi, M. Maekawa, S. Okada, and A. Ichimiya. Si(111) - (7$\times$7) surface probed by reflection high-energy positron diffraction. *Phys. Rev. B*, 68(24):241313(R), 2003.

[199] Y. Fukaya, A. Kawasuso, K. Hayashi, and A. Ichimiya. Observation of Si(111) - $\sqrt{3} \times \sqrt{3}$ - Ag surface at room temperature by reflection high-energy positron diffraction. *Appl. Surf. Sci.*, 244(1-4):166–169, 2005.

[200] Y. Fukaya, A. Kawasuso, and A. Ichimiya. Structural analysis of Si(111) - $\sqrt{21} \times \sqrt{21}$ - Ag surface by reflection high-energy positron diffraction. *Surf. Sci.*, 600:3141–3146, 2006.

[201] Y. Fukaya, A. Kawasuso, and A. Ichimiya. Structural analysis of Si(111) - $\sqrt{21} \times \sqrt{21}$ - (Ag, Au) surface by using reflection high-energy positron diffraction. *Surf. Sci.*, 601(22):5187–5191, 2007.

[202] Y. Fukaya, I. Matsuda, R. Yukawa, and A. Kawasuso. Structural analysis of Si(111) - $\sqrt{21} \times \sqrt{21}$ - (Ag, Cs) surface by reflection high-energy positron diffraction. *Surf. Sci.*, 606(23-24):1918–1921, 2012.

[203] A. Kawasuso, Y. Fukaya, M. Hashimoto, A. Ichimiya, H. Narita, and I. Matsuda. Atomic scale study of surface structures and phase transitions with reflection high-energy positron diffraction. *Mater. Sci. Forum*, 607:94–98, 2008.

[204] Y. Fukaya, M. Hashimoto, A. Kawasuso, and A. Ichimiya. Surface structure and phase transition of Ge(111) - 3$\times$3 - Pb studied by reflection high-energy positron diffraction. *Appl. Surf. Sci.*, 254(23):7827–7830, 2008.

[205] Y. Fukaya, A. Kawasuso, and A. Ichimiya. Structural analysis of Ge(111) - 3$\times$3 - Sn surface at low-temperature by reflection high-energy positron diffraction. *Surf. Sci.*, 600(18):4086–4088, 2006.

[206] Q. Wang, A. R. Oganov, Q. Zhu, and X.-F. Zhou. New reconstructions of the (110) surface of rutile TiO_2 predicted by an evolutionary method. *Phys. Rev. Lett.*, 113(26):266101, 2014.

[207] I. Mochizuki, Y. Fukaya, A. Kawasuso, K. Yaji, A. Harasawa, I. Matsuda, K. Wada, and T. Hyodo. Atomic configuration and phase transition of Pt-induced nanowires on a Ge(001) surface studied using scanning tunneling microscopy, reflection high-energy positron diffraction, and angle-resolved photoemission spectroscopy. *Phys. Rev. B*, 85(24):245438, 2012.

[208] Y. Fukaya, S. Entani, S. Sakai, I. Mochizuki, K. Wada, T. Hyodo, and S. Shamoto. Spacing between graphene and metal substrates studied with total-reflection high-energy positron diffraction. *Carbon*, 103:1–4, 2016.

[209] Y. Fukaya, I. Mochizuki, M. Maekawa, K. Wada, T. Hyodo, I. Matsuda, and A. Kawasuso. Structure of silicene on a Ag(111) surface studied by reflection high-energy positron diffraction. *Phys. Rev. B*, 88:205413, 2013.

[210] Y. Fukaya, I. Matsuda, B. Feng, I. Mochizuki, T. Hyodo, and S. Shamoto. Asymmetric structure of germanene on an Al(111) surface studied by total-reflection high-energy positron diffraction. *2D Mater.*, 3:035019, 2016.

[211] Y. Endo, Y. Fukaya, I. Mochizuki, A. Takayama, T. Hyodo, and S. Hasegawa. Structure of superconducting Ca-intercalated bilayer graphene/SiC studied using TRHEPD. *Carbon*, 157:857–862, 2020.

[212] Y. Fukaya, A. Kawasuso, and A. Ichimiya. Inelastic scattering processes in reflection high-energy positron diffraction from a Si(111) - 7×7 surface. *Phys. Rev. B*, 79(19):193310, 2009.

[213] Y. Fukaya, A. Kawasuso, and A. Ichimiya. Surface plasmon excitation at topmost surface in reflection high-energy positron diffraction. *e-J. Surf. Sci. Nanotechnol.*, 8:190–193, 2010.

[214] Y. Fukaya, A. Kawasuso, and A. Ichimiya. Reflection high-energy positron diffraction study on Si(111) - $\sqrt{3} \times \sqrt{3}$ - Ag surface. *Phys. Rev. B*, 75(11-15):115424, 2007.

[215] Y. Fukaya, A. Kawasuso, K. Hayashi, and A. Ichimiya. Precise determination of surface Debye-temperature of Si(111) - (7×7) surface by reflection high-energy positron diffraction. *Appl. Surf. Sci.*, 237(1-4):29–33, 2004.

[216] Y. Fukaya, A. Kawasuso, K. Hayashi, and A. Ichimiya. Dynamics of adatoms of the Si(111) - (7×7) surface studied by reflection high-energy positron diffraction. *Phys. Rev. B*, 70(24):245422, 2004.

[217] C. Hugenschmidt, H. Ceeh, T. Gigl, F. Lippert, C. Piochacz, P. Pikart, M. Reiner, J. Weber, and S. Zimnik. The upgrade of the neutron induced positron source NEPOMUC. *J. Phys. Conf. Ser.*, 443:012079, 2013.

[218] C. Piochacz, G. Kögel, W. Egger, C. Hugenschmidt, J. Mayer, K. Schreckenbach, P. Sperr, M. Stadlbauer, and G. Dollinger. A positron remoderator for the high intensity positron source NEPOMUC. *Appl. Surf. Sci.*, 255(1):98–100, 2008.

[219] M. Dickmann, W. Egger, G. Kögel, S. Vohburger, and C. Hugenschmidt. Upgrade of the NEPOMUC remoderator. *Acta Phys. Pol. A*, 137:149–151, 2020.

[220] T. Schmidt. *Messung der Brillianz des Positronenstrahls an NEPOMUC*. Bachelor Thesis, TU München, 2017.

[221] Website Staib Instruments GmbH. https://www.staibinstruments.com/rheed-30, acessed 28.09.2020.

[222] N. Grill, C. Piochacz, S. Zimnik, and C. Hugenschmidt. Novel pulsed particle accelerator for energy dependent positron re-emission experiments. *Rev. Sci. Instrum.*, 87(5):053304, 2016.

[223] M. Dickmann, J. Mitteneder, G. Kögel, W. Egger, P. Sperr, U. Ackermann, C. Piochacz, and G. Dollinger. Radio frequency elevator for a pulsed positron beam. *Nucl. Instrum. Meth. A*, 821:40–43, 2016.

[224] Private communication with Prof. T. Hyodo, Dec. 2020.

[225] J. Stanja, U. Hergenhahn, H. Niemann, N. Paschkowski, T. S. Pedersen, H. Saitoh, E. V. Stenson, M. R. Stoneking, C. Hugenschmidt, and C. Piochacz. Characterization of the NEPOMUC primary and remoderated positron beams at different energies. *Nucl. Instrum. Meth. A*, 827:52–62, 2016.

[226] E. Lachner. *Design and Construction of a New Deposition Chamber For Sample Preparation for PAES, EAES and XAES*. Diplomarbeit, TU München, 2012.

[227] B. Straßer. *Aufbau einer Anlage zur positroneninduzierten Auger-Elektronenspektroskopie*. PhD thesis, TU München, 2002.

[228] M. Stadlbauer, C. Hugenschmidt, and K. Schreckenbach. New design of the CDB-spectrometer at NEPOMUC for T-dependent defect spectroscopy in Mg. *Appl. Surf. Sci.*, 255(1):136–138, 2008.

[229] Product catalogue Goodfellow GmbH, Hamburg, 2021.

[230] N. Oshima, R. Suzuki, T. Ohdaira, A. Kinomura, T. Narumi, A. Uedono, and M. Fujinami. Brightness enhancement method for a high-intensity positron beam produced by an electron accelerator. *J. Appl. Phys.*, 103:094916, 2008.

[231] M. Thalmayr. *Ausheilen eines Ni(100) Einkristalls zur Positronenremoderation mittels einer neuen Heizvorrichtung*. Bachelor Thesis, TU München, 2014.

[232] Private communication with T. Gigl, Nov. 2017.

[233] J. T. Yates. *Experimental Innovations in Surface Science*. Springer International Publishing, 2nd edition, 2015.

[234] Website National Aeronautics and Space Administration (NASA). Outgassing data for selecting spacecraft materials online. https://outgassing.nasa.gov, accessed 03.10.2020.

[235] Technical Information MCP Assembly, Hamamatsu Photonics, 2006.

[236] Product catalog attocube systems AG, 2015/16.

[237] M. Reiner, P. Pikart, and C. Hugenschmidt. In-situ (C)DBS at high temperatures at the NEPOMUC positron beam line. *J. Phys. Conf. Ser.*, 443:012071, 2013.

[238] A. Elovskii. *Surface Structure of α-Al_2O_3 (0001) and $SrTiO_3$ Analyzed with a new RHEED Setup*. Master Thesis, TU München, 2019.

[239] K. G. Saw. Surface reconstruction of α-(0001) sapphire: An AFM, XPS, AES and EELS investigation. *J. Mater. Sci.*, 39:2911–2914, 2004.

[240] Data Sheet CapaciTorr D400-2, SAES Getters S.p.A., 2016.

[241] D. A. Duncan, J. H. K. Pfisterer, P. S. Deimel, R. G. Acres, M. Fritton, P. Feulner, J. V. Barth, and F. Allegretti. Formation of a thermally stable bilayer of coadsorbed intact and deprotonated thymine exploiting the surface corrugation of rutile TiO_2(110). *Phys. Chem. Chem. Phys.*, 18(30):20433–20442, 2016.

[242] F. Osaka, T. Ishikawa, N. Tanaka, M. López, and I. Matsuyama. Scanning tunneling microscopy of Cl_2-gas etched GaAs (001) surfaces using an ultrahigh vacuum sample transfer system. *J. Vac. Sci. Technol. B*, 12:2894, 1994.

[243] Y. Watanabe, Y. F. Nishimura, R. Suzuki, H. Uehara, T. Nimura, A. Beniya, N. Isomura, K. Asakura, and S. Takakusagi. Portable ultrahigh-vacuum sample storage system for polarization-dependent total-reflection fluorescence X-ray absorption fine structure spectroscopy. *J. Vac. Sci. Technol. A*, 34:023201, 2016.

[244] G. Firpo, F. Buatier de Mongeot, C. Boragno, and U. Valbusa. High performance portable vacuum suitcase. *Rev. Sci. Instrum.*, 76(2):026108, 2005.

[245] C. Piochacz, E. Erdnüß, T. Gigl, N. Grill, and C. Hugenschmidt. Enhancement and transformation of the phase space density of the NEPOMUC positron beam. *J. Phys. Conf. Ser.*, 505:012027, 2014.

[246] M. Kolíbal, J. Čechal, M. Bartošík, J. Mach, and T. Šikola. Stability of hydrogen-terminated vicinal Si(111) surface under ambient atmosphere. *Appl. Surf. Sci.*, 256(11):3423–3426, 2010.

[247] A. H. Castro Neto, F. Guinea, N. M. R. Peres, K. S. Novoselov, and A. K. Geim. The electronic properties of graphene. *Rev. Mod. Phys.*, 81(1):109, 2009.

[248] A. K. Geim and K. S. Novoselov. The rise of graphene. *Nat. Mater.*, 6:183–191, 2007.

[249] K. S. Novoselov, A. K. Geim, S. V. Morozov, D. Jiang, M. I. Katsnelson, I. V. Grigorieva, S. V. Dubonos, and A. A. Firsov. Two-dimensional gas of massless Dirac fermions in graphene. *Nature*, 438:197–200, 2005.

[250] P. R. Wallace. The band theory of graphite. *Phys. Rev.*, 71(9):622, 1947.

[251] N. D. Mermin. Crystalline order in two dimensions. *Phys. Rev.*, 176(1):250, 1968.

[252] X. Du, I. Skachko, A. Barker, and E. Y. Andrei. Approaching ballistic transport in suspended graphene. *Nature Nanotech.*, 3:491–495, 2008.

[253] J. S. Bunch, S. S. Verbridge, J. S. Alden, A. M. van der Zande, J. M. Parpia, H. G. Craighead, and P. L. McEuen. Impermeable atomic membranes from graphene sheets. *Nano Lett.*, 8:2458–2462, 2008.

[254] K. S. Novoselov, V. I. Fal'ko anf L. Colombo, P. R. Gellert, M. G. Schwab, and K. Kim. A roadmap for graphene. *Nature*, 490:192–200, 2012.

[255] W. A. de Heer, C. Berger, X. Wu, P. N. First, E. H. Conrad, X. Li, T. Li, M. Sprinkle, J. Hass, M. L. Sadowski, M. Potemski, and G. Martinez. Epitaxial graphene. *Solid State Commun.*, 143(1-2):92–100, 2007.

[256] K. Emtsev, A. Bostwick, K. Horn, J. Jobst, G. L. Kellogg, L. Ley, J. L. McChesney, T. Ohta, S. A. Reshanov, J. Röhrl, E. Rotenberg, A. K. Schmid, D. Waldmann, H. B. Weber, and T. Seyller. Towards wafer-size graphene layers by atmospheric pressure graphitization of silicon carbide. *Nature Mater.*, 8:203–207, 2009.

[257] W. J. Choyke, H. Matsunami, and G. Pensl, editors. *Silicon Carbide Recent Major Advances*. Springer, 2004.

[258] N. Day (Chemistry Department, University of Cambridge). Crystallography Open Database. http://www.crystallography.net, accessed 09.07.2021.

[259] K. Emtsev. *Electronic and Structural Characterizations of Unreconstructed SiC{0001} Surfaces and the Growth of Graphene Overlayers*. PhD thesis, Friedrich-Alexander Universität Erlangen-Nürnberg, 2009.

[260] P. N. First, W. A. de Heer, T. Seyller, C. Berger, J. A. Stroscio, and J.-S. Moon. Epitaxial graphenes on silicon carbide. *MRS Bull.*, 35:296–305, 2010.

[261] L. S. Ramsdell. Studies on silicon carbide. *Am. Mineralogist*, 32(1-2):64–82, 1947.

[262] A. J. Van Bommel, J. E. Crombeen, and A. Van Tooren. LEED and Auger electron observations of the SiC(0001) surface. *Surf. Sci.*, 48(2):463–472, 1975.

[263] I. Forbeaux, J.-M. Themlin, and J.-M. Debever. Heteroepitaxial graphite on 6H-SiC(0001): Interface formation through conduction-band electronic structure. *Phys. Rev. B*, 58(24):16396, 1998.

[264] U. Starke and C. Riedl. Epitaxial graphene on SiC(0001) and SiC(000$\bar{1}$): from surface reconstructions to carbon electronics. *J. Phys.: Condens. Matter*, 21(13):134016, 2009.

[265] F. Varchon, P. Mallet, J.-Y. Veuillen, and L. Magaud. Ripples in epitaxial graphene on the Si-terminated SiC(0001) surface. *Phys. Rev. B*, 77(23):235412, 2008.

[266] S. Goler, C. Coletti, V. Piazza, P. Pingue, F. Colangelo, V. Pellegrini, K. V. Emtsev, S. Forti, U. Starke, F. Beltram, and S. Heun. Revealing the atomic structure of the buffer layer between SiC(0001) and epitaxial graphene. *Carbon*, 51:249–254, 2013.

[267] C. Riedl, C. Coletti, T. Iwasaki, A. A. Zakharov, and U. Starke. Quasi-free-standing epitaxial graphene on SiC obtained by hydrogen intercalation. *Phys. Rev. Lett.*, 103(24):246804, 2009.

[268] K. V. Emtsev, F. Speck, T. Seyller, L. Ley, and J. D. Riley. Interaction, growth, and ordering of epitaxial graphene on SiC{0001} surfaces: A comparative photoelectron spectroscopy study. *Phys. Rev. B*, 77(15):155303, 2008.

[269] J. B. Hannon, M. Copel, and R. M. Tromp. Direct measurement of the growth mode of graphene on SiC(0001) and SiC(000$\bar{1}$). *Phys. Rev. Lett.*, 107(16):166101, 2011.

[270] C. Riedl, C. Coletti, and U. Starke. Structural and electronic properties of epitaxial graphene on SiC(0001): a review of growth, characterization, transfer doping and hydrogen intercalation. *J. Phys. D: Appl. Phys.*, 43:374009, 2010.

[271] F. Speck, M. Ostler, S. Besendörfer, J. Krone, M. Wanke, and T. Seyller. Growth and intercalation of graphene on silicon carbide studied by low-energy electron microscopy. *Ann. Phys.*, 529(11):1700046, 2017.

[272] F. Speck, M. Ostler, J. Röhrl, J. Jobst, D. Waldmann, M. Hundhausen, L. Ley, H. B. Weber, and T. Seyller. Quasi-freestanding graphene on SiC(0001). *Mater. Sci. Forum*, 645-648:629–632, 2010.

[273] F. Speck, J. Jobst, F. Fromm, M. Ostler, D. Waldmann, H. B. Weber M. Hundhausen and, and T. Seyller. The quasi-free-standing nature of graphene on H-saturated SiC(0001). *Appl. Phys. Lett.*, 99(12):122106, 2011.

[274] S. Oida, F. R. McFeely, J. B. Hannon, R. M. Tromp, M. Copel, Z. Chen, Y. Sun, D. B. Farmer, and J. Yurkas. Decoupling graphene from SiC(0001) via oxidation. *Phys. Rev. B*, 82(4):041411, 2010.

[275] C. Virojanadara, A. A. Zakharov, S. Watcharinyanon, R. Yakimova, and L. I. Johansson. A low-energy electron microscopy and X-ray photo-emission electron microscopy study of Li intercalated into graphene on SiC(0001). *New J. Phys.*, 12:125015, 2010.

[276] I. Gierz, T. Suzuki, R. T. Weitz, D. S. Lee, B. Krauss, C. Riedl, U. Starke, H. Höchst, J. H. Smet, C. R. Ast, and K. Kern. Electronic decoupling of an epitaxial graphene monolayer by gold intercalation. *Phys. Rev. B*, 81(23):235408, 2010.

[277] A. L. Walter, K.-J. Jeon, A. Bostwick, F. Speck, M. Ostler, T. Seyller, L. Moreschini, Y. S. Kim, Y. J. Chang, K. Horn, and E. Rotenberg. Highly p-doped epitaxial graphene obtained by fluorine intercalation. *Appl. Phys. Lett.*, 98(18):184102, 2011.

[278] S. Forti, A. Stöhr, A. A. Zakharov, C. Coletti, K. V. Emtsev, and U. Starke. Mini-Dirac cones in the band structure of a copper intercalated epitaxial graphene superlattice. *2D Mater.*, 3(3):035003, 2016.

[279] P. D. Bentley, T. W. Bird, A. P. J. Graham, O. Fossberg, S. P. Tear, and A. Pratt. Formation of quasi-free-standing graphene on SiC(0001) through intercalation of erbium. *AIP Adv.*, 11(2):025314, 2021.

[280] NIST X-ray Photoelectron Spectroscopy (XPS) Database. http://dx.doi.org/10.18434/T4T88K, accessed 11.12.2020.

[281] V. Borovikov and A. Zangwill. Step bunching of vicinal 6H-SiC{0001} surfaces. *Phys. Rev. B*, 79(24):245413, 2009.

[282] D. M. Pakdehi, P. Schädlich, T. T. N. Nguyen, A. A. Zakharov, S. Wundrack, E. Najafidehaghani, F. Speck, K. Pierz, T. Seyller, C. Tegenkamp, and H. W. Schumacher. Silicon carbide stacking-order-induced doping variation in epitaxial graphene. *Adv. Funct. Mater.*, 30(45):2004695, 2020.

[283] A. Kawasuso, M. Maekawa, M. Yoshikawa, and A. Ichimiya. Positron diffraction study of SiC(0001) surface. *Appl. Surf. Sci.*, 244(1-4):149–152, 2005.

[284] J. E. Boschker, L. A. Galves, T. Flissikowski, J. M. J. Lopes, H. Riechert, and R. Calarco. Coincident-site lattice matching during van der Waals epitaxy. *Sci. Rep.*, 5:18079, 2016.

[285] RHEED SIM developed by Hobara Rei. http://rei.to/software.html, accessed 2019.

[286] C. Virojanadara, A. A. Zakharov, R. Yakimova, and L. I. Johansson. Buffer layer free large area bi-layer graphene on SiC(0001). *Surf. Sci.*, 604(2):L4–L7, 2010.

[287] N. Sieber, T. Seyller, L. Ley, D. James, J. D. Riley, R. C. G. Leckey, and M. Polcik. Synchrotron X-ray photoelectron spectroscopy study of hydrogen-terminated 6H-SiC{0001} surfaces. *Phys. Rev. B*, 67(20):205304, 2003.

[288] Private communication with P. Schädlich, Dec. 2020.

[289] J. D. Emery, V. D. Wheeler, J. E. Johns, M. E. McBriarty, B. Detlefs, M. C. Hersam, D. K. Gaskill, and M. J. Bedzyk. Structural consequences of hydrogen intercalation of epitaxial graphene on SiC(0001). *Appl. Phys. Lett.*, 105(16):161602, 2014.

[290] T. Hanada, H. Daimon, and S. Ino. Rocking-curve analysis of reflection high-energy electron diffraction from the Si(111) - ($\sqrt{3} \times \sqrt{3}$) R30° -Al, -Ga, and -In surfaces. *Phys. Rev. B*, 51(19):13320, 1995.

[291] T. L. Cottrell. *The Strengths of Chemical Bonds*. Butterworths London, 1958.

[292] Y. Baskin and L. Meyer. Lattice constants of graphite at low temperatures. *Phys. Rev.*, 100:544, 1955.

[293] A. Markevich, R. Jones, S. Öberg, M. J. Rayson, J. P. Goss, and P. R. Briddon. First-principles study of hydrogen and fluorine intercalation into graphene-SiC(0001) interface. *Phys. Rev. B*, 86(4):045453, 2012.

[294] L. H. de Lima, A. de Siervo, R. Landers, G. A. Viana, A. M. B. Goncalves, R. G. Lacerda, and P. Häberle. Atomic surface structure of graphene and its buffer layer on SiC(0001): A chemical-specific photoelectron diffraction approach. *Phys. Rev. B*, 87(8):081403(R), 2013.

[295] A. Sinterhauf, G. A. Traeger, D.M. Pakdehi, P. Schädlich, P. Willke, F. Speck, T. Seyller, C. Tegenkamp, K. Pierz, H. W. Schumacher, and M. Wenderoth.

Substrate induced nanoscale resistance variation in epitaxial graphene. *Nat. Commun.*, 11(555), 2020.

[296] T. Sumi, K. Nagai, J. Bao, T. Terasawa, W. Norimatsu, M. Kusunoki, and Y. Wakabayashi. Structure of quasi-free-standing graphene on the SiC(0001) surface prepared by the rapid cooling method. *Appl. Phys. Lett.*, 117:143102, 2020.

[297] J. Sforzini, P. Hapala, M. Franke, G. van Straaten, A. Stöhr, S. Link, S. Soubatch, P. Jelínek, T.-L. Lee, U. Starke, M. Švec, F. C. Bocquet, and F. S. Tautz. Structural and electronic properties of nitrogen-doped graphene. *Phys. Rev. Lett.*, 116(12):126805, 2016.

[298] J. D. Emery, B. Detlefs, H. J. Karmel, L. O. Nyakiti, D. K. Gaskill, M. C. Hersam, J. Zegenhagen, and M. J. Bedzyk. Chemically resolved interface structure of epitaxial graphene on SiC(0001). *Phys. Rev. Lett.*, 111(21):215501, 2013.

[299] M. Conrad, J. Rault, Y. Utsumi, Y. Garreau, A. Vlad, A. Coati, J.-P. Rueff, P. F. Miceli, and E. H. Conrad. Structure and evolution of semiconducting buffer graphene grown on SiC(0001). *Phys. Rev. B*, 96(19):195304, 2017.

[300] S. Zimnik, F. Lippert, and C. Hugenschmidt. Upgrade of the surface spectrometer at NEPOMUC for PAES, XPS and STM investigations. *J. Phys. Conf. Ser.*, 505:012003, 2014.

[301] L. Papula. *Mathematische Formelsammlung für Ingenieure und Naturwissenschaftler*. Vieweg und Teubner Verlag, 10th edition, 2009.

[302] L. C. Andrews. *Special Functions of Mathematics for Engineers*. Oxford University Press, 2nd edition, 1998.

[303] E. Kuffel, W. S. Zaengl, and J. Kuffel. *High Voltage Engineering Fundamentals*. Butterworth-Heinemann, 2nd edition, 2000.

Acknowledgement

Many people contributed to this work and supported me during my doctorate. In particular, I would like to thank:

- Prof. Dr. Christoph Hugenschmidt, who draw my attention to the interesting field of positron physics and gave me the possibility to work in his research group. Thank you for many fruitful discussions, the overall support and the unique opportunity to design a new instrument at NEPOMUC.

- Prof. Dr. Winfried Petry for reading and assessing my thesis.

- Dr. Thomas Gigl, who gave me advice regarding the simulation and mechanical construction of the electrostatic beam optics. I benefit a lot from your experience, especially in the beginning.

- Sebastian Vohburger, who supported the mechanical assembly of the experiment. Without your hands-on mentality and the realistic assessment of the practical feasibility, this would not have been possible.

- All bachelor, master and working students who contributed to the project, namely: Shaghaiegh Azyzy, who developed the LabView control software, Artur Elovskii, who put the RHEED system into operation, Leon Chryssos, who implemented the python script for the camera readout and Wenjun Zhang as well as David Vogl, who helped with mechanical work.

- Dr. Marcel Dickmann and Dr. Francesco Guatieri, for their support, in particular during the beamtime at NEPOMUC.

- My colleagues Dr. Michael Leitner, Dr. Benjamin Rienäcker, Dr. Pascal Neibecker, Dr. Samantha Zimnik, Josef Ketels, Vassily Burwitz, Markus Singer, Ulrike Zweck, Lucian Mathes, Johannes Mitteneder, Matthias Thalmayr, Thomas Schmidt, Georg Zagler, Lukas Beddrich, Eicke Hecht, Rayi Pin-Yi Chiu, Martin Grosshauser and all others from the NEPOMUC group for hiking trips, barbecue and the great working atmosphere.

- The team of the FRM II workshop and the physics department (Zentralwerkstatt), for the discussion and manufacture of various components. In particular, I like to emphasize the great work of Lukas Winterhalter and Nicolas Siart, who actively contributed with their expertise to ensure the stringent requirements.
- Claudia Schweiger, Katarzyna Danielewicz, Michael Stanger and Susanne Mayr from the crystal laboratory, who fabricated customized insulators and performed the Laue characterization of the Si wafer.
- Thomas Rapp and Hermann Hagen, who gave design notes on the HV potentiometer and helped to enhance the HV stability of the setup.
- Eva Ernst, Andreas Schmid and Malte Kress for their help with the transfer of the setup to the experimental hall.
- Milan Antic who contributed to the laser safety concept that allows the operation of the sample heater at the FRM II.
- Dr. Wolfgang Braun for the advice to test the RHEED system with sapphire samples and the discussion of diffraction patterns.
- David Vogl, Claudia Paulus and Prof. Dr. Martin Brandt (WSI), who supported the etching of Si(111) with buffered HF.
- Philip Schädlich, Peter Richter, Dr. Florian Speck and Prof. Dr. Thomas Seyller (TU Chemnitz), for the growth and characterization of two sets of graphene samples. Peter also helped me a lot with the graphical representation of the XPS data.
- Prof. Izumi Mochizuki, Prof. Ken Wada and Prof. Toshio Hyodo (SPF, KEK) for their overall support during the entire project, starting from a kick-off meeting to discuss the Munich instrumentation to the beamtime during Covid-19. I got to know the Japanese culture, including the delicious food, and was impressed by your hospitality. ありがとうございます。
- My grandmother Inge, my brother Jens and my parents Heidi and Dieter for their constant encouragement during my doctorate and their belief in me. Finally, I like to thank my fiancée Kangkang, for her love and moral support during difficult times.